POLITECNICO DI TORINO

Corso di Laurea Magistrale in Ingegneria Biomedica

Tesi di Laurea Magistrale

SURFACE MODIFICATION OF TITANIUM FOR IMPROVEMENT OF SOFT TISSUE ADHESION AND REDUCTION OF BACTERIAL CONTAMINATION

Relatrici

Prof.ssa Silvia Maria Spriano
Ing. Sara Ferraris

Candidata

Alice Sartori

Aprile 2018

TABLE OF CONTENTS

CHAPTER III

TOPOGRAPHIC MODIFICATION TECHNIQUES AT THE MICRO AND NANO SCALES

CHAPTER IV

MATERIALS AND METHODS

CHAPTER V
RESULTS AND DISCUSSIONS

In orthodontics, to ensure the goodness and success of the prosthesis implant, it is necessary to achieve primary and secondary stability. Within the scope of the research, progress has been made with regard to the threaded portion of the prosthesis, which is in contact with bone tissue, while the possibility to obtain soft tissue adhesion without increasing bacterial adhesion is still an unmet need. The geometry, shape and topography of a dental implant affect its interaction with biological tissues, in particular for the collar and abutment regions, they should be designed with the main purpose of promoting the adhesion of gingival fibroblasts (HGFs), soft tissue cells of the oral cavity and minimizing bacterial adhesion. The purpose of this dissertation is to study the effect of surface modification on commercially pure titanium (grade 2) in the context of soft tissue interaction and reduction of bacterial contamination. The rationale of the work is to modify titanium surfaces from the topographical, chemical and biological point of view. As far as topography is concerned oriented nanogrooves have been produced in order to guide fibroblast alignment without increasing bacterial adhesion. Grooves have been produced by means of the *Electron Beam structuring* technique at the University of Graz. As far as the biological modification is concerned keratin nanofibers were deposited on titanium substrates by the *Electrospinning* technique at Consiglio Nazionale delle Ricerche (CNR-ISMAC) of Biella. The choice of keratin is due to its ability to increase adhesion, proliferation and cell differentiation. Afterwards, keratin coated samples were enriched with silver, known for its antibacterial properties. All samples thus processed have undergone superficial characterizations, e.g., roughness, FESEM, XPS and zeta potential. The biological response to modified surfaces was evaluated by means of

bacterial tests and cellular assays using the *S. aureus* strain and HGFs cells respectively at Eastern Piedmont University (Novara). From the analysis of the experimental data obtained, it can be concluded that Electron Beam obtained nanogrooves can promote cell orientation, while at the same time reducing bacterial adhesion on the surface. In addition, silver-enriched keratin nanofibres coatings exhibit antibacterial behaviour, and result a suitable substrate for cell adhesion and proliferation (no cytotoxicity effects). Considering the here summarized results the modified surfaces investigated in the present thesis appears as promising for the development of innovative dental implants (collar region).

KERATIN

The term "keratin" (Greek kératos, meaning horn) generally refers to insoluble proteins that contain the sulfur-rich cystine amino acid. In nature, it's possible to find different keratonic biomaterials with specific important roles, i.e., displaying of dominant behavior entangling animal horns and claws; facilitating mobility in the use of quills and hooves, guarding against environment by hair, wool, and feathers. Besides, natural patterns and colors of some keratins are expressive for survival behavior of animals e.g. for gender identification. Human keratins are found in hair and nails as well as in the epidermal layers of the skin and in general are found in the epidermal tissues of vertebrates. Some keratin materials occurred relevant value through technological developments and scientific understanding, engineering advances were paralleled by developments in the chemical and dye industries. This improvement, together with the development of synthetic fibers, has provided the great range of applications of keratin fibers that stays at the present time. Among the recent applications of sheep wool, we find: woolen fabrics for sportswear, ultrafine drawn and set wool-fibers, insect-resistant and moth-proofed wool batts, surface-treated wool fibers attached to the surface of polyester, reusable medical sheep skins to reduce pressure ulcers, which can be sterilized by laundering at high temperature. Moreover, the improved performance of the mechanical properties of keratin materials have been made practicable by a better understanding of their physical and chemical properties (1).

1 STRUCTURE AND COMPOSITION

Keratin is part of the family of fibrous, structural proteins, and its materials present many similarities among their primary, secondary and tertiary protein structures. The molecular weight of this protein in mammal changes in ranges from 40 to 70 kDa (2). A single keratin protein polymer chain is made of a polypeptide backbone that have side chains which include the salt-forming aspartic and glutamic acid residues, the lysine and arginine residues as well as the sulfur-rich cysteine that crosslinks the peptide chains (figure 1) and contributes to the physical and chemical stability of the keratins.
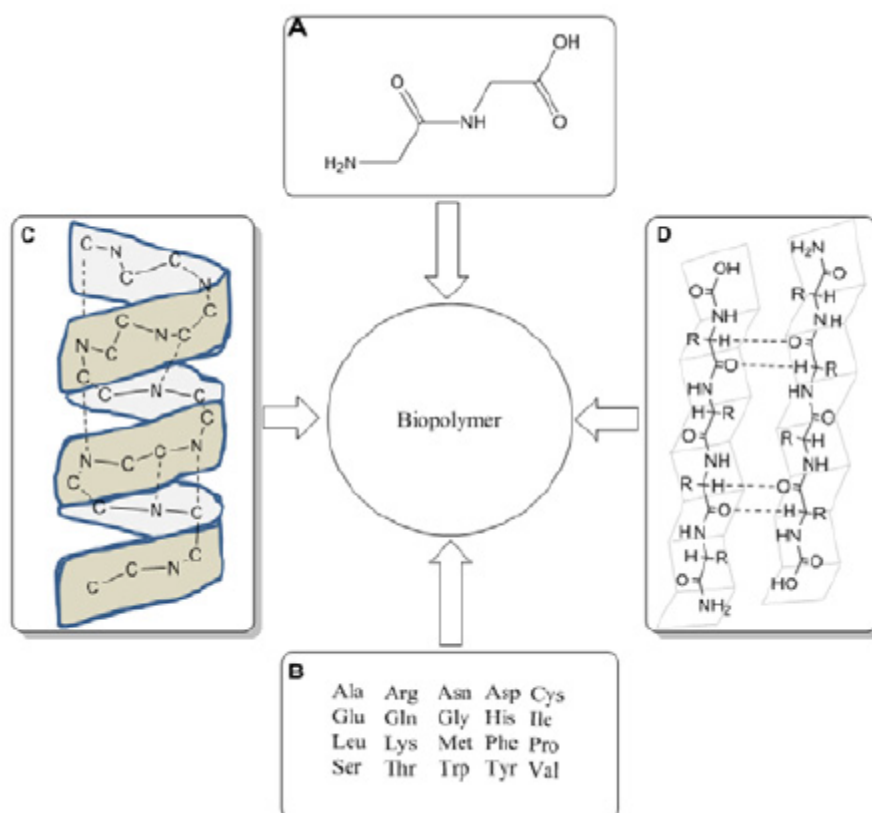
Figure 1. Schematic diagram of different components of keratin; (A) polypeptide single unit, (B) amino acid sequence, (C) α-helix, and (D) β-Sheets conformations of keratin protein (F1)

These side chains are also involved in the reactivity of the keratins when they are modified physically or chemically for commercial aims. The distribution of the amino acids changes from component to component of a given keratin (3). There are many types of keratins, one kind of differentiation is based on the isoelectric point, e.g., the distinction between type I (acidic or subfamily A) keratins and type II (basic or subfamily B) keratins. In humans, type I keratins have a pI of 4.9–5.4, while type II keratins have a pI of 6.5–8.5 (4). In bovines, type I keratins have a pI < 5.6 and type II keratins have a pI > 6.0.

Keratins that are specific to hair, nail or wool have a pI of 4.7–5.4 (5). In spite of the differences in the isoelectric point, 30% of the amino acid types and sequences are the same in the acidic and basic types of keratins and in other intermediate filaments (6), (7). Generally, keratins may be classified into α-, β- or amorphous by their x-ray diffraction patterns, reflecting the nature of the ordered, or not, molecular arrangements. The α-pattern is characteristic of mammalian keratin structures and refers to the α-helical conformation of the keratin protein, which chain gives many of the physical and mechanical properties of the biopolymer keratin, while the β-pattern is obtained from the avian keratins and the stretched form of mammalian keratins. A right handed α-helix is stabilized by hydrogen bonding, which occurs between the amide hydrogen and the carbonyl oxygen of the peptide groups, which are separated by three amino acid residues. The x-ray pattern of a keratin fiber includes reflections, which have been interpreted to represent larger molecular assemblies than the α-helix, e.g., a coiled coil rope consisting of α-helices. Other important structural parts of the fiber structure include the intermediate filament, which consists of several coiled coils embedded in an amorphous matrix. The intermediate filaments are similar in diameter in many keratins, while their packing changes from one type of keratin to another. The morphological and structural features of a keratin fiber as illustrated by a Merino wool fiber are: α-helix (1 nm), coiled coil rope (2nm), intermediate filament, like microfibril (7 nm), macrofibril (l00 nm), cortical cell (200 nm), cortex (20 pm), and cuticle (~ 1 pm thick)[1].

---

[1] Note: The numbers in parentheses indicate the approximate cross-sectional diameter or membrane thickness.
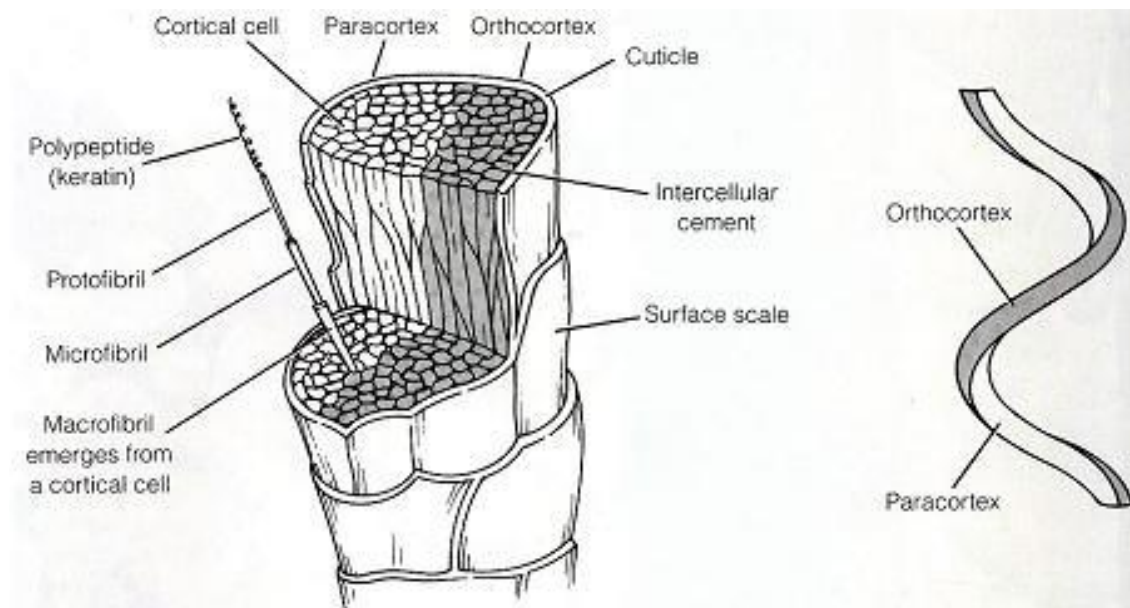
Figure 2. Section of a wool keratin fiber (F2)

The outer sheath of a fiber is the cuticle, which consists of fine overlapping scales that are smoother in the direction of fiber growth. The scale structure consists of a thin outer epicuticle followed by the exocuticle and the endocuticle layers, the principal difference between these is the relative cystine amino acid content ranging from 35% in the exocuticle to ~ 3% in the endocuticle. The cell membrane complex is a complicated system consisting of several thin layers embedded into an intercellular cement; one of the most important ones, the P-layer, contains lipids, about 50% 18-methyl eicosanoic acid. The bulk of the fiber is contained in the cortex, which consists of tightly packed cortical cells that present the same orientation of the fiber axis. Fine fibers have two bilaterally distributed populations, para- and ortho-cortices: The para-cortex is richer in sulfur than the orthocortex. Cortical cells contain intermediate filaments embedded in a cystine-rich cortical matrix and packed into macrofibrils. Besides the para and ortho cortex cells, there is another called the meso cortical cell, in which the intermediate filaments are packed even more regularly than in the para-type cells. The third component of a keratin fiber is the medulla, generally represented by empty space running more or less continuously down the center of a fiber but is practically absent in fine fibers. Another common component of a keratin fiber is melanin, which is the coloring matter of fibers and are ovoid or rod-shaped. While the composition and structure of a helical rope present similarities, the globular terminal domains differ from one keratin to another and only a few cystine cross-links are thought to bridge the two protein chains in the helical rod.

Pairs of coiled coil ropes interact to form groups of four α-helices and seven or more of these groups arrange themselves on the periphery of the microfibril. Although wool and other mammalian fibers are chemically inert under normal environmental conditions, they are reduced in the pH range 10-12 by sodium thioglycollate into two S-carboxy-methylkerateines (SCMK) labeled A and B, which can be separated. The SCMKA fraction is low in sulfur instead of SCMKB, which is high in this element (8).

1.1. Physical Properties

Mechanical and physical properties of keratins are conditioned by temperature, time, moisture content and physical modifications. Whereas properties of the keratins are sensitive to the moisture content, it is common to carry out measurements in water. The stress-strain curve of a keratin fiber under environment conditions has three regions: For the Hooks region, the Young's modulus values are similar to that of ice (~ 10 GPa), while an extended keratin fiber (up to 30% extension) immersed in water, for about 1 hour at 50°C, presents a recovery of mechanical properties, and this behaviour suggests that only cohesive hydrogen bonding and coulombic forces are involved. In the postyield region, if extention is continued, irretrievably of mechanical properties occurs, which points to a breakdown of covalent bonds. Moreover, no chemical damage to wool fibers in water is distinctly observed below 55 °C, but above this temperature and close to the boiling point, cysteine hydrolysis is detectable. This reaction is pH dependent (9).

1.2. Swelling and Contraction

Relevant structural diametrical and longitudinal variations can take place when keratin polymers are exposed to media and conditions that promote the breakage of cohesive forces or covalent bonds. This is the principal cause of the contraction and swelling of the material. A keratin fiber extended in water at 100°C (or higher), into the yield region generally presents a loss in stiffness of about 30% and a significant contraction in length (9).

2. KERATIN EXTRACTION

In natural state keratin biomaterials are covered to an extent with substances that are generally removed before any treatment. These waxy lipids offer chemical and physical protection from chemical attack derived from external environment, for this reason keratins are sometimes referred to as inert biomaterials. Moreover, these cleaning procedures are involved into the surface conditioning of a fiber (1).

Niloofar Eslahi at al. (10), propose an enzymatic hydrolisis which most important parameters are enzyme loading, type of substrate and surfactant, reducing agent concentration and hydrolysis time. The optimal condition to obtain maximum extraction is made using 1 g/L sodium dodecyl sulfate (as surfactant) and 2.6% (v/v) protease (as savinase), in addiction to 8.6 and 6.4 g/L sodium hydrogen sulfite (as reducing agent) for wool and feathers, respectively, at liquor to fiber ratio of 25 mL/g for 4 hr. Their results indicate higher degradation of wool fiber in comparison with feathers, due to the higher hydrophilic nature of the former. Sodium dodecyl sulfate polyacrylamide gel electrophoresis (SDS-PAGE) patterns shows that molecular weights of the extracted keratin proteins from wool and feather were lower than those for the untreated fibers. Likewise, FTIR spectra indicates no relevant changes in the chemical structure of the hydrolyzed fibers (10).

Prachi Kakkar et al**.** (11), provide the extraction of pure keratin from bovine hooves and characterized them with the manner of employment as an alternative material for tissue engineering applications. The keratin protein take from the pulverized hooves is extract by reduction and two polypeptide chains of molecular weight in the range of 45–50 and 55–60 KDa is determine using SDS-PAGE assay. Besides, FTIR analysis establish that hoof keratin adopts α-helical conformation with admixture of β-sheet. The keratin from the hoof expose a biocompatible behavior when analyzed with MTT assay using fibroblast cells, revealing more than 90% cell viability, for this reason hoof keratin would be useful for biomedical applications (11).

3. INTERACTION BETWEEN BACTERIA AND KERATIN

3.1. General features of oral bacteria

The environment in the human oral cavity provides a source of water, nutrients and moderate temperatures that allow the growth of characteristic microorganisms. The oral cavity is formed by the lips, cheeks, palate, teeth and gingival sulcus. Microorganisms range from Protozoa, Mycetes, Viruses to the dominators in numerical terms that are the Bacteria. Saliva plays an important role in the oral cavity, which is produced by the homonymous glands in quantities of 0.8-1.5 l per day (saliva production is considerably reduced during the night hours) and with antero-posterior pattern it is swallowed. This contains ions Na, K, Cl, Phosphates, Carbonates at a pH of 6.75 with a modest buffering power that aims to limit the cariogenic activity of bacteria. It also contains glycoproteins (which represent a potential nutrient for many micro-organisms), lysozyme, lactoperoxidase, lactoferrin, immunoglobulins, and the $OSCN^-$ and H_2O_2 thiocyanate ion. (14) The bacterial species prevalent in the oral cavity of healthy individuals include:

GRAM-POSITIVE	GRAM-NEGATIVE
	Actinobacillus
Actinomyces	*Bacteroides*
Arachnia	*Capnocytophaga*
Bacterionema	*Eikenella*
Bifidobacterium	*Fusobacterium*
Lactobacillus	*Haemophilus*
Micrococcus	*Leptotrichia*
Peptostreptococcus	*Moraxella*
Propionibacterium	*Neisseria*
Rothia	*Selenomonas*
Streptococcus	*Simonsiella*
Treponema	*Veillonella*
	Wolinella

Table 1. Bacterial species in the oral cavity of healthy individuals (T1)

Gram-positive bacteria are those that remain colored blue or purple after having undergone Gram staining, due to the peptidoglycan layer present in their cell wall. While, Gram-negative bacteria retain other contrasting colors (safranin or fuchsin) and appear red or pink. The different behavior with respect to Gram staining is due to the fact that Gram-negative bacteria have a decidedly thinner layer of peptidoglycan. Furthermore, peptidoglycan is located between two cell membranes: an internal cell membrane and an external bacterial membrane. Subdividing the bacteria according to the coloration they present after being subjected to the Gram method is the most used way to distinguish the different bacteria, even if this does not involve any degree of phylogenetic relationship between the different bacterial species. (15) Bacterial adhesion is particularly important for oral bacteria and gingival fissure area, which are tooth support structures, providing a habitat for a variety of anaerobic species. Bacteria accumulate on both hard and soft oral tissues in the form of biofilms. Oral bacteria have developed mechanisms to sensitize their environment and escape or modify the host. Furthermore, there is a dynamic balance between dental plaque bacteria and the innate host defense system. Of particular interest is the role of oral microorganisms in the two main dental pathologies: dental caries and periodontal disease (16).

3.2. Keratin and bacteria

Numerous study groups have analyzed the behavior of keratin extracted and treated against different bacterial strains. In literature, it is possible to find reports showing the antibacterial capacity of keratin but at the same time there are studies showing some bacterial keratinolytic ability, so it is a study topic to be further investigated in order to better classify the role and the capabilities of the keratin itself.

Sundaram et al. (17) synthesised keratin nanoparticles from chicken feathers. The structure and morphological characteristic of keratin nanoparticles were examined by using SEM and XRD while the antibacterial activity of keratin nanoparticle was identified by diffusion method against bovine mastitis, Staphylococcus aureus isolated from milk and *E. coli*. The zone of inhibition was found to be 11 mm in diameter against Staphylococcus aureus and 9.5 mm against *E. coli* at 100μg/ml concentration. The results show that the zone of inhibition formed for keratin nanoparticles is higher than the keratin extract (Table 2).

Organism	Concentration (µg/ml)	Zone of inhibition(mm)	
		Staphylococcus aureus	E.coli
Keratin Extract	25	4.5	5
	50	5	6
	75	6	6.5
	100	7.5	9
Keratin Nanoparticles	25	6	6.5
	50	7	8
	75	8.5	9
	100	9.5	11

Table 2. Antibacterial activity of Keratin nanoparticle and keratin (T2)

Despite this, many studies have shown the presence of a group of enzymes capable of hydrolyzing keratin. Examples of such enzymes are keratinase, beta-keratinase and protease which are produced by some microorganisms such as P. aeruginosa, Candida albicans, Aspergillus flavus, A. fumigatus, Trychophyton sp. and Bacillus subtilis (18). In the case study, attention was focused on oral cavity bacteria. The microbial invasion of gingival tissues has been observed in periodontal diseases. Proteases and, in particular, keratinases could be involved both in the dissemination of invading microorganisms and in the release of nutrients by host tissues.

Mikx et al. (19) measured keratinolytic activity by labeling keratin with isothiocyanated fluorescein (FITC). The insoluble nature of this substrate was used to separate it from degradation products labeled with FITC, directly measurable in the surfactant of the reaction mixture. It has been seen that DTT (dithiothreitol) stimulates keratinolytic activity, because reducing disulfide bridges and makes keratin more accessible to enzymatic degradation. This group also demonstrate that the keratinolytic activity may vary between the different bacteria and the strains of the same species (Table 3). For many bacteria, the proteolytic activity is an unstable fraction and the loss of proteolytic activity may occur due to the subculture.

Bacterium	Origin (no. of strains tested)	Mean keratinolytic activity ± SD (μmol of FITC released/liter per 5 h per OD unit)
Staphylococci		
Staphylococcus epidermidis	Human (3)	2.52 ± 3.00
Staphylococcus haemolyticus	Human (2)	0.34 ± 0.04
Staphylococcus hominis	Human (2)	0.11 ± 0.04
Staphylococcus saprophyticus	Human (1)	0.15 ± 0.03
Coryneforms		
Brevibacterium linens	Cheese (1)	2.80 ± 0.05
Brevibacterium epidermidis	Human (3)	0.96 ± 1.20
Corynebacterium glutamicum	Human (1)	0.03 ± 0.02
Corynebacterium minutissimum	Human (1)	0
Corynebacterium ovis	Sheep (1)	0
Rhodococcus equi	Horse (1)	0
Oral bacteria		
Treponema denticola	Human (1)	2.68 ± 0.28
Bacteroides gingivalis	Human (5)	2.43 ± 2.73
Bacteroides gingivalis	Dog (2)	15.86 ± 0.41
Bacteroides intermedius	Human (2)	0
Actinomyces odontolyticus	Human (9)	0

Table 3. Cell-bound keratinolytic activity of cutaneous and oral bacteria measured by the release of soluble fluorescent products of FITC-labeled keratin (T3)

Riffel et al. (20) selected bacteria with high keratinolytic activity, isolating them from a poultry processing plant, which has properties of keratinolytic activity and the ability to degrade keratin waste. A previously characterized Chryseobacterium sp. strain, designated as kr6, that presented keratinolytic activity was used for comparison. Bacterial identification was based on colony morphology, microscopic examination of Gram-stained cells, and biochemical tests and comparing the data obtained with standard species. To test the effect of temperature on growth and proteolytic activity were prepared milk agar plates for a primary screening and bacteria were inoculated onto plates and incubated at 22, 30, 37, 46, and 55°C for 24 h. Thus, only those strains that produced clearing zones in this medium were selected. These bacteria present different characteristics, i.e. a wide range of growth temperatures. Optimal proteolytic activity was found between 30-37 °C, while the principal known keratinolytic bacteria, e.g., some species of Bacillus, actinomycetes and fungi, mostly have a high temperature feather degradation activity. This study showed that pH value increase during feather degradation, a trend similar to other microorganisms with large keratinolytic activity.

This tendency may be associated with proteolytic activity, resulting in the release of excess nitrogen as ammonium ions. The increase in pH during cultivation is indicated as an important indication of the level of keratinolytic potential of microorganisms. In addition, the selected bacteria isolated were able to develop and show keratinolytic activity in different keratin waste. This would be useful for using these residues. These new insulates have potential biotechnological use in processes involving the hydrolysis of keratin.

Samen et al. (21) demonstrated in a study that Srr-1 protein is localized on the surface of S. agalactiae cells and that it is able to interact with human K4 (keratin type 4). The domain interacting with this mammalian protein was found to be restricted to one region of 157 aa. Finally, it was shown that Srr-1 promotes adherence of S. agalactiae to immobilized K4 and to epithelial HEp-2 cells. A growing set of reports describe the involvement of keratins in the interaction between host and pathogens (22). However, that is the first report describing a bacterial binding partner for K4.

Keratin

Keratin source	Treatment	Final material	Used Bacteria	Results	Ref.
Keratin nanoparticles from chicken feathers, keratin extract	100 mg of isolated keratin was suspended in 2ml of deionised water. 8ml of absolute ethanol was added to it under constant stirring.1 µl of 8% glutaraldehyde was added to it for the formation of keratin nanoparticles and it was stirred for 24hours. Nanoparticles were collected by centrifugation at 20,000rpm for 20 min. The prepared keratin nanoparticle was lyophilized and stored	Solution	Staphylococcus aureus, E.coli	The microbial invasion of gingival tissues has been observed in periodontal diseases. Proteases and, in particular, keratinases could be involved both in the dissemination of invading microorganisms and in the release of nutrients by host tissues.	**(17)**
Humans and animals cells	To obtain keratin, human callus was washed in water at 5C, defatted with a mixture of chloroform-methanol and ground in a mortar in liquid nitrogen. The keratin was then labeled with FITC. Keratin (20 g) and 250 mg of FITC were mixed in 200 ml of 0.2 M carbonate bicarbonate buffer (pH 9.6) and stirred for 4 h at room temperature of 20C. Labeled keratin was pelleted by centrifugation at 15,000 x g for 10 min and washed with the same bicarbonate buffer until the excess of free FITC was removed. To collect the finest keratin particles, the final suspension was allowed to settle for 10 min, and then 70 ml of the upper part of the 200-ml suspension was collected and pelleted by centrifugation. The labeled keratin was weighed, suspended to 2% (wt/vol) in sterile 0.2 M sodium phosphate buffer (pH 7.2), and stored at 4°C.m temperature(20°C).	Suspension	Staphylococci, Coryneforms, oral bacteria	The keratinolytic activity may vary between the different bacteria and the strains of the same species. For many bacteria, the proteolytic activity is an unstable fraction and the loss of proteolytic activity may occur due to the subculture.	**(19)**
Feather keratin	The organisms were cultivated in feather meal broth for up to 8 days at 30ºC. Enzymes were obtained by centrifugation at 10,000 g for 5 min, and culture supernatants were used as crude enzyme extracts. Keratinase activity was assayed at different cultivation times.	Enzymes	Proteobacteria Cytophaga-Flavobacterium group	Bacteria presenting high keratinolytic activity were selected	**(20)**
Human k4	S. agalactiae 6313 is a serotype III clinical isolate obtained from an infected neonate.E. coli DH5α was used for cloning purposes, and E. coli BL21 and ER2566 served as hosts for the production of Srr-1 and K4 fusion proteins. S. agalactiae was cultivated at 37°C in Todd-Hewitt yeast broth containing 1% yeast extract. S. agalactiae clones. E. coli was grown at 37°C in Luria-Bertani broth.The cell line HEp-2 was obtained from the HEp-2 is a human epidermoid carcinoma cell line of larynx. Tissue cultures were incubated in a humid atmosphere at 37°C with 5% CO2.	Tissue colture	Streptococcus Agalactiae, E. Coli	Srr-1 promotes adherence of S. agalactiae to immobilized K4 and to epithelial HEp-2 cells. A growing set of reports describe the involvement of keratins in the interaction between host and pathogens	**(21)**

Table 4. Summary of the studies above mentioned

12

4. INTERACTION BETWEEN FIBROBLAST AND KERATIN

4.1. General features of fibroblasts

Fibroblasts are mesenchymal cells that perform many vital functions during growth and in adulthood. They are responsible for the synthesis of extracellular matrix in connective tissue and play important roles in wound healing. This type of cells launches the inflammation process in the presence of invasive microorganisms, in addition to, induces the synthesis of chemokines through the exposure of receptors on its surface. The immune cells in response to chemical signals expressed by fibroblasts, initiate a cascade of events for eliminating the invasive microorganisms (23). Receptors present on the surface of fibroblasts also allow the regulation of the hematopoietic cells and provide a path for the immune cells to regulate the fibroblasts themselves. A series of diseases are associated with fibroblasts, both because fibroblasts are involved in their etiology or because of fibrosis that accompanies the damage of other cell types. Fibroblasts are one of the most accessible of mammalian cells and one of the simplest forms of cells to be able to grow in culture. Gingival fibroblasts (GF) are the most abundant types of cells present in the periodontal connective tissues and have distinct functional activities in the repair of the periodontal tissue as in the case of inflammatory diseases and periodontal diseases. Human gingival fibroblasts (HGF) express a wide variety of surface molecules including:

- CD26, that is a widely distributed 110 kDa cell-surface glycoprotein with known dipeptidyl-peptidase IV (DPP-IV) activity in its extracellular domain.
  This ecto-enzyme is capable of cleaving amino terminal dipeptides from polypeptides with either L-proline or L-alanine in the penultimate position. (24)
- CD71, that is also known as Transferrin receptor protein 1, TfR, sTfR, p90, TfR1, Trfr, which belongs to the peptidase M28 family and M28B subfamily. CD71 /TFR contains one PA, protease associated, domain. CD71 / TfR1 is required for iron delivery from transferrin to cells. CD71 is a potential new target in cases of human leukomia & lymphoma. (25)
- CD86, this gene encodes a type I membrane protein that is a member of the immunoglobulin superfamily. This protein is expressed by antigen-presenting cells, and it is the ligand for two proteins at the cell surface of T cells. (26)
- CD99, the protein encoded by this gene is a cell surface glycoprotein involved in leukocyte migration, T-cell adhesion, ganglioside GM1 and transmembrane protein transport, and T-cell death by a caspase-independent pathway. (27)

They also express mRNA for the protease-activated receptor-1 (PAR-1) and PAR-3. Furthermore, human gingival fibroblast (HGF) may be used as stem cells for periodontal tissue engineering (28).

4.2. Keratin and fibroblasts

Wang et al. (29) in order to evaluate the suitability of keratin hydrogels as substrates for cell culture, have fabricated hydrogels using keratins extracted from human hair by inducing polymerization with Ca^{2+} into an aqueous environment. These hydrogels exhibit highly branched and porous micro-architectures (figure 3). L929 murine fibroblasts have been used in a preliminary cell culture study to compare the in vitro biocompatibility of the keratin hydrogels with collagen type 1 hydrogels of similar viscoelastic properties. Results reveal that keratin hydrogels are comparable with collagen hydrogels in terms of the promotion of cell adhesion, proliferation and the preservation of cell viability. Furthermore, cells remain clustered in proliferative colonies within the keratin hydrogels but are homogeneously distributed as single cells in collagen hydrogels.
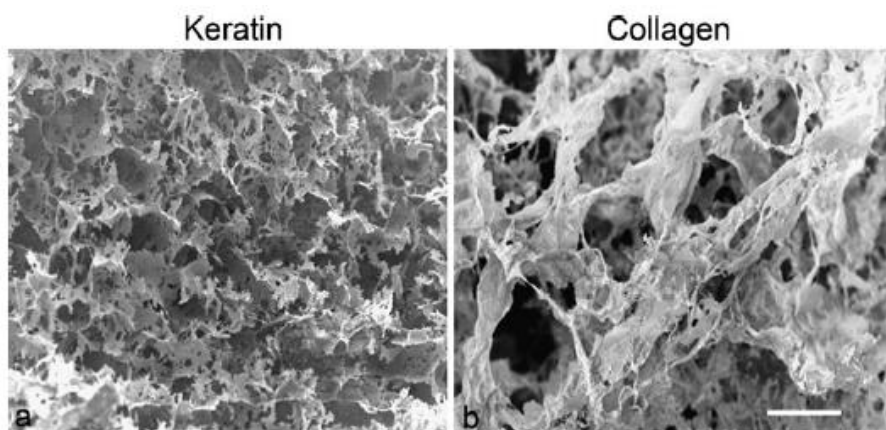

Figure 3. Scanning electron microscopic images of lyophilized keratin (a) and collagen type 1, (b) hydrogels, showing their highly porous and interconnected microarchitecture. Bar 200 μm. (F3)
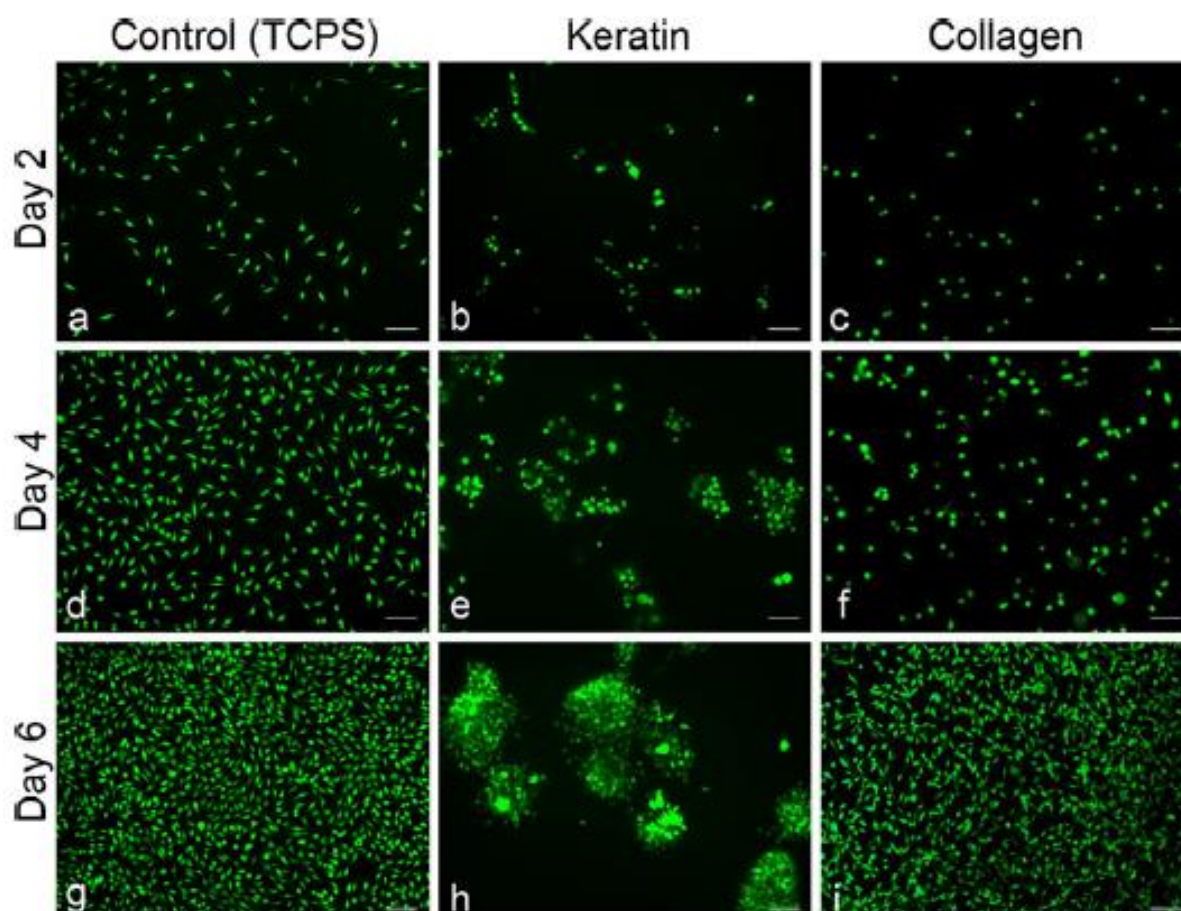
Figure 4. Fibroblasts morphology and distribution. For all groups, cells were seeded at a density of 10,000/cm2. Live cells were labelled green by calcein AM and observed under a fluorescent microscope at days 2, 4 and 6 post-seeding. Bars 100 μm. (F4)

As it possible to see from figures 4a, 4d and 4g, cells grown on tissue culture plastic surfaces (Control (TCPS)) in 24- well plates show typical spindle morphology at all time points and proliferate progressively to reach near 100% confluency by day 6. Images b, e, h cells grown on keratin hydrogels exhibit spindle morphology by day 6 of culture and proliferate in localized clusters. Images c, f, i only a small proportion of cells grown on collagen hydrogels exhibit spindle morphology at day 4 of culture. Cell distribution is comparable with that of controls (23).

Zackroff et al. (30) investigate some biochemical and immunological properties proteins isolated from BHK-21 and mouse 3T3 cells. These lines were chosen because they are classified as fibroblasts because of their morphology and they have been shown by immunofluorescence criteria to be "keratin-negative". Intermediate filaments, isolated from that variety of cultured fibroblasts, are composed principally of proteins of

molecular weights of 54 kDa and 55 kDa and are capable of forming paracrystals that exhibit a light or dark banding pattern when negatively stained with uranyl acetate. The dark bands are composed of longitudinally aligned filaments with a diameter of 2 nm. The center-to-center spacing between either dark or light bands is 37-40 nm. These dimensions are consistent with the secondary structure of IF polypeptides and suggest that the dark bands represent lateral alignment of a-helical coiled-coil domains. Immunoblotting, secondary structure, as well as amino acid composition data indicate that the paracrystal polypeptides with a molecular weight of 60 kDa-70kDa are similar to keratin. Thus, polypeptides with biochemical and immunological properties of epidermal keratin are present in cells normally considered to be fibroblasts.

Tachibana et all. (31) have fabricated wool keratin sponge scaffolds by lyophilization of an aqueous wool keratin solution after controlled freezing. To obtain stable sponges, with 1 cm in diameter, the freezing process was performed at -20 °C for three days. Thus, the resulting sponges did not show significant changes once they were subjected to a heat treatment of 60 °C for several hours. The characterization of the material at SEM (Scanning Electron Microscopy) have revealed a porous and homogeneous microstructure with pore size of ≈100 μm. At one day from seeding, cell adhesion was observed and subsequently cellular spreading on the surface of the sponge occured. At long-term cultivation, 23–43 days, cells were regularly counted to be ≈4.2–7.4 million per sponge. The maximum cell number was ≈37 times higher than on the same area of a commercially available plastic culture dish. After the long-term cultivation, SEM observation have revealed no abnormal morphology of living cells (figure 5a). In conclusion, results have shown that wool keratin sponges are useful scaffolds for long-term and high-density cell cultivation (figure 5b).
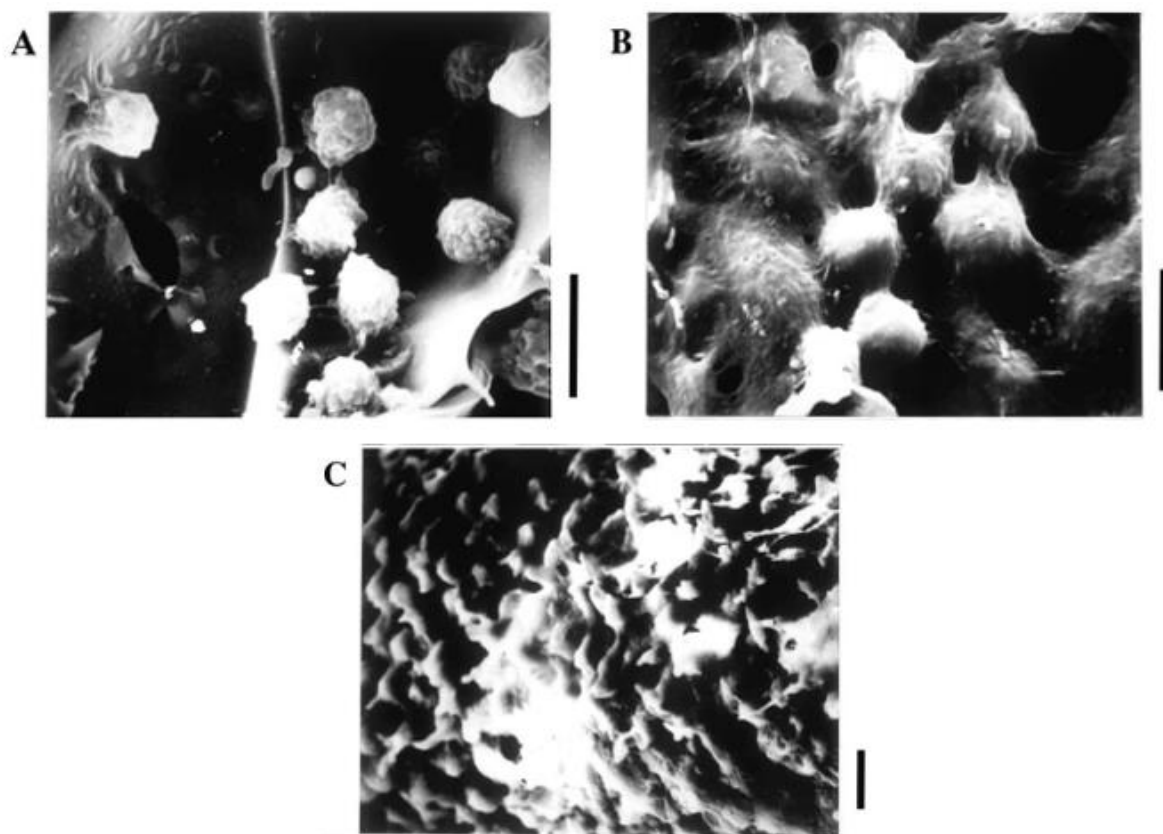
Figure 5a. SEM observation of fibroblast cells adhesion and colonization on keratin sponge. (A) At 1 h after seeding, ball-shaped cells adhered on the pore wall of the sponge. (B) At 1 day, fibroblasts spreading on the sponge. (C) At 23 days, fibroblasts were obs (F5)
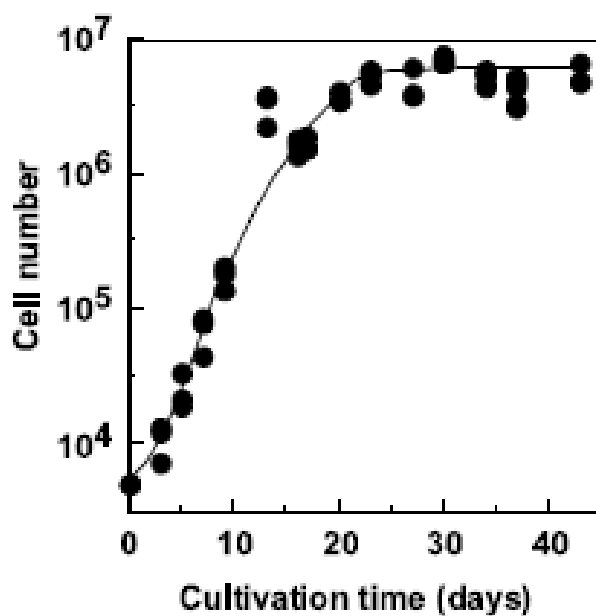

Fig 5b. Cell growth on keratin sponge. A number of 5000 fibroblast cells were seeded onto the sponges. Cell counting was performed by the MTT method within 10 days and by the Burton method over 10 days. (F6)

Keratin

Keratin source	Treatment	Final material	Fibroblast type	Results	Ref.
Keratin extracted from human's hair	Polymerization with Ca ions into aqueous enviroments	Keratin hydrogel	L929 murine fibroblast	Results reveal that keratin hydrogels are comparable with collagen hydrogels in terms of the promotion of cell adhesion, proliferation and the preservation of cell viability. Furthermore, cells remain clustered in proliferative colonies within the keratin hydrogels but are homogeneously distributed as single cells in collagen hydrogels.	**(29)**
Keratin extracted from wool	Lyophilization of an aqueous wool keratin solution after controlled freezing.	Keratin scaffold	L929 murine fibroblast	At one day from seeding, cell adhesion was observed and subsequently cellular spreading on the surface of the sponge occured. After the long-term cultivation, the maximum cell number counted was ≈37 times higher than on the same area of a commercially available plastic culture dish. In conclusion, results have shown that wool keratin sponges are useful scaffolds for long-term and high-density cell cultivation.	**(31)**

Table 5. Summary of the studies above mentioned

5. INTERACTION BETWEEN SILVER AND KERATIN

5.1. Antibacterial properties of silver

With the discovery of antibiotics, the use of silver as an antimicrobial agent, known since the Middle Ages, decreased drastically, but the presence of bacterial strains resistant to antibiotics has led to a renewed interest in silver. Only in recent years the availability of innovative technologies such as the use of radioactive isotopes and electronic microscopy has allowed to study the mechanism of action of silver as an antibacterial element. There are various hypotheses about the mechanism of action of antibacterial silver. It is believed that silver binds to the thiol groups -SH present in the enzymes causing their deactivation: silver forms stable S-Ag bonds with the compounds containing the -SH groups present in the cell membrane that are involved in energy production and in the Ion transport. Silver could also take part in the catalytic oxidation reactions leading to the formation of R-S-S-R disulfide bonds. The silver-catalyzed disulfide bridging, leads to variation in the structure of the enzymes, influencing their functions. In one of the suggested activity

mechanisms for antimicrobial silver, Ag + ion enters the cell and intercepts between complementary purine and pyrimidine bases, resulting in denaturation of the DNA molecule. Although this is still to be demonstrated, it is certain that silver ions are associated with DNA once they enter the cell. Most of the proposed mechanisms however provide that silver enters the cells by damaging them and is believed to be able to use membrane proteins that have, inter alia, the function of transporting molecules through the membrane by means of pores, ion channels, ion pumps or specific carriers. In order to carry out its antimicrobial activity, silver must be in ionic form, e.g., in the form of silver nitrate or a zeolite matrix or in the form of nanoparticles. The latter are of particular interest in their simplicity of production as well as for the high antimicrobial action and the ability to adhere to many products such as surgical masks and cotton fibers (32).

Sondi et al. (33) have carried out bacteriological tests using Luria-Bertani (LB) medium on solid agar plates and liquid systems, integrating them with different concentrations of silver nanoparticles. For the characterization of the bactericidal action of this nanoscale material, electronic scanning microscopy and electronic transmission microscopy have been used. The bactericidal effect of silver nanoparticles was investigated using approximately 10^5 colony forming units of *E. coli* strain B, cultured on LB agar plates supplemented with nano-sized silver particles in concentrations of 10 to 100 $\mu g\ cm^{-3}$. Silver-free LB plates cultured under the same conditions were used as a control. All plates were incubated for 24 h at 37 ∘C and the numbers of colonies were counted.
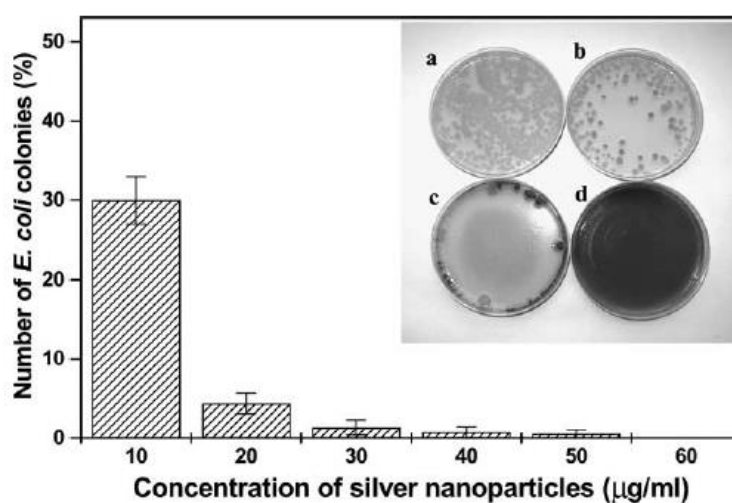

Figure 6. Number of E. coli colonies as a function of the concentration of silver nanoparticles in LB agar plates expressed as a percentage of the number of colonies grown on silver-free control plates.

(F7)

The image, in the upper right corner of the figure 6 above, shown LB plates containing different concentrations of silver nanoparticles: (a) 0, (b) 10, (c) 20, and (d) 50 µg cm^{-3}. To examine the bacterial growth rate, *E. coli* bacteria were grown in 100 cm^3 of liquid medium LB, supplemented with 10, 50 and 100 µg of silver nanoparticles per cm^3 of medium. Furthermore, growth rates and bacterial concentrations were determined by measuring the optical density at 600 nm every 30 min (OD of 0.1 corresponds to a concentration of 108 cells per cm^3). Results confirmed that treated *E. coli* cells were damaged while silver nanoparticles were found to accumulate in the bacterial membrane. A membrane with such morphology has a significant increase in permeability, resulting in death of the cell.

Kim et al. (34) have prepared stable silver nanoparticles characterizing their shape and size distribution by particle characterizer and transmission electron microscopic study. The antimicrobial activity of silver nanoparticles was investigated against *Escherichia coli* and *Staphylococcus aureus*. In those tests Muller Hinton agar plates were used and silver nanoparticles of various concentrations were enhanced in liquid systems. The effect of free-radical generation by nanoparticles on the inhibition of microbial growth was studied by electron spin resonance spectroscopy. In conclusion, *E. coli* was inhibited at the low concentration of silver nanoparticles, while the growth-inhibitory effects on *S. aureus* were mild, thus have suggest that silver nanoparticles can be used as growth inhibitors in different microorganisms, making them applicable to various medical devices and antimicrobial control systems.

5.2. Keratin and antibacterial silver

Wool fabric is a natural textile material with excellent characteristics and can form a skin-like micro-environment due to its protein composition, which is the same of human skin surface. Current approaches to the preparation of antibacterial fibers include coating, pad-dry-cure, chemical modification and electro-less plating processes with metallic elements, photo-catalytic materials and quaternary ammonium agents (35). Among them, durability of antibacterial properties is not so good by coating and pad-dry-cure. Chemical modification process can solve this problem, but it does damage to fabric's mechanical strength, as it is a chemically aggressive process. Silver electro-less plating is an effective way to give to the substrate antibacterial, antistatic properties and good durability. This technique can be started on the catalyzed surface, so for textiles it can be difficult to achieve due to the lack of reactive groups on the surface of the fiber. The adhesion between the metal layer and the wool fabric is intrinsically poor and this can be unfavorable to the use of metallization of textiles (35). The following study groups show the relationship that may arise between silver nanoparticles and keratin nanofibers.

Hadad et al. (36) have deposited silver nanoparticles on the surface of natural wool with the aid of powered ultrasound. Sonochemical irradiation is an effective method for the synthesis of nanophase materials and for the deposition and insertion of nanoparticles onto and into mesoporous and ceramic supports such as polymers (37). The sonochemical irradiation of a slurry containing wool fibers, silver nitrate, and ammonia in an aqueous medium for 120 min under an argon atmosphere produced a silver–wool nanocomposite. By varying the gas and reaction conditions, it was possible to control the deposition of metallic silver particles on the surface of the wool fibers. The efficiency of sonochemistry comes from the explosive collapse of the bubbles forming in the liquid as a result of sonochemical irradiation. The effect of very high temperatures obtained upon the collapse of the bubbles, following by high cooling rates, leads to the creation of nanostructure products. The advantage of this method is the achievement of a homogeneous coating with a small particle size distribution (37). The resulting wool samples deposited in silver were characterized by a variety of techniques, e.g., X-ray diffraction, transmission electron microscopy, high-resolution transmission electron microscopy, high resolution scanning electron microscopy, Brunauer and Teller physical adsorption method, X-ray photoelectron spectroscopy and diffused reflection optical spectroscopy.

The results shown that strong adhesion of silver to wool protein fibers was the consequence of the absorption and interaction of silver with the sulfur parts of the cysteine group.
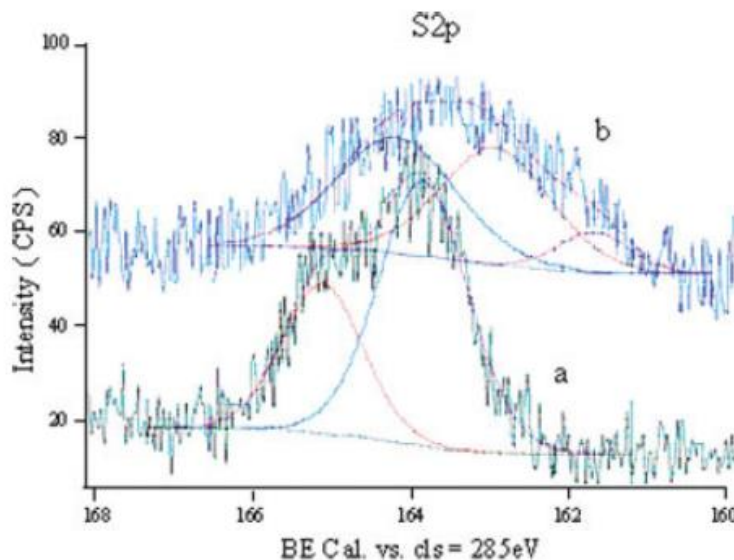

Figure 7. XPS spectra of (a) neat and (b) silver-coated wool fibers (F8)

In particular, XPS studies have revealed that silver nanoparticles were attached to the keratin fibers as a result of the interaction between either Ag^{+1} or Ag clusters and sulfur. The origin of these sulfur atoms is most likely the partial disconnection of the S-S bond in the keratin fibers at 161.7 eV band, as can be seen in figure 7. The stability of the coating is maintained even after several cycles of thermal treatments and simulation of washing and no change of silver concentration has been detected (37).

Lü et al. (38) based their study on a series of recent focal points in nanotechnologies that include the application of nanoparticles in biology, with variable dimensions, depending on conditions such as pH, temperature, substrate concentration, and reaction time. In addition to the fact that microorganisms, DNA and proteins can be used in the synthesis of silver nanoparticles through a strong affinity to silver with ligands -SH, $-NH_2$ and -COOH. They have decided to use keratin as capping agent of silver nanoparticles, as it has several advantages over other agents: First, keratin is one of the most abundant renewable proteins, also keratin content is greater than 50% in wool and feather.

The characterization of the material obtained during the experiment includes: The use of UV-vis spectroscopy, X-ray photoelectron spectrometer and X-ray diffraction spectrometers for the study of this metal nanoparticles formation. The scanning electron microscopy in vacuum and atomic force fluid microscopy to study the morphology. The Fourier Transform Infrared Spectroscopy (FTIR) to investigate the potential interactions between the silver core and the capping agent. Finally, the effects of keratin concentration on nanoparticles incubation were observed by UV-Vis spectra. In conclusion, it was found that under alkaline condition the incubation process was much faster than that under neutral pH conditions and experimental results have shown that keratin is a good stabilizer for silver nanoparticles. This is the first report that uses keratin as a nanoparticle capping agent.

Keratin

Keratin Source	Treatment	Final material	Characterization techniques	Principal results	Ref.
Keratin fibers from wool	Silver nanoparticles has been deposited on the surface of natural wool with the aid of powered ultrasound. The sonochemical irradiation of a slurry containing wool fibers, silver nitrate, and ammonia in an aqueous medium for 120 min under an argon atmosphere produced a silver–wool nanocomposite	Silver nanoparticles on the surface of natural wool	X-ray diffraction; Transmission electron microscopy; High-resolution transmission electron microscopy; High resolution scanning electron microscopy; Brunauer and Teller physical adsorption method; X-ray photoelectron Spectroscopy; Diffused reflection optical spectroscopy;	Silver nanoparticles were attached to the keratin fibers as a result of the interaction between either Ag+1 or Ag clusters and sulfur. The stability of the coating is maintained even after several cycles of thermal treatments and simulation of washing and no change of silver concentration has been detected	**(36)**
Keratin extracted from wool	The reducing agent, NaBH4 (0.3 mol/L), was passivated in a clean beaker at 30 C for 16h before using. Ag NPs were synthesized by adding the passivated NaBH4 solution in the mixed solution of AgNO3 (0.5 mol/mL) and keratin. The NP incubation was performed at room temperature for several days. The molar ratio of NaBH4/AgNO3 was kept constant at 5:1. The effects of pH and Keratin concentration was studied in two ways: (a) keeping the pH under the neural conditions; (b) keeping the molar ratio of keratin/AgNO3 at 1:20 while varying the pH of the keratin-AgNO3 solution (pH 7). Solutions were treated with the following procedure to remove excess salts and unbound keratin: The excess salts were removed by dialysis the solution against DI water for 24 h. To remove the unbound keratin, the dialyzed solution was treated by centrifugation at 13,000 rpm for 30 min. The unbound keratin will stay in the clear liquid after centrifugation. The Ag NPs solution without salts and unbound keratin is obtained by dissolving the precipitate after centrifugation.	Mixture	UV-vis spectroscopy; X-ray photoelectron spectrometer; X-ray diffraction spectrometers; Scanning electron microscopy in vacuum and atomic force Fluid microscopy; Fourier Transform Infrared Spectroscopy (FTIR); UV-Vis spectra;	Under alkaline condition the incubation process was much faster than that under neutral pH conditions and experimental results have shown that keratin is a good stabilizer for silver nanoparticles.	**(38)**

Table 6. Summary of the studies presented above

STRATEGIES TO REDUCE BACTERIAL ADHESION OVER DENTAL IMPLANTS

1. ORAL CAVITY

The oral cavity is delimited by the palate, the oral floor, the cheeks and lips, as well as from the uvula and the palatine arches, which extend laterally from the latter. The inside of the oral cavity is composed of the upper jaw and lower jaw teeth. The "oral cavity" (*Cavum ori*) is therefore definable as the region comprising the front and side portions of the dental area, which is largely covered by the tongue. The space between the teeth and the lips or cheeks is defined as "oral vestibule "(*Vestibulum oris*).
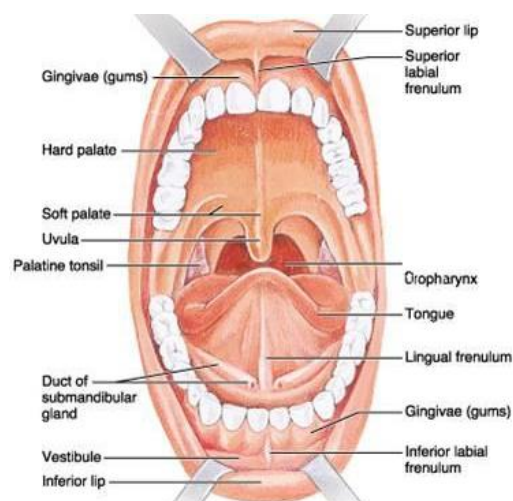

Figure 8. Oral cavity structure (F9)

The oral mucosa, which completely covers the oral cavity, is kept constantly wet by saliva produced by the salivary glands and contains sensory receptors for temperature and sense of touch.

While the surface mucous portion of the tongue has a predominance of sensory receptors for the sense of taste. The transition zone between the mucosa of the lips or cheeks and the mobile mucosa of the alveolar process is also called "vestibular plica". In the cheeks region, single mucous membrane protrudes towards the alveolar process, resulting in so-called "lateral vestibular frenules". In addition, from the mucosa of the upper and lower lip radiates a labial frenulum, which reaches the mucosa of the alveolar process. The mobile mucosa located around the rows of teeth turns into the gum, which is fixed to the maxillary bone. The lower limit of the oral cavity is the oral floor that is formed by the mylohyoid muscle, which extends from the lower jaw to the hyoid bone. In the anterior region of the oral floor there is a fold of mucous plica, which extends from the center up to the alveolar process, called "lingual frenulum". On the right and on the left of the lingual frenulum, two small bulges are visible, corresponding to the orifices of the submandibular salivary glands. Laterally the orifices begin the sublingual plica, where the sublingual salivary glands have several output ducts (Figure 8). (39)

1.1. Structure and shape of the teeth

Basically, in each tooth, it is possible to distinguish between the crown and one or more roots. In the transition area between the crown and the root lies the tooth collar. In the tooth region near the root apex, called "apical", there is a small opening (apical foramen) through which blood vessels, lymph vessels and nerves pass, entering the tooth to provide nourishment and innervation. The teeth, consist of three hard substances enamel, dentine and cement and a soft substance (dental pulp). Dental crowns visible in the oral cavity are covered with enamel, which represents the toughest substance of the human body. The enamel is formed for about 96% by calcium, phosphorus, carbonate, magnesium and potassium compounds, as well as water and organic compounds. Most of the tooth is made of dentine, which is surrounded by enamel at the coronal level and, in the root area, is covered with cement. Dentine is the second toughest substance in the human body and is composed of about 70% by inorganic substances, and by 20% by organic material and water. Dentine is produced by odontoblasts whose cellular bodies are located on the dental pulp edge. The cement covers the surface of the roots and has a structure similar

to that of the human bones. Cement is produced by cementoblasts, and is made up of 65% by inorganic compounds, mainly calcium and phosphate (39) (Figure 9).
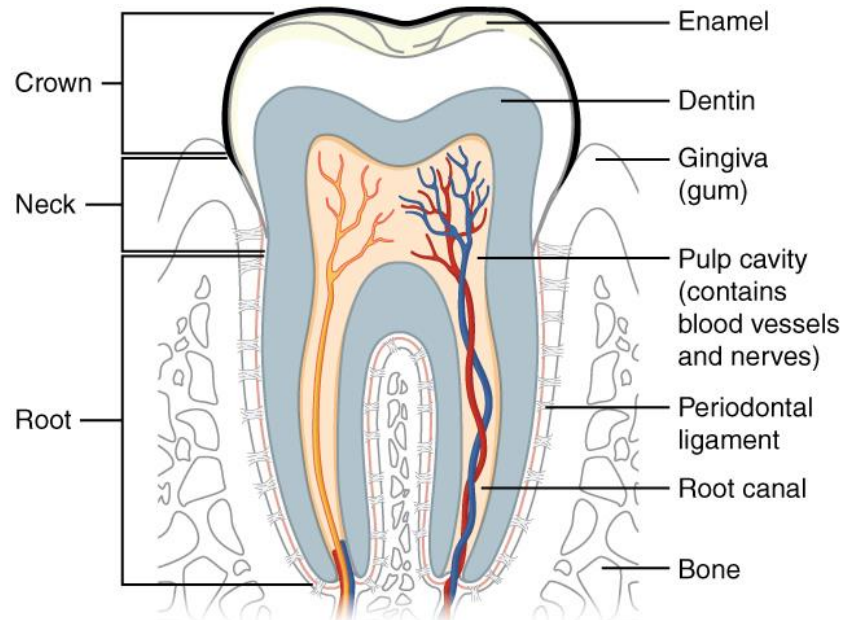

Figure 9. Tooth structure (F10)

1.2. Periodontum

All the elements that contribute to the anchoring of the teeth are part of the periodontium. The structure of the periodontium also helps to dampen the forces acting on the teeth, forces that, with the tight bite, can correspond to a weight of up to 80 kg. The tissue parts which fix the teeth and form the periodontium are:

- Periodontal ligament (desmodont or alveolar-dental ligament)
- Alveolar process (processus alveolaris)
- Cementum

The cement covers the root of the tooth from the neck to the root apex. Above it, fibers of the periodontal ligament develop and adhere to the alveolar bone. Therefore, it mainly serves to anchor the tooth inside the alveolus. Periodontal ligament consists mainly of connective tissue fibers, which connect the alveolar process to the tooth cement and extend into the compact bone layer of the alveolar wall. Therefore, single teeth do not grow with the alveolar bone, but are fixed to the membrane by connective tissue fibers. In this way, in biting and chewing the loading pressure becomes a tensile load.

Aside from the connective tissue fibers, the periodontal ligament contains a dense network of blood vessels that, in addiction to nourishing the cells of the cement and those of the connective tissue, dampen the chewing pressure. In the periodontal ligament, there are also nerve fibers that transmit to the teeth the sense of pressure and contact. In a healthy periodontium, the bone starts at about 1-2 mm below the cement-enamel line. (39) The gum covers the area of the dental neck as well as the top of the alveolar process and, as an interdental gum, forms an interdental papilla at the level of the spaces between each tooth. The free or marginal gingiva appears as a thin, uniform, wavy margin running parallel to the dental collars, whose width ranges from 1.5 to 2.5 mm. Within the marginal gingiva, connective tissue fibers adhere, inter alia, to cement and alveolar bone. In the area of dental neck, the marginal gingiva adheres by means of a special junctional epithelium, while between the tooth surface and the marginal gingiva is present a gingival sulcus (Sulcus gingivae) deep by 1 to 2 mm. The junction epithelium surrounds the dental neck as a ring, it forms the floor of the gingival groove or periodontal pouch and adheres to the tooth, protecting the bone from the external influences of the oral cavity. Unlike the marginal gingiva, the adherent gingiva, wide from 1 to 9 mm, is anchored to the alveolar bone and is immobile with respect to the underlying tissue. It also presents a pale pink appearance and has an opaque, dotted surface. These stippling are produced by the traction of the connective tissue fibrous bundles on the underside, which ensure fastening to the periosteum of the alveolar process and cement. In this way, the fastening is strong enough to resist the action of the forces in the chewing and bite. Finally, from the mucogingival junction line, the adherent gum turns in the mobile mucosa of the alveolar process (Figure 10). (39)
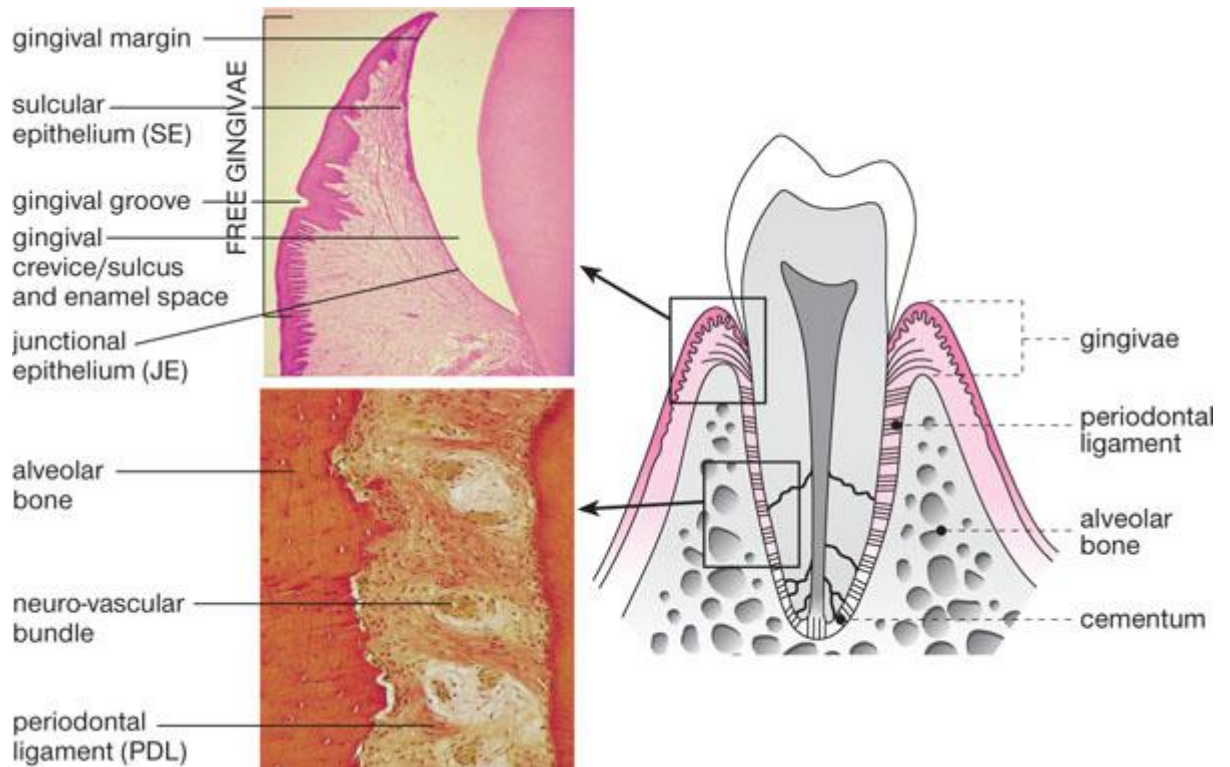
Figure 10. Anatomy of Periodontium (F11)

1.3. Periodontal Diseases

Periodontal inflammatory diseases are gingivitis and periodontitis. The most common primary cause of both is the bacterial plaque, whose formation can be accelerated by other factors defined as secondary causes and classified as Local Factors or Endogenous Factors. The former includes: Plaque, caries, oral breathing, reduced salivation, plaque retention points, edges of protruding crowns as plaque retention points, fillings poorly executed as a plaque retention points, anatomical features that make oral hygiene difficult and smoking. The latter refers to metabolic disorders such as diabetes mellitus, allergies, smoking, bad eating habits, hepatic disease, immune system disorders, stress, hormonal imbalances. The inflammation development, which is a defense response of the immune system, is crucial as it determines the extent and inflammation course itself. The local defense action is reinforced by increased blood flow. If the immune system fails to prevent the spread of the sublingual plaque, the junction epithelium is the first portion of tissue that is lost. As a result, the gap becomes permeable to bacteria and gingivitis becomes periodontitis, whose further course involves dental mobility and loss of teeth. (39)

In case of gingivitis, the spread of the disease is limited to the gum. In periodontitis, all parodontal tissues (gingiva, alveolar bone, desmodont and cement) are affected. Gingivitis from the plaque is an inflammation of the gum resulting from soft bacterial deposits and the main clinical symptoms are redness, swelling, loss of characteristic stippling appearance. In addition to gingivitis caused by the plaque alone, there are gingivitis caused by systemic factors such as hormonal upheavals that affect the immune system, resulting in a change in the inflammatory processes of the gums. Furthermore shapes, dimensions and particular positions of the teeth involving the presence of interstices, protruding edges of crowns and fillings, absence of contact points for the use of crowns or fillings and incorrect support of dental prostheses. In most cases, gingival and periodontal recessions are a clear indication of aggressive brushing techniques: excessive frequency or pressure, use of too hard bristle brushes (Figure 11).
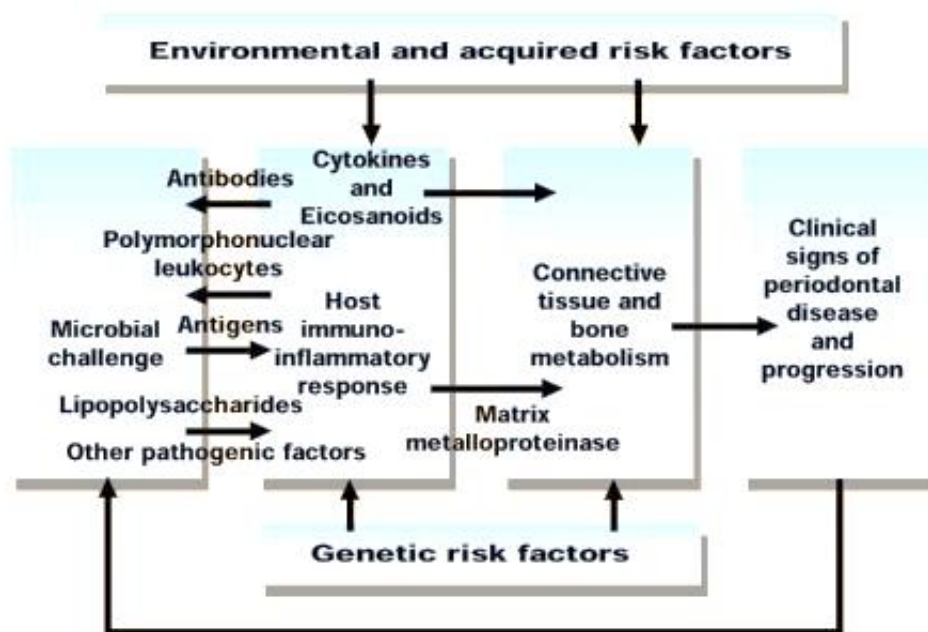

Figure 11. Current paradigm of periodontitis. (F12)

Treatment of periodontal diseases involves the following procedure:

- Blocking the Infection. The first step involves consulting the patient, followed by removal of plaque, concretions and tartar;

- Elimination of causes through careful removal of concretions close to dental roots, including removal of gum to facilitate access, removal of granulocyte tissue (rich in capillaries and inflamed) from gum and bone pouches, antibiotic accompanying therapy in case of aggressive course of the pathology and mucogingival surgery;

  - Conserving the result. Maintenance therapy is associated with the patient's constant follow-up with supportive measures, such as smoothing of any protruding edges of the filling. (39)

2. DENTAL IMPLANTS

2.1. General features of dental implants

The term "implant" refers to the insertion into the body of artificial or human material, partially or totally, in the latter case it is defined as transplantation. Dental implantology focuses mainly on the insertion of artificial roots into the jaw for replacing one or more teeth or for attaching a removable prosthesis. Implants can replace individual missing teeth or act as artificial bridges with fixed or removable support, and also contribute to stabilizing total prostheses and thus improving chewing function. (39) Dental implants are made up of inert, alloplastic materials and embedded in the jaw for the treatment of tooth loss and to help replace the lost structures following trauma, cancer and congenital defects. The most common type of dental implant is the endosseous, comprising a single implant unit and screw or cylinder shapes, arranged in a hole in the dental or alveolar bone. Commercially pure titanium and titanium alloy are the most common constituents of dental implants. However, alternative materials include ceramics such as aluminum oxide and other alloys (gold and nickel-chrome-vanadium). Generally, endosseous implants have a coating that may include plasma sprayed titanium or a hydroxyapatite layer to enhance initial bone osseointegration. (40) 'Osseointegration' was discovered by P. I. Branemark in 1969, when he observed that a piece of titanium embedded in a rabbit bone became firmly anchored and difficult to remove. Following one year of observation, no inflammation was detected in the peri-implant bone, while soft tissue had formed an attachment to the metal and bone to the titanium. (41)

The Branemark system of dental implants was introduced in 1971. After endosseous implant fixtures are surgically inserted into bone, the process of osseointegration begins. Osseointegration is considered "a direct, structural and functional connection between organised vital bone and the surface of a titanium implant, capable of bearing the functional load". (42) This is possible because the titanium surface oxide layer, mainly titanium dioxide, is biocompatible, reactive and spontaneously forms calcium phosphate apatite. In addition, the titanium oxide surface of the implants results in a union with the superficial gingival that can block the entry of oral microorganisms. As a result, the interface between the soft tissue and the implant is similar to the union between the tooth and the gum. Dental implants are predominantly placed in primary care settings, commonly in general dental practice in local anesthesia. Despite this and the contaminated oral surgical field through which they are placed, success rates are reported as being as high as 90% e 95%. (43)

Dental implants are generally divided into five typologies (Figure 12):

- Subperiostal implants: a metallic structure that is surgically placed between the bone surface and the periosteum. The implant pillars pierce at some points the mucosa that covers it. These implants are seldom used due to the shape that is unlike natural roots, thus less reproducing the right incentive to osteointegration, which is why they have high percentages of failure;

- Endosseous implants: the implant is inserted into the bone in a direct way; while the closed ones, under the periosteum, cannot communicate with the oral cavity, the open ones are equipped with a pillar having such function; most part of endosseous implants are of the latter type. Moreover, there is a subtype of endosseous implant that will remain underneath an integer epithelial layer for several months (cicatrization phase) and is only exposed later on. These are the most commonly used systems, for the sake of simplicity of surgical techniques and for the possibility of applying a new implant in case of failure. Subperiostal endosseous implants are a combination of the two previous types (one part is above the bone; one part is inside it);

- Transosseous implants: are specific to the jaw and through vertically it;

- Transdental implants: they are also called endodontics as they stabilize the teeth in which they are placed, as if they had a kind of "biological collar" for the anchorage between the separation seal with the oral cavity and the periodontium of a natural tooth;

- Intramucosal implants: they are inserted into the lining mucosa by fixing to a base prosthetic and because they do not perforate the lining epithelium and do not remain permanently in the implant site, they are more suitable for classical prosthesis rather than implant prostheses. (44)
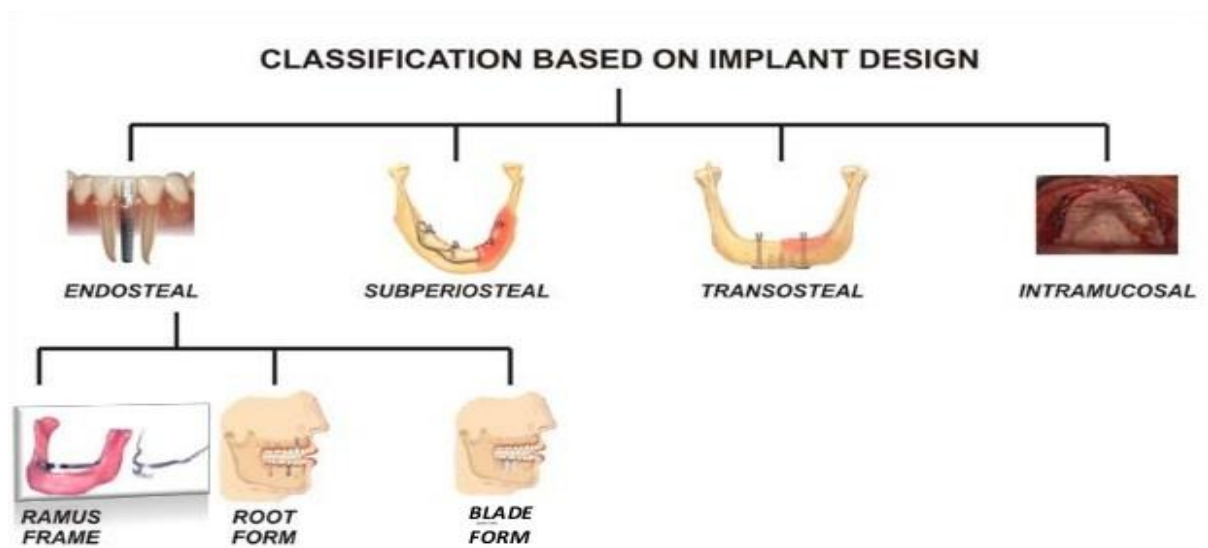

Figure 12. Types of dental implants. (F13)

2.2. Parts of a dental Implant

Dental implantology is the branch of dentistry that is concerned with implants aimed at replacing the missing teeth. (45) Dental implant, like the endosseous or the subperiostal implant, as an artificial root, is inserted firmly into the alveolar bone and can successfully support a single capsule or a bridge, or it can act as an excellent anchor to an unstable or bad denture tolerated by the patient. Depending on needs, is possible to insert one or more implants, to replace only one tooth, multiple teeth (partial dental prosthesis) or all the teeth of the arch (full dental prosthesis).

A dental implant consists essentially of 3 parts (Figure 13):

Figure 13. Parts of dental implant. (F14)

- Prosthesis: artificial crown replacing the natural one;
- Abutment: small structure that connects the prosthesis implant;
- Implant: structure, generally screw, which comes inserted into the bone; The transmucosa area of the implant is in contact with gingival tissues and serves to ensure a good integration of the gingival mucosa; (46)

The dental implant can be done according to two distinct techniques of implant surgery: Immediate loading implantology and deferred loading implantology. The former provides the insertion of the implant and the anchorage of the crowns taking place in one phase. For this type of operation, dental implants are used in monobloc, that is composed of only one piece equipped with the stump, or modular, in which the stump is placed at the same time as the implant. The latter is a technique that is performed in two phases: in the first step, a gingival patch is opened and the implant, on which a top is placed, is inserted; Then the gum is closed with stitches. The success of insertion depends on how much bone tissue grows around the implant, incorporating it into its structure, in the next three or six months after operation. The second step involves inserting and positioning the prosthesis. (47) The time span between one phase and another Is generally 3-4 months for the mandible and 5-6 months for the upper jaw. (48)

Currently, thanks to the scientific research concerning the surface and the shape of the implants, it is possible to imagine an immediate load after the intervention, i.e. the patient can have a permanent prosthesis within 12 hours. (46) Implant stability can be seen as a combination of:

- Mechanical stability, which is the result of the compressed bone holding the implant firmly, in situ;
- Biological stability, which is the result of the formation of new bone tissue, which forms on the implant site thanks to osteointegration.

Mechanical stability, named also primary stability, is generally high at once after insertion of the implant. This stability is due to the mechanical compression of the bone when the system is inserted, and it decreases over time. Biological stability or secondary stability, however, does not occur immediately after placement. It becomes clear only when new bone cells are formed in the implant site and Increases with time. In conclusion, as a result of the osteointegration, initial mechanical stability is strengthened and replaced by biological stability and the final stability level of an implant is the sum of the two. However, stability does not remain constant after implant insertion, for example, an initial diminish in stability occurs, followed by a next increase when the plant becomes biologically stable (Figure 14). (49)
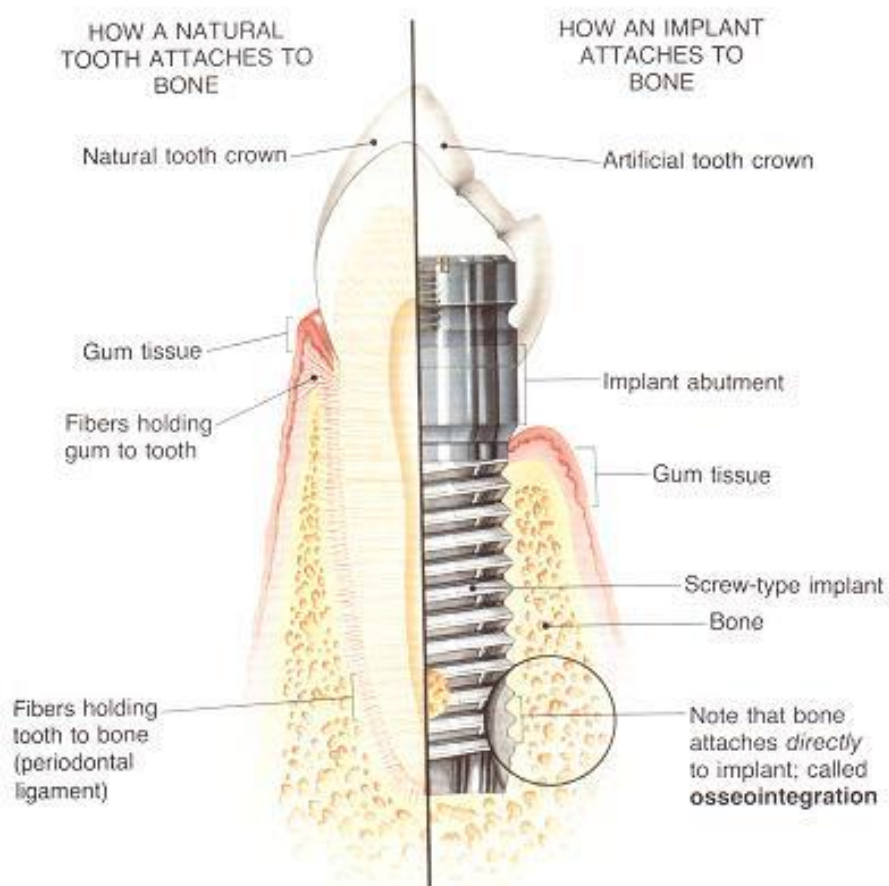
Figure 14. Comparison between implant and healthy tissue. (F15)

2.3. Materials of a Dental Implant

The most commonly used material for dental implants is commercially pure titanium, grade 2 or grade 4. This material has demonstrated a high rate of success due to it biocompatibility and the ability to be osteointegrated allowing to use it in direct contact with living bone. In addition to biocompatibility, titanium has a high resistance to corrosion, property conferred by the formation of a thin layer of titanium inert oxide on its surface, e.g. TiO_2. (46) Another advantage resulting from this corrosion resistance is the absence of taste, once inserted into the oral environment. Finally, the thermal conductivity of commercially pure titanium is particularly low, approximately 20 W $(m*K)^{-1}$, value which is 3.2 times lower than that of alloys CrCo and 13.5 times less than gold. This helps to avoid irritation of the dental pulp, as opposed to other alloys. The patient can then enjoy drinks and hot or cold foods without accusing the discomfort of over-temperature overlays too high.

Other materials used, though more limited, are titanium alloys and in particular the Ti6Al4V alloy, which has both higher tensile strength and yield strength than titanium (860 MPa and 795 MPa respectively). However, these alloys are less used because of their corrosion resistance, which is lower than that of commercially pure titanium. Figure 8 shows some properties that make commercially pure titanium a desirable material for orthodontic implants (Figure 15).

Bar (ASTM B348) Plate (ASTM B265)		GRADE 1	GRADE 2	GRADE 3	GRADE 4
MAX CHEMISTRY LIMITS (%)					
O_2	Bar	0.18	0.25	0.35	0.40
	Plate	0.18	0.25	0.35	0.40
Fe	Bar	0.20	0.30	0.30	0.50
	Plate	0.20	0.30	0.30	0.50
H_2	Bar	0.015	0.015	0.015	0.015
	Plate	0.015	0.015	0.015	0.015
C	Bar	0.08	0.08	0.08	0.08
	Plate	0.08	0.08	0.08	0.08
N_2	Bar	0.03	0.03	0.05	0.05
	Plate	0.03	0.03	0.05	0.05
MIN MECHANICAL PROPERTIES					
Ultimate Tensile Strength (ksi)	Bar	35	50	65	80
	Plate	35	50	65	80
Yield Strength* (ksi)	Bar	20	40	55	70
	Plate	20–45	40–65	55–80	70–95
Elongation (%)	Bar	24	20	18	15
	Plate	24	20	18	15
PHYSICAL PROPERTIES					
Density (lbs/in³)		0.163	0.163	0.163	0.164
Elastic Modulus (×10⁶ psi)		14.9	14.9	14.9	15.1
Beta Transus Temp (°F)		1630	1675	1690	1740
Weldability		Excellent	Excellent	Good	Good

*Min–max range for plate

Figura 15. Data sheet of commercially pure Titanium (F16)

Despite the great success of titanium as a material used in these types of implants, a growing interest in metal-free, non-metal dental materials emerged recently.

Ceramic materials have a reduced tendency to corrosion, they are also relatively inert and have low solubility; they have good resistance to temperature and low electrical conductivity. Besides, the use of titanium may be a disadvantage with regard to aesthetics if a thin layer of gum occurs, a problem that could also be accentuated locally by the reactions of the soft tissue with titanium. Ceramic materials, instead, do not present this aesthetic issue. (46) Table 7 shows the materials used mainly for the various parts of a dental implant:

PART OF IMPLANT	MATERIAL
Implant	Titanium
	Zirconia
Abutment	Titanium
	Ceramic
	Metal-Ceramic
Prosthesis	**Ceramic**
	Gold

Table 7. Material used for specific part of implant (T4)

2.4. Issues with perimplant soft tissue

Dental implants, among all types of medical implants, are the only ones that can create two interfaces: one with the bone and the other with the gums. Maintaining both interfaces is essential for the goodness and durability of the implant. The gingival epithelial tissue, at the point where the natural tooth emerges from the bone, forms a barrier between the inner and outer environment. The tissue must then be regenerated around the neck to protect the underlying connective tissue, thus preventing mobility and worse, detachment of the implant. (50) The adhesion of the soft tissue, i.e. the gingiva, to the collar of the dental implants is an underdeveloped problem, unlike the adherence of the bone tissue to the threaded part of the implant, however, is a key point to ensure the success of the implant. In addition, as can be seen in Figure 16, both bone tissue and soft tissue developing around a dental implant are different from the configuration around the natural tooth (Figure 16).
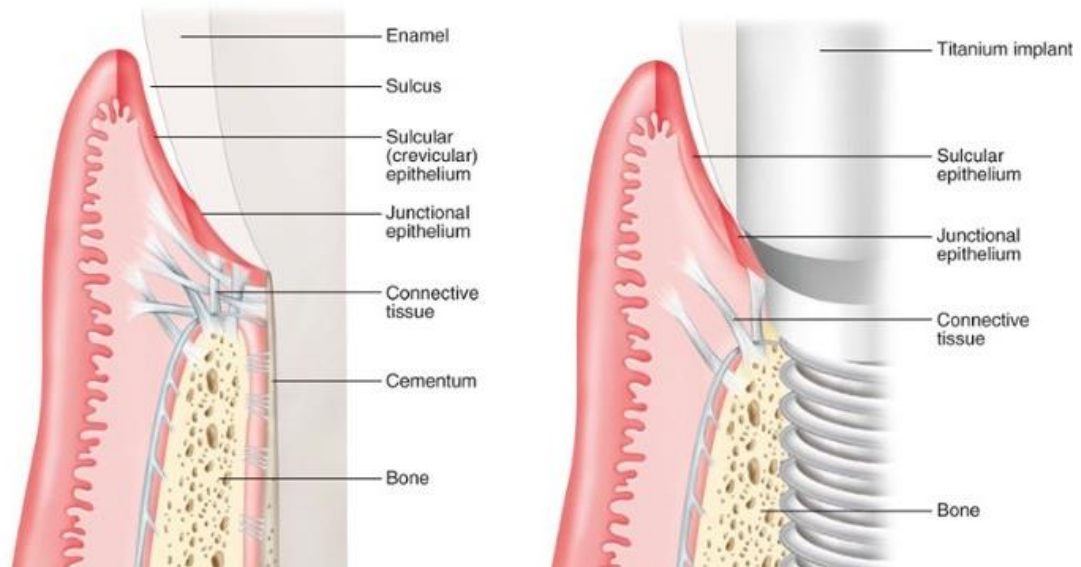
Figura 16. Comparison between pre - and post - implant tissue. (F17)

In natural teeth the continuity between epithelium, connective tissues and tooth is guaranteed by the basal lamina, which connect the dental enamel and the epithelium adhering to the natural tooth. These structures are missing in tissues close to dental implants. (51) Another fundamental difference between periodontal and perimplantary tissues is the soft tissue anchoring, in fact, while the periodontal mucosa is attached to the tooth by means of collagen fibers inserted into the supra-crestal portion of the root, the mucosa around the implant does not possess this anchor type. One possible consequence of this absence is the mucosa detachment from the surface of the implant. (52) In addition, peri-implant epithelium has less ability to act as a defense mechanism than the natural junction epithelium. For these reasons, dental implants require the use of a biological closure system to inhibit epidermal degradation and bacterial colonization on the subepithelial connective tissue and the interface with the implant. Usually, the surfaces in contact with the soft tissue are kept smooth to discourage bacterial adhesion, while physical closure is obtained by the contraction of the fibrous connective tissue, which occurs during the wound healing process. However, the formation of a fibrotic capsule on the smooth surface may not be sufficient to ensure the biological closure required to inhibit septic decline. (51) The soft tissue collar surrounding the dental implants is considered a critical point for the protection of the bone-implant anchorage, in fact this soft tissue region has to replacing the gum in the role of defense of the periodontium. (53)

Franco Bengazi et al. evaluate how the position of the margin of recession of the gum changed over a period of 2 years after the implantation of a fixed prosthesis. The results shown that recession of soft tissue occurs during the first follow-up phase, i.e. in the first six months of the implant. In addition, recession of the soft tissue is correlated with the initial height of this tissue, which increases as the initial height increases, but is not influenced by the quality or mobility of the perimplant mucosa. (52) It is essential to prevent this soft tissue recession as it may lead, in addition to aesthetic issues, to loss of support tissue, loss of osteointegration and failure of the whole implant. In this regard, it is important to investigate the role of the topography of the plant in preventing this problem. A 2011 study shows that the anodizing of the top of the collar provides a smooth surface, the which reduces the deposition of dental plaque and hence prevents tissue recession. However, the bottom of the collar should be micro-threaded to counter bone resorption, in accordance with Wolff's law, and to increase the shear strength and optimize the stability of the implant. (54) The above studies introduce the importance of locating the correct topography of the plant to ensure that it is as durable as possible. In particular, we will focus on the surface topography of the collar and its effects on the integration of gingival tissues. The affected cells are fibroblasts, as the parodontal tissue is mainly composed of gingival fibroblasts and periodontal ligament fibroblasts. It is desired that fibroblasts do not adhere and proliferate rapidly in the endosseous area of the implant to avoid the fibrous encapsulation of the dental envelope which would cause the plant to detach itself. (55) A different tissue response and consequently a reduced bone loss is observed when applying the concept of platform switching. It consists of using a lower diameter abutment than the diameter of the implant's neck and an extremely precise Morse cone connection that greatly reduces the gap between the components of the implant. (56)

2.5. Bacterial loading issue

Infection represents one of many factors contributing to the failure of dental implants. Presently, no single micro-organism has been closely associated with colonization or infection of any implant system. Failing dental implants are associated with a microbial flora traditionally associated with periodontitis. (43). The microbial complex in the oral cavity is called biofilm. Biofilm formation is a multistage process. Saliva give the major source of nutrients to the bacteria. The thin film covering the tooth called as acquired pellicle is derived from the salivary proteins and covers the enamel within seconds after brushing. Proteins and the glycoproteins are the molecules binding implant to the tooth surface. These molecules primarily act to promote the adhesion and coaggregation of the oral bacteria. The bacterial adherence to the pellicle is facilitated specially by the lectins present on the bacterial cell surface. Further intercellular bacterial adhesion and secretion of the extracellular polysaccharides, form the multilayered bacterial colonies suspended in the polymer matrix. Slow aggregation of the bacterial colonies leads to the formation of the multilayered cell clusters in the polymer matrix. (57) The colonization process of the surface by bacteria needs 4 hours. This process starts by the Streptococci. The planktonik bacteria take the aid of their receptors to bind to the cell surfaces of the initial colonizing bacteria and finally on to the tooth surface. This bacterial cell to cell reaction that occurs or the coaggregation happens to be an important mechanism leading to the bacterial colonization and dental biofilm formation. Secondary colonizers bind to the bacteria predominantly comprising of the Actinomycesspecies, *S. mutans*, *S. sobrinus*. The bacteria multiply and co aggregate with the partner species. Fusobacterium nucleatum has the property to co-aggregate with multiple bacteria hence this species is an important link in the dental biofilms bridging the early and the late colonizers. (58) The oral bacteria thrive for their nutrient supply from saliva, gingival crevicular fluid, sugar rich food metabolic products of other bacteria, and food debris. The plaque begins to behave as a complex microorganism with an inherent "circulatory system.". Metabolic products and evulsed cell wall constituents (lipopolysaccharides, vesicles) activate the host response. Specialized cell-cell communication is exhibited by the bacteria that coordinate the gene expression. This communication is passed on as signals. Bacteria sense the changes in the local environment (cues) and receive the information of the adjacent population. Specific interspecies communication within the biofilms is mediated through the metabolic exchange, genetic exchange, and the quorum sensing. Quorum

sensing is genetically governed chemical communication among bacteria in response to cell density and influence several functions of the bacteria, e.g., virulence, acid tolerance, and the biofilm formation. (59)

The oral bacteria produce two specific signaling molecules:

- Gram-positive bacteria communicate via small diffusible peptide channel called as "Competence Stimulating Peptides (CST) and AI-2." AI-2 (autoinducer-2) is a popular signaling molecule exhibited by both gram-positive;
- Gram-negative bacteria responsible for the quorum sensing. (60)

The biofilm acts as a barrier for the bacteria against host immunity and the antimicrobial agents. The anaerobic microflora succeeds to occupy the subgingival environment gradually as the plaque starts maturing. Supra-gingival plaque sets up the stage for the disease process of gingivitis and the subgingival microbial colonies advance the gingivitis to an established form of periodontitis. Thus, a transition is observed from a predominately Gram-positive non-motile, aerobic and facultative anaerobic composition towards a flora with a greater proportion of Gram-negative, motile, anaerobic bacteria. If this predominates for significant time periods, then peri-implantitis and eventual implant failure may occur. (61)

Type of implant (no. of patients/implants)	Method of detection	Most prevalent microbes detected (% sites infected with bacteria)
Brånemark (37/1–4 per patient)[32]	Culture	Prevotella intermedia/P. nigrescens 60% Actinobacillus actinomycetemcomitans 60% Staphylococci, coliforms, Candida spp. 55%
Not stated (41/not stated)[33]	Culture/indirect immunofluorescence	Bacteroides forsythus 59% Spirochetes 54% Fusobacterium spp. 41% Peptostreptococcus micros 39% Porphyromonas gingivalis 27%
Titanium hollow cylinder implants (7/not stated)[34]	Culture/dark field microscopy	Bacteroides spp., Fusobacterium spp., spirochetes, fusiform bacilli, motile and curved rods (% not stated)
Not stated (13/20)[36]	Culture	Staphylococcus spp. 55%
Not stated (21/28)[37]	Checkerboard DNA–DNA hybridization technique	P. nicrescens, P. micros, Fusobacterium nucleatum (% not stated)
IMZ (12/18)[38]	Culture	Bacteroides spp. 89% Actinobacillus actinomycetemcomitans 89% Fusobacterium nucleatum 22% Capnocytophaga spp. 27.8% Eikenella corrodens 17%
Various (10/12)[39]	PCR	Porphyromonas gingivalis 67% Campylobacter rectus 42% Eikonella corrodens 42% Treponema denticola 42% Prevotella intermedia 33% Tannerella forsythia 33% Actinobacillus actinomycetemcomitans 17%
9 Astra 16 Brånemark 5 ITI Staumann (17/30)[40]	Culture	Actinomyces spp. 83% F. nucleatum 70% P. intermedia/nigrescens group 60% Steptococcus anginosus (milleri) group 70% P. micros 63% Enterococcus spp. 30% Yeast spp. 30%

Table 8. Summary of studies investigating microbiology of failing implants (T5)

Table 8 highlights studies investigating the microbiology of failing implants. Interestingly, micro-organisms not usually associated with periodontitis or dental abscesses such as staphylococci, coliforms and Candida spp. are commonly isolated from peri-implant lesions in some studies. Staphylococci are present within the oral cavity and their isolation from peri-implant infection is significant as both Staphylococcus aureus and coagulase-negative staphylococci are frequently responsible for infections associated with metallic biomaterials and medical infections in general. (62) More recently, Staphylococcus aureus has been demonstrated to have the ability to adhere to titanium surfaces. This may be significant in the colonization of dental implants and subsequent infections. (43) There are few published guidelines on infection control during the placement of dental implants. Those available advocate that the surgical field should be isolated and free of contamination.

This is clearly not readily achievable within the oral cavity. However, it has been elucidated that contamination of the operative site by patient's saliva does not preclude success. Additionally, no significant differences were found in osseointegration success rates for implants placed under controlled operating conditions compared to a less environmentally controlled dental school clinic. This may imply that the operative environment is not as critical to the success of dental implants compared to implant placement within other body sites. Several strategies to reduce contamination from the oral flora during surgery have been postulated. One such strategy involves rinsing pre-operatively with chlorhexidine as this may reduce microbial complications following implant placement. During the surgical procedure, the implant should be stored in the manufacturer's sterile packaging and only used in conjunction with the recommended instruments. Previously, the drills used for bone preparation were not designated single use and were decontaminated according to local protocols. Manufacturers are gradually introducing single-use drills for use with their implant systems. (43)

3. PLATFORM SWITCHING

The "*platform switching*" is a concept that has only recently been introduced in clinical practice which refers to a simple and effective way to control circumferential bone loss around dental implants. By altering the horizontal position of the microgap, the horizontal component of bone loss after abutment connection can be reduced. (63) This implant shape refers to placing screwed or friction fit restorative abutments of narrower diameter on implants of wider diameter, instead, to placing abutments of similar diameters, which refers to as "*platform matching*". The benefits of platform switching have become the focus of implant-related research with increasing frequency. Numerous peer-reviewed articles and recent systematic reviews have revealed that platform switching can be considered a means of preventing initial peri-implant bone loss. (64) It has been observed that some degree of bone resorption occurs at the crest of bone following implant placement. Bone resorption around the implant neck depends on both biological and mechanical factors such as surgical trauma to the periosteum, characteristics of the implant neck design, prosthetic components, size of the microgap between the implant and abutment, bacterial colonization of the implant sulcus and imbalance in host parasite equilibrium. (64) The remodeling of crestal bone occurs in response to the stress that develops between the neck of an implant system and cortical bone. Since cortical bone is 65% more susceptible to shear forces than compressive forces, the bone loss may be explained by the lack of mechanical stress distribution between the coronal portion of the implant and the surrounding bone. Peak bone stress that appear in marginal bone have been hypothesized to cause bone microfracture and may be responsible of the peri-implant bone loss after prosthetic loading. Prevention of horizontal and vertical marginal peri-implant bone resorption is fundamental in maintaining stable gingival levels and profiles around implant-supported restorations. Reduced stress in the coronal portion helps to prevent crestal bone loss. Also, the extent of bone resorption is related to both the surfaces of the implant and abutment and the morphology of the implant-abutment junction (IAJ). The IAJ is always surrounded by an inflammatory cell infiltration and to protect the underlying bone from this microbiologic invasion, healthy connective tissue is needed to establish a biologic seal comparable to that around natural teeth. Thus, the current theory of the benefit of platform switching is related to the physical repositioning of the implant-abutment junction away from the outer edge of the implant and the

surrounding bone, thereby containing the inflammatory infiltrate within the width of the platform switch (Figure 17). (65)
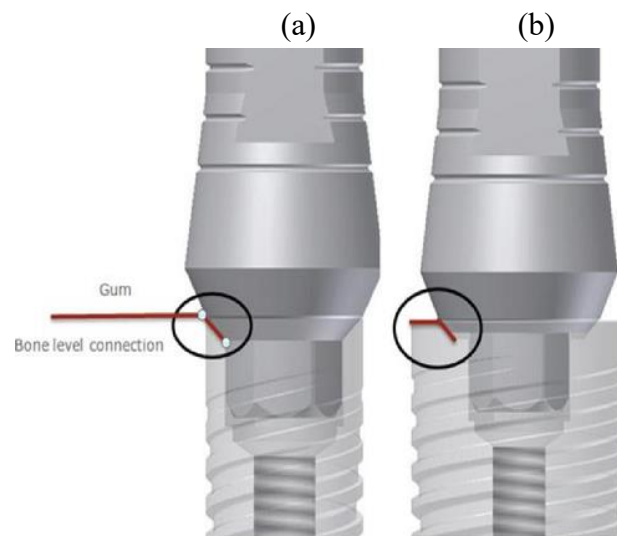

(a)   (b)

Gum

Bone level connection

Figure 17. Traditional connection (a) vs Platform Switching (b). (F18)

Lazzara et all. define in two different publications Platform Switching as "The coupling of an implant with a small diaphragm component with the gradient of 90° between the two parts". This "abnormal" coupling seems to reduce peri-implant bone resorption. The discovery was casual and was born following the introduction of wide implants types on the market, replacement of failed implants, which were protected with standard components. (66)

Despite the recent discovery of a literature review, it was found that already in 1992 were recorded clinical cases of prosthetic abutment with a smaller diameter.
Wagenberg et all. carried out a prospective study on 94 Plants with Switch platforms, the results show that 88% of the total 94 plants with bone loss below 0.8 mm appear very far from 1.5 mm recommended by Smith and Zarb. (67)

Rodriguez in 2009 conducted a prospective study by placing restored plants according to the concept of platform switching at a distance less than 3 mm, while with the traditional method the minimum intrusion distance to allow a bone peak greater than or equal to 0.4 mm is 3.5 mm. In the case of the switch, an average vertical re-absorption rate of 0.62 mm is obtained and a horizontal re-absorption rate of 0.60 mm, with a mean bone peak higher than the line of the two implants of 0.24 mm. (68)

Yu et all. conduced a short-term clinical study on 78 prostheses, implanted with platform switching and with average follow-up of 11.8 months from surgery and 7.4 months from prosthesis. The implants showed a 100% survival with a bone remodeling of 0.16 mm and with a standard variation of 0.8 mm or less. (69)

Despite rapid grownth of body of evidence with regard to platform switching, further substantiation with experimental and clinical outcomes with larger sample size and longer follow-up periods is still needed to determine the viability of this technique. More accurate long-term studies with more relevant number of patients are required to allow proper conclusions related to soft and hard tissue reaction to this alternative restorative protocol. (64)

The clinical relevance of platform switching concerns:

- Increased biomechanical support;
- Effect on soft tissue esthetics around dental implants;
- Effect on crestal bone stress levels in implants with microthreads. (64)

Several hypotheses have been made to explain this phenomenon and protection against crestal bone by platform switching:

I. Mechanical theory indicates greater stress on the entire surface of the neck in the traditional implant, while in the one with platform switching the stress zone moves to the center of the implant and not to the peripheral area;

II. Bacterial-inflammatory theory predicts that the infiltrate on the abutment-implant junction will be moved horizontally towards the center of the implant, thus moving away from the adjacent crestal bone. (56)

4. MORSE TAPER CONNECTION

The mechanical stability of the implant-abutment connection is an important issue in modern implantology although the problems surrounding implant-attachment remain unsolved. At present, most commonly used systems for fastening the abutment on the implant involve screw connections. In these systems, the effectiveness of the consolidation of the interface between the abutment and the implant depends on the preload of the screw, which is generated by applying a specific torque during the installation. Maintenance of screw tightening is accomplished when the force, exerted by the abutment screw exceeds the separating forces generated by occlusal contacts acting on the assembly. However, dynamic loading forces, during physiologic functions, that do not exceed the maximum resistance of an implant–abutment connection or even that are far below, can loosen the implant– abutment connection gradually or make it fail suddenly because of fatigue. Furthermore, in case of exceeding the preload, eccentric occlusal loads can lead to plastic deformation of the screw. The immediate consequence of these phenomena is the occurrence of mechanical complications, such as the loss of connection between implant and abutment. These complications are a biologic issue because micromovements at the implant–abutment interface can stimulate crestal bone resorption. To overcome these difficulties, implant manufacturers have introduced different systems, adopting screw-type internal connections. The most recent screw-type connections with an internal hexagon are now associated with various forms of taper. Morse Taper implant–abutment connection is based on the principle of ''cold welding'' obtained by high contact pressure and frictional resistance between the surfaces of the implant and the abutment. This type of connection, depending on the taper angle, can have different mechanical characteristics, in terms of fatigue strength (due to the presence of cyclic applied loads, i.e. mastication), and a different degree of mechanical coupling with the bone in which the connection itself is inserted. For example, the connection is defined as ''self-locking'' if the taper angle is less than 5°. Recent studies have clearly demonstrated that the morse taper implant–abutment connection can resist eccentric loading complexes and bending moments, ensuring an absolute mechanical stability and significantly reducing the incidence of prosthetic complications at the implant–abutment interface (Figure 18). (70)
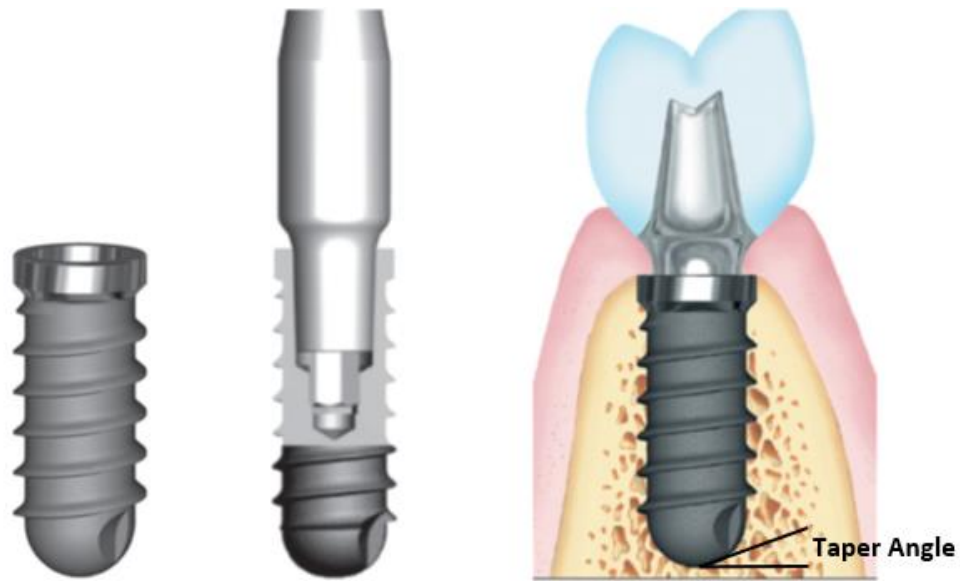
Figure 18. Drawing of an implant with a cone Morse taper interference–fit locking taper combined with an internal hexagon. The Morse taper presents a taper angle of 1.5°. (F19)

Therefore, implant systems differ in terms of the geometry of the implant–abutment interface with particular differences between both conical and nonconical connection systems. The implant–abutment connection represents the weakest point of dental endosseous implant fixtures, as it must constantly resist to masticatory forces as well as penetration by bacteria. The formation of a marginal gap between the implant and abutment might lead to increased loss of marginal bone because of the penetration of bacteria into the implant–abutment interface, i.e. compared to an implant without a gap that permits bacterial invasion. It has been claimed that, with conical implant–abutment connection systems, is not so high the risk as the gap is much smaller with less leakage at the implant–abutment interface (71), retarding or preventing bacterial colonization. However, there are no endosseous dental implant systems that can provide a complete seal at the implant–abutment interface and so this is still an important clinical issue. Regarding the mechanical properties of implant connections, it has been assumed that different abutment connections might provide greater resistance to displacement that is caused by excessive occlusal forces. In this regard, it has been speculated that this displacement will increase stress/strain on the endosseous implant promoting the acceleration of marginal bone loss. (72) Clearly, at this time, it is unknown as one connection system currently available might be superior to others. To focus more specifically on the performance of conical morse taper implant–abutment connection systems and to compare them with each other and with implant systems with non-conical

interfaces, to determine whether there might be improved clinical outcomes with one of these systems. (73) Table 9 shows the study characteristics and outcomes for in vitro studies regarding the seal performance, specifically eight trials that examined the bacterial leakage of the implant–abutment interface.

Author/Year	Connection	System	Samples	Insertion Torque
Ricomini Filho et al., 2010	Internal cone 1 (one piece), internal cone 2 (two pieces), external hex, locking taper	Not mentioned	11 per system	Morse Taper 1: 35 Ncm, Morse Taper 2 and external hexagonal: 15 Ncm, (recommended by the manufacturer)
Aloise et al., 2010	Internal cone, internal cone	Bicon Implant System (Bicon), Ankylos (Dentsply Friadent)	10 per system	Ankylos 25 Ncm, Bicon tapped, (recommended by the manufacturer)
Koutouzis et al., 2011	Internal cone, four grooves internal cone	Ankylos (Dentsply Friadent), Bone level (ITI Straumann)	14 per system	Ankylos 25 Ncm, Bone level 35 Ncm, (recommended by the manufacturer)

Author/Year	Objective	Used Bacteria	Method	Results
Ricomini Filho et al., 2010	Bacterial leakage into the implant abutment interface subjected to thermal cycling and mechanical fatigue, Preload loss after thermal cycling	E. coli	Connection, thermal cycling and mechanical fatigue testing, sterilization and contamination to bacterial medium, detorque measurements and SEM analysis	Bacterial leakage after loading: Morse Taper 1 (67%), Morse Taper 2 (50%), external hexagonal (0%), locking taper (60%) Preload loss after cycling: Morse Taper 1 (12.5%), Morse Taper 2 (-23.3%), external hexagonal (-23.1%).
Aloise et al., 2010	Bacterial leakage from the implant-abutment interface	S. sanguinis	Inoculation S. sanguinis, connecting abutment and implant, incubation and proof of bacterial presence or absence	Bactarial leakage: Ankylos 20%, Bicon 20%
Koutouzis et al., 2011	Bacterial leakage into the implant-abutment interface during loading. Torque value loss after loading	E. coli	Implant abutment connection, loading in E. coli medium, disconnection measuring loosening torque, incubation and measuring CFUs	Ankylos: 1 out of 14, mean CFUs 14.07652.56, torque increase (2.8563.23 Ncm), Bone level (ITI): 12 out of 14, mean CFUs 184.646242.32, torque decrease (-5.0062.77 Ncm)

Table 9. Summary of trials that examined the bacterial leakage of the implant–abutment interface_Part 1

Author/Year	Connection	System	Samples	Insertion Torque
Assenza et al., 2011	Internal cone, internal trilobed, cemented	Ankylos (Dentsply Friadent), Replace Select (Nobel Biocare), Bone System	10 per system	According to the recommendation of the manufacturer
Teixeira et al., 2011	Internal cone, internal hex	Titamax CM, Titamax II Plus (Neodent)	20 per system	Titamax II Plus 20 Ncm, Titamax CM 32 Ncm, (recommended by the manufacturer)
Tripodi et al., 2012	Internal cone, internal hex	Universal II HI and CM, (Implacil De Bortoli)	10 per group, 5 per bacterial species	According to the recommendation of the manufacturer

Author/Year	Objective	Used Bacteria	Method	Results
Assenza et al., 2011	Bacterial leakage from the implant-abutment interface	P. aeruginosa, A.Actinomycetemcomitans	Bacterial inoculation of the implant and abutment connection and measuring bacterial leakage	Bacterial leakage: internal conical 1 out of 10, internal trilobed 6 out of 10, cemented 0 out of 10
Teixeira et al., 2011	Bacterial leakage into the implantabutment interface, Bacterial leakage from the implant-abutment interface	S. aureus	1.Bacterial contamination; 2. After implant-abutment connection, incubation and colony growth calculation.	Into: Conical 70% and internal hex 100% leakage. From: Conical 77.7% and internal hex 100% leakage
Tripodi et al., 2012	Bacterial leakage from the implant–abutment interface	P. aeruginosa, A.Actinomycetemcomitans	Bacterial inoculation of the implant and abutment connection and detecting bacterial leakage	For PS inoculation: 2 out of 5 in the conical group and 2 out of 5 in the internal hex group, for AA: 0 out of five in the conical and 3 out of5 in the internal hex group

Table 9. Summary of trials that examined the bacterial leakage of the implant–abutment interface_Part 2

5. SURFACE MODIFICATION FOR ABUTMENT TO REDUCE BACTERIAL LOADING

Titanium is considered by the medical and scientific community as gold standard for dental implants, as it demonstrates excellent biocompatibility and osteointegration properties. However, it is influenced by surface morphology and peri-implant infections that can affect both the implant and the outcome of long-term bone osseointegration. It is possible to reduce the bacterial contamination on the abutment portion by acting on the surface.

There are different strategies that can be exploited for this purpose:

- The creation of a coating that on one hand, adheres to the surface of the implant and, on the other hand, once the prosthesis has been inserted in the oral cavity environment, it is able not only to withstand environmental conditions, but also to perform an antibacterial action preventing, for example, bacterial adhesion along the whole coating. Therefore, the chemical composition of a coating on implant-abutment junction surface (IAJ) should have a key role in preventing bacterial infection; (74)

- The modification of the geometry of the internal connections and abutment interface, which are parts of the prosthesis, usually more susceptible to bacterial contamination, as they promote the formation of an ideal micro-environment for bacterial adhesion. In this case, an uncoated, commercially pure titanium surface is obtained, which not only improves the adhesion of soft tissues and fibroblasts, but also reduces bacterial colonization at the interface.

Lauritano et al. (74) tested in an *in vitro* model a new antimicrobial polysiloxane coating functionalized with chlorexidine digluconate (PXT) in order to evaluate its effectiveness in reducing bacterial loading inside and outside IAJ. The PXT product provided by Edierre, is composed by an alcoholic solution containg polysiloxane-titanate oligomers and chlorexidine digluconate at 1%. The product has the ability of binding the titanium surface via interaction of the OH functionalities present on the polysiloxane chains and at the titanium surface. The role of the alkyl chains presents on the siloxane units consist of trapping through Van der Waals interactions chlorhexidine molecules, allowing their slow release while in contact with an aqueous medium. Coating of the internal chamber

of the implants was realized by filling with the PXT solution, followed by draining and implant heating at 60°C for 45 min. Coating of the abutments and screws was realized by immersion in the PXT solution followed by centrifugation on a sintered glass filter and subsequent heating at 60°C for 45 min. The microbial species used are Staphilococcus aureus, ATCC 6538, Pseudomonas aeruginosa, ATCC 15442, Escherichia coli, ATCC 10536 and were cultured in lysogeny broth (LB) containing both Kanamycin and Ampicillin (50ug/ml both) at 37°C for 24h in a shacking incubator. A first preliminary microbiological test on ten implants coated with PXT was performed by contaminating the internal implant chambers with 20μl of a microbial pool constituted by: Staphilococcus aureus, Escherichia coli, Pseudomonas aeruginosa, at the concentration level of $1–5 \times 106$ ufc/ml.

After 15 minutes of contact, development in LBA (Luria-Bertani Agar) and incubation at 37°C for 24h, the developed colonies were counted. On the remaining ten implants treated with PXT, twenty microliters of sterile culture medium with antibiotics (kanamycin and ampicillin, each at 50ug/ml) were placed in the internal chamber of each implant, the abutments were screwed at 35 newton and fixtures placed in plastic tubes. After this time, the capsule was examined evaluating the colonies proliferation (figure 19).
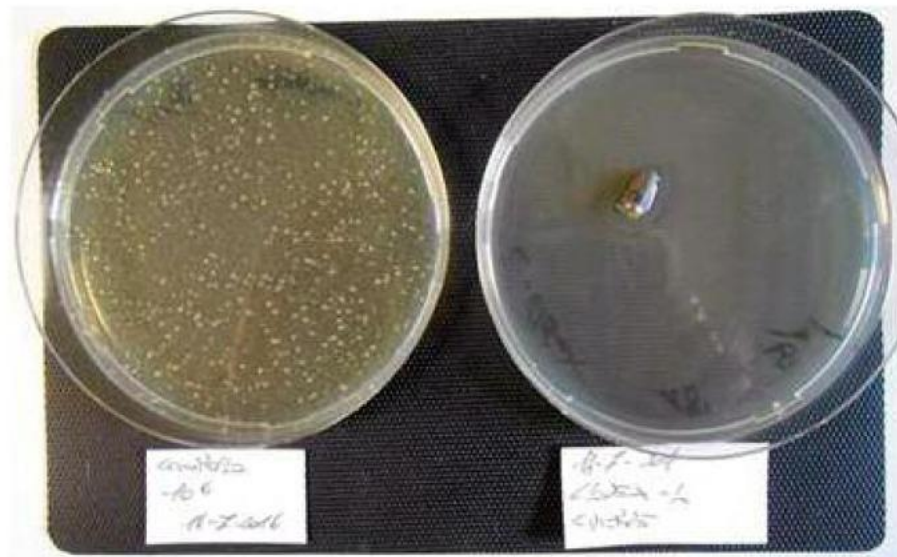
Figure 19. Left, control plate seeded with 20μl of the microbial pool after incubation. Right, Petri with the coated implant after contamination and incubation showing absence of colony forming units. (F20)

Figure 19 shows the complete absence of colonies in the treated sample for all the coated implants, with respect to the control plates in which a 20μl amount of the same microbial pool were seeded in the Petri dishes. In the microbiological evaluation, no living bacteria were detected in the internal part of the treated implants as well as in the external culture medium. Covering IAJ surfaces with coatings by adding biomimetic bioactive substances to improve its biological characteristics has been recently investigated. Modifications of IAJ using various strategies aim to improve prevention of bacterial infection and promote faster healing times. These aspects are important in modern dentistry, since immediate or early loading has become a predictable treatment protocol. Moreover, coating IAJ surfaces with cell-adhesive proteins, improves cells attachment, proliferation, and activity. (75) The results demonstrate that the applications of the PXT antimicrobial coating to the IAC surface prevents the bacterial growth inside the implant chamber, eliminating thus one of the possible cause of infection, with differences between treated and untreated samples which are statistically significant. The microbiological experiments show that in the internal part of the implants bacterial growth is not observed. The external culture medium behaves similarly, this can be interpreted as a consequence of the contact between the culture medium and the abutment treated with the antimicrobial PXT which can release during the 48h of immersion the active species chlorhexidine. Furthermore, PCR analysis shows that in 48 h only 0.3% ca of the bacterial contaminating the external of the implant-abutment junction penetrates the internal implant chamber and is then completely inactivated, as demonstrated by microbiological tests. In summary, this study has clearly demonstrated that the new coating determines a remarkable reduction of bacterial loading inside and outside IAJ, becoming a very useful medical device in preventing peri-implantitis which are the main cause of failure in implantology. (74)

Nassar et al. (76) evaluate the bacterial leakage of two different internal implant abutment connections in vitro. The amount of bacterial colonization between the implants and abutments depends on the fit accuracy between the fixture and abutment, their tightening torque and micromovements between the connected components during mastication. External and internal connections, such as hexagonal, Morse taper or a combination of both, are generally the most commonly used connections.

The internal implants abutment connection is reported as being more favorable to the infiltration of fluids than other joints. The microgap in this implant design varies from 1 to 49 µm, depending on the type of abutment that is selected. Biologically small molecules like toxins and molecular constituents of the bacterial wall are responsible for inflammatory reactions. It is well known that endotoxin, a small molecule complex of lipopolysaccharides and proteins, is one of the most important toxins of gram-negative bacteria and plays a major role in bone destruction processes. (77) Twenty dental implants of titanium alloy-resorbable blast textured (rbt) body 4.0x12 mm (BioHorizons Implant Systems Inc.) were divided into two equal groups and compared basing on their fixture abutment interface microgap geometry. Group 1, fixtures with an internal hexagonal geometry connected to standard straight abutments with a height of 6 mm; Group 2, fixtures with a tri-lobe internal connection were connected to 3-mm high abutments (Figure 20).

Figure 20. Internal hexagon connection on the left and tri-lobe connection on the right. (F21)

A bacterial suspension of cultivated Staphylococcus aureus was prepared in brain heart infusion (BHI) broth and incubating it for 24 h at 37°C. The abutments were carefully connected to the implants according to the manufacturer's instructions.

All implant-abutment assemblies were firstly submerged in sterile BHI broth to determine whether there was any external contamination and then incubated at 37°C for 14 days. After this time, all implant-abutment assemblies were submerged in sterile tubes containing 4 mL of S. aureus broth culture and were incubated at 37°C for 14 days. The specimens were removed from the test tubes using sterile pliers, immersed in 70% alcohol for 3 min to prevent external contamination, and dried with sterile gauze. After disassembling of the specimens, the inner surfaces of the implants were sampled by sterile

paper points for bacterial contamination. Then, the paper points were immersed in test tubes containing sterile BHI broth, from which culture was done on blood agar plates and incubated at 37°C for 24 h. Thereafter, the resulting colonies were identified by Gram's stain and biochemical reactions. The incidence of loads and unscrewing of the prosthetic abutment can increase infiltration, whereas optimal adaptation, minimal micromovement and exceptional prosthetic and occlusal planning are factors that can minimize microleakage. (78) Current implant systems cannot completely prevent microbial leakage and bacterial colonization of the inner part of the implant. The penetration of oral microorganisms through the implant abutment interface may produce soft-tissue inflammation and constitute risk to the clinical success of the implants. Loading forces on implants may also contribute to the bacterial colonization of the fixture abutment interface microgap. In summary, bacterial leakage seems to be unavoidable but fixture abutment interface geometry plays an important role in the amount of leakage. Tri-lobe internal connection showed less amount of bacterial leakage than internal hexagonal connection under static condition. Several in vitro studies have described the occurrence of bacterial leakage along the implant-abutment interface of systems with different internal connection designs in static or dynamic loading conditions. (78)

Steinebrunner et al. (79) evaluated in an in vitro experiment the bacterial leakage along the fixture abutment interface microgap using loading forces and discovered statistically significant differences between five implant systems with respect to the number of chewing cycles and bacterial colonization.

TOPOGRAPHIC MODIFICATION TECHNIQUES AT THE MICRO AND NANO SCALES

1. GENERAL FEATURES

Surface topography of a material to be treated can be modified by mechanical machining, chemical patternings or even electric fields. After processing, the material will form surface waves, known as capillary waves, as a result of the inherent entropy of the system balancing the increased energy of the greater surface area. (80) Biological interactions with a surface have also been found to depend on its topography. A good review of the topological control of cell adhesion and activity on a surface has been made by Curtis and Wilkinson (81). Such considerations are relevant for a number of in vivo and in vitro applications, such as biological sensors, hip replacements, and more complex tissue implants such as replacement bone, where the growth of cells within the artificial structure is to be encouraged. The larger scale topography was found to lead to less favorable spheroidal cells that formed fewer intercellular connections. In some cases, the topography of a surface may be carefully controlled to promote cell adhesion and to reduce the bacterial one. (82) Already by the beginning of the 1980s, surface structure was identified as one of the six factors particularly important for implant incorporation into bone (83), a statement that has been confirmed in later published research. Faster and stronger bone formation may provide better stability during the healing process, thus allowing more rapid loading of the implant. For many years, the Branemark implant was

considered the gold standard for implant surfaces, its surface was machined with a turning process with specific topographical properties such as anisotropy and a rather small average height deviation. However, a machined surface can actually be turned, electro discharged, end milled, ground, sandblasted, fly cut, bored, slap or polished, to mention just a few techniques (84). Such surfaces have very different topographies and different machining methods can be detected due to differences in the topographical appearance. In oral implant research, machined surfaces have been used synonymously with a Branemark turned implant without a particular turning process applied for this particular implant. Thus, very different surfaces have been used as 'machined' controls when investigating new and rougher surfaces. An increasing number of surface modifications are introduced and despite the comparison with 'machined' surfaces with new rough surfaces, it is not clear whether, in general, one surface modification is better than another. Moreover, not only is surface topography changed with many techniques but also surface chemistry and both result in a change in the chemistry and vice-versa. Albrektsson & Wennerberg (2004) suggested smooth surfaces to have an S_a value of 0.5 µm; minimally rough surfaces were identified with an S_a of 0.5-1 µm, moderately rough surfaces with S_a 1-2 µm, and rough surfaces with an S_a of 42 µm. (85)

2. TOPOGRAPHIC TECHNIQUES ON DENTAL IMPLANTS

Moderate micron-scale (1.0-2.0 µm range) topographic modification of the cp Titanium surface is generally accepted in the endosseous dental implant market place. (86) The belief that micron-level surface topography results in greater accrual of bone at the implant surface is supported by some clinical evidence. (87) Today, a growing aspect of endosseous implant surface research is focused on further enhancing the activity of bone forming cells and limiting adhesion of bacteria at the tissue implant interface. Current trends in clinical dental implant therapy include use of endosseous dental implant surfaces embellished with nanoscale topographies. Nanotechnology offers engineers and biologists new ways of interacting with relevant biological processes. Moreover, nanotechnology has provided means of understanding and achieving cell specific functions. Implant surface character is one implant design factor affecting the rate and extent of bacterial adhesion, soft tissue attachment and osseointegration. Nanotechnology has been defined as ''the creation of functional materials, devices and systems through control of matter on the nanometer length scale (1–100 nm), and exploitation of novel

phenomena and properties (physical, chemical, and biological) at that length scale'', moreover, nanotechnology involves materials that have a nano-sized topography or are composed of nano-sized materials. These materials are also classified according to their form and structure as nanostructures, nanocrystals, nanocoatings, nanoparticles, and nanofibers. Application of nanotechnology to the dental implant surface involves a two-dimensional association of surface features, i.e. across and away from the mean surface plane (Figure 21). (88)
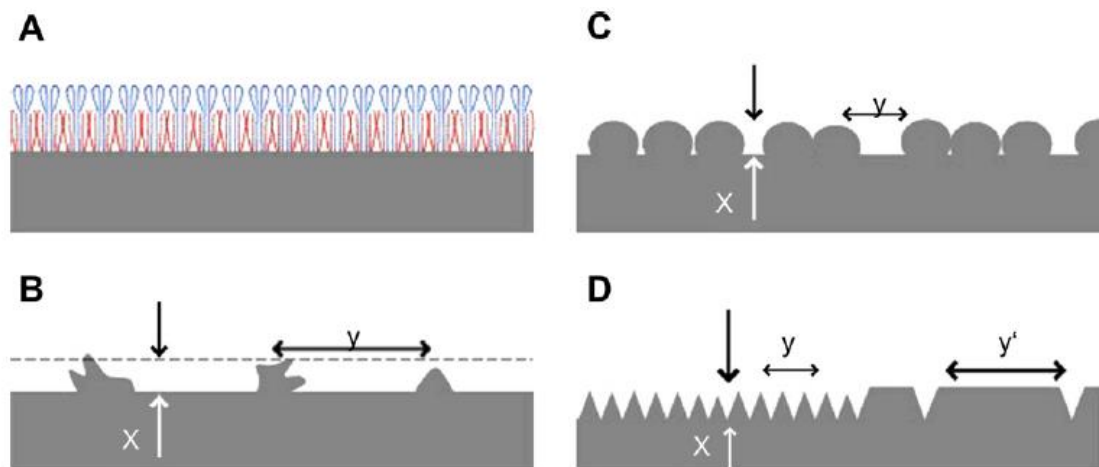
Figure 21. Nanoscale surface modification. (A) Self-assembled monolayers (SAMs) can change the topography and chemistry of a surface to impart novel physical and/or biochemical properties. (B) Deposition or chemical modification techniques can apply nanoscale features in nanoscale distribution. The cell response to surfaces represented by (B) or (C) may be different. (D) Isotropic surfaces can be created in the nanoscale (x < 100 nm) by subtractive or additive methods. The distribution can be in either the nano- (y) or micron-scale (y'). It is thought that some nanosurfaces mimic natural cell environments. (F22)

These nanofeatures can be arranged in an organized or unorganized manner, also defined as isotropic or anisotropic respectively, often depending on the method of manufacture of the surface topographies that have been applied to a dental implant surface. The topography is often characteristically anisotropic, instead, isotropic features such as nanogrooves or nanopits that are created largely by optical methods are predominantly applied to complex screw shaped objects. When these concepts are applied to the endosseous implant surface, implied is the embellishment of the surface with nanometer-scale features that lead to novel physicochemical behavior, e.g. bone bonding, or biochemical events, e.g. altered protein adsorption, cell adhesion with changes in cell behavior and bacterial adhesion. Nanoscale modification of the titanium endosseous implant surface may affect both the topography as well as the chemistry of the surface.

(88) Recent studies have shown that the best implant–body interface adherence is observed for hybrid micro–nano and multi-modal surfaces, with conclusion that roughness in few micrometer range favors strength of prosthesis–body interlock. The classic Ti modifications encompass mechanical sandblasting, acid etching, anodization and plasma spraying, which allow for cleaning, alter chemical composition and surface topography. The main complication of the surface treatments listed above is their propensity to contaminate the substrate material. This problem can be reduced by non-contact surface modifications like laser roughening techniques. Previous laser modificationreports supply promising results. Chen et al. (89) showed that the combination of laser micro grooving and the chemical functionalization improves implant–bone adherence and accelerate osteointegration.

Branemark et al. (90) noticed 250% increasement in removal torque of laser modified prosthesis relative to standard machined surface. Improvement in the surface-tissue interlock is assigned to the roughness modification as well as the creation of thicker oxide structures (91). Despite positive results, conventional laser technologies are limited to formation homogenous instead of controlled multimodal topography with nano- and micrometer components. (92)

2.1. Laser Welding

Laser Welding (LW) is a non-contact process which requires access to the weld zone from only one side of the parts being welded. The laser weld is formed as the intense laser light rapidly heats the material typically calculated in milliseconds. Three type of laser welds can be achieved with laser welding: conduction, conduction/penetration and penetration or 'keyhole.' Conduction welds are performed at low energy, resulting in wide, shallow weld nuggets. Conduction/penetration welds utilize a medium energy density and result in a deeper weld nugget. Penetration or keyhole welds are resultant of direct energy delivery into the material being welded resulting in deep, narrow nuggets. As laser welding is a non-contact process, there are many joint geometries that can be welded, but there must be a close fit-up at the joint interfaces. Laser welders can join a wide range of steels, nickel alloys, titanium, aluminum, and copper. As with other joining technologies, some materials are difficult to laser weld unless they meet specific characteristics, namely, reflectivity, the effect of high thermal cycling, and the vaporization of volatile

alloying elements. With laser welding, it is possible to join parts by self-welding of the metal components themselves. Laser welding causes changes to the microstructure of NiCrMo and CoCrMo cast alloys due to the rapid heating and solidification processes. Cracks appeared in the welded area due to thermal residual stresses during the welding stage and/or changes in microstructure that affect the quality of the welded parts. The influence of laser beam quality, power and other physical parameters on the penetration depth of metals has been researched primarily for industrial purposes. Specific data relating to the choice of laser parameters to weld dental alloys successfully, to enhance laser penetration and to avoid surface damage are lacking in the literature. Parameters due to the operator are: dexterity, eyesight (has an influence on the adjustment of the laser beam focusing) and knowledge (concerning the possible disfunction of the machine). Physical parameters are: power and pulse duration of the laser radiation to determine the best settings to improve the beam's penetration depth and ensure success in the welding procedure (function of the wire diameter and thermal conductivity of the alloy). After the melting, the alloy exhibits large grains (Figure 22). Due to these modifications in the microstructure, the welded area is softer (HV 0.1=290) than the non-welded alloy (HV 0.1=410). The change in the hardness of the welded area is due to the re-crystallisation of the alloy. Various surfaces have been optimized and patented by companies using the techniques outlined, such as laser lock from biohorizon, Synthegra by Geass. (93)
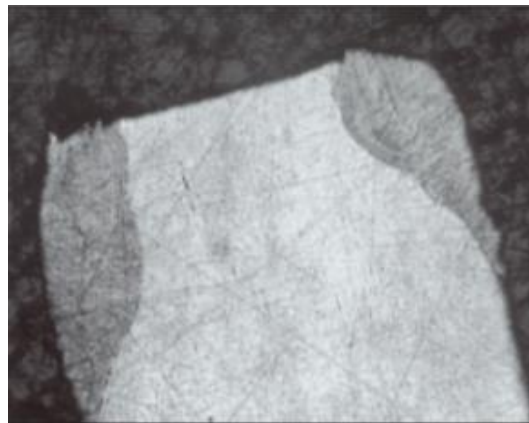
Figure 22. Microstructure of the wire: Interface between the welded and non-welded area. (F23)

P. Kwasniak et al. (94) used two-step functionalization of Ti grade 2 surfaces. The employed methods include initial chemical etching and direct laser interference lithography (DLIL) technique which is based on the interference of two laser beams. The surface treatments were performed on semi-finished industrial products—sheet with thickness of 1 mm and 0.3 mm diameter wire to investigate the effect of curvature on

surface architecture. The obtained structures were characterized in terms of shape, roughness, chemical composition, mechanical properties and microstructures of substrate material. The first step consists of chemical treatment of Ti to remove oxide, contamination and smoothing surface defects remaining after previous plastic deformation during samples preparation. In all the cases, fluoridrid acid is used to dissolve TiO_2 thin films. The second step consists of manufacturing of periodic surface topography, executed with DLIL, using lasers with large power density (from MW/cm^2 to GW/cm^2). This method allows for forming micro- and sub-micrometer structures with well-defined large range ordering. Direct laser interference lithography method was used to produce periodic and striated Ti surface. Such configurations allow for fast fabrications of 1 cm^2 square periodic structures. The laser surface functionalizations were running on air atmosphere using previously etched samples and energy density in range 400–600 mJ/cm^2.
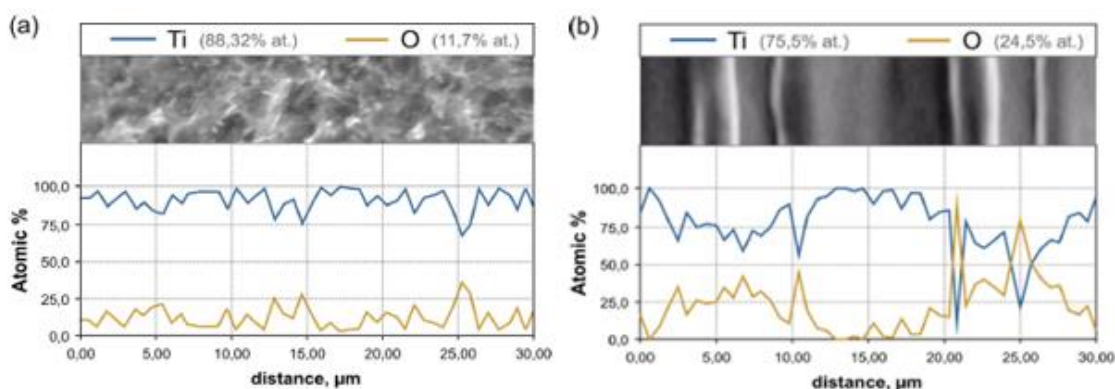
Figure 23. Chemical composition of the Ti plate surface: (a) after chemical etching, (b) after DLIL surface modification (400 mJ/cm2); (energy dispersive spectroscopy linear scan) (F24)
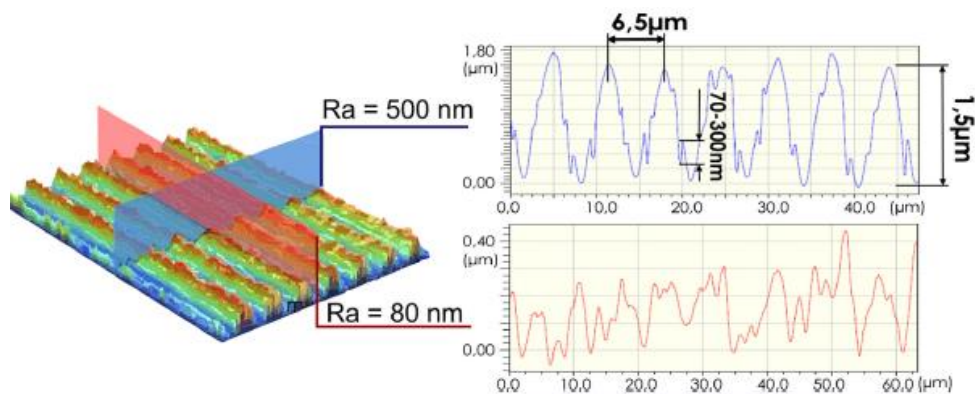
Figure 24. Sample ridge shape profiles acquired from optical profilometry of place modified using DLIL technique (400 mJ/cm2) (F25)

The conclusions arising from investigation carried out, can be listed as follow:

- DLIL technique employed to Ti grade 2 allows for obtaining hierarchical surface composition with multimodal roughness in 10-500 nm scale;

- Clean and smooth surface is obtained directly after etching of semi-finished industrial products;

- Chemical composition of created surface striations, indicates gradient distribution of oxygen concentration which is the effect of short-lived, high temperature phenomena, local melting, sublimation and condensation (Figure 23);

- Interaction of laser beams with substrate forms the 0.6-1.5 μm thick, continuous layer consisting of nanograins which improves hardness of Ti (Figure 24);

- DLIL method does not modify original macro topography and can be applied for modification of the flat and curve Ti surfaces. (94)

Alkhodary et al. (95), utilized laser direct writing to produce 10 microns wide uniform grooves on the surface of Ti-6Al-4V dental implants (prosthesis and neck), and the tri-peptide RGD coating to produce a micro-mechanical and a chemical union with the tissues around the implant-crest module and minimize crestal bone loss. By controlling the size of laser machined grooves, cells can be induced to grow into the grooves and orient themselves accordingly. This phenomenon is known as contact guidance and can be used to regulate where bone grows, and ultimately, what sort of bone develops. This spatial and material control means that isotropic and anisotropic properties can be controlled. Moreover, there is evidence that suggests that the groove geometry plays a role in determining what sort of tissue develops. For instance, 10 microns grooves are thought to induce bone stem cells to differentiate into cortical bone. In biological terms, RGD is a cell adhesion receptor molecule that interacts with membrane bound talin and vinculin proteins to promote the cellular surface adhesion process and to accelerate the process of tissue binding to the implant surface (Figure 25).
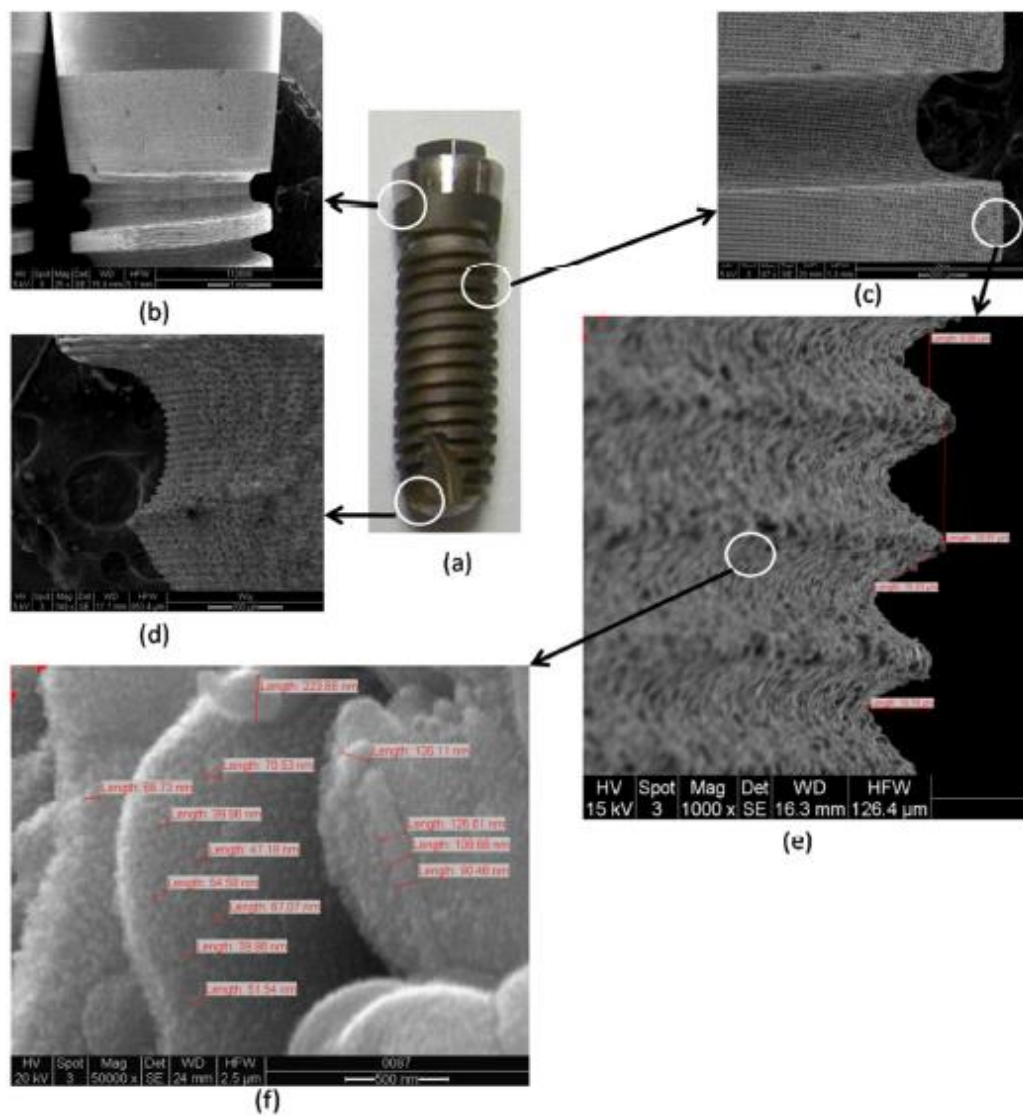
Figure 25. SEM of the laser microgrooved dental implant: (a) Macroscopic appearance of a laser microgrooved implant, (b) SEM of the implant head, original magnification x25, (c) SEM of the threads, original magnification x97, (d) SEM of the foot, original magnifi
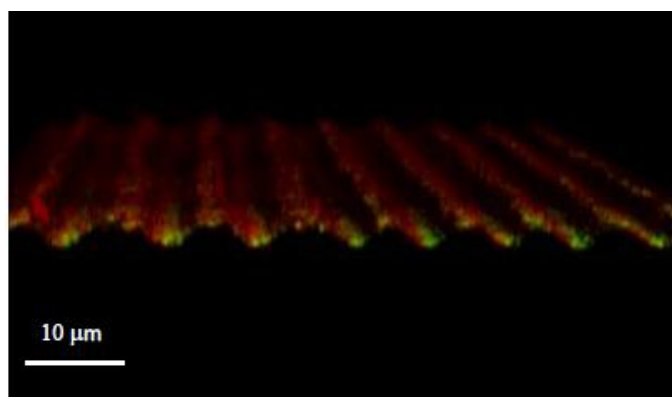
Figure 26. FT-IR spectroscopy: Immunofluorescent Microscopy Image of Laser-grooved Surface Funtionalized with the Alkyl Phosphonate (AP), the Linker Molecule to the RGD (F27)

This study was conducted in a trial to improve the adhesion of the bone to the implant surface both micro-mechanically and chemically, with consequent better stress distribution to the surrounding bone, and ultimately, a better peri-implant bone healing and remodeling that provides a long-term support of the implant and the prosthesis it retains. The results of this study demonstrated higher bone density profiles next to the laser micro-grooved implants coated with the RGD than those only having the laser micro-grooves. Further studies need to be conducted to compare the results of this study and other studies using titanium dental implants with random surface roughness, to validate the hypothesis of contact guidance, and other surface coatings to compare the effect of RGD surface functionalization (Figure 26).

Chen et all (10) designed, produced and evaluated titanium surfaces for levels of osseointegration into the femurs of rabbits. A total of 36 Ti-6Al-4V pins were prepared into three experimental groups. These were designed to test the effects of osseointegration on laser grooved, RGD coated, and polished control surfaces, as well as combined effects. Circumferential laser grooves were introduced onto pin surfaces (40 µm spacing) using a UV laser (λ=355 nm). Of the prepared samples, surface morphology and chemistry were analyzed using scanning electron microscopy (SEM) and immunoflourescence (IF) spectroscopy, respectively. The experimental pin surfaces were surgically implanted into rabbit femurs. The samples were then harvested and evaluated histologically. In the case of the RGD coated and laser grooved surfaces, histological results showed accelerated bone growth into the implant, pull-out tests were also used to compare the adhesion between bone and the titanium pins with/without laser textures and/or RGD coatings.
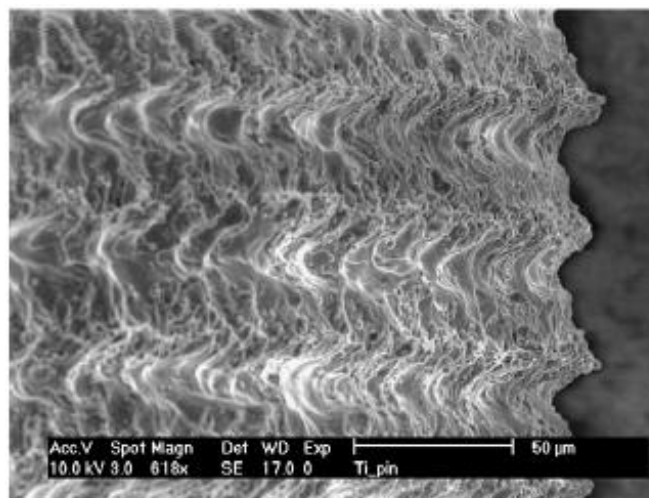
Figure 27. Laser grooved pin SEM (F28)

Prior to laser grooving, the surfaces of the Ti-6Al-4V specimens were polished to a uniform roughness using 320 grit polishing paper. Grooves with 25 μm wide and 40 μm spacing were machined on to the surface of the pins. A spot size of 20 μm was obtained using a microscope objective and each pin was rotated at 2800 rpm on an X–Y stage. The laser was fired at 1000 Hz for 1.25 s (75 rotations of the pin) to produce one circumferential groove. The pin was then translated laterally in increments of 40 μm to produce multiple grooves. The resulting grooves were 25±2 μm wide, with a spacing of 40±1 μm. The average groove depth was 11±2 μm, as determined by profilometry. The laser-grooved pins were characterized in a scanning electron microscope (SEM) that revealed uniform machined grooves, as well as the nano-scale and sub-micro-scale roughness left behind by the laser ablation process (Figure 27).

2.2. Electron Beam Welding

Another widely-developed technique for nanophotography is electron beam welding (EBW): the process where high speed electrons are concentrated in a thin beam directed towards the workpiece, generating heat vaporizing the material. EBW, compared to other thermal cutting processes, and surface finishing, is better because it allows a narrower cutting width. A difference in laser beam welding, this requires that the piece be placed in a room where the vacuum was previously produced. (96) EBW is a thermoelectric process; the remarkable resemblance to laser beam machining is due to the high temperatures and thermal density that can be reached. In the electron gun, in addition to the anode and the cathode, there is a third electrode defined as Wehnelt Lens, which is connected to the cathode and has the function of regulating the electrons flow. (56) The voltage between the anode and the cathode, called accelerator voltage, affects the velocity of the electrons and the thermal energy that can be developed by electronic bombardment and is therefore proportional to the voltage; they generally do not exceed 60 KW of power. The gun is placed in a vacuum chamber and is equipped to move vertically; the bundle remains generally stationary and the workpiece is moved to the desired speed under the electronic beam (power supply). The temperatures obtainable are sufficient to vaporize the tungsten (with a melting temperature of 3370 ° C) or any other known material and the vacuum pressures reached in the chamber, ranging from 10-2 to 10-5 Torr (mmHg), depending on of the room area. In the machining zone, the vacuum

pressure must be at least 10-4 Torr, and the electrons fired from the cannon reach a speed between 50,000 and 200,000 Km/sec (Figure 28).
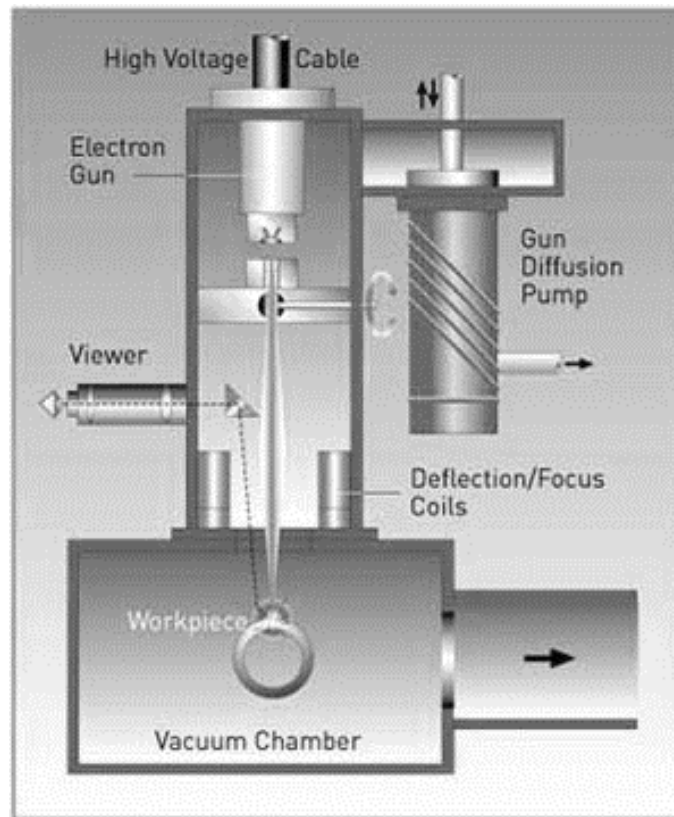
Figure 28. Schematic representation of an Electron Beam Welding system. (F29)

Modern electron-beam welders are usually designed with a computer-controlled deflection system that can traverse the beam rapidly and accurately over a selected area of the work piece. Thanks to the rapid heating, only a thin surface layer of the material is heated. Applications include hardening, annealing, tempering, texturing, and polishing (with argon gas present). If the electron beam is used to cut a shallow trough in the surface, repeatedly moving it horizontally along the trough at high speeds creates a small pile of ejected melted metal. With repetition, spike structures of up to a millimeter in height can be created. These structures can aid bonding between different materials and modify the surface roughness of the metal. (97)

Ramskogler et al. (2016) studied the effect of a designed surface on the osteoblast behaviour and the influence of the electron beam on the microstructure of titanium base alloys. Commercially pure titanium of grade 2 (TiGr2) and titanium alloy Ti6Al4V were structured under vacuum by a high energy electron beam. Moreover, structured figures

were designed following different criteria in order to develop a specific topography and roughness on the surface (Figures 29 and 30).

Material	Cultivation time	Deflection figure parameter		
		Polygon figure	Beam travel direction	Arm number #
Ti6Al4V	24h, 48h, 72h	hexagonal	wallarray	96
	24h	hexagonal	wallarray	156
		hexagonal, square	pinarray	96, 100
		hexagonal wallarray and additional etching		96
		heat treated sample without structuring		
TiGr2	24h, 48h	hexagonal	wallarray	96
	24h	hexagonal	wallarray	156
		square	pinarray	100
glass	24h, 48h, 72h	control glass plates		

Figure 29. Material and deflection figure parameters for cell cultivation. (F30)
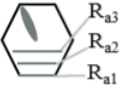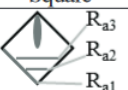
Hexagonal	Material	Deflection figure parameter			Roughness measurements R_a [µm]		
		Polygon figure	Beam travel direction	Arm number #	R_{a1}	R_{a2}	R_{a3}
	Ti6Al4V	hexagonal	wallarray	96	4.96 ±0.66	17.51 ±4.60	58.46 ±11.83
		hexagonal	wallarray	156	4.80 ±1.99	12.86 ±1.66	50.15 ±2.35
		hexagonal	pinarray	96	8.48 ±2.73	7.43 ±2.64	39.74 ±2.34
		sqaure	pinarray	100	12.89 ±2.00	10.56 ±1.94	34.31 ±3.80
	TiGr2	hexagonal	wallarray	96	2.97 ±0.23	8.78 ±2.15	43.38 ±4.81

Figure 30. Surface roughness of EB structured Ti6Al4V and TiGr2 samples (F31)

During electron beam structuring, the energy input of the electron beam process created a melt pool on the surface and the subsequent fast cooling have formed a gradient of microstructure for both materials. The microstructure change was independent of the geometry of the figures but was strongly influenced by the current of the beam. The morphology of pre-osteoblast cells (MC3T3-E1) after culturing for 24h, 48h and 72h on Ti6Al4V, TiGr2 and cover glass were examined with SEM (Figure 31). MC3T3-E1 cells appeared well spread out with a polygonal morphology on the surface of each structure and the cells connected to each other through elongated actin filaments were extended in various directions. (98)
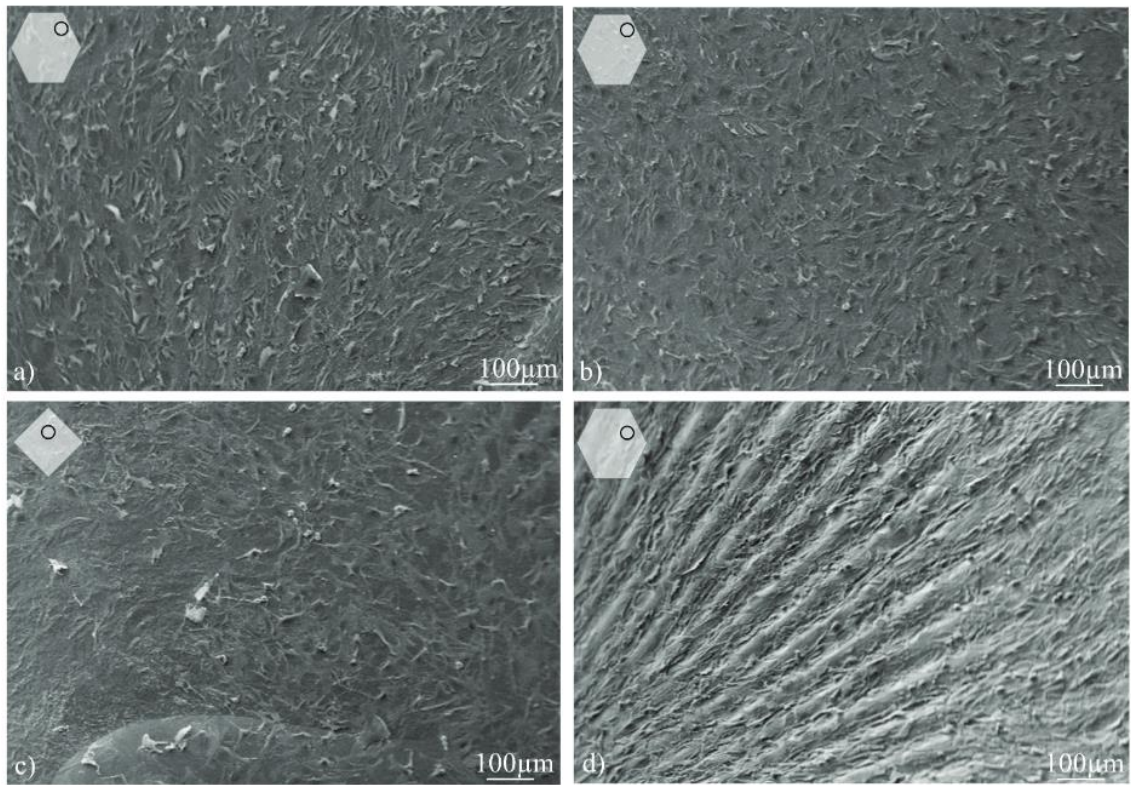
Figura 310. SEM images; MC3T3-E1 a) Ti6Al4V, hexagonal wallarray 96 arms + chemical milling, 24h cultivation b) TiGr2, hexagonal wallarray 96 arms, 48h cultivation c) TiGr2, square pinarray 100 arms, 24h cultivation d) Ti6Al4V, hexagonal wallarray 96 arms, 72h cul

In summary, the beam travel direction and the number of arm produced in the designed figure influenced on the surface roughness. Under same conditions, commercially pure titanium (TiGr2) shown lower Ra values in comparison to Ti6Al4V. (98)

2.3. Laser Beam Welding vs Electron Beam Welding

Laser welding energy sources utilize either a continuous wave (CW) or pulsed output of photons. With CW systems, the laser beam is always on during the welding process. Pulsed systems are modulated to output a series of pulses with an off time between those pulses. The laser beams may be delivered directly to the part via classical hard-optics, or through a highly flexible fiber optic cable capable of delivering the laser energy to distant workstations. It is the high energy density of the laser that allows the surface of the material to be brought to its liquidus temperature rapidly, allowing for a short beam interaction time compared to traditional welding methods such as GTAW (TIG welding) and similar processes. Energy is thus given less time to dissipate into the interior of the workpiece. This results in a narrow heat-affected zone and less fatigue debit to the component. Beam energy output can be highly controlled and modulated to produce

arbitrary pulse profiles. Weld seams may be produced by overlapping individual pulses, which reduces heat input by introducing a brief cooling cycle between pulses, giving a great advantage for producing welds in heat sensitive materials. CW lasers can achieve penetrations up to and exceeding 0.5 inches, while pulsed lasers typically achieve only 0.030-0.045 inches, but these results may vary between laser systems and are largely dependent on processing parameter choice and joint design. The laser's high-power density results in small heat-affected zones and ensures that critical components are unharmed. This has particular advantage for surgical instruments, electronic components, sensor assemblies and many other precision devices. Unlike EBW, LBW does not generate any x-rays and is easily manipulated with automation and robotics. Generally, LBW has simpler tooling requirements as well, and there are no physical constraints of a vacuum chamber. Shorter cycle times translate to cost advantages without decrease quality.

The main advantages of continuous wave and pulse LBW are:

- Lower capital equipment-cost advantage over EBW: No physical constrains of an exclosure or vacuum chamber enables simplified setup, rapid cycling, and less complex single station tooling;

- Shorter cycles than EBW times translate to lower cost;

- Simpler tooling requirements than EBW;

- Small heat affected zone;

- Scalable, one laser servicing several platforms;

- Many OEMs support the technology;

- No x-rays generated. (99)

Widely accepted across many industries, EBW permits the welding of refractory and dissimilar metals that are typically unsuited for other methods such as laser welding. The kinetic energy of the electrons is converted to heat energy, which in turn is the driving force for fusion. Usually no added filler material is required or used, and post-weld distortion is minimal. Ultra-high energy density enables deep penetration and high aspect ratios, while a vacuum environment ensures an atmospheric gas contamination-free weld that is critical for metals. However, the main necessity for operating under vacuum is to control the electron beam precisely. Scattering occurs when electrons interact with air molecules; by lowering the ambient pressure electrons can be more tightly controlled.

Modern vacuum chambers are equipped with state-of-the-art seals, vacuum sensors, and high-performance pumping systems enabling rapid evacuation. These features make it possible to focus the electron beam to diameters of 0.3 to 0.8 millimeters. By incorporating the latest in microprocessor Computer Numeric Control (CNC) and systems monitoring for superior part manipulation, parts of various size and mass can be joined without excessive melting of smaller components. The precise control of both the diameter of the electron beam and the travel speed allows materials from 0.001" to several inches thick to be fused together. These characteristics make EBW an extremely valuable technology. The process puts a minimal amount of heat into the workpiece, which produces the smallest possible amount of distortion and allows finish machined components to be joined together without additional processing. Since most EB welding is performed inside a vacuum chamber, it is an excellent fit for joining advanced materials used in such industries as aerospace, power generation, medical and nuclear, which need to be produced in a vacuum environment to protect them from oxygen and nitrogen found in an open-air environment. EBW parts require a minimum of post weld machining and heat treatment and, unlike other fusion welding processes, EBW requires no shielding gases. The process is extremely efficient (typically 95%), all the process parameters are carefully controlled and the process fully automated.

The main advantages of EB welding are:
- Welding in a vacuum ensures no gas contaminance;
- Deeper penetration than LBW with high aspect ratios;
- Energy absorption indipendent from the surface material conditions;
- Similar heat affected zone to LBW;
- Permits welding of refractory and dissimilar metals not weldable with conventional welding processes;
- Proven track record, widely accepetd;
- Included in many welding specifications. (99)

The following Table 10 sums up the most significant advantages and disadvantages for LBW and EBW:

	Electron Beam Welding	Laser Welding
Single pass welding of thick sections	60 kV 6 kW beam power gives over 20 mm penetration. Weld depth to width ratio up to 40:1	Nd-YAG lasers have lower power resulting in restricted penetration. Weld depth to width ratio 10:1
High welding speed	High speed deep penetration welds possible	High welding speeds achievable but lacks penetration
Automated Process	Can be highly automated with evacuation time of the chamber in a few seconds. Typical cycle times found within the automotive industry 40 seconds per component. Time is dependent upon length/complexity of weld	Can be highly automated with production rates higher than those for EB as the evacuation time is removed (non-vacuum process)
Component Size	Component size is restricted by the size of vacuum chamber. In most high production systems component size does not alter to a great degree. Chamber volumes are kept to a minimum to reduce evacuation times	Not restricted by component size; Nd-YAG fibre optic delivery systems can be used allowing the welding head to be remote from the power source
Weld quality	High quality weld due to inert atmosphere, very stable and repeatable. Deep penetration welds on a wide variety of materials including dissimilar metal combinations can be made	Some porosity is normally found within the weld bead and root, as the shield gas does not totally eliminate air from the weld area. Inferior weld quality
Vacuum environment	Vacuum aids in the weld quality as it has a tendency to pull contamination out away from the weld pool	Not applicable - no vacuum. Laser uses atmosphere with additional shielding gas
Filler gas or shielding gas	Not required	Needs the shielding gas normally nitrogen or argon to stop oxidisation of the weld area and weld pool
Wearing components	Filaments. Metal vapours can deposit on viewing prism with no effect on weld characteristics. Prism can be cleaned	Optical devices such as mirrors and lenses can be coated by metal vapour produced during the welding process leading to drop in beam power impinging on work surface resulting in reduced penetration. Laser or shielding gas, Optical elements, Mirrors
Running cost	Cooling water (normal quality), pump oils, electricity, compressed air (for valve actuation)	Requires high purity water in cooling system to cool beam source. Water must be held at ± 1°C constant temperature. Consumption of shield gas high electricity
Power efficiency	80-90%	7-10%
Price (approximate prices)	0 kV, 4 kW (610 mm³) electron beam welder including CNC controlled work manipulation systems £220,000.00	4 kW laser £250,000.00 excluding work manipulation system

Table 10. Advantages and disadvantages for LBW and EBW. (T6)

Proponents of laser beam welding (LBW) and electron beam welding (EBW) each pronounce the singular praises of their favored technology, but often the best solution for a customer is to use both technologies together. Both processes are well suited to joining components with complex geometries, and capable of meeting the most stringent. Using both laser and electron beam technologies in a single facility can streamline the manufacturing process when a component's design incorporates multiple weld joints separately tailored for one process or the other. Examples include sensors, medical devices, and products that require an inert gas or vacuum to be sealed within the finished part. Laser processing is required either when the size of the final assembly is too large for an EB welding chamber, some component in an assembly is incompatible with vacuum processing, or when the weld is inaccessible to an electron beam source. Electron beam will be the primary choice when the completed assembly must be sealed with internal components under vacuum, when weld penetrations exceed 1⁄2", when the material is challenging to initiate laser coupling, or when the weld must not be exposed to atmospheric conditions until it has cooled to an acceptable temperature. Examples are aerospace welding of titanium and its alloys, and many refractory metals such as tungsten, niobium, rhenium, and tantalum. (99)

3. TOPOGRAPHIC EFFECT ON BACTERIA

Many studies are underway to determine with certainty whether and how sub micrometric and nanometric surface topographies affect bacterial adhesion. The small size of the bacteria, in the order of a few μm, make the bacteria susceptible to superficial characteristics with the size of the microgrooves, especially with a $R_a \geq 0.2$ μm gap dimensions. In addition, the bacteria have a very rigid cell wall and this feature limits the interaction between bacteria and surfaces with topographic features of smaller size than the size of the bacterium such as nanogrooves. (100)

Katrina J. Edwards et al. (101) have shown that the greater the effect on the alignment of bacteria is the shape of the grooves rather than the size. In this study, two types of grooves, U-shaped and V-shaped, respectively, were made on pyrite substrates, and the bacterial adhesion energy (Thiobacillus caldus, radius about 0.32 mm) was calculated in feature of the groove dimension (r). The results have shown that the different shape of the grooves can alter the bond strength, especially when the topography characteristics are of the same order of magnitude as the bacterium, in particular a higher adhesion force for the substrate with U -shaped.

Truong et al. (102) demonstrated that two bacterial strains, *Staphylococcus aureus* and *Pseudomonas aeruginosa*, exhibited different attachment affinities towards two types of molecularly smooth commercially pure titanium (grade 2 and grade 4, with an average grain size of 20 and 30 μm respectively) surfaces each possessing a different nanoarchitecture. They also found that the attachment of S. aureus cells was not restricted on surfaces that had an average roughness (Sa) less than 0.5 μm. In contrast, P. aeruginosa cells were found to be unable to colonise surfaces possessing an average roughness below 1 μm, unless sharp nanoprotrusions of approximately 20 μm in size and spaced 35.0 μm apart were present. Thus, they postulated that the enhanced attachment of P. aeruginosa onto the surfaces possessing these nanoprotrusions was facilitated by the ability of the cell membrane to stretch over the tips of the nanoprotrusions as confirmed through computer simulation, together with a concomitant increase in the level of extracellular polymeric substance (EPS) being produced by the bacterial cells. Billets from these materials, were processed by equal channel angular pressing (ECAP) to produce an ultrafine grain structure together with the application of back pressure under the

temperature regime selected, ensuring production of samples containing a uniform distribution of predominantly equiaxed grains. The physical-chemical characteristics of the surfaces as received and modified by the ECAP have been analyzed and found substantially similar. Analysis of AFM height tapping results and AFM phase imaging on areas of 1 μm × 1 μm provided further insights into the differences between the two surface architectures, named Ti EG2 and Ti EG4, respectively, whose different microstructure of most of the two grades gave rise to two different types of surface topography (EG2 and EG4) on a nanometer scale. The surface of the Ti EG2 exhibited a number of broad valleys and peaks, which appeared in highly contrasting colours that highlighted a distinction between the peaks and the valleys (Figure 32).
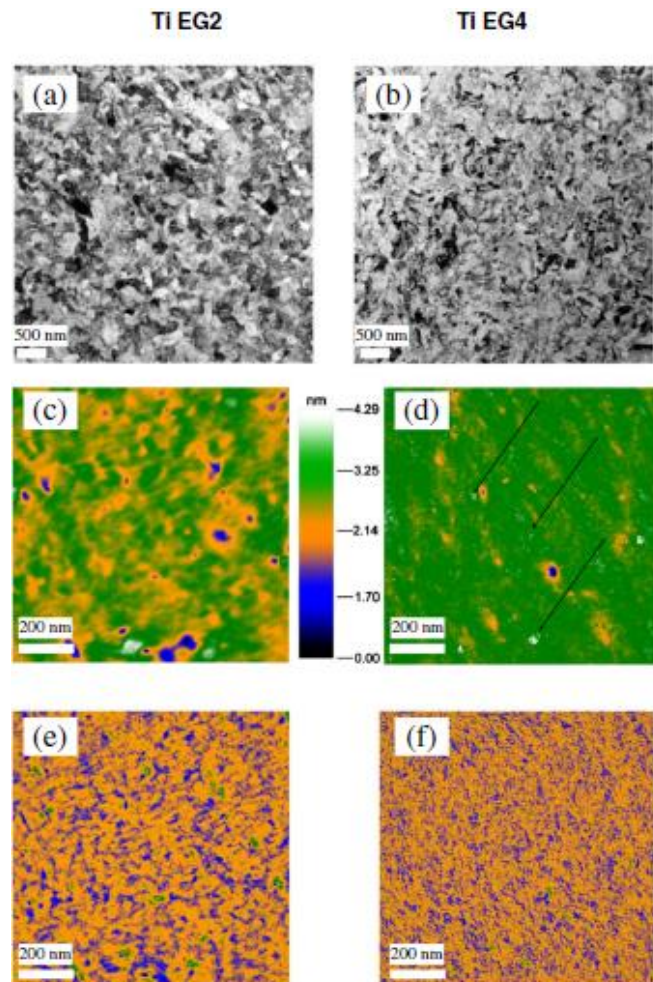
Figure 32. Surface architecture of Ti EG2 and Ti EG4 at sub-nanometric scale. (a, b) Transmission electron micrographs visualising the differences in geometry and orientation of nanograins; c, d surface architecture of EG2 and EG4 presented by AFM height images. Ti EG2 surfaces exhibit wide and broad peaks and valleys; in contrast, Ti EG4 surfaces exhibit a number of sharp peaks protruding off homogenously flat surfaces; the arrows indicate sharp nanoprotrusions (white spots); e, f corresponding AFM phase images of c and d which demonstrate that surface architectures are influenced by organisation of Ti nanograins (orange), grain boundary (blue) and sub-nanograin structure (green). (F33)

Bacterial strains	Initial cell density x 10^6 (number of cells per mm^2)	Attached cell density x 10^4 (number of cells per mm^2)		Biovolume (µm^3/µm^2)	
		Ti EG2	Ti EG4	Ti EG2	Ti EG4
S. aureus	20.8±1.7	28.1±3.1	30.2±4.5	4.8±1.5	5.9±1.8
P. aeruginosa	13.0±1.5	0.5±0.3	2.6±0.8	0.5±0.3	6.3±1.2

Table 11. Retained bacterial cells on the Ti surfaces. (T7)

In summary, in this study, it is found that a threshold existed for S. aureus bacteria attaching onto titanium substrates with varying average surface roughness. In cases where the average roughness was below 0.5 µm, similar S. aureus attachment patterns were found even if the detail of surface morphology was different. In contrast, P. aeruginosa bacterial cells were found to be unable to colonise Ti substrate surfaces with an average roughness below 1 µm, unless sharp nanoprotrusions of approximately 20 µm in diameter were present (Table 11).

Puckett et al. (103) have performed an in vitro study on titanium surfaces having different nanoprography as a means to reduce bacterial adhesion. Nanorough titanium (Figure 33b) is obtained by means of a Temescal electronic beam evaporator and exhibits a decrease in bacterial adhesion compared with the case of untreated conventional titanium (Figure 33a). However, nanotubular titanium, with an internal diameter of 60 ÷ 70 nm, obtained by anodising in 1.5% HF for 10 minutes and nanotextured titanium, obtained by anodizing in 0.5% HF for 1 min, show increased bacterial adhesion despite these superficial surfaces exhibit higher surface energy and greater adsorption of fibronectin than conventional titanium. The fluorine present on the nanotubular and on the nanotextured Ti surfaces increased bacterial adhesion compared to conventional and nanorough ones. Moreover, examining bacteria attachment on the anodized nanotubular surfaces revealed the highest bacteria attachment compared to the anodized nanotextured surfaces, this is a possible role of greater bacteria attachment correlated with fluorine concentration. Another factor is the presence of amorphous TiO$_2$ on nanotextured and nanotubular surfaces, while nanorough and conventional titanium contain TiO$_2$ crystalline (anatase and rutile). Research has shown that the amorphous phase promotes bacterial adhesion in contrast to anatase, which is known for its antibacterial properties. (104)
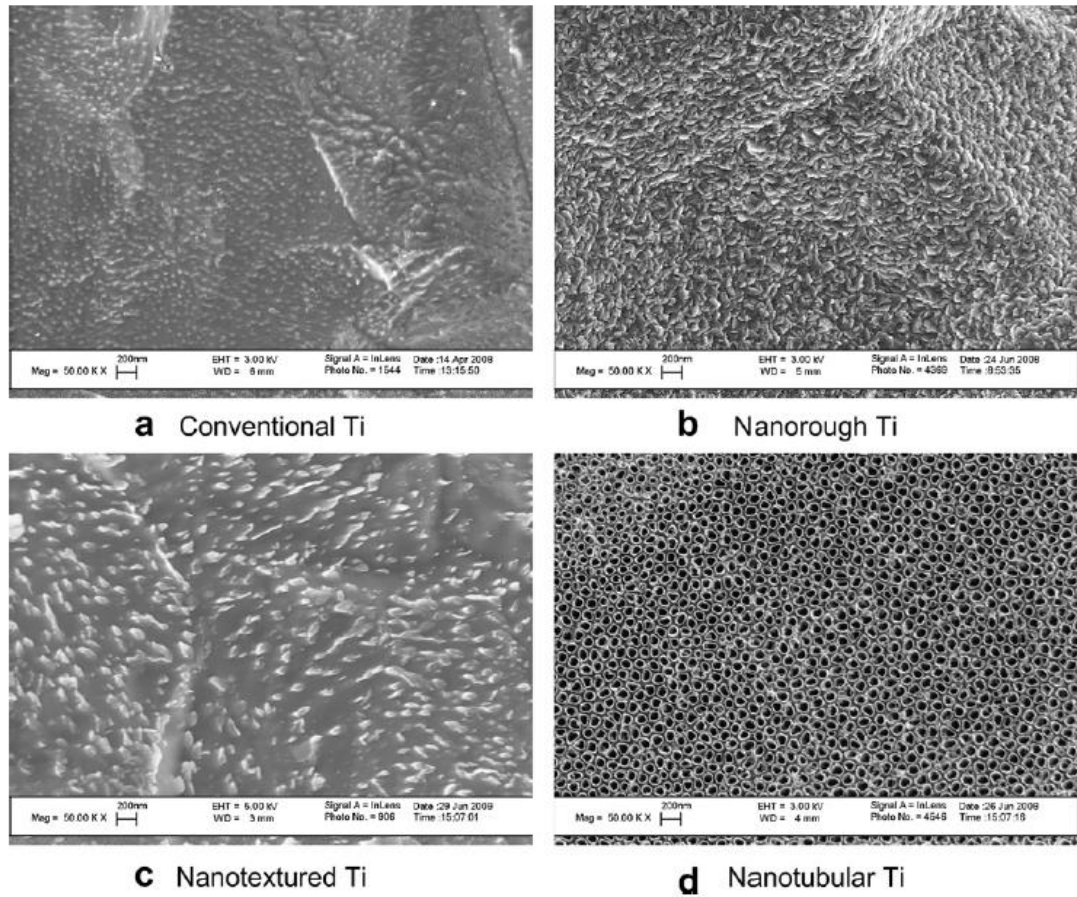
Figure 33. SEM micrographs of Ti before and after electron beam evaporation and anodization: (a) conventional Ti as purchased from the vendor; (b) nanorough Ti after electron beam evaporation; (c) nanotextured Ti after anodization for 1 min in 0.5% HF at 20 V; (d) nanotubular Ti after anodization for 10 min in 1.5% HF at 20 V. Scale bars=200 nm. (F34)

Truong et al. (105) discuss the effect of extreme grain refinement in the bulk of commercially pure, grade 2, titanium on bacterial attachment to the mechano-chemically polished surfaces of the material. The ultrafine crystallinity of the bulk was achieved by plastic deformation through equal channel angular pressing (ECAP). It was found that physico-chemical surface characteristics of the untreated pure titanium and the ECAP-modified one, did not differ in any significant way, instead of the surface roughness at the nano-scale. Optical profilometry performed on large scanning areas (225 μm x 300 μm) revealed that there was no significant difference between the roughness parameters Ra and Rq for surfaces in the two conditions, the overall level of roughness being lower for the ECAP-processed one. It was found that the bacterial strains used in this study as adsorbates, i.e. Staphylococcus aureus CIP 65.8 and Pseudomonas aeruginosa ATCC

9025, showed preference for surfaces of ECAP-processed titanium. S. aureus cells were found to have a greater propensity for attachment to surfaces of ECAP-modified titanium, while the attachment of P. aeruginosa, while also showing some preference for the ECAP-processed material, was less sensitive to the ECAP processing.
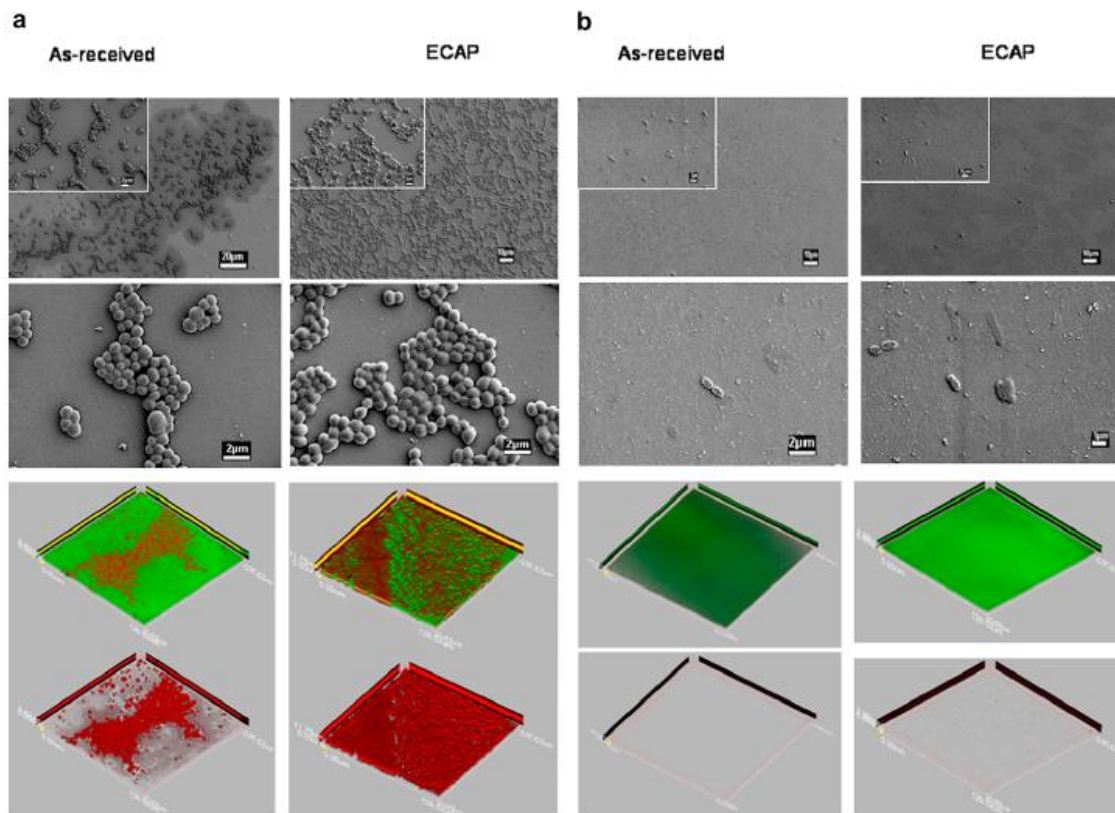
Figure 34. Representative S. aureus (I) and P. aeruginosa (II) attachment patterns on the as-received (left column) and ECAP (right column) titanium surfaces after 18 h incubation. SEM images (a) represent an overview of the attachment pattern. CSLM images (b) reveal the production of EPS (stained green with concanavalin A 488) and viable cells (stained red with SYTO_ 17 Red). (F35)

Bacterial strain	Water contact angle θ (°)	Zeta potential Z (mV)	Initial density x 10^6 (number of cells per mm^2)	Retained cells x 10^4 (number of cells per mm^2) Ti surfaces	
				As-received	ECAP
S. aureus	72.2± 8	-35.2± 1.0	20.8± 1.7	14.67± 3.34	30.57± 7.36
P. aeruginosa	43.3± 8	-14.4± 0.7	13.0± 1.5	0.06± 0.02	0.37± 0.06

Table 12. Bacterial cell surface characteristics and retained cells on the surfaces of as-received and ECAP-processed titanium after mechano-chemical polishing. (T8)
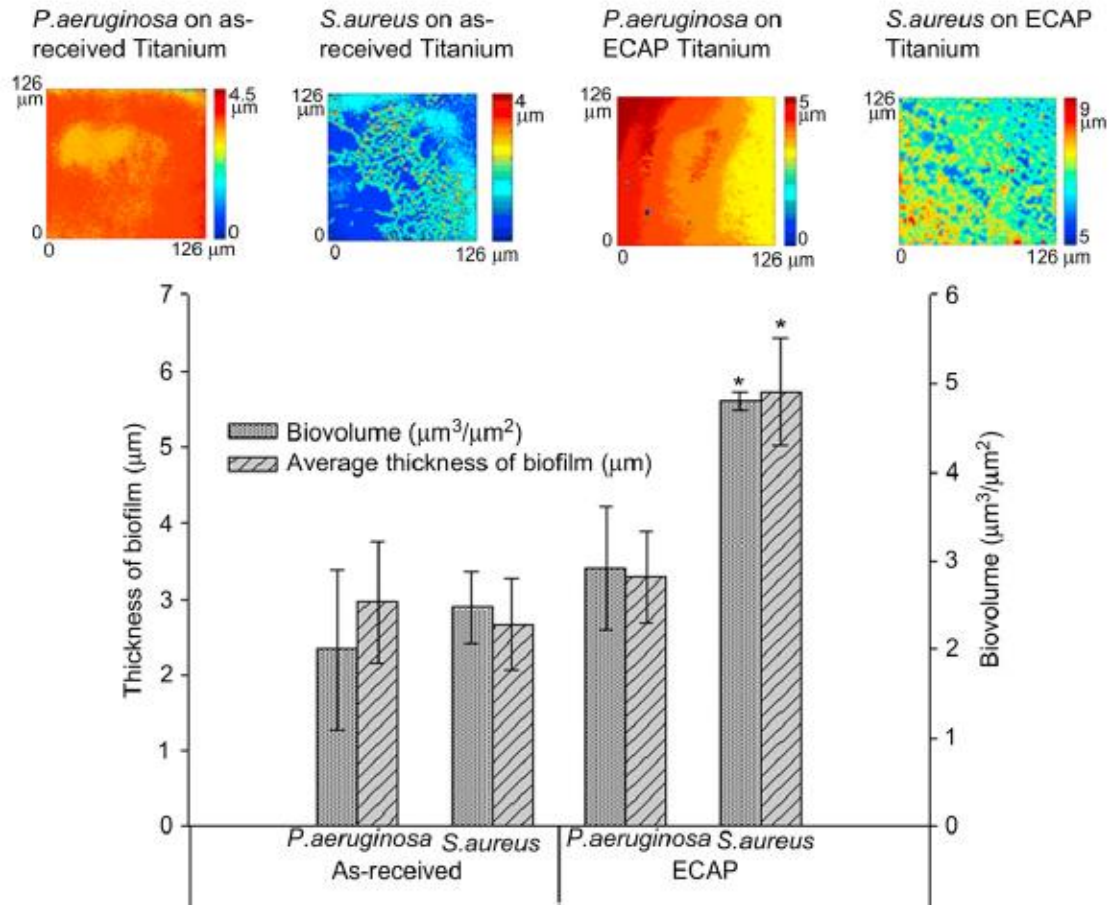
Figure 35. Biovolume and average biofilm thickness of P. aeruginosa on surfaces of as-received and ECAP titanium. (F36)

The analysis of SEM and CSLM images (Figures 34 and 35 and Table 12) revealed different attachment responses of S. aureus and P. aeruginosa grown on the as-received and the ECAP-modified titanium surfaces. After 18 h incubation, S. aureus cells were able to colonise titanium surfaces of both types (Table 12). A statistically significant increase in the number density (30.57×10^4 cells per mm^2) of S. aureus attached to the surfaces of ECAP-processed Ti was recorded (t=0.002, p < 0.05). In contrast with the attachment response of S. aureus, the overall response of P. aeruginosa cells to surfaces of both as-received and ECAP-processed titanium was fairly poor, as demonstrated by SEM analysis and CSLM imaging. Thus, only 0.37×10^4 P. aeruginosa cells per mm^2 were retained on the surfaces of as-received Ti. It should be noted, however, that the biovolume and the average thickness of P. aeruginosa biofilms on titanium surfaces of both types were not much different (t=0.29 and 0.30 respectively, p > 0.05) and were comparable to those of S. aureus (Figure 32). This means that P. aeruginosa cells produced a

considerable amount of EPS, which was retained on the surface of Ti. The degree of the biofilm heterogeneity of P. aeruginosa on surfaces of the as-received material was much higher than that on the surfaces of ECAP-processed material (Figure 32 refers to the biofilm distribution maps). (105)

Scheuerman et al. (106) studied the effect of substratum topography on bacterial surface colonization using a chemically homogeneous single crystal 1, 1, 1 silicon coupon smoothed at the micrometer level. Grooves were 10μm deep, and widths were within 20% of the predicted value. The cross-sectional shape of the grooves was more u-shaped than rectangular. Based on the ability of a bacterium suspended in fluid to reach the surface is influenced by sedimentation, attractive interactive forces, and a velocity component toward the surface provided by collisions between flowing particles, *Pseudomonas aeruginosa* and *Pseudomonas fluorescens* were cultured on micrometric grooves perpendicular to the flow of bulk water fluid, into a flow cell under specific flow conditions, chemostat media (except for glucose which was 0.4 g/L), and chemostat cell growth rate (0.2/h). They observed significant differences in the number of bacteria attached to the downstream and upstream parts of the tops of the grooves. These differences were probably due to variations in bacteria–surface initial contacts induced by the different flow regimes present at the material surface. These results suggest that bacterial responses to topographical nanofeatures may also be affected by the flow regime. Therefore, studies on the influence of topographical surface nanofeatures on bacterial adhesion should consider both static and dynamic experimental approaches to the bacterial surface colonization.

Harris et al. (107) showed that polishing a titanium surface or coating titanium with various treatments (shown in Table 13) that decreased the surface's coefficient of friction, had no signicant effect on minimising S. aureus adhesion to these surfaces under static conditions in comparison to standard medical grade titanium. The R_a and R_q roughness parameters, are represented in Table 14. Differences in roughness were observed between the samples, with TS, THY, TIG, TLF, and TAST showing comparable roughness, TSS and TC were smoother, wishlist TE and TM were the smoothest. SEM images of the surface topographies confirmed the roughness parameter results (Figure 36, surface clearly seen behind the bacteria).

LABEL	DESCRIPTION
TSS	Unalloyed Ti, gold anodised, Supplier A
TS	Unalloyed Ti, gold anodised, Supplier B
TLF	Low friction grey anodised Ti, Supplier A
TIG	Nitrogeni on implanted TSS
THY	TSS grefted with sodium hyaluronate
TAST	TSS with polymer cell promotion
TC	Chemically polished Ti, gold anodised, Suppler B
TE	Electropolished Ti, gold anodised, Suppler B
TM	Mechanically polished Ti, gold anodised, Supplier

Table 13. List of the surfaces used in that case of study, including surface label and description of the surface treatment. (T9)
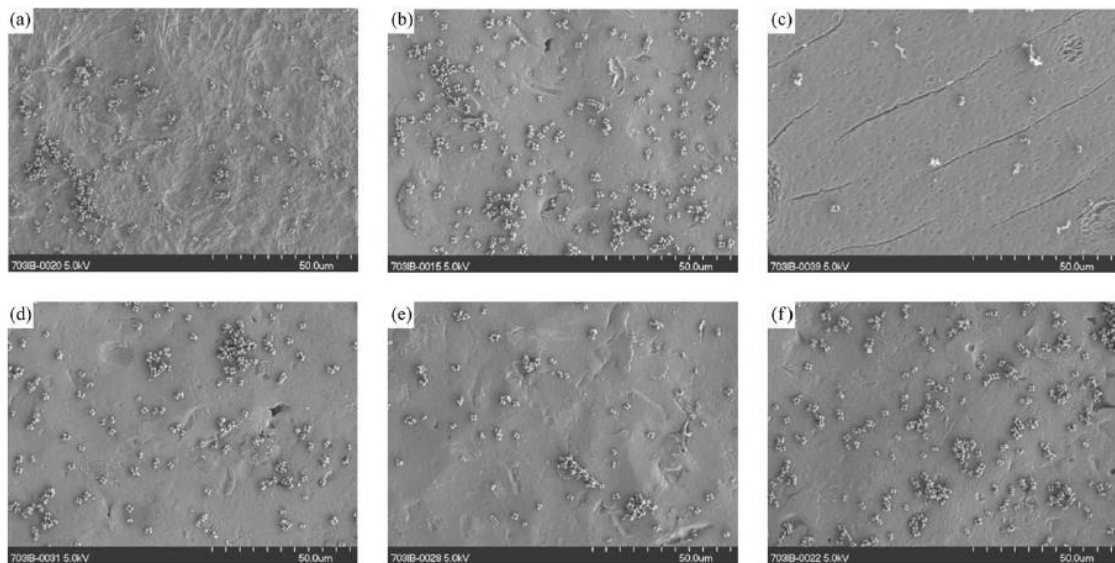
Figure36. SEM images of S. aureus adhered to the standard titanium surfaces and coated surfaces after 1h culturing. (a) TS, (b) TSS, (c) THY, (d) TIG, (e) TLF, (f) TAST. Very few bacteria are seen on the THY surface compared to the other surfaces, where small.

SEM images of the coated surfaces showed that S. Aureus adhered to all the surfaces prepared (Figure 36) with exception of the THY surface (Figure 33c). The density of bacteria on TS, TE and TM were comparable despite differences in surface roughness (Table 14). The only coating that significantly decreased the density of adhering S. aureus was the titanium surface coated with sodium hyaluronate. Thus, such a coating could have potential use as a coating for dental implants.

Test surface	TS	TSS	THY	TIG	TLF	TAST	TC	TE	TM
Ra	1.15	0.83	1.09	1.05	1.14	1.09	0.67	0.18	0.15
Rq	1.45	1.08	1.35	1.31	1.42	1.46	0.85	0.23	0.20.2

Table 14. Surface roughness parameters for the different treated titanium surfaces. Ra is the arithmetic mean and Rq the root mean square. (T10)

The following tables are schematic summary of the studies cited above:

Roughness R_a	Technique	Results	Ref.
1,8,10 nm	Etching on glass	A decrease in the size of the topographic features causes an increase in the number of bacteria that adhere to the surface. Bacteria respond to topography in a different way depending on the species: some become wider on etching surfaces without major changes in shape, others become smaller and less elongated on etching surfaces than those that have not undergone this treatment.	(100)
	Machining on pyrite	What is most affecting the alignment of bacteria is the shape rather than the size of the grooves. Topography can alter the binding force, especially when the topography characteristics are of the same order of magnitude as the bacterium. There is a bacterial alignment parallel to the main axes of crystallographic pyrite planes.	(101)
0.3-0.5 nm	ECAP process	In cases where the average roughness was below 0.5 nm, similar S. aureus attachment patterns were found even if the detail of surface morphology was different. In contrast, P. aeruginosa bacterial cells were found to be unable to colonise Ti substrate surfaces with an average roughness below 1 nm, unless sharp nanoprotrusions of approximately 20 nm in diameter were present. It is suggested that the enhanced attachment of P. aeruginosa onto surfaces possessing nanoprotrusions of this magnitude is likely to be a result of their ability to form stable contacts with the surface, which is facilitated by the cell membrane stretching over the tips of the nanoprotrusions as confirmed through increase in the level of EPS production.	(102)
	Electron beam evaporation, anodization, surface characterization	The decreased adhesion of S. aureus, S. epidermidis, and P. aeruginosa (bacteria that limit orthopedic implant function and efficacy) on nanorough Ti surfaces created through electron beam evaporation while nanotubular and nanorough Ti created through anodization resulted in an increase of bacteria attachment. This research demonstrated that through careful selection of nanometer surface properties to increase fibronectin adsorption, while maintaining favorable chemistry and crystallinity (specifically, anatase TiO_2) it was possible to decrease bacteria adhesion	(103)

Table 15. Summary of the studies cited above_Part 1

Roughness R_a	Technique	Results	Ref.
(83.02 ± 56.82) nm for 225 µm x 300 µm scanning area	ECAP process	Ultrafine crystallinity of commercial purity titanium achieved in the bulk material by means of equal channel angular pressing is also reflected in its characteristic, rich surface architecture at nanoscale. Moreover, two human pathogenic strains, S. aureus and P. aeruginosa, showed preferential bacterial attachment to ECAP-modified titanium. These results suggest that the surface architecture of the ultrafine-grained titanium at nano-scale may be one of the major factors influencing bacterial attachment.	(105)
	Etching on a silicon coupon	The flow cell experiments with the three organisms showed that there were differences in the attachment rates of the bacteria, but not the patterns. For all bacteria the rate was independent of groove size and was greatest on the downstream edges of the grooves (10 µm deep and 10, 20, 30, and 40 µm wide were etched on the coupon perpendicular to the direction of flow). The presence of grooves perpendicular to flow resulted in preferential attachment to the downstream edges of the grooves, and to a lesser extent to the upstream edges. For motile bacteria, the initial attachment rate at the control position between grooves on the surface was similar to the bottom of the grooves. Non-motile bacteria were not found in the bottom of the grooves. When the cell concentration was held constant and the flow velocity increased, the rate of attachment increased, with a decrease in the importance of position relative to the grooves. The widths of the grooves displayed no effect, even though the hydrodynamic model predicted differences in flow relative to the widths. Inert beads did not behave like the nonmotile bacteria, except that both beads and nonmotile cells showed little coverage at the bottoms of the grooves.	(106)
0.15-1.15 nm	Gold Anodization, Sodium Hyaluronate Grafting, Chemical and Mechanical Electro-polishing	Polished or coatied surfaces do not have a significant effect on minimizing S. aureus adhesion, except for sodium hyaluronate coated surface, which significantly decreased the density of S. aureus adhering to the surfaces, and could have potential use in osteosynthesis, orthopaedics or dental applications. The study confirmed that TAST surface could promote bacterial adhesion, as well as cell adhesion it is designed to promote.	(107)

Table 15. Summary of the studies cited above_Part 2

4. TOPOGRAPHIC EFFECT ON FIBROBLASTS

One of the basic requirements of a biomaterial used for implantology is the ability to promote cell adhesion, from which it will be colonized. The contact points between the cells and the ECM are defined as Focal Adhesions (FA). They are specialized, flat and elongated organelles that occupy an area of a few microns square and are often located at the periphery of the cell. FAs are anchoring sites with which the ECM is indirectly linked to the actin cytoskeleton through a complex membrane protein network. Anchor proteins perform both a signal function for the activation of specific metabolic pathways such as tyrosine kinase proteins, GTPase, phosphatase and other enzymes, as well as a structural function of binding to actin fiber bundles such as tensine, vinculin, α-actinine and mica. (108) At the level of the cell-substrate site there are small point-like structures defined as focal complexes. With the maturation of the focal complex there is a thickening or clustering of the integrins and the reorganization of actin filaments in large stress fibers, which in turn promotes further clustering of the integrins. At these structures, there is intracellular fast-assembly of specialized proteins: adhesion plaque proteins. (47)

The adhesion complexes mature, following the pattern:

- Nascent adhesion: 3-5 integrins Groups;
- Focal complex: Approximately 500 nm;
- Focal adhesion: Up to 2-3 microns.

The most common anchoring molecules are integrins, which are transmembrane heterodimeric proteins and have a size of some nanometer (8-12 nm). Therefore, considering the size of focal complexes (micron order) and integrins (order of nanometers), adhesion of cells to a substrate, hence their subsequent migration and proliferation, is influenced by topographies of both scales. It is well documented that many cells, including fibroblasts, respond to these topographies by changing their proliferation and adhesion, orienting themselves in a preferential direction (Figure 37). Moreover, especially for fibroblasts, the best surface condition becomes when surface roughness is so moderate, instead of osteoblasts and bacteria. (109)
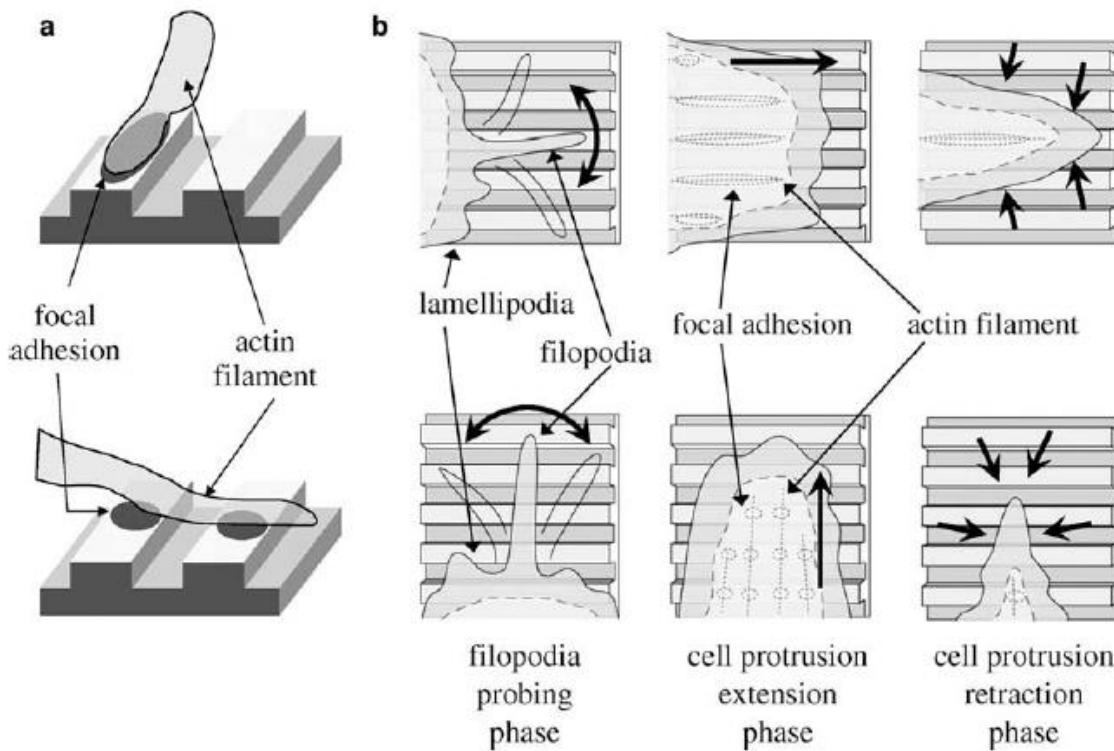
Figure37. Model for cell alignment on the nanogrooved substrate. (a) Actin filaments parallel to the grooves form wide focal adhesions at filament terminations. On the other hand, termination of perpendicular filaments is fragmented because focal adhesions form only on the ridge. (b) Filopodia movements are isotropic. Cell protrusions extended isotropically, but some that were perpendicular to the nanogrooved pattern retracted more rapidly than those parallel to the nanogrooved pattern. These cell protrusion dynamics force a cell to elongate and align along the nanogrooved pattern. (F38)

Andersson et al. (2003) suggested that the alignment of individual cells occurs only in the presence of a continuous edge, that is, only if it accompanies the groove along its entire length, without interruption or gap. This effect is known as "*Contact Guidance*". (110)

Teixeira et al. (2004) achieved grooves on silicone surfaces on which keratinocytes were cultured and showed that these cells adhere better to larger grooves and to a smooth substrate than nanogrooves; alignment however occurs only in the presence of grooves, instead of on smooth substrates where keratinocytes are randomly placed. They noticed that 70% of cultured keratinocytes aligned with substrates where the sum of the widths of the ridges and grooves is at least 800 nm; if that sum reaches 400 nm, the alignment rate is 45%. Samples were made using electron beam lithography (E-beam lithography). After 12 hours of incubation, the pattern with the fewest number of adherent cells was 400-nm pitch (Figure 38) than with wider pitches. While the highest level of alignment of keratinocytes is observed in topography with pitch of 800 nm. (111)
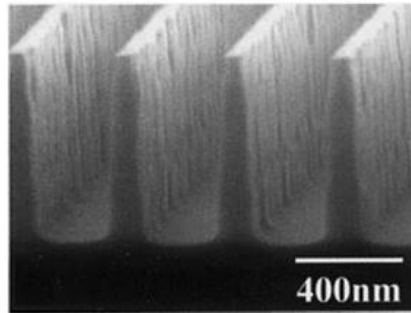
Figure 38. Sample pattern with pitch of 400nm. (F39) (34)

Hamilton and Brunette (2005) conducted a study to understand the response of human gingival fibroblasts (HGF) in the presence of discontinuity. The topography provided repeated open squares with an opening in each corner. It emerged that the cells were guided in their movements despite the absence of a continuous edge due to the location of focal adhesions and a reorganization of the cytoskeleton, the actin microfilaments and especially the microtubules. Cells showed a gap guidance, migrating diagonally from one gap to the other at the corners of the panel, attesting that substrate continuity is not a basic requirement for aligning fibroblasts. (112)

Su-Yeon Kim et al. (2009) made titanium surfaces with microgrooves of 15, 30 and 60 μm wide and deep 3.5, 5 and 10 μm and some of these samples were acidified, i.e., Samples E15 / 3,5 E30 / 5 E60 / 10. On these surfaces, later, human gingival fibroblasts were cultured in vitro. The results showed that the width of 60 μm and the depth of 10 μm of the grooves obtained better results in terms of cell proliferation and expression of those genes coding for fibronectin involved in the formation of ECM. (113)

Nevins et al. (2012) demonstrated that by constructing micro-channels with laser technique on circumferential abutment, with a range of amplitude and depth of 8-12 μm, the behavior of epithelium, fibroblasts and osteoblasts is altered. In this way, the orientation of the connective tissue is changed, allowing it to act as an anatomical barrier to the migration of the junctional epithelium. Such microchannels, placed adjacent to the abutment-implant interface, allow adhesion of the supracrestal connective tissue perpendicularly to the surface of the implant, mitigating the negative influence of the microgap formed at the abutment-implant interface and preventing the epithelium migration junctional. The result was a minimal loss of crestal bone and as in natural teeth,

a perimeter soft tissue layer of 3 mm wide was formed. The microgap that forms at the interface between abutment and implant tends to promote the formation and activation of osteoclasts and the repositioning of peri-implant connective tissue. (114)

Wieland et al. (2002) used a two-stage replica technique with a subsequent titanium-coating treatment, using commercially pure grade 2 titanium, to replicate topographies of mechenically polished (PO), acid-etched (AE), machined-like (MA), finely blasted (FB), coarsely blasted (CB), coarsely blasted and acidetched (SLA), and Ti plasma-sprayed Ti surfaces(TPS). The replicas were used to study the influence of different rough surface topographies on the response of human fibroblasts in vitro, under conditions of constant surface chemistry for all the surfaces. To judge the ability of the impression technique to replicate complex topographies, SEM and stereo- SEM investigations were performed on original Ti surfaces (PO, MA, AE, FB, CB, SLA, and TPS) and their replicas. A combination of LPM and stereo-SEM was used to characterize surface topographies because each method has its own limitations in terms of resolution and scan range and therefore it is not possible to measure topographic features across a wide range of dimensions with just one method. (36) In summary, the wavelength-dependent roughness evaluation demonstrated that over the wavelength range from 100 nm to 1 mm, the original surfaces and their replicas were congruent, and no significant differences could be found ($p > 0.05$). Different surface topographies markedly altered cell morphology of fibroblasts as has previously been found for fibroblasts cultured on microfabricated or native Ti surfaces. (11,25) Cells cultured on smooth (PO) replicas were well spread, but cells on rough surfaces (SLA and TPS replicas) provided multiple points of attachment that might be influenced by submicrometer features. However, such observations of cell morphology give no quantitative information about cell shape (Figure 39). (38)
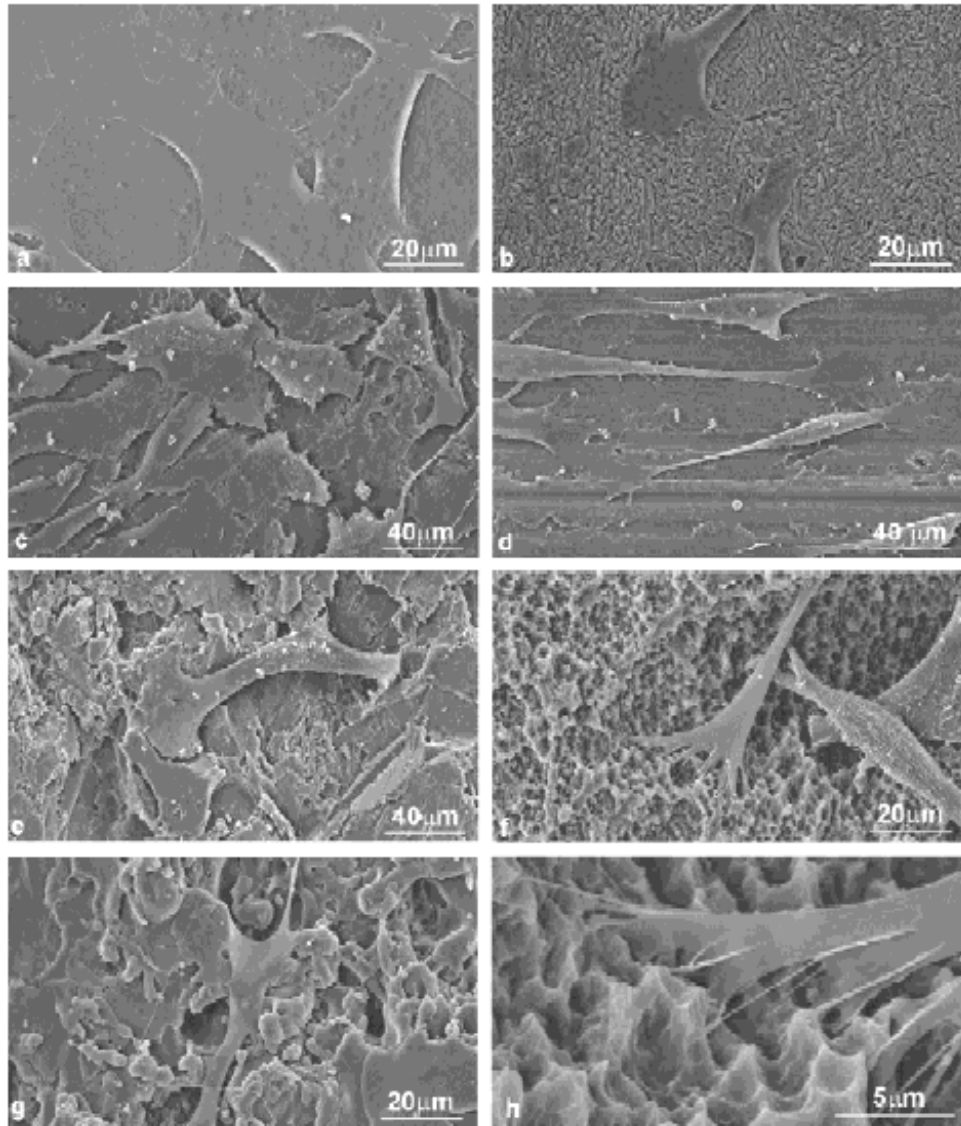
Figura 39. SEM micrographs of fibroblasts cultured for 24 h on Ti-coated epoxy-resin replicas of (a) PO (original magnification ×1000), (b) AE (original magnification ×1000), (c) FB (original magnification ×500), (d) MA (original magnification ×500), (e) CB (original magnification ×500), (f) SLA (original magnification ×1000), and (g) TPS (original magnification ×1000) surfaces. (h) SLA surfaces provide multiple points of attachment that appear to depend on the sub-micrometer range (original magnification ×5800). (F40)

- It allows investigating the influence of surface topography on cell responses based on the same

  controlled chemical composition for all surfaces;

- Epoxy-resin replicas can easily be sectioned, and prepared for light microscopy and transmission electron microscopy;

- It enables one to fabricate multiple samples of implants with the same complex surface topography;

- The fabrication cost is much cheaper than that of corresponding Ti samples.

The 3D reconstruction of cells used here enabled the determination of cell thickness and volume for cells cultured on surfaces with complex topographic features. Cell thickness and morphology, but not cell volume, were affected by surface roughness. (115)

Pecora et al. (2009) evaluated in a prospective, controlled clinical trial a tapered dental implant subjected to Laser-Lok [LL] surface treatment, with a 2mm wide collar, that has been laser micromachined in the lower 1.5 mm to accomplish bone and connective tissue attachment while inhibiting epithelial downgrowth. (116)
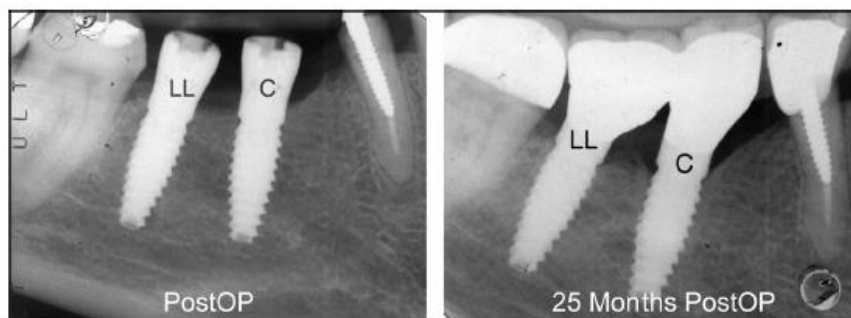
Figure 40. At implant placement and 25 monhs postoperative, 44 years, male. Control and silhouette with Laser Lock surface treatment (LL). (F41)

The implants are placed adjacent to machined collar control implants of the same design. At all measurement periods there are significant differences in the probing depths and the crestal bone loss differences are significant after 7 months (P < 0.001). At 37 months the mean probing depth is 2.30 mm and the mean crestal bone loss is 0.59 mm for LL versus 3.60 and 1.94 mm, respectively, for control implant. Also, comparing results in the mandible versus those in the maxilla demonstrates a bigger difference (control implant-LL) in the mean in crestal bone loss and probing depth in the maxilla (Figure 40). The consistent difference in probing depth between LL and control implant demonstrates the formation of a stable soft-tissue seal above the crestal bone. The LL implant was found to be comparable with the control implant in safety endpoints plaque index and sulcular bleeding index. There is a non-statistically significant suggestion that the LL crestal bone retention superiority is greater in the maxilla than the mandible.

Grew et al. (2007) demonstrates that the attachment, morphometry, growth, migration, and orientation of fibroblastic cells are moderated by substrate microgeometry, both within a collagenous matrix and when grown as individual cells. A well-studied fibroblastic cell line was employed to verify that substrates were capable of orienting cells, directing their substrate-attachment tendencies, and organizing their constituents in a fashion that is consistent with the results of other investigators who examined cells grown directly on microgrooved or otherwise modified surfaces. (117) Microgrooved silicon-wafer templates having parallel, square-wave microgrooves with different periodicities 3.55-23.75 µm were created with computer-aided design and multiple reactive-ion etching techniques. An example of a template surface is shown in figure 41.
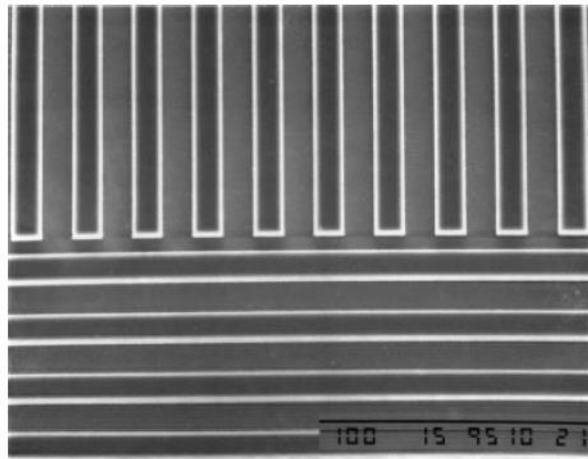
Figure 41. Scanning electron micrograph of a portion of a silicon-wafer mold bearing 12 µm microgrooves.
Bar =100 µm. (F42)

Cell culture substrates were created from the templates by solvent-casting polystyrene (15 g in 100 mL ethyl acetate) under a vacuum. After air-drying, the substrates were coated with titanium oxide, affixed within 24-well tissue culture plates or 60-mm Petri dishes, and ethanol-sterilized.
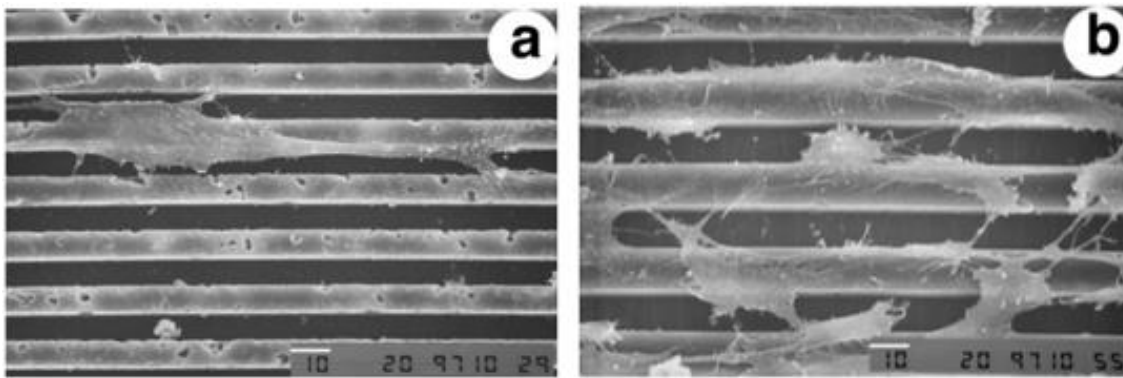
Figure 42. Scanning-electron micrographs of NIH-3T3 fibroblasts grown on 8 μm (a) and 12 μm (b) microgrooved substrates for 8 days. The individual cell grown on 8 μm grooves is attached to several adjacent ridges, bridging the intervening grooves. The cells grown on 12 μm grooves most frequently lie atop the ridges or within the grooves. Both microgroove dimensions impose a strong orientation effect upon the cells. Bar=10 μm. (F43)

The lengths, widths, aspect ratios, and attachment areas of individual cells reveal that microgroove dimension affected the sizes of cells (rat tendon fibroblasts RTF) and their abilities to spread. Cell densities reflect the rates of cell proliferation that occurred on each type of substrate. Cell orientations, determined by measuring the angular deviation of the direction of the long axis of each cell from the direction of the underlying microgrooves, indicate the ability of the various microgroove dimensions to direct the organization of the cells' contents. Cells grown on microgrooved substrates were nearly uniformly oriented in parallel with the direction of the microgrooves (Figure 42). (117) The following table is a schematic summary of the studies cited above:

Grooves dimensions	Technique	Results	Ref.
400- 800- 1200- 2000 nm (pith)	E-beam lithography	The highest level of alignment of keratinocytes occurs in topographic fields with a pitch of 800 nm. Focal adhesions for both types of cells are essentially along the surface ridges.	(111)
Width x depth, (34x34 – 65x65) μm x (4-10) μm		HGFs and epithelial cells of the porcine periodontal ligament are oriented diagonally in the panels made on the surface of the substrate, proving that no continuous border for aligning these cells is required.	(112)
Width x depth, 200 μm × 100 μm; Distance between microgrooves, 50 μm	Photolithography on cp Ti	(22.351±2.766) μm	(113)
8-12 μm	Laser	The distance between the base and the free margin of the gingiva (probing depth) is lower, as well as the crestal bone loss around the implant.	(114)
	Stamping procedures and Sputtering over cp Ti samples	XPS investigations indicated that the chemical composition of the Ti-coated epoxy-resin replica samples was the same for all surfaces independent of the roughening processes such as blasting or etching originally used to produce the different topographies of the cpTi samples. Thus, these replica surfaces can be used to investigate the effects of surface topography on cell behavior under conditions of constant surface chemistry.	(115)
Width x depth, 12 μm x 10 μm	Laser Lock	The consistent difference in probing depth between LL and control implant demonstrates the formation of a stable soft-tissue seal above the crestal bone. LL limited the crestal bone loss to the 0.59 mm range as opposed to the 1.94 mm crestal bone loss reported for control implant. The LL implant was found to be comparable with the control implant in safety endpoints plaque index.	(116)
Parallel, square-wave microgrooves with periodicities of 3.55, 12.83, 15.75, and 23.75 μm. Grooves dimensions are, respectively: 1.80x1.75x1.75 μm³ 6.50x6.33x5.00 μm³ 8.00x7.75x7.50 μm³ 12.00x11.75x7.50 μm³	Multiple reactive ion etching	Microgrooves are powerful determinants of cell orientation in vitro. Cellular orientation, expressed as degrees of deviation from the direction of microgroove direction, was profoundly and significantly reduced in cultures grown on microgrooves, compared with the high deviation from horizontal seen in cultures grown on flat, control surfaces.	(117)

Table 16. Summary of the studies cited above

MATERIALS AND METHODS

1. CUTTING, MARKING AND POLISHING OF SAMPLES

This thesis work has been carried out on commercially pure titanium of grade 2, ASTM B348, Titanium Consulting and Trading, which is more osteointegrable but less resistant than commercially pure titanium of grade 4, vice versa, suitable for small section systems, e.g. dental implants, the main final application designed for the superficial changes developed in this thesis work. Samples dimensions are in the form of disks of 10 mm of diameter and 2 mm thick, obtained by cutting cylindrical bars. The cutting machine used is the ATM "Brilliants 220" automatic cutter, with an alumina blade (Al_2O_3) and a speed of 0.020 mm/s (Figure 43).

Figure 43. Cutting Machine for cutting samples in disks with 2mm thickness

Samples shown clear signs of cuts, imperfections and scrap. So, the faces of each sample obtained were undergone to two different procedures. The sample's face that will not affected by the processing techniques and the subsequent tests were marked using an electric pen, the other one, instead, i.e. the unmarked face, was firstly polished and then used for next treatments. The polishing machine used is the Struers -LaboPol-2 polisher (Figure 44).
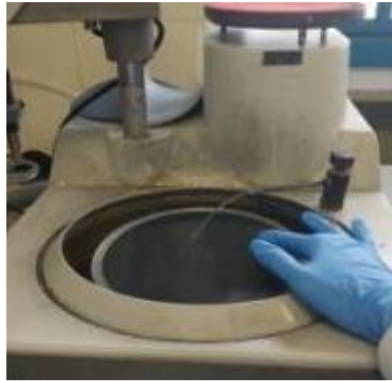
Figure 44. Polishing machine

The polished samples were obtained by the following polishing protocol:

- 1 minute with paper 320;
- 1 minute with paper 600;
- 1 minute with paper 800;
- 1 minute with paper 1000;
- 5 minutes with paper 2500;
- 10 minutes with paper 4000.

Figure 45. Samples obtained following the polishing process

Afterward, 4000 abrasive paper was replaced with a special cloth and a mirror polishing step was performed using a colloidal silica suspension based on 25 ml of silica suspension and 10 ml of ultrapure water and then sonicated for 5 min. (Figure 45)

The rough samples were produced using a sequence of abrasive papers to obtain a roughness, Ra, in the range of 0.1-0.15 μm, useful for adhesion and alignment of fibroblasts and such that it does not increase the bacterial adhesion.

2. SAMPLES WASHING

To remove contaminations introduced on the surface of the samples because of the previous operations, disks were washed in an ultrasonic bath. Particularly, by accomplishing a specific protocol, three washings were performed at room temperature. First, the samples were immersed in 30 ml of acetone, placing the marked side, which is not of interest, in contact with the bottom of the becher and leaving up the polished or rough side, i.e. the one on which the subsequent treatments will be made. This was done by working under laminar flow cabinet and with HEPA filter. After that, the bechers were covered with aluminum paper and transferred to the sonicator by setting a 5-minute working time. At the end of 5 minutes, the samples were transferred under the laminar flow cabinet and immersed in 50 ml of distilled water and re-inserted into the sonicator for 10 minutes. This last washing was repeated a second time with new ultrapure water. The instrument used, the sonicator (Figure 46), ensures the separation of residuals and contaminations of various sorts, thanks to the transmission of mechanical vibrations amplified by a high frequency electric current, equal to about 20 kHz, in a tank containing water, in which the bechers containing samples are placed; this electric energy is transformed into an acoustic impact energy between the detergent liquid, i.e. the water, and the surface to be cleaned. At the end of the washing, disks could dry under a laminar flow cabinet and then packed in special sealed envelopes.

Figure 46. Utrasonic machine

3. SURFACE TREATMENT OF EBW SAMPLES

A part of the samples used in this work, after having been polished according to the protocol described in the previous paragraph, has undergone a surface treatment by means of Electron Beam Welding (EBW) at the Technical University of Graz. Three types of samples have been created with different widths of the grooves, respectively of 5, 10 and 30 micrometers. (Table 17) The dimensions chosen are those studied in previous works and which showed the ability to condition the behavior not only of the adhesion of gingival fibroblasts but also of the adhesion of bacteria. (47) (56)

SAMPLE NOMENCLATURE	AMOUNT	STEP SIZE
EBW 5	3	5 µm
EBW 10	3	10 µm
EBW 30	3	30 µm

Table 17. Summary table of samples produced by Electron Beam Structuring

An important feature of the EBW technique is deep penetration. This effect is achieved thanks to the highly accelerated electronic beam. Electrons hit the surface and penetrate slightly beneath it, releasing most of their kinetic energy, which becomes heat. This leads to enormous heating in the beam region of the beam and therefore to the partial evaporation of the base material. The beam can cross the vapors with greater ease than the solid metal, thus facilitating the penetration of electrons into the metal itself.

The width of the molten zone is therefore extremely limited: the depth/width ratio can exceed the value of 20/1. The thermal input of this technique on the sample is controlled by 4 variables:

- Beam current;
- Acceleration potential;
- Beam spot size;
- Welding speed.

The penetration level increases by increasing the beam power density. In order to vary the level of penetration, the first two parameters are crucial, while the third and the fourth essentially serve to control the process.

4. SURFACE ACTIVATION WITH PLASMA O2

Plasma activation is a method of surface modification employing plasma processing, which improves surface adhesion properties of many materials including metals, glass, ceramics, a broad range of polymers and natural materials. Plasma processing achieves this effect through a combination of reduction of metal oxides, ultra-fine surface cleaning from organic contaminants, modification of the surface topography and deposition of functional chemical groups. Particularly, the plasma activation can be performed at the atmospheric pressure using air or typical industrial gases including hydrogen, nitrogen and oxygen. Thus, the surface functionalization is achieved without expensive vacuum equipment or wet chemistry, which positively affects its costs, safety and environmental impact. Fast processing speeds further facilitate numerous industrial applications. (118)

In this work, surface treatment with oxygen plasma was carried out in order to make the surface of the samples more reactive for the subsequent adhesion of keratin nanofibers coating by electrospinning technique. Samples were placed in special housings inside a vacuum chamber. Once the chamber has been sealed, oxygen is inserted in the form of gas and an electric field is applied to allow plasma formation (Figure 47).

Loaded ions, affecting the exposed surface of the samples, modified Ti surface bonds, making it more responsive. The samples at the end of the treatment were placed in Petri Plates of 12 wells, two of them were sealed in air at room temperature and the other two were sealed in a physiological solution at room temperature. The purpose of this different

packing of samples was to maintain the reactivity of the treated surfaces and to study how the different type of packaging could affect the goodness of the adhesion of keratin nanofibers coating.
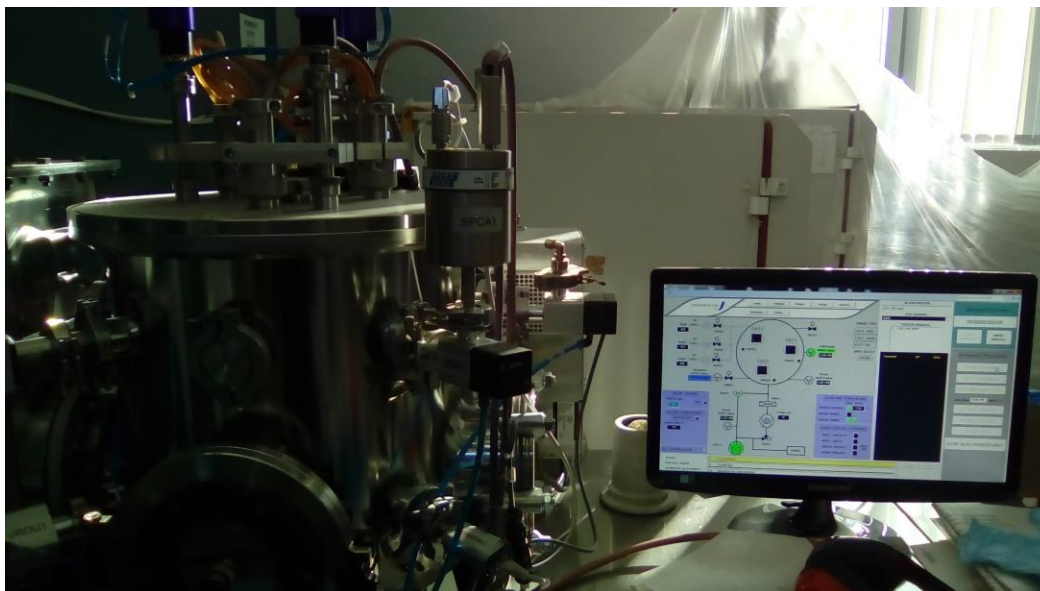
Figure 47. Instrument for oxygen plasma activation.

5. UV ACTIVATION

Titanium is a very reactive metal, if exposed to the atmosphere or to an environment containing free oxygen, on its free surface occurs an oxidation reaction that forms a thin, tenacious oxide film. This passive oxide layer, or even defined protective oxide, whose thickness is about 5 nm, gives to the material excellent corrosion resistance in a wide range of aggressive media. If the environment in which titanium is placed is sufficiently rich in oxygen, the oxide film is able to regenerate itself in a short time if mechanically damaged. (119) The nano-structured titanium dioxide has photocatalytic properties: for example, it can absorb the light-emitting radiation by generating photo-catalytic effects, that is, it can take advantage of the electromagnetic radiation energy absorbed to cause chemical reactions in other molecules that are very close to surface of metal particles. This process is only effective using ultraviolet radiation, whose wavelength λ belongs to the range of 400 nm ÷ 10 nm. (120) The absorption by the TiO_2 of UV radiation generates electron-gap pairs, the titanium dioxide gap discomposes the molecules of water in hydrogen and hydroxyl ions/radicals, the electron instead, reacts with the oxygen molecules to form superoxide ions. (121) For this reason, ultraviolet pretreatment of

titanium, especially the TiO$_2$ layer, before functionalization can make improvements, ascribable to an increase in superficial OH groups. (122) The irradiation took place after the deposition of keratin coating, in order to stabilize and strengthen the adhesion of the coating to the metal oxide substrate. The lighting was obtained with a low power 300 W lamp with monochromatic emission at wavelength $\lambda = 365$ nm (Figure 48).

The distance between the lamp and the samples is 25 cm and the environmental conditions were:

- Temperature 20 °C
- Humidity 65%

Samples subjected to UV irradiation were:

- Smooth-Ti cp/Keratin;
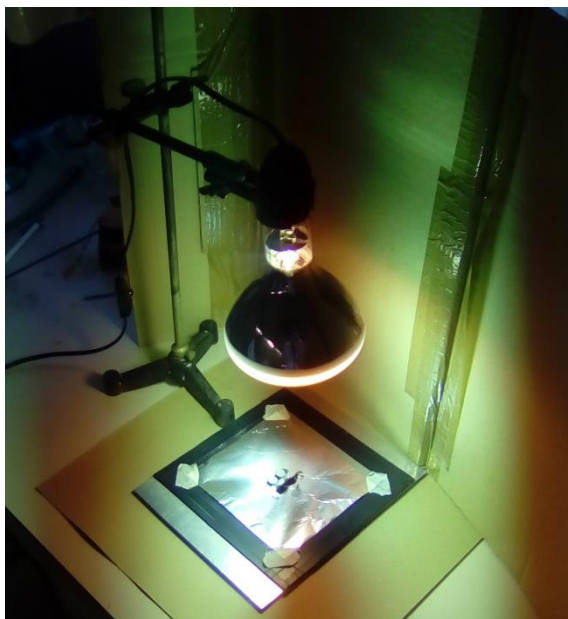
Figure 48. Lamp for UV activation

6. ELECTROSPINNING TECHNIQUE

Electrospinning is a production method through which fibers having a diameter of hundreds of nanometers can be produced using an electrostatic guiding system that allows their controlled deposition over a substrate. (123) Unlike conventional spinning techniques, it is possible to obtain fibers with a diameter below micrometers reaching up to a few nanometers. The main features of these nanofibers are the following:

- Ultra-fine diameters, less than 100 nm;

- Large surface areas;

- Allow to create structures like the ECM (Extra Cellular Matrix) or porous structures with pore sizes of a few micrometers;

The electrospinning process is performed with a syringe (or micrometric nozzle) containing a polymeric solution, which will be pushed in a pump-controlled manner to generate a constant flow. A high-power generator creates the potential difference between nozzle and collector. The polymeric fiber jet is stretched up to a few micrometers from the electric field that has to cross and then it is gathered on a metal collector.
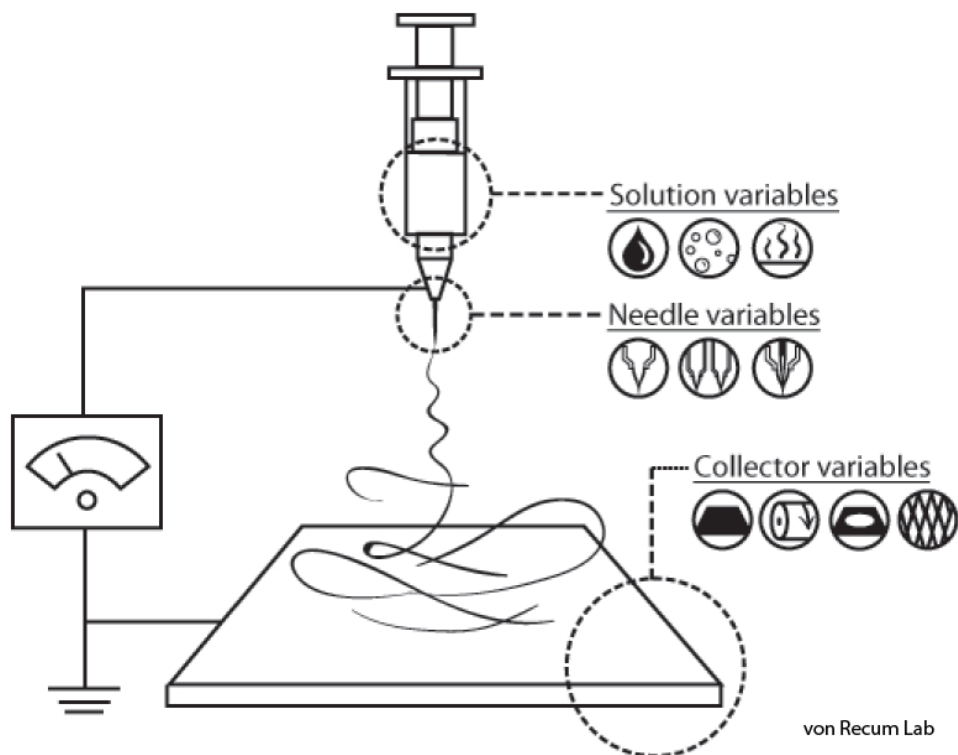
Figure 49. Electrospinning Process. Vertical configuration. (F44)

From figure 49 is possible to observe that the output of the syringe nozzle creates the Taylor Cone, which causes drastic reduction of fiber sizes. This cone varies depending on the viscosity of the solution and on the force of the electric field (3-12 kV). During Taylor's cone formation, the surface tension forces and the electric field forces 'squeeze' the solvent to evaporate the solution. Using traditional nozzles, full fibers can be obtained. Modified nozzles can also be used to obtain, for example, empty or bicomponent fibers. In addition, it is possible to use multiple nozzles in one electrical field to optimize the yield of the manufacturing process.
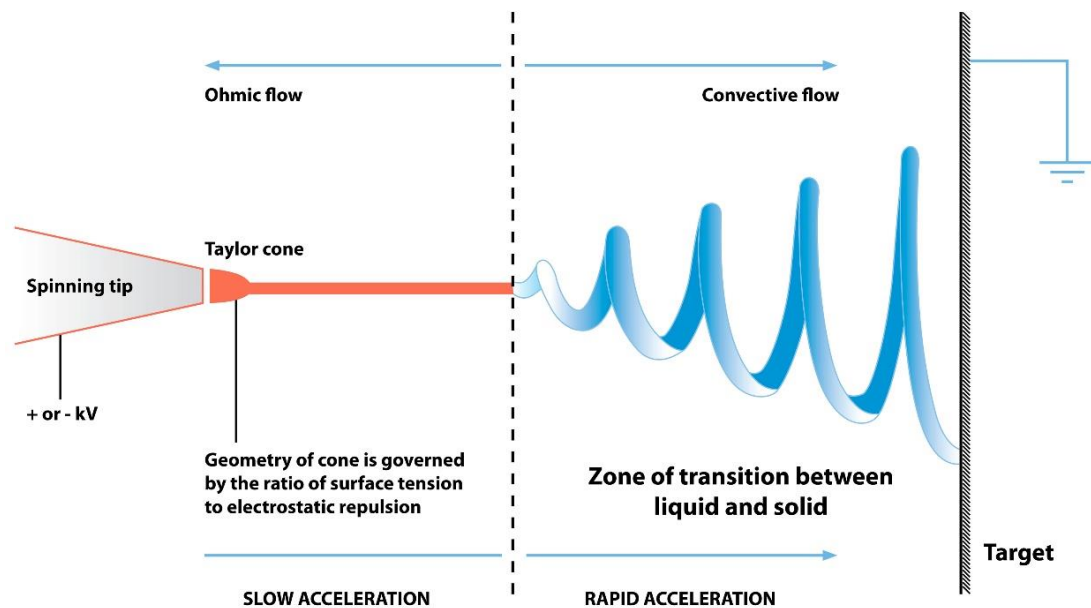
Figure 50. Electrospinning Diagram. (F45)

At the end of Taylor's Cone, the jet goes through what is called the Instability Zone, within which the jet undergoes a three-dimensional distortion and further reduces its diameter (Figure 50). The filament collection area, that is, the metal collector, can be a plane, a rotating cylinder or other geometries. Depending on the geometry chosen, clusters, cracks or other configurations of deposited fibers are obtained. (123)

6.1. Spinning flaws

Electrospinning is a technique with several critical factors. During spinning, we can create impurities in the texture such as beads, ribbons and surface defects that compromise its purity:

- **Beads** are fibrous swellings provoked by too slow evaporation of the solvent occurred after deposition on the collector;
- **Ribbons** are still rich in solvent fibers that collapse on them, losing their cylindrical geometry;
- **Surface defects** are the index of a not optimized spinning system.

6.2. Critical process factors

These are factors that play a key role in determining the success of spinning and can be treated by dividing them into three categories.

1. **System parameters**, which mainly concern the properties of the solution and the properties of the polymer:

    Solution properties

    - **Concentration.** There is a minimum concentration under which is established an electrospray process and a maximum concentration above which the solution is too viscous to ensure a continuous process;
    - **Viscosity.** For too low values the fibers that are formed are not continuous, at too high values the polymeric jet has difficulty forming;
    - **Conductivity.** A factor that depends on the nature of the polymer, the solvent and the presence of salts in the solution. For excessively low values there are discontinuous fibers and beads, for excessively conductive solutions the instability region is very marked and fibers with very uneven diameters are produced;
    - **Surface Tension**. It depends mainly on the solvent. For low values, the prospect of having beads in fibers will be lower;

Polymer properties

- **Molecular weight.** It influences viscosity, surface tension and conductivity of the solution and dielectric strength. The more easily filamented polymers generally have high molecular weights, otherwise beads can be formed. As the molecular weight increases, the fiber diameter also increases;

- **Structure.** A linear structure polymer is easier to thread, because of major inter-chain interactions;

Process parameters

- **Voltage.** There is a minimum voltage above which the fibers can be obtained. When the voltage increases, the fibers have a lower diameter. Above a threshold value the diameters increase again, because the jet increases at the output of the nozzle;

- **Flow.** The flow influences the speed of the process. Low flow rates allow for better evaporation of the solvent before deposition over the collector. High flow rates, hence faster, will have larger fiber diameters and larger pores of electrophilic membranes;

- **Tip-Collector Distance.** Below a minimum distance the solvent does not have the time to evaporate and consequently the fibers do not have time to form;

2. **Environmental parameters.** These parameters influence not only the fiber morphology but also the external electrical field.

- **Humidity.** The high humidity causes the formation of pores on the surface of the fibers. Conversely, if low, the solvent evaporates quickly, and the needle becomes clogged after a few minutes;

- **Pressure.** Decreasing pressure does not improve the electrospinning process; (123)

In this dissertation work, smooth samples, underwent electrospinning technique at the laboratories of CNR-ISMAC (Institute for Macromolecular Studies) of Biella, Piedmont. The instrument used for electrspinning was Spellman High Voltage Electronics Corporation, SL 50, Power supply, KDS 200, KD Scientific Inc. in bottom-up configuration. The deposition took place under the following conditioins:

Environmental Conditions	Average Value	Standard Deviation
Temperature [°C]	26,36	0,76
Humidity (%)	40,24	0,76

Table 2. Environmental conditions for the deposition of keratin

The electrophilic solution, 15% by weight of keratin in formic acid (HCOOH), was prepared 20 hours before the process and mixed with a magnetic stirrer, then inserted into a syringe of 5 ml size and connected to a stainless-steel capillary with internal diameter of 0,2 mm and the external one of 0,4 mm, which acts as cathode (Figure 51). The collector, which is the anode, is a stainless-steel plate on which the sample is placed. Moreover, the collector is covered with an aluminum foil to prevent the keratin jet from getting it dirty when it does not reach the sample (Figure 52).

Figure 51. Syringe containing the keratin solution

Figure 52. Metal collector coated with aluminum foil

The solution jet starts from the bottom, crosses the capillary and rises upward in the direction of the collector. To direct the jet well, the capillary passes through the hole of an insulating box (Figure 53).

Figure 53. Detail of the electrospinning instrument

The following process parameters have been set:

- Voltage 25 kV;
- Rate 0.002 ml/min;
- Capillary- Collector distance 20 cm.

A preliminary spinning test was carried out without placing the sample on the collector to verify the deposition, that is, the formation of a white patina on the surface. It was chosen as a deposition time of 5 min and no inclination of the sample with respect to the collector because of the previous work these were the optimal deposition conditions. (56) Samples used were:

- 2 Smooth-Ti cp, as control;
- 2 Smooth-Ti cp, which after the electrospinning process were treatd with UV irradiation, at the CNR of Biella;
- 2 Smooth-Ti cp, previously subjected to oxygen plasma treatment and stored dry until the deposition of keratin;
- 2 Smooth-Ti cp, previously subjected to oxygen plasma treatment and stored in physiological solution up the deposition of keratin;

The keratin used in this thesis work was extracted from sheep wool. The wool belongs to the group of proteins called keratins, which have a high content of cystine or sulfur residues and can be classified as hard or soft according to their tactile properties. There is about 3% more sulfur in hard keratins, i.e. wool, compared to soft keratin, i.e. the skin. Furthermore, the wool contains only 82% of keratin proteins, in fact the rest is composed of proteins with a low cystine content, such as waxy lipids and polysaccharides. (124) Usually to extract the keratin from the wool it is necessary to break the SS sulfur bridge bonds by reduction with thiols (thioglycolic acid, dithiothreitol or 2-mercaptoethanol), oxidation with peracetic acid and performic acid or by sulphite, reaction obtained with sulfite ions, bisulphite or m-bisulphite. All these agents must be used in pairs with a protein denaturant, such as urea, which breaks up hydrogen bridge bonds. Since most of the reducing and oxidizing agents are harmful, the extraction of keratin from sheep wool, carried out by the CNR-ISMAC of Biella, was obtained by

sulphytolysis, a reaction according to which the SS bonds of cystine residues are broken down. in cysteine residues and cistein-S-sulphonate residues, called Bunte salts, even if with this method the extraction yields are lower. (124)

7. THERMAL TREATMENT AND STERILIZATION

Samples coated with nanofibers of keratin for 5 min and EBW samples were left in the Petri dishes (Figure 54) and have been subjected to a heat treatment in an oven at 180 °C for 2 h, in order to stabilize the coating and to make a previous sterilization.
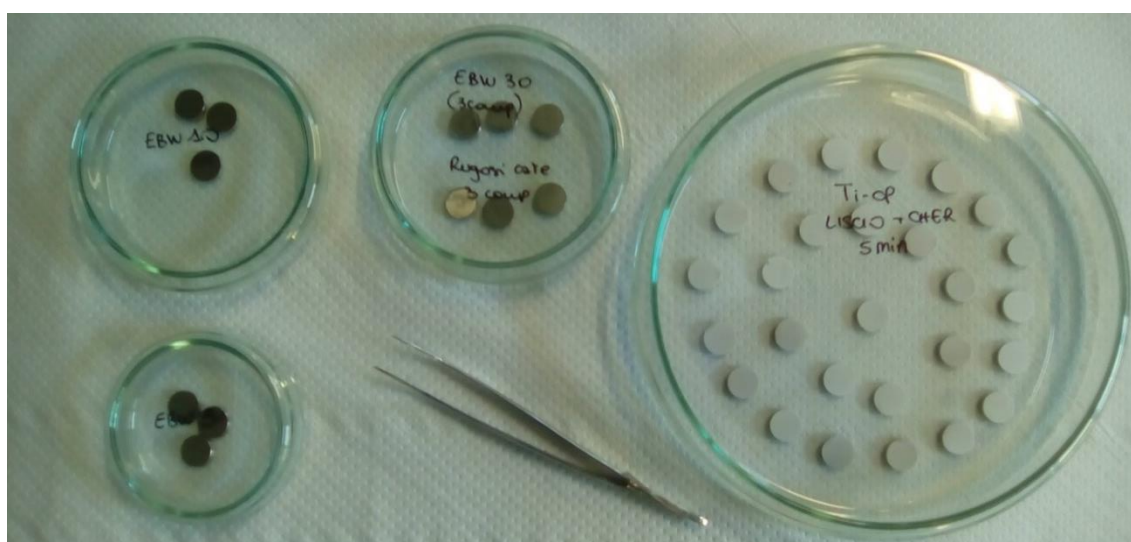
Figure 54. Detail of heat treated material

On completion of treatment, the Petri dishes were enveloped in paper-plastic bags to preserve the sterility during storage. All the materials necessary for the subsequent silver treatment were then sterilized and autoclaved. The packaging envelope has a transparent side to allow to recognize the content and the process indicators; the closure of the envelope is done by heat sealing.

Sterilization in autoclave (Figure 55 and Figure 56) at 121 ° C, 1 bar for 30 min of:

- 21 jars for samples;
- bottles of bi-distilled water;
- bechers;
- 2 clamps;
- pipettes;
- 2 spatulas;
- 2 magnetic stirrers.

Figure 55 e 56. Autoclave instrument for sterilization and detail of sterilized material

The sterilization is verified by the process indicator which is turned from light to dark brown. All samples upon completion of treatment, were left in the Petri dishes closed with aluminum foil and wrapped, waiting for the subsequent treatments for bacterial and cell cultures.

8. ANTIBACTERIAL TREATMENT WITH SILVER

Treatment with silver aims to reduce the problem of bacterial adhesion to dental implants. Three concentrations of silver were chosen and listed below:

- Low concentration of AgNO3;

- Intermediate concentration of AgNO3;

- High concentration of AgNO3.

The treatment was carried out at room temperature, maintaining the pH of the solution as prepared, and subsequently using it as a control parameter for each of the three concentrations. For each type of concentration, six samples were used and each of them was immersedin 10 ml of solution. All operations were carried out under laminar flow hood and with HEPA filter (Figure 57). The pH was measured in the three solutions for a short time. In this way, there is a good compromise between efficiency and time of treatment, because when the concentration of the solution is increased, a good amount of silver on the samples is guaranteed and the short time allows to speed up the operations.

Figure 57. Laminar flow hood and jars containing the samples immersed in the corresponding agno3 solution

Samples subjected to Ag treatment were:

- 6 smooth-Ti cp/keratin/Low AgNO$_3$;

- 6 smooth -Ti cp/keratin/Intermediate AgNO$_3$;

- 6 smooth-Ti cp/keratin/High AgNO$_3$;

The six samples used for each solution were subdivided into two groups of three samples, the first group to be subjected to cellular testing, while the second group to be subjected to bacterial adhesion tests.

9. SURFACE CHARACTERIZATION

9.1. FESEM-EDS

The Field Emission Scanning Electron Microscope (FESEM) is an analysis instrument that allows observing the surface of a sample by exploiting electrons released from a field emission source. Inside a high vacuum column, the so-called primary electrons are focused and deflected by electronic lenses in such a way as to produce a narrow beam which bombards the object to be analyzed. As a result, the object emits secondary electrons, whose angle and velocity are related to the surface structure. A detector captures secondary electrons and produces an electronic signal which is amplified and transformed into a video image. In standard electronic microscopes, electrons are generated predominantly by heating a tungsten filament, exploiting the Joule effect generated by the current passage. In FESEM, however, a "cold" source is used, i.e., a thin and pointed tungsten needle with a 10^{-7}-10^{-8} m tip diameter that functions as a cathode in front of a primary and secondary anode. The voltage between these is in the order of 0.5-30 kV and it is necessary to achieve a high degree of vacuum, 10^{-8} Torr, in the microscope column. The electron beam produced is about 1000 times smaller than that of a standard microscope and therefore the image quality is much higher. For this reason, FESEM is used to expose very small topographic details on the surface of objects. Biologists, chemists and physicists apply this technique to the analysis of structures that can be small up to 1 nm. Images can be viewed in two modalities:

- Secondary electron (SE)

- Backscattered electron (BSE)

The SE is used to map the surface of a sample, so it is necessary to detect type 1 secondary electrons (SE1) and this is done efficiently by a detector located in the optical path. A second detector is placed on the wall of the chamber that contains the sample and allows to detect secondary electrons having a small backscattered component. The working distance therefore exerts a significant influence on the efficiency of this mode: the detector works particularly well over long distances and, since it is mounted with a certain angle with respect to the sample, the view is always lateral and offers good information on the surface. The BSE mode instead, is intended to show the compositional differences within the sample. Since the BSE detector is placed below the last lens, it offers a solid wide angle to detect backscattered electrons. The resulting contrast in BSE images depends on the presence of elements with different atomic numbers and their distribution (Figure 58).
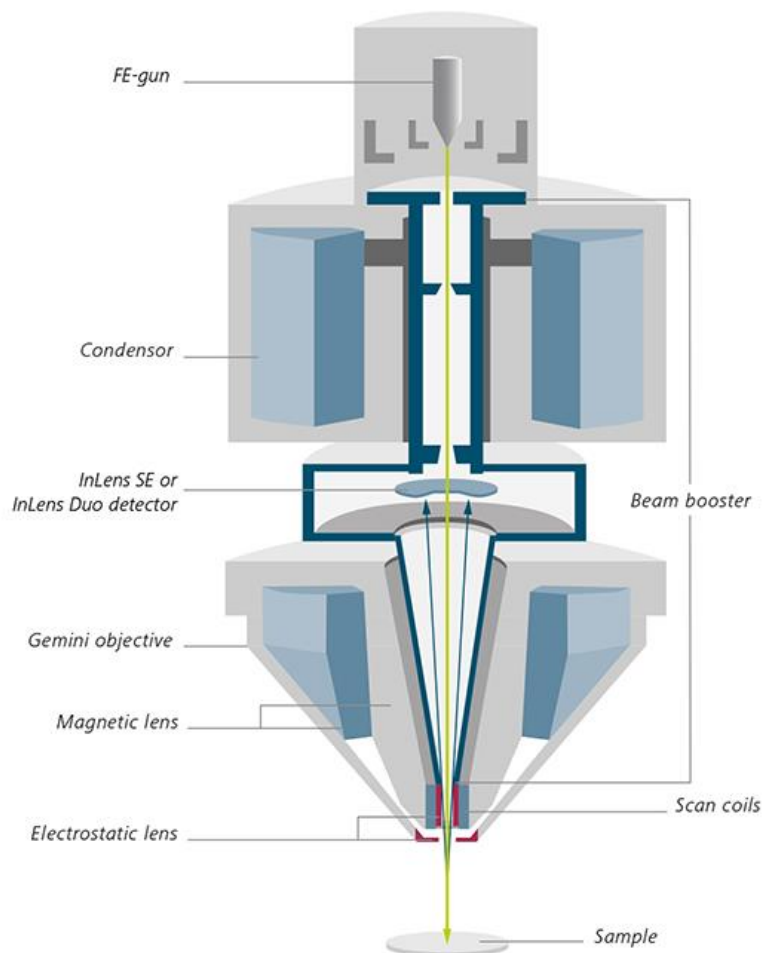
Figure 58. FESEM scheme (F46)

In addition to this kind of analysis, FESEM also enables Energy Dispersive X-ray Spectrometry (EDS), which is an instrumental analysis that identifies the elements present on the surface and their relative proportions such as, for example, their atomic percentage. It uses the X-ray emission from a sample hit by an accelerated electronic beam. The graph shows the X-ray spectrum of the scanned area: Axis-x reports the number of X-rays received and processed by the detector while on the y axis is reported the corresponding energy level. Anelastic interactions between the electron beam and sample atoms produce two types of X-ray: those resulting from the electron-ejection contained in an internal atomic shell and those resulting from the interaction of the beam with the atomic nucleus. The former appear as peaks on a continuous X-ray background and their energy depends on the atomic number of the element. The X-rays may derive from deeper areas of the sample compared to secondary and backscattered electrons (Figure 59).
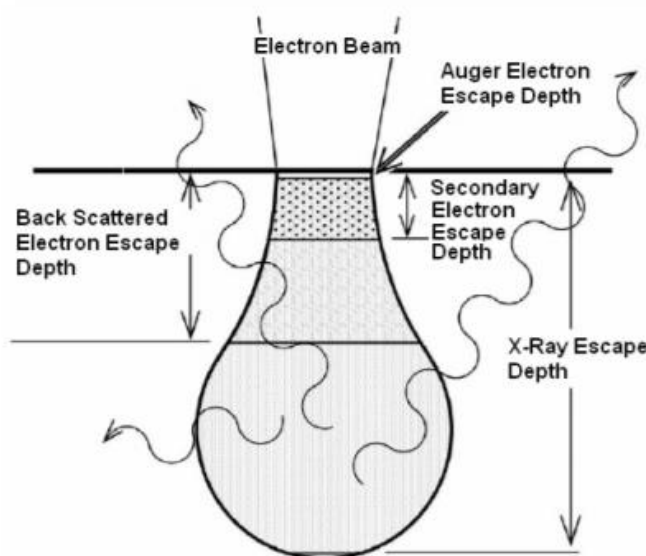
Figure 59. Emission depth of various types of electrons and X-rays (F47)

However, retro-diffused electrons come from a volume that approximates more the one from which X-rays are emitted and therefore BSE images are often correlated with this type of analysis. The qualitative analysis, namely the identification of elements present in the sample, is a prerequisite for subsequent quantitative analysis. (125)

The FESEM analysis was conducted on:

- Five samples, using the instrument Merlin Gemini, Zeiss:
    - Smooth-Ti cp/Keratin/Ag0.01;
    - Smooth-Ti cp/Keratin/Ag0.05;
    - Smooth-Ti cp/Keratin/Ag0.1;

For samples treated with silver, the secondary and back scattering images were captured in magnifications of 2000x, 5000x, 10000x, 50000x and 100000x. For the other two samples were captured only secondary images at 2000x 5000x, 10000x, 30000x and 100000x. The aim was to identify the presence and the atomic percentages of indicative elements of keratin such as C, O, S, N and silver;

- Eight samples with thin coating, silver treatment and in both cellular and bacterial tests using the instrument SUPRATM 40, Zeiss, making possible to observe the morphology of deposited keratin and to evaluate the presence and distribution of bacteria and cells:
    - Smooth-Ti cp/Keratin/cells seeding of 72 h;
    - Smooth-Ti cp/Keratin/Ag0.01/ cells seeding of 72 h;
    - Smooth-Ti cp/Keratin/Ag0.05/ cells seeding of 72;
    - Smooth-Ti cp/Keratin/Ag0.1/ cells seeding of 72
    - Smooth-Ti cp/Keratin/bacteria seeding of 72 h;
    - Smooth-Ti cp/Keratin/ Ag0.01/ bacteria seeding of 72 h;
    - Smooth-Ti cp/Keratin/ Ag0.05/ bacteria seeding of 72 h;
    - Smooth-Ti cp/Keratin/ Ag0.1/ bacteria seeding of 72 h;

9.2. **XPS**

X-ray Photoelectron Spectroscopy (XPS) is a quantitative analysis technique that allows to determine the chemical elements present on the surface of a sample. The object to be analyzed is irradiated with a low energy monochromatic X-ray beam, generated by an aluminum anode. Based on the number and kinetic energy of the electrons emitted, it is possible to determine their binding energy, which is specific to each element and allows the chemical characterization of the sample. The range of depth of the XPS analysis is about 1-10 nm (Figure 60), reason why it is widely used to know the surface chemical composition of a sample. If the X-ray beam can penetrate the sample in depth, the emitted electrons originate from the more superficial layers, because, for energies around 1.4 keV, the electrons emitted from depths greater than 10 nm have a low probability to leave the surface without encountering energy loss events, thus contributing to the underlying signal rather than to the well-defined peaks of primary photoelectrons. (126)
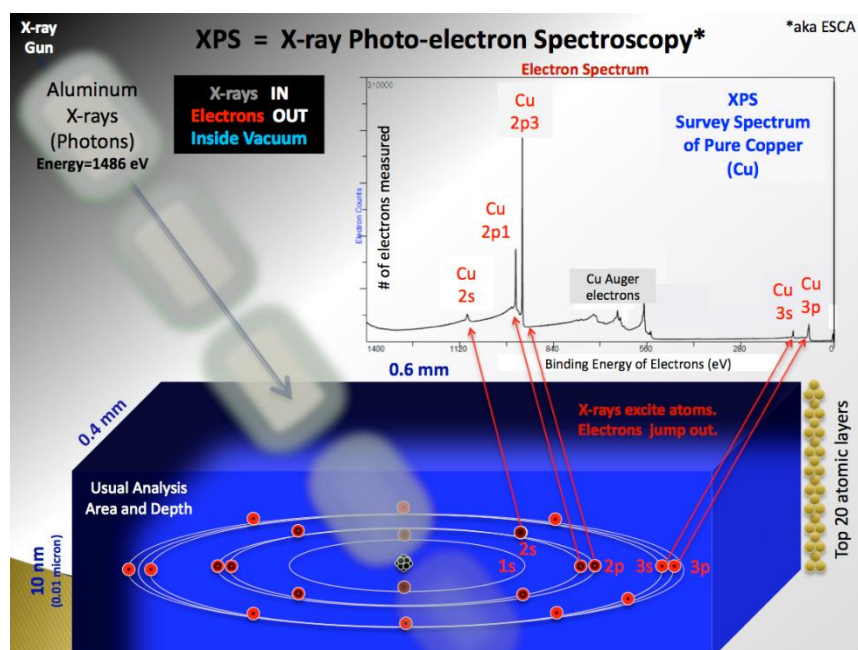
Figure 60. Depth of information of XPS analysis (F48)

A typical XPS spectrum, the Survey spectrum, is a graph showing the number of electrons detected as a function of their binding energy. Each chemical element produces a characteristic set of peaks at specific energy values. The number of electrons counted for each of these peaks is correlated with the amount of that element in the sampling volume of the XPS. The quantification of XPS spectra assumes that the number of electrons

detected is proportional to the number of atoms in each state. The basic instrument for measuring the number of electrons recorded for a specific atomic layer is the quantification region whose primary goals are to define the range of energies on which the signal can be attributed to the transition of interest and to define the type of appropriate approximation to remove the background signal that does not belong to the peak, although for some transitions, such as peaks p, d and f, data appear in double-form. The best way to compare XPS intensities is by atomic percentage concentrations, since not all electrons emitted by the sample are detected by the instrument. In this way, intensities are represented as a percentage, correlating the intensity of interest to the total intensity of the electrons involved in the measure. With XPS is also possible to perform a high-resolution analysis, useful not only in the case of distinct elements that show overlapping but also in the case of a single element of which you want to know the oxidation state and the chemical around. In these cases, the peaks are matched by Gaussian or Lorentzian curves, which model the envelope of the data. The XPS analysis was conducted on the same samples analyzed by FESEM-EDS with the XPS, PHI 5000 Versa Probe, Physical Electronics. It was possible to accurately determine the chemical composition of the first superficial layers and to add more information about the chemical elements of interest. The high-resolution spectrum revealed the types of chemical bond in which the keratin is involved and allowed to understand how the keratin restrain silver and other elements. (127)

This analysis was conducted on the following samples:

- Smooth-Ti cp/keratin (as control);
- Smooth-Ti cp/keratin/UV treatment;
- Smooth-Ti cp/Plasma O_2 dry/keratin;
- Smooth-Ti cp/Plasma O_2 physio-sol/keratin;
- Smooth-Ti cp/keratin/Ag 0.01;
- Smooth-Ti cp/keratin/Ag 0.05;
- Smooth-Ti cp/keratin/Ag 0.1.

9.3. **Tape test**

Adhesion is defined as a set of physico-chemical phenomena that occur in the molecular attraction between two different of materials placed in contact, as in this case that one that has been established between the nanofibres of keratin and commercially pure titanium surface. The adhesion force is that one required to separate the two materials at interface between them. Because of the wide variety of coating materials, their thicknesses and their deposition methods, doesn't exist a gold standard method for assessing adhesion. The following are the most commonly used ones:
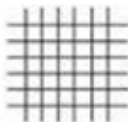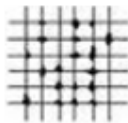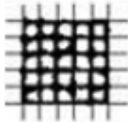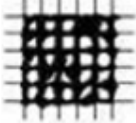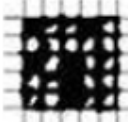
- Tape Test;
- Scrape Test;
- Pull-Off Test;
- Burnishing Test;
- Heat-Quench Test.

In this work, the Tape Test was performed, which consist of a semiquantitative evaluation of the adhesion assessment and was conducted by reference to the Standard Test Methods for Measuring Adhesion by Tape Test, ASTM D 3359-97.
The experimental procedure includes the following steps:

- Creating cuts with a sharp tool to produce edges from which the coating can be lifted. Note that the cut patterns can be different, in this case is used the grid cut one;

- Application of an adhesive tape, conforming to EN ISO 2409, above the cutting zone, then performing a certain pressure to ensure adhesion of the tape itself;

- Removing the adhesive tape, parallel to the surface;

- Examination of the tested area with the aid of a magnifying glass;

- Evaluation of adhesion strength, depending on the amount of coating removed.

Figure 61 shows the table for the evaluation of the results from the norm ASTM D 3359-97:

Classification	Description	Appearance of surface of cross-cut area from which flaking has occurred*
0	The edges of the cuts are completely smooth; none of the squares is detached	
1	Detachment of small flakes of the coating at the intersections of the cuts. A cross-cut area greater than 5 %, is affected	
2	The coating has flaked along the edges and/or at the intersections of the cuts. A cross-cut area greater than 5 %, but not greater than 15 %, is affected	
3	The coating has flaked along the edges of the cuts partly in large ribbons, and/or it has flaked partly on different parts of the squares. A cross-cut area greater than 15 %, but not greater than 35 %, is affected	
4	The coating has flaked along the edges of the cuts in large ribbons and/or some squares have detached partly or wholly. A cross-cut area greater than 35 %, but not greater than 65 %, is affected	
5	Any degree of flaking that cannot even be classified by classification 4	-

*The figures are examples for a cross-cut within each step of the classification. The percentages stated are based on the visual impression given by the pictures and the same percentages will not necessarily be reproduced with digital imaging

Figure 61. shows the table for the evaluation of the results from the norm ASTM D 3359-97: classification of adhesion test results (F49)

The instrument used is the Elcometer 107 Cross Hatch Cutter, made up of 6 blades with a cutting distance of 1 mm, suitable for up to 60 μm on hard surfaces, in accordance with ASTM regulation (Figure 62).

Figure 62. Elcometer 107 Cross Hatch Cutter (F50)

Samples were observed under an optical microscope before and after the tape test, in order to have a better evaluation of the permanence and the eventual removal of the keratin nanofibers.

9.4. FT-IR

Fourier transform spectroscopy is a type of non-destructive analysis for the identification of materials by the analysis of vibration of chemical bonds. It is based on the absorption of infrared radiation by the materials and the ability to seize all components of the infrared spectrum in the detector, which makes it unnecessary to scan the wavelength. This is possible by transforming the polychromatic infrared radiation emitted from the source by an interferometer into an interferogram where absorption is not a function of frequency but of time. By means of a computer, which makes the Fourier transform, it is possible to switch from interferogram to spectrum, which represents the variation of the intensity of the signal according to the radiation wave number. (128) The operating diagram is shown in figure 63.
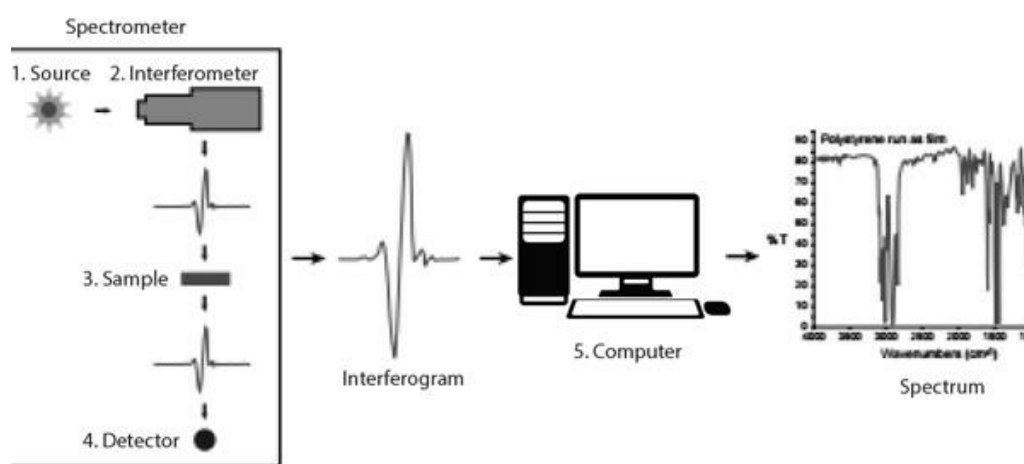
Figure 63. FTIR operating diagram (F51)

The IR spectrum is specific to each molecular structure, so FT-IR analysis provides accurate information on the organic and inorganic groups present on the surface of the sample to be analyzed. Spectrum peak amplitude has a direct proportionality with the amount of substance present on the sample. In this type of analysis, it is necessary to have a background, i.e., a reference material, and to do a compensation for H_2O and CO_2, as they absorb the IR radius, to obtain the correct spectrum for the sample. In this work, FT-IR analysis was performed to observe the type of keratin atomic bonds on the surface of commercially pure Ti samples coated using the electrospinning technique.

This analysis was conducted on the following samples:

- Smooth-Ti cp/keratin (as control);
- Smooth-Ti cp/keratin/UV treatment;
- Smooth-Ti cp/keratin/Tape test;
- Smooth-Ti cp/Plasma O_2 dry/keratin;
- Smooth-Ti cp/Plasma O_2 physio-sol/keratin;
- Smooth-Ti cp/keratin/Ag 0.01;
- Smooth-Ti cp/keratin/Ag 0.05;
- Smooth-Ti cp/keratin/Ag 0.1.

FT-IR analysis was used as the radius penetration depth on the surface of the sample is about 1 μm and the keratin coating has a thickness of some micrometers. The measurement was set in such a way as to obtain a spectrum resulting in reflection, which reflects the reflectance peaks according to the wave number. The instrument used was the IR Hyperion 2000, Bruker.

9.5. **Wettability**

Wettability is the ability of a liquid to remain in contact with a solid surface due to intermolecular interactions that develop at the interface between the two. The degree of wettability is given by the balance between cohesive forces and adhesion forces: The first type of force lends the liquid drop a spherical form that minimizes the contact with the solid, while the second one causes a drop of liquid that expands on the surface of the solid. By measuring the contact angle (θ), it is possible to determine the degree of wettability, this angle is measured on the drop section and is formed by the encounter between the direction of the solid-liquid interfacing stress and the direction of the liquid-vapor interfacing stress, tangent to outer surface of the drop with the vertex in the three-phase solid-liquid-vapor point as shown in figure 64. (129)
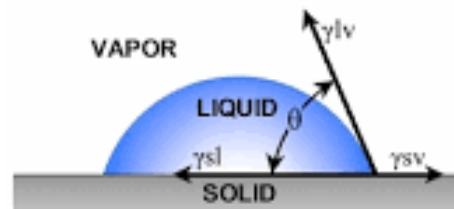
Figure 64. Contact angle (F52)

Where Υ^{sl} is the solid-liquid interfacial free energy, Υ^{sv} is the solid surface free energy, Υ^{lv} is the liquid surface free energy. In the case of a smooth and homogeneous surface, or rather an ideal condition as there is always a slight roughness, wettability is defined by Young's equation, which establishes the balance of horizontal forces acting on a drop of volume negligible in relation to the surface:

$$\Upsilon^{sv} - \Upsilon^{sl} = \Upsilon^{lv} \cos\theta$$

Depending on the contact angle value, it is possible to determine the degree of wettability of a surface (Table 19).

Contact Angle	Wettability Degree	Adhesion Force	Cohesion Force
$\theta = 0°$	Perfect	Very strong	Very weak
$0° < \theta < 90°$	High	Strong/Weak	Strong/Weak
$90° < \theta < 180°$	Low	Weak	Strong
$\theta = 180°$	Null	Very weak	Very strong

Table 19. Relationship between contact angle, degree of wettability and forces involved (T11)

There is a relationship between wettability and surface energy that quantifies the breakdown of intermolecular bonds that form the surface itself. High-energy solid surfaces have strong chemical-type bonds, i.e., ionic, metallic or covalent, and are completely wet with most of the polar liquids. While low-energy solid surfaces are made up of atomic species held together by physical bonds such as Van der Waals bonds and hydrogen bonds and can be completely or partially wet depending on the liquid being considered. Still different is the case for liquids, for which surface tension coincides with surface energy. In the case of biomaterials, the study of wetting is of great importance in predicting interaction with the biological environment. (129) The purpose of this work was to evaluate whether and how the topography of titanium, the presence and topography of the keratin coating and the presence of silver modify the wettability. Two wettability tests were performed, both under ambient conditions. The first test was performed on samples stored in Petri dishes, the second test, however, was performed on the same samples but previously stored in bacterial broth, in order to detect any change in the hydrophilic/hydrophobic characteristics of the sample surface. A thermal microscope was used to perform the analysis by working at room temperature. The sample was placed on a horizontal plate and a front microscope made it possible to capture sample images during the test. For each sample, two measurements were made, depositing, at a distance from each other, 5 µl of milli-Q water with the aid of a micropipette. Once captured, the images were processed with the ImageJ software and the static contact angle measurement was made. The instrument used was a KRUSS DSA 100.

Samples used were:

- 2 smooth samples;
- 2 mechanical rough samples;
- 2 EBW5 samples;
- 2 EBW10 samples;
- 2 EBW 30 samples.

9.6. **Zeta potential**

The concept of zeta potential (ζ) is related to colloidal systems such as particle or emulsion dispersion and its colloidal chemical applications are discussed in many textbooks. Although primarily described as a colloidal analysis parameter, the theoretical background is the same regardless of whether it is applied for colloidal or solid surface characterization. In this case a different approach is required, the zeta potential is indicative of the charge surface that is formed when the material is in contact with an aqueous system. The behavior of charges on the solid-liquid interface can be explained using the double electrical or electrochemical model, according to which, due to the charge that the solid assumes in water, stationary liquid and a counter-ion mobile layer compensating for surface charge. The zeta potential is defined at the *shear plane*, which is the separation zone between the moving liquid phase and the stationary liquid phase (Figure 65). (130)
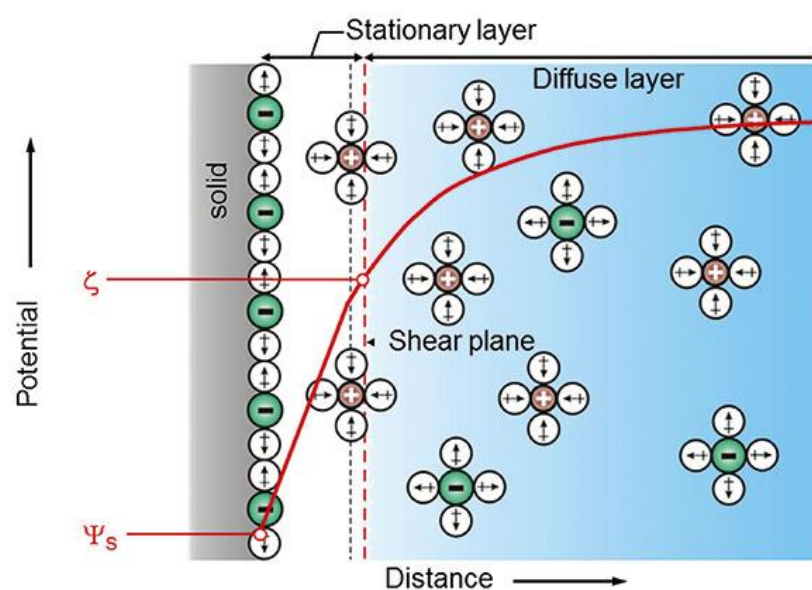
Figure 65. Model of double electrochemical layer at solid-liquid interface (F53)

Knowledge of zeta potential goes through the measurement of electrokinetic phenomena occurring at the interface between a solid, liquid or gaseous phase and a liquid phase when there is a relative motion between them. Particularly, when an aqueous solution flows through a capillary system, a continuous voltage or DC current is generated, depending on how the measurement is made. The capillary through which the aqueous solution flows can be of irregular shape, such as the voids between the fibers of a fibrous matrix, or as regular as the channel that is created between two planar surfaces of a material. When the aqueous solution is slid, shear forces are generated on counter-ions, which begin to move in the direction of flow. Between the capillary inlet and outlet generates a charge separation that creates an electric force that is opposed to the flow. Thanks to two electrodes placed at the ends of the capillary it is possible to detect the flow potential.

Measurement depends on the following parameters:

- **Volumetric flow rate** of the solution;
- **Capillary size**;
- **Ionic Force**: The effect of ionic strength on the reproducibility of zeta potential can be eliminated by providing a known aqueous ionic solution; in general, a 1:1 electrolyte (NaCl, KCl, KNO_3) to the ionic strength of 0.001 mol/l.
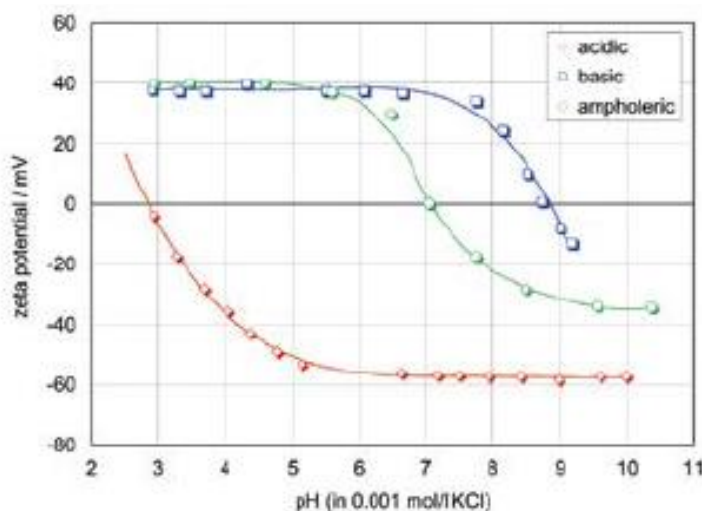
Figure 66. Dependence of the zeta potential for material surfaces with acidic, basic, amphoteric behavior. (F54)

The experimental set-up consists of a sample cell, two electrodes, a voltmeter, a case containing the measuring fluid and connected to the cell, a grounded metal cage to protect against external electromagnetic fields, a pump, pressure transducers and probes for pH

measurement and conductivity of the solution. Solid-liquid interface charge is mainly driven by acid-base reactions between surface functional groups and water and the physical adsorption of aqueous ions. Since these processes strongly depend on the pH of the aqueous solution, pH is the most important parameter of the liquid phase that affects the zeta potential. The zeta potential data must then refer to the pH of the aqueous solution used for the analysis. Titration has as its main objective the estimate of the isoelectric point (IEP), which is the pH at which the zeta potential changes with a value of 0 mV. This is equivalent to a net electrokinetic charge of 0 C/m^2 and thus to a balance between the superficial groups loaded positively and negatively. The IEP is a good indicator of the chemistry of the functional groups present on the surface of a solid. In the case of surfaces that exhibit only one type of functional group, the zeta potential is described as a function of pH by well-defined curves, which show a plateaux in a variable position depending on whether the surface has an acid, basic or amphoteric behavior. (130)

However, in most cases, the samples analyzed show a heterogeneous composition of functional groups and hence the curve that will be obtained will be different from the one shown in figure 66. Furthermore, there is no evidence that the zeta potential is dependent on the size of the sample and the roughness of the surface.

In this dissertation work the ζ potential has been studied on the following couples of samples:

- EBW5;
- EBW10;
- EBW30;
- Smooth-Ti cp;
- Metallic Ag.

In this way, it was possible to ascertain how surface roughness, surface topography, and presence of silver influence on the surface charge of the samples. The Surpass electrokinetic analyzer, Anton Paar was used (Figure 67).

Figure 67. Electrokinetic analyzer for zeta potential measurement

The samples were fixed with a suitable adhesive to the sample holder, which in turn have been inserted into the slots dedicated present in the measuring cell to leave a small gap between them. This space was brought by rotating one of the graduated wheels included in the cell at 100 μm in the initial step of adjusting the measurement parameters. Prior to mounting the cell, the instrument was washed with distilled and ultra-filtrated water by interposing a connecting tube between the two electrodes, then performing the closed-loop filling procedure without titration, using as electrolyte solution 45 mg of KCl in 600 ml of milli-Q water. Thereafter, flow control was performed by instrument software, which returns the flow, expressed in [ml/min], as a function of the pressure, expressed in [mbar], by tracing two curves; the first relative to the flow from left to right and the second to the flow in the opposite direction, thus allowing the detection of the pressure value to be set for a flow of 100 ml/min. The first measurement was done without titration to find the zeta potential of the sample at the pH of the electrolyte. In this work it was decided to perform the basic titration first. For basic titration, an increase in ml of NaOH 0.05 M was set to add during the measurement and for each step the software returned four measurements with corresponding average value. At the end of the basic titration, two washings of the instrument were carried out with milli-Q water, leaving the cell mounted, then passing to the titration with 0.05M HCl. The way to proceed was quite similar to the one described for the basic titration and the parameters that were measured are: pH, conductivity, temperature, flow current, pressure and flow.

10. BIOLOGICAL TESTS

10.1.   Bacterial adhesion test

Bacterial adhesion tests were also conducted in the laboratories of the Department of Health Sciences at the University of Eastern Piedmont Amedeo Avogadro and involved the following samples:

Samples used were:

- 3 EBW5;
- 3 EBW10;
- 3 EBW30;
- 3 Smooth-Ti cp/Ker/Ag 0.01;
- 3 Smooth-Ti cp/Ker/Ag 0.05;
- 3 Smooth-Ti cp/Ker/Ag 0.1;
- 3 Smooth-Ti cp/Ker (as control).

The bacterial strain that has been investigated is Staphylococcus aureus, cultivated in Luria-Bertani (LB, Sigma-Aldrich, MO, USA) agarized solid soil plates at 37 °C in a humid environment until the emergence of single colonies. Plates were maintained at 4 °C and from the formation of these colonies and before each experiment, a new culture was carried out in LB liquid medium at $1\text{x}10^7$ bacteria per ml (turbidity according to standard MCFarland 1.0). Subsequently the samples were lying in the wells of a 24-well plate and submerged with a volume of 1 ml of the bacterial culture prepared as described above. The plate was placed for 90 minutes at 37 °C by stirring (120 rpm) to favor biofilm cell adhesion to the sample surface (separation phase). At the end of 90 minutes, supernatants containing planktonic cells were removed from each well and replaced with 1 ml of fresh LB soil (biofilm growth phase). The biofilm was then cultivated on sample surfaces for 24 hours at 37 °C. After 24 h the grown biofilm on the surfaces was analyzed by XTT (sigma-Aldrich) colorimetric test to evaluate its bacterial vitality.

The assay was performed by carrying out the following steps:

- Samples gently washed with PBS to remove non-adherent bacteria;
- 1 ml of a solution of XTT powder (3 mg/ml) and PBS-menadione (0.1μM) was added in each well;
- The plate was incubated 3 hours in the dark at 37 °C;
- 100 μl of XTT solution were taken from each well and transferred to a 96-well plate (Nunc Delta).

The number of bacteria on the surface of the samples was evaluated by counting the unit forming colonies (CFUs). Biofilm cells were detached from the samples by sonicator (AcquaSonic, VWR PBI International, Milan, Italy) and vortex (5 cycles of 30 seconds per sample). The biofilm detached was diluted in 1 ml of PBS (mother solution) and used to run a series of 6 dilutions 1/10 in PBS (20 μl of mother solution and 180 μl of PBS). From each dilution were collected 20 μl, which were placed in Petri dishes containing LB agar. Plates were incubated at 37 °C and the following day the number of colonies was counted as follows (131):

$$\text{Number CFU} = [\text{Number of colonies} \times \text{Dilution factor} \times 10^{\wedge} (\text{Serial dilution})]$$

To determine the vitality of the bacteria, the following kit was used: Molecular Probes, Life Technologies Italy, Monza, Italy, comprising two fluorophores:

- SYTO9: Color both vital and dead bacteria;
- Propidium iodide: colors only the dead bacteria.

Subsequently, 1 ml of each fluorophore solution was inserted into 3 ml of PBS and, after mixing, the solution was distributed in the plates containing the samples and incubated at room temperature for 15 minutes in the dark. The samples were examined by a fluorescence microscope (Leica 6500, Leica Microsystems, Basel, Switzerland). Finally, the number of dead bacteria was calculated as a percentage of the total number of bacteria using the following software: ImageJ (NIH, Bethesda, USA). Finally, statistical analyzes were performed using the following software: SPSS v20.0, IBM Co. Armonk, NY, with a 5% significance level.

10.2.   **Cell test**

These tests were conducted in the laboratories of the Department of Health Sciences, University of Eastern Piedmont Amedeo Avogadro and involved the following samples:

Samples used were:

- 3 Smooth-Ti cp/keratin/Ag 0.01;
- 3 Smooth-Ti cp/keratin/Ag 0.05;
- 3 Smooth-Ti cp/keratin/Ag 0.1;
- 3 Smooth-Ti cp/keratin (as control);

The types of cells used were primary human fibroblasts (HGFs), isolated from the human gingiva, surgically removed from healthy patients. Dermatome was used to remove thin mucous layers and the epithelial layer was enzymatically separated by a digestion with 0.5% of dispase at a temperature of 4°C overnight.

Cells thus obtained were cultured in α-MEM (Sigma) supplemented with 10% FBS fetal bovine serum (Sigma) inactivated by heat action and with 1% of antibiotics-antimycotics (penicillin/streptomycin/amphotericin B, Anti-Anti, Sigma) at 37 °C in a humidified atmosphere at 10% of CO_2.

The cytocompatibility was evaluated in vitro by means of direct and indirect tests:

- **Direct Test**: Samples were placed in 24-well plates; $2x10^4$ cells were sown on the surfaces of each sample and allowed to adhere for 4 hours. Subsequently, each well was filled with 1 ml of culture medium. Vitality was evaluated with the Blue Alamar Test (Sigma-Aldrich) after 48 hours. Finally, the supernatant optical density (O.D.) was measured at a wavelength of 590 nm with a spectrophotometer (Conte Spectra, Packard Bell);

- **Indirect Test**: The α-MEM medium was incubated without cells for 1 week at 37 °C, 5% of CO_2 in direct contact with the samples at a ratio of 1 mL/sample for a total of 10 mL/test tube. The medium was then supplemented with 10% of FBS fetal bovine serum and used to cultivate HGFs. The cells were sown on 24-well plates (Star Cell Phone, International PBI, Milan, Italy) and cultivated for 48 hours at 37 °C, 5% of CO_2. Subsequently, cell viability was evaluated by means of the Blue Alamar assay as described for the direct cytocompatibility assay.

After 48 hours of direct cultivation, the cells were fixed with 3% paraformaldehyde (Sigma-Aldrich) in PBS for 2 hours and then washed in 1 mol of sodium cacodylated 1-l buffered solution, dehydrated with 70%, 80%, 90% and 100% ethanol (10 min each). The morphology of the cells cultured on samples was investigated by immunofluorescence (IF) and FESEM, placing the samples on an aluminum housing with conductive carbon tape, covered with a layer of chrome and observed by FESEM (SUPRATM 40, Zeiss) at various magnifications. The dyes used for immunofluorescence were:

- Anti-vimentin (AbCam, 1: 150 in PBS, 5% goat serum, 1% BSA) and anti-type collagen II
  (AbCam, 1: 100 in PBS, 5% goat serum, 1% BSA) for 1 hour;
- Falloin (AbCam, 1: 500 in PBS);
- 4,6-diamidino-2-phenylindole (DAPI, Sigma) to visualize F-actin and nucleus.

The images were obtained using a fluorescence microscope (Leica 6500, Leica Microsystems, Basel, Switzerland).

RESULTS AND DISCUSSIONS

1. ADHESION STUDY

1.1. Tape test

The following samples, mirror polished and subsequently coated with keratin, were subjected to the Tape Test to evaluate the adhesion of this coating:

- Smooth-Ti cp/Ker (as control);
- Smooth-Ti cp/PlasmaO$_2$Dry/Ker;
- Smooth-Ti cp/PlasmaO$_2$Physio/Ker;
- Smooth-Ti cp/Ker/UV.

From the following table (Table 20) it is possible to observe the samples during the Tape Test. Although the adhesion test was very aggressive towards the coating deposited for electrospinning, it was noticed that the test only removed the outermost layers of the coating, probably because of its high thickness.
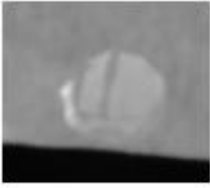
Type of Sample	Sample before the test	Sample after the test	Removed layer
Smooth-Ti cp/Ker			
Smooth-Ti cp/PlasmaO₂Dry/Ker			
Smooth-Ti cp/PlasmaO₂Physio/Ker			
Smooth-Ti cp/Ker/UV			

Table 20. Images of the samples subjected to the evaluation of the adhesion coating keratin

It was decided to proceed with a series of analyzes such as FESEM-EDS, XPS and FT-IR, in order to study the surface chemical composition and the type of bonds established within the coating.

1.2. FT-IR

The FT-IR analysis was carried out to observe on the surface of the samples the presence and the type of atomic bonds. In this case, the atomic bonds characteristic of keratin, in order to study the quality of the adhesion of the nanofibers to the metal substrate. This analysis was conducted on the following samples:

- Smooth-Ti cp/Ker
- Smooth-Ti cp/Ker/UV
- Smooth-Ti cp/PlasmaO$_2$Physio/Ker
- Smooth-Ti cp/PlasmaO$_2$Dry/Ker
- Smooth-Ti cp/Ker/Tape

Below are the FT-IR spectra of each sample in a single chart:
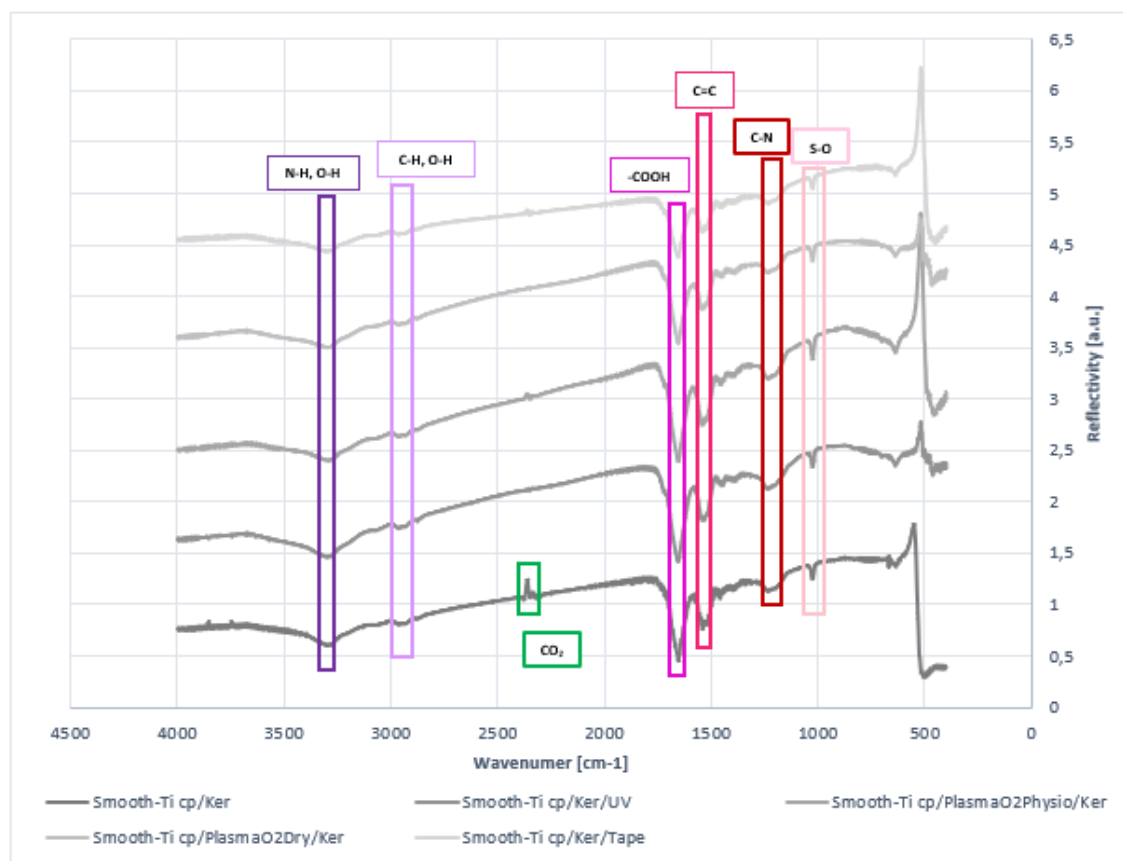
Figure 68. FT-IR characterization of the samples used for the adhesion study

The peaks highlighted in figure 68 are related to the following chemical bonds (132):

- **N-H, O-H** at 3278 cm^{-1};

- **C-H**, **O-H** at 2921 cm^{-1};

- **CO$_2$** not well compensated at 2355 cm^{-1};

- **-COOH** at 1650 cm^{-1};

- **C=C** at 1523-1542 cm^{-1};

- **C-N** at 1221 cm^{-1};

- **S-O** at 1020 cm^{-1};

In Figure 68 it is observed that most of the peaks present in the spectra of the samples analyzed are identifying the same types of bonds, although the intensity is sometimes weaker. This may be due not only to a homogeneous distribution of the keratin coating but also to its thickness, which could prevent the detection of different chemical bonds despite the different treatments carried out on the surfaces of the samples. In particular, we can note the presence of the amide band A (centered at 3282 cm^{-1}) connected to the stretching vibration of the N-H bonds, the presence of the amide II (1580-1510 cm^{-1}) deriving mainly from the bending of the N-H in the plane with a certain contribution of the vibrations of stretching C-N and of the amide III (1300-1220 cm^{-1}), which depends on the nature of the side chains and hydrogen bonding. (133) Substantial differences between the signals of the samples are not visible, excluding the not well-balanced CO$_2$ peak at 2355 cm^{-1} for the control sample. The peaks present are those typical of keratin nanofibers present in literature (133), even if present at different intensities, increasing with respect to the control sample. The sample after the Tape test does not show substantial differences compared to the others, which means that on the surface remains a layer of keratin with a thickness greater than the depth of penetration of the FTIR analysis. A very thin layer is then removed. This shows how large the thickness of the keratin coating is and how much it is characterized by the same bonds in the various layers. It is important to note that this type of analysis is able to reach depths close to 1μm, not sufficient to reach the interface area between the keratin coating and the titanium substrate with surface treatment, instead providing information on the chemical characteristics of the nanofibrous keratin coating.

1.3.**XPS**

Table 21 shows the atomic percentages obtained from the Survey spectra of the various samples:

Element	Smooth-Ti cp/Ker	Smooth-Ti cp /PlasmaO$_2$Physio/Ker	Smooth-Ti cp /PlasmaO$_2$Dry/Ker	Smooth-Ti cp /Ker/UV
C	60.70	59.00	60.40	59.10
O	21.10	22.80	21.50	23.00
N	14.00	14.80	15.00	13.30
Na	2.30	1.50	1.10	2.70
S	1.90	1.90	2.00	1.90

Table 21. Atomic percentages from the four-sample Survey spectra

It can be seen that, with regard to carbon, this is always present on the surface of our samples for two reasons: both for the superficial reactivity of titanium and for the presence of keratin. A significant amount of nitrogen and a moderate amount of sulfur, attributable to keratin, is observable. The presence of sodium is instead attributable to contamination.

Below, in figures 69a, 69b, 69c and 69d, the Survey spectra for the four samples are shown:
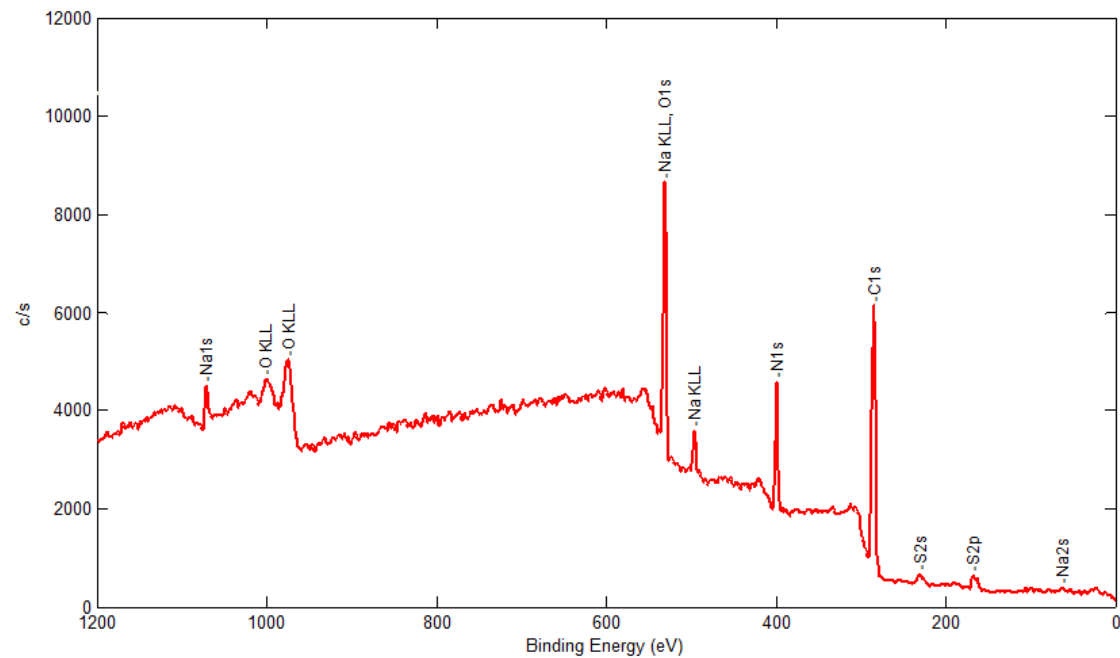
Figure 69a. Survey spectrum of Smooth-Ti cp/Ker sample
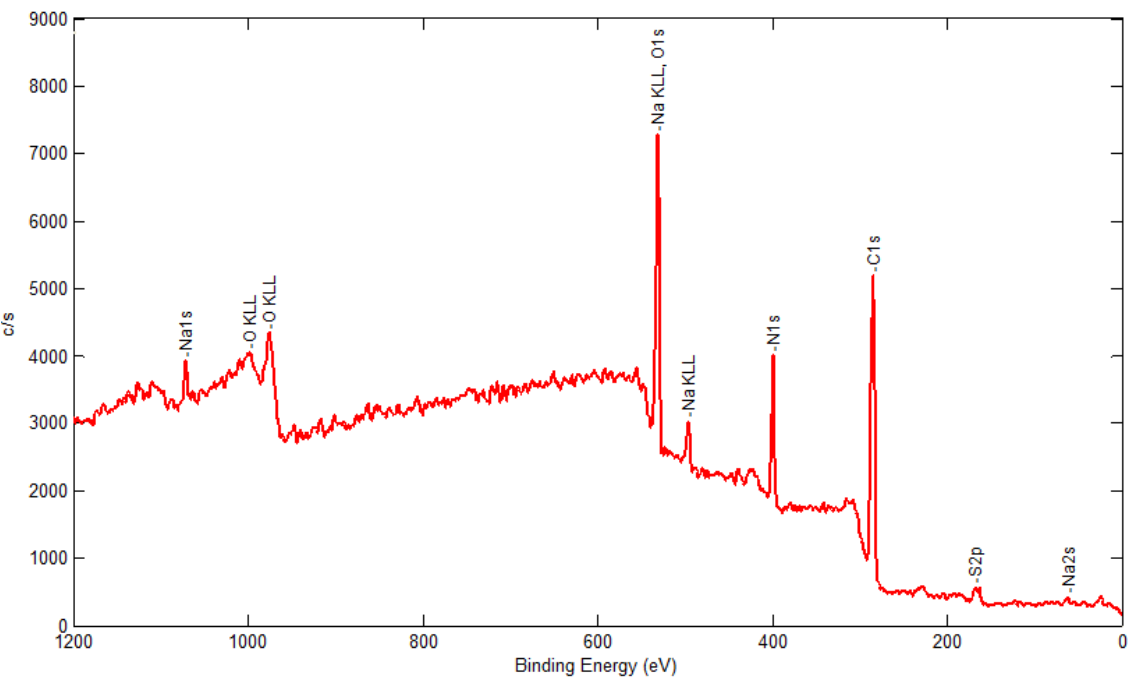
Figure 69b. Survey spectrum of Smooth-Ti cp/PlasmaO2Physio/Ker sample
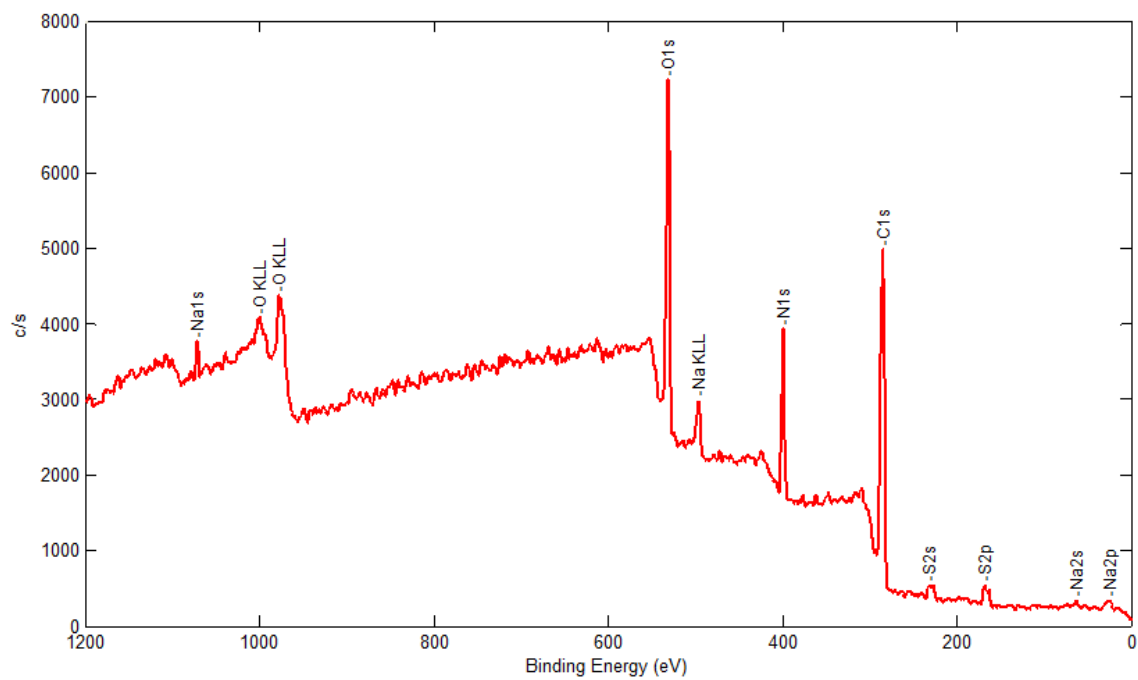
Figure 69c. Survey spectrum of Smooth-Ti cp/PlasmaO2Dry/Ker sample
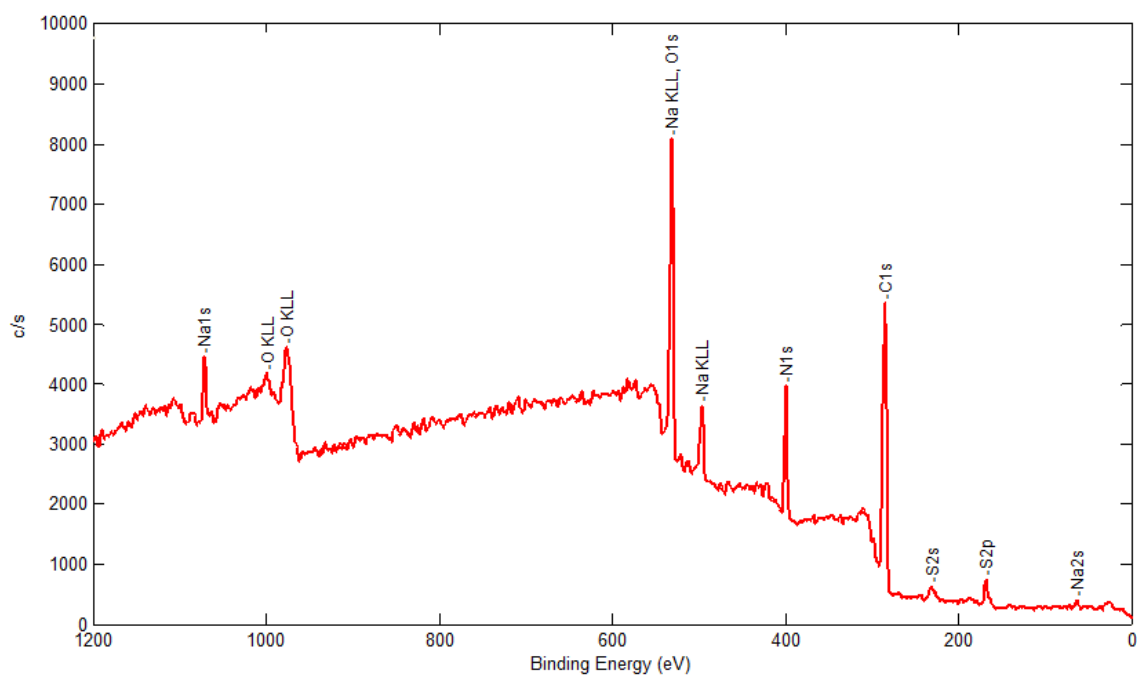
Figure 69d. Survey spectrum of Smooth-Ti cp/Ker/UV sample

For each sample the high-resolution HR spectra of the carbon, oxygen, nitrogen and silver regions were then acquired. The binding energies were corrected by matching the main carbon peak to the bonding energy of 284.6 eV, according to conventional use. (134) The possible attribution of the individual peaks was made on the basis of what reported in the literature. (135) (136)

In the following figures, the possible attributions of the binding energies detected during the analysis are listed according to the detained element.
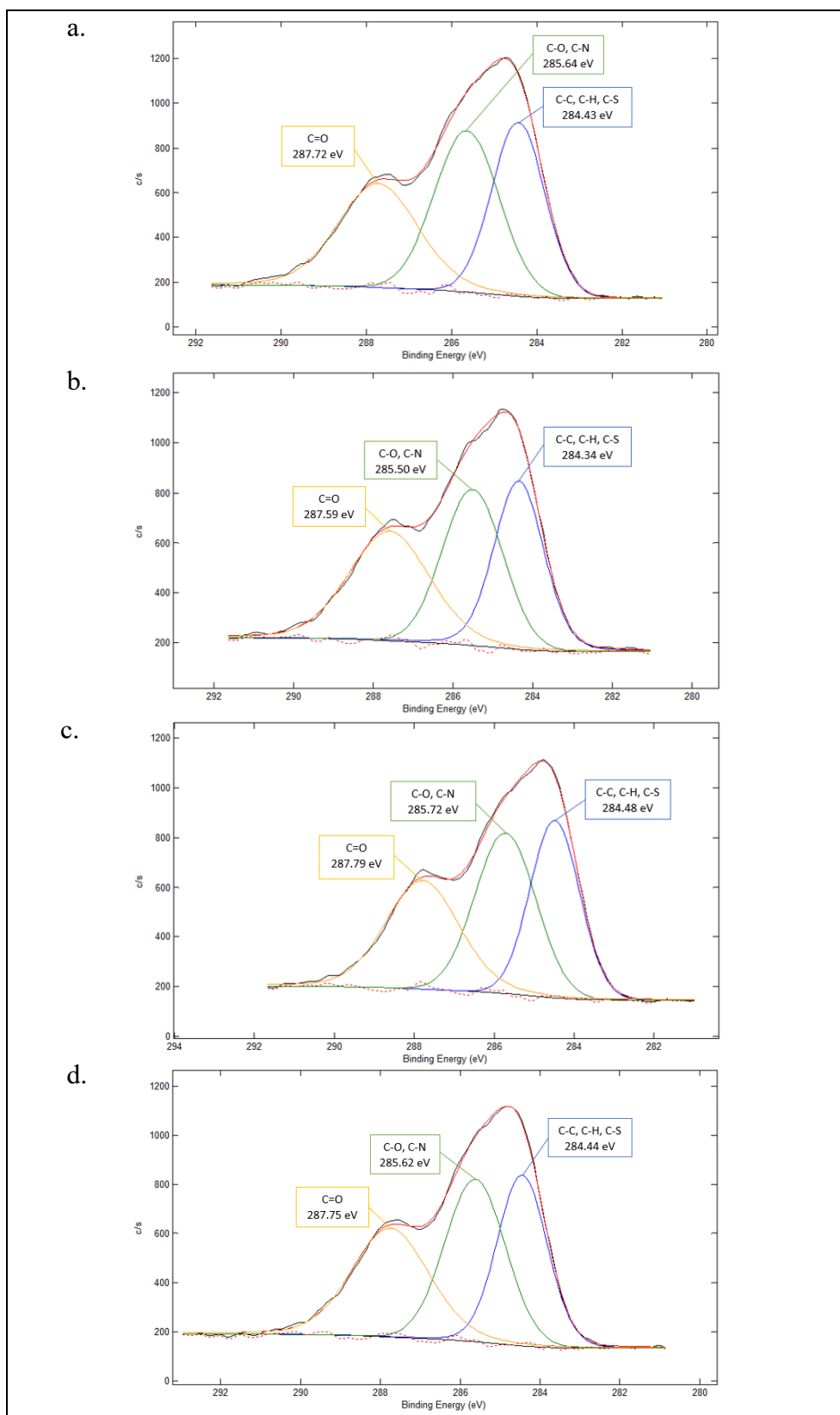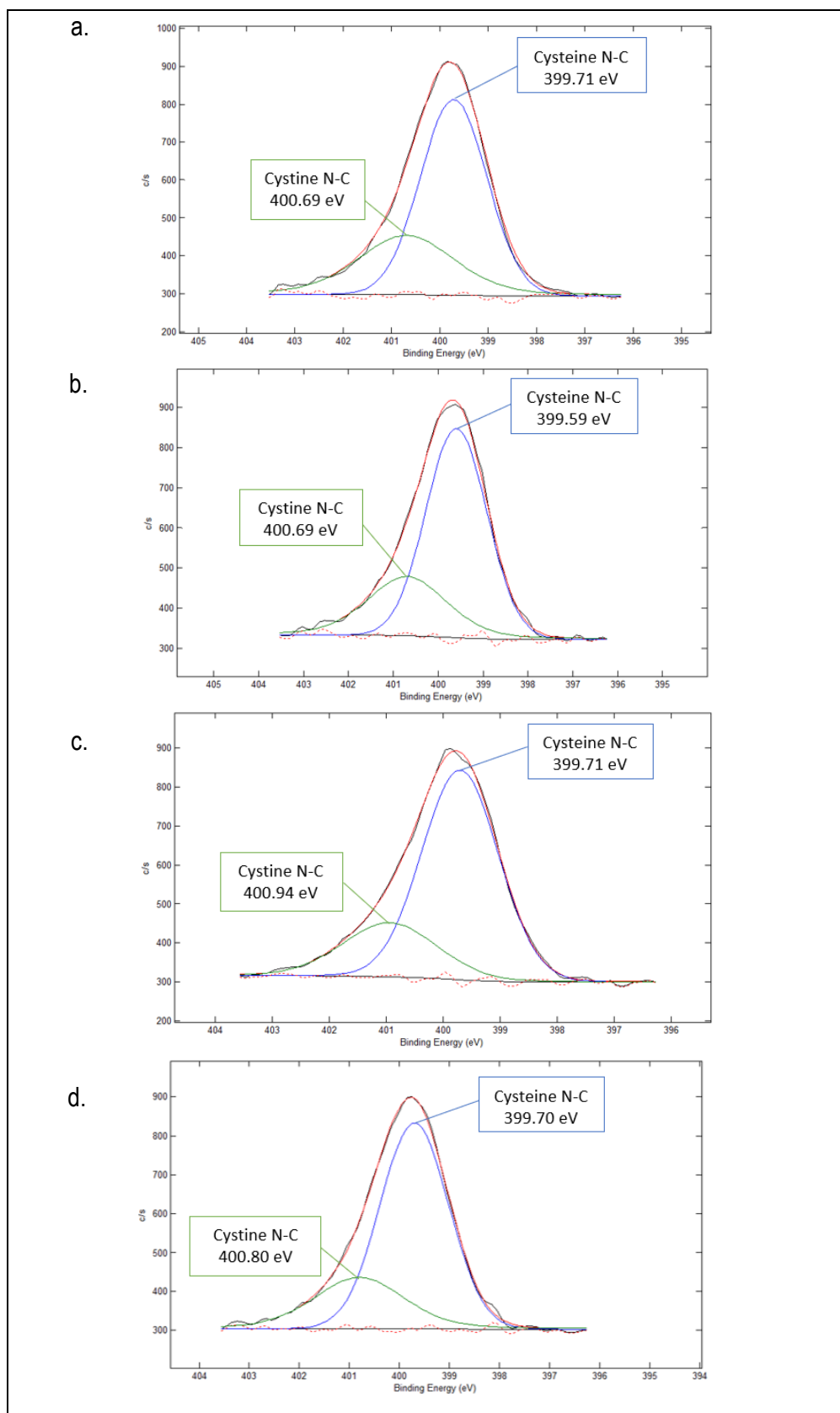
Figure 70. HR carbon spectra for: a. Smooth Ti-cp/Ker, b. Smooth-Ti cp/PlasmaO2Physio/Ker, c. Smooth-Ti cp/PlasmaO2Dry/Ker, d. Smooth-Ti cp/Ker/UV

The C-C, C-H, C-O and C=O bonds that appear in the spectra of Figure 70 are attributable to the carbon present as a contaminant. These bonds, together with the C-S and C-N, also present in figure 70, are also contained in the primary structure of keratin, so the contribution to the peaks in question is twofold. (137) (138)

For each sample the ratio between the percentage area of the detected peaks and the percentage area of the peak at 284 eV taken as reference was calculated (Table 22). It is observed for all the samples, in figures 70a., 70b., 70c. and 70d., the presence of a relative abundance of the C-O/C-N attribution relative to the reference, except for the sample with ultraviolet surface treatment, figure 70d., for which there is no relative abundance with respect to the reference. For the attribution C=O a relative abundance is observed with respect to the reference in each sample, and in particular for the sample with ultraviolet treatment. This result might suggest that the surface UV treatment, performed following the deposition of the nanofibers in order to stabilize the coating, has favored especially the exposure of that type of bond.

Smooth Ti-cp/Ker	Area [%]	Ratio
284.43 eV	32.24	1
285.64 eV	36.16	1.12
287.72 eV	31.60	0.98

Smooth-Ti cp/PlasmaO2Physio/Ker	Area [%]	Ratio
284.34 eV	31.86	1
285.50 eV	33.69	1.057
287.59 eV	34.45	1.081

Smooth-Ti cp/PlasmaO2Dry/Ker	Area [%]	Ratio
284.48 eV	32.35	1
285.72 eV	35.63	1.101
287.79 eV	32.02	0.989

Smooth-Ti cp/Ker/UV	Area [%]	Ratio
284.44 eV	31.62	1
285.62 eV	35.45	1.121
287.75 eV	32.93	1.041

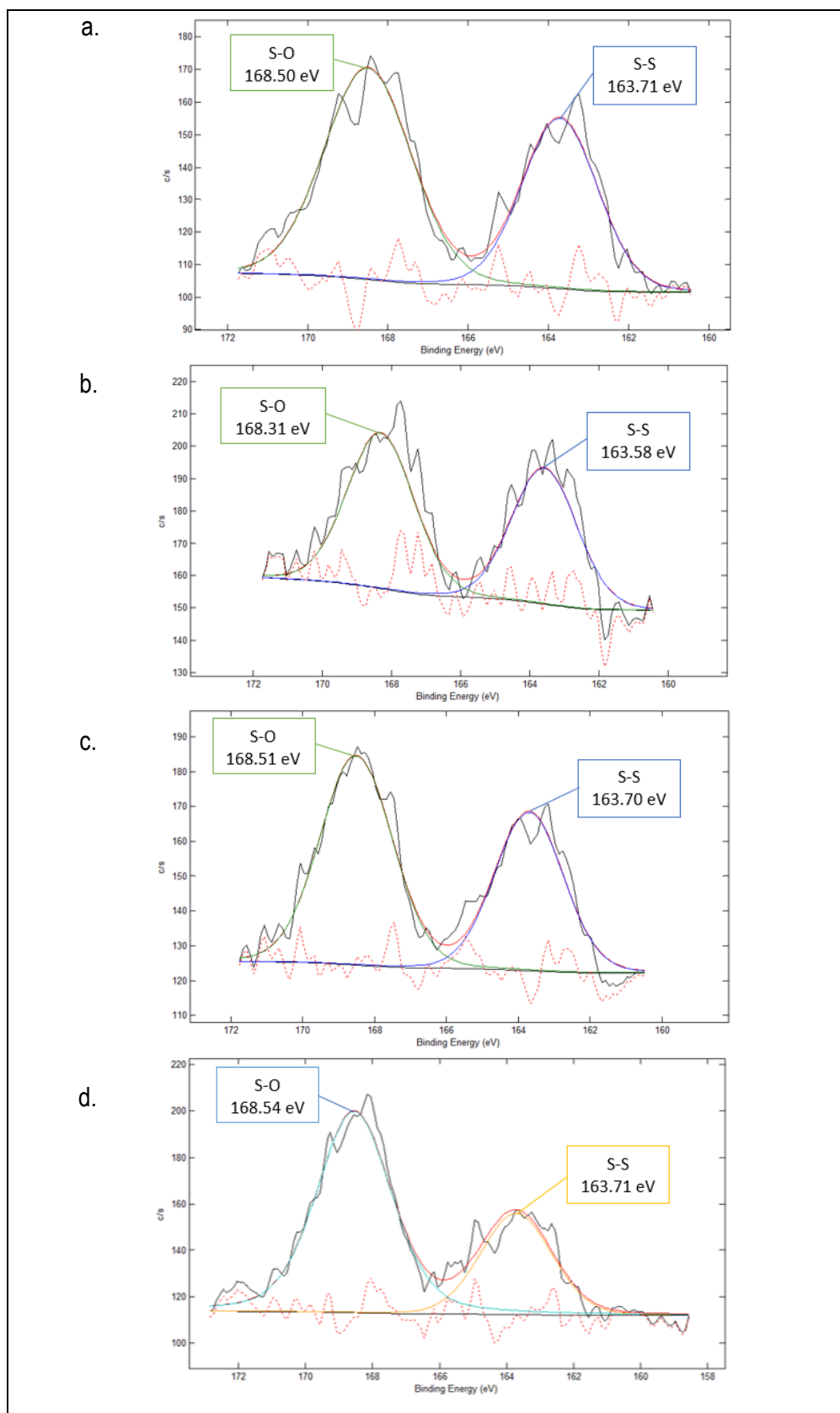*Table 22. Summary of the percentage areas and ratios for the HR carbon spectra*
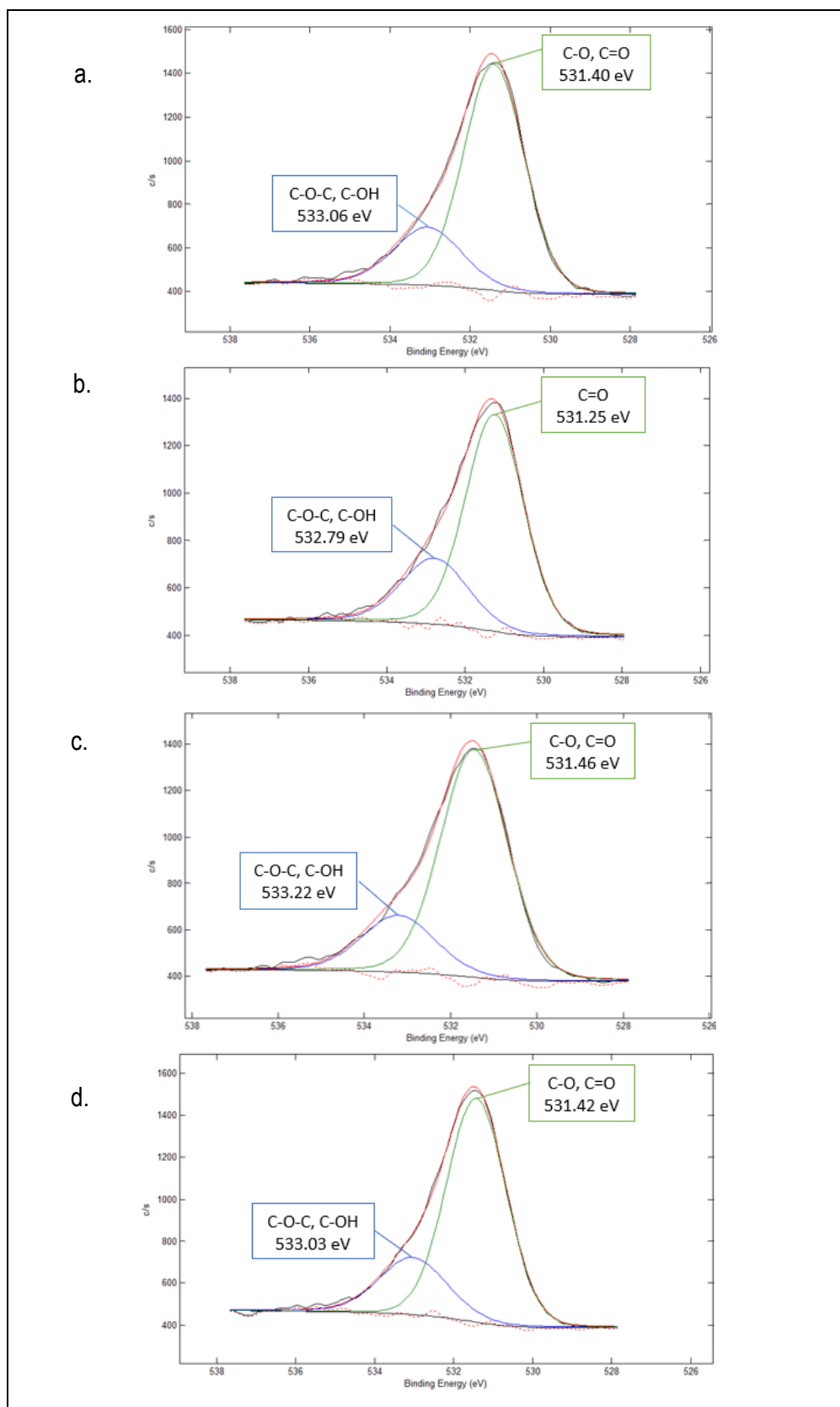
Figure 71. HR oxygen spectra for: a. Smooth Ti-cp/Ker, b. Smooth-Ti cp/PlasmaO2Physio/Ker, c. Smooth-Ti cp/PlasmaO2Dry/Ker, d. Smooth-Ti cp/Ker/UV

In Figure 71 for all the four samples, two peaks can be identified, each corresponding to a specific oxygen bond. The presence of the C=O double bond and the O-H hydroxyl groups, probably derive from the keratin coating. (138) (139)

For each sample, in Figures 71a., 71b., 71c. and 71d., the ratio between the percentage area of the peak at lower energy and that of the peak at higher energy was calculated (Table 23). The presence of a constant relative abundance of the C-O/C=O attribution is observed for all the samples with respect to the peak attributed to the C-O-C/C-OH bond. This result could suggest that none of the surface treatments has made the substrate surface differently reactive, but most likely the absence of differences between the surface treatments is due to the thickness of the coating that prevents this type of analysis from providing information regarding the interface between the nanofibrous coating and the titanium substrate.

Smooth Ti-cp/Ker	Area [%]	Ratio
531.40 eV	76.40	1
533.06 eV	23.60	0.308
Smooth-Ti cp/PlasmaO2Physio/Ker	Area [%]	Ratio
531.25 eV	73.31	1
532.79 eV	26.69	0.364
Smooth-Ti cp/PlasmaO2Dry/Ker	Area [%]	Ratio
531.46 eV	77.57	1
533.22 eV	22.43	0.289
Smooth-Ti cp/Ker/UV	Area [%]	Ratio
531.42 eV	76.21	1
533.03 eV	23.79	0.312

Table 23. Summary of the percentage areas and ratios for the HR oxygen spectra

Figure 72. HR nitrogen spectra for: a. Smooth Ti-cp/Ker, b. Smooth-Ti cp/PlasmaO2Physio/Ker, c. Smooth-Ti cp/PlasmaO2Dry/Ker, d. Smooth-Ti cp/Ker/UV

Regarding the nitrogen HR spectra, in Figure 72, the nitrogen peaks were attributed to cysteine N-C (at 400 eV) and cystine N-C (at 401 eV) due to the confirmed presence of sulfur fractions both in Table 21 and in the HR spectra in Figure 73. However, due to the variety of amino acids present in keratin and the overlapping binding energies of cystine in HR spectrum of nitrogen (N 1s), i.e. glycine, which is also present in the polypeptide chain, these cannot be definitively assigned. (140)

For each sample the ratio between the percentage area of the peak attributed to the cysteine N-C bond and the percentage area attributed to the N-C cystine bond was calculated (Table 24). It is observed for all samples the presence of an increasing relative abundance of the cysteine N-C attribution with respect to cystine N-C, starting from the control sample then following the samples with oxygen plasma treatment (Figures 72a., 72b. and 72c.), with the exception of the sample with ultraviolet surface treatment, figure 72d., for which there is no relative abundance of the cysteine N-C attribution compared to cystine N-C that has an intermediate ration value to that calculated for the samples treated with oxygen plasma. This result could suggest that the UV treatment, carried out following the deposition of the nanofibers in order to stabilize the coating, has favored especially the exposure of that type of bond.

Smooth Ti-cp/Ker	Area [%]	Ratio
399.71 eV	66.53	1
400.69 eV	33.47	0.503
Smooth-Ti cp/PlasmaO2Physio/Ker	Area [%]	Ratio
399.59 eV	70.36	1
400.69 eV	29.64	0.421
Smooth-Ti cp/PlasmaO2Dry/Ker	Area [%]	Ratio
399.71 eV	74.98	1
400.94 eV	25.02	0.333
Smooth-Ti cp/Ker/UV	Area [%]	Ratio
399.70 eV	72.72	1
400.80 eV	27.28	0.375

Table 24. Summary of the percentage areas and ratios for the HR nitrogen spectra

Figure 73. HR sulfur spectra for: a. Smooth Ti-cp/Ker, b. Smooth-Ti cp/PlasmaO2Physio/Ker, c. Smooth-Ti cp/PlasmaO2Dry/Ker, d. Smooth-Ti cp/Ker/UV

Regarding the sulfur HR spectra, in Figure 73, the peaks were attributed to S-O (at 168.2-168.7 eV), i.e. oxidised disulfide bonds of the cysteic acid residues of keratin, and to S-S (at 163.9-164.0 eV), i.e. cystine disulfide bonds. As can be seen from Figure 73, all the spectra exhibit very noisy signals due to the weakness of the signal. (141) For each sample the ratio between the percentage area of the peak with attribution S-O and that of the peak with attribution S-S was calculated (Table 25). It is observed for all the samples the presence of a relative abundance of the S-O attribution relative to the peak attributed to the S-S bond, in particular the sample with oxygen plasma treatment and maintenance in physiological solution, in figure 73b., presents the lowest relative abundance in fact in this case the percentage areas of the two contributions are visually more similar. Whereas, the UV treated sample has the highest relative abundance of the S-O attribution (Figure 73d.). As in the previous cases, the UV treatment of slight peculiarities, suggesting that this treatment has favored the formation and stabilization of this type of bond.

Smooth Ti-cp/Ker	Area [%]	Ratio
163.71 eV	41.18	1
168.5 eV	58.82	1.428
Smooth-Ti cp/PlasmaO2Physio/Ker	Area [%]	Ratio
163.58 eV	46.14	1
168.31 eV	53.86	1.167
Smooth-Ti cp/PlasmaO2Dry/Ker	Area [%]	Ratio
163.70 eV	41.87	1
168.51 eV	58.13	1.388
Smooth-Ti cp/Ker/UV	Area [%]	Ratio
163.71 eV	30.58	1
168.54 eV	69.42	2.270

Table 25. Summary of the percentage areas and ratios for the HR sulfur spectra

In summary, these results suggest that the absence of differences between surface treatments is most likely due to the thickness of the coating, which prevents this type of analysis from providing information regarding the interface between the nanofibrous coating and the titanium substrate. However, the XPS analysis made it possible to make a slight distinction for the UV treatment, which having been carried out on the surface of the coating and not on the surface of the titanium substrate, found small differences compared to other treatments, especially for the areas distribution of most types of links identified.

2. ANTIBACTERIAL TREATMENT STUDY

2.1. FESEM-EDS

FESEM

FESEM-EDS after Ag treatment of the samples coated with keratin

The samples analyzed were:

- Smooth-Ti cp/Ker/Ag001
- Smooth-Ti cp/Ker/Ag005
- Smooth-Ti cp/Ker/Ag01
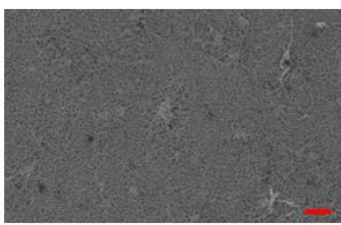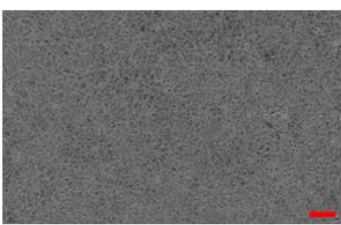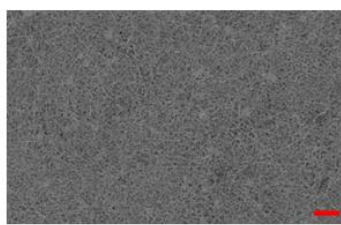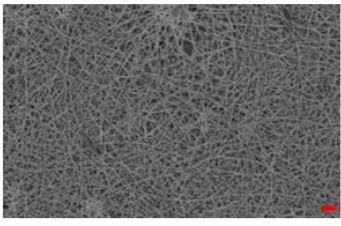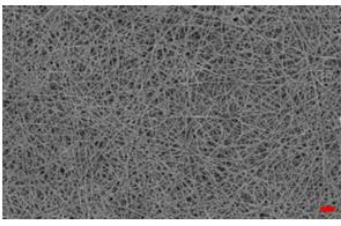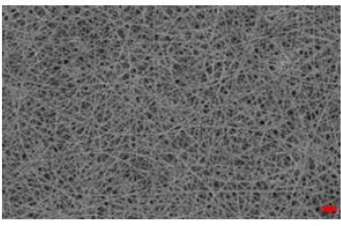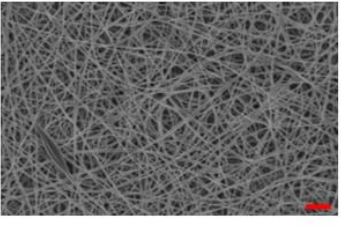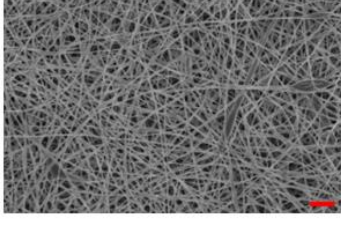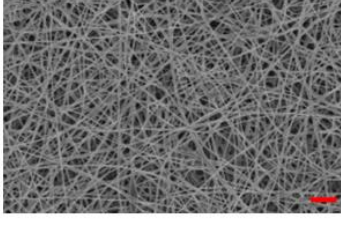
Figure 74. FESEM images (SE) of the three samples treated with AgNO3 at increasing magnifications for the study of keratin globules. Bar scale= 10µm at magnification 2000x, bar scale= 2µm at magnification 5000x and bar scale= 2µm at magnification 10000x

From the images of Figure 74, at different magnifications of 2000x, 5000x and 10000x respectively, it is observable not only a uniform distribution of the keratin coating over the titanium substrate, but also a random orientation of the fibers and the absence of silver precipitates. In particular, at 2000x magnification, it is possible to observe that the sample with a higher concentration of Ag has a much more homogeneous coating, which is rich in nanofibers compared to that of medium and low concentration samples. About samples with medium and high concentration of Ag it is also possible to observe that the distribution and orientation of the nanofibers is not influenced by the presence and therefore by the level of concentration of Ag, since the deposition of Ag was performed after the deposition of the keratin nanofibers. The causes of the different morphology of deposited keratin may be due to factors that have influenced the electrospinning process, such as incorrect positioning of the sample on the collector or a variation in humidity that did not favor the deposition of the fibers. At 1000x magnification, the morphology of keratin nanofibers becomes clearly visible, particularly, the nanofibers are randomly arranged in the form of tangles.
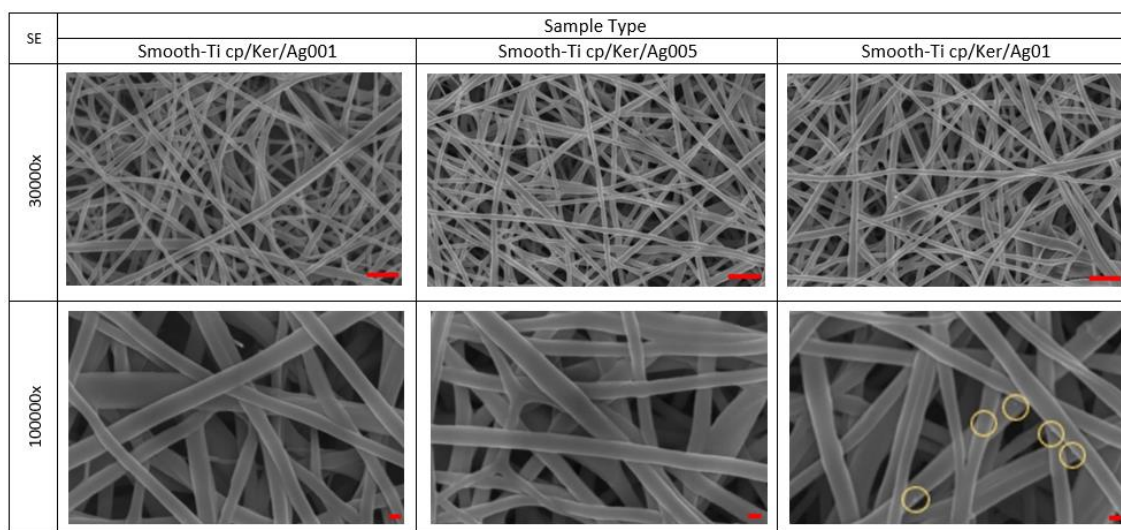
Figure 75. FESEM images (SE) of the three samples treated with AgNO3 at increasing magnifications for the study of silver precipitates. The orange circles highlight some of the micrometric subunits. Bar scale= 1μm at magnification 30000x and bar scale= 100nm at magnification 100000x

At magnifications of 30kx and 100kx, in Figure 75, the conformation and the spatial arrangement of the keratin nanofibers for each of the three samples taken into consideration can be observed in more detail. As regards the sample with the highest concentration of Ag, it is possible to observe the presence of submicrometric entities on

the surface of some nanofibers. From the images to the FESEM one cannot, however, conclude if such entities are precipitated of silver or superficial defects of the keratin nanofibers. In Figure 75a, below, there are FESEM images of the three samples with the relative diameters of the nanofibers, measured in a generic point of the surface of each sample. It is possible to observe how the distribution of the nanofiber dimensions is homogeneous.
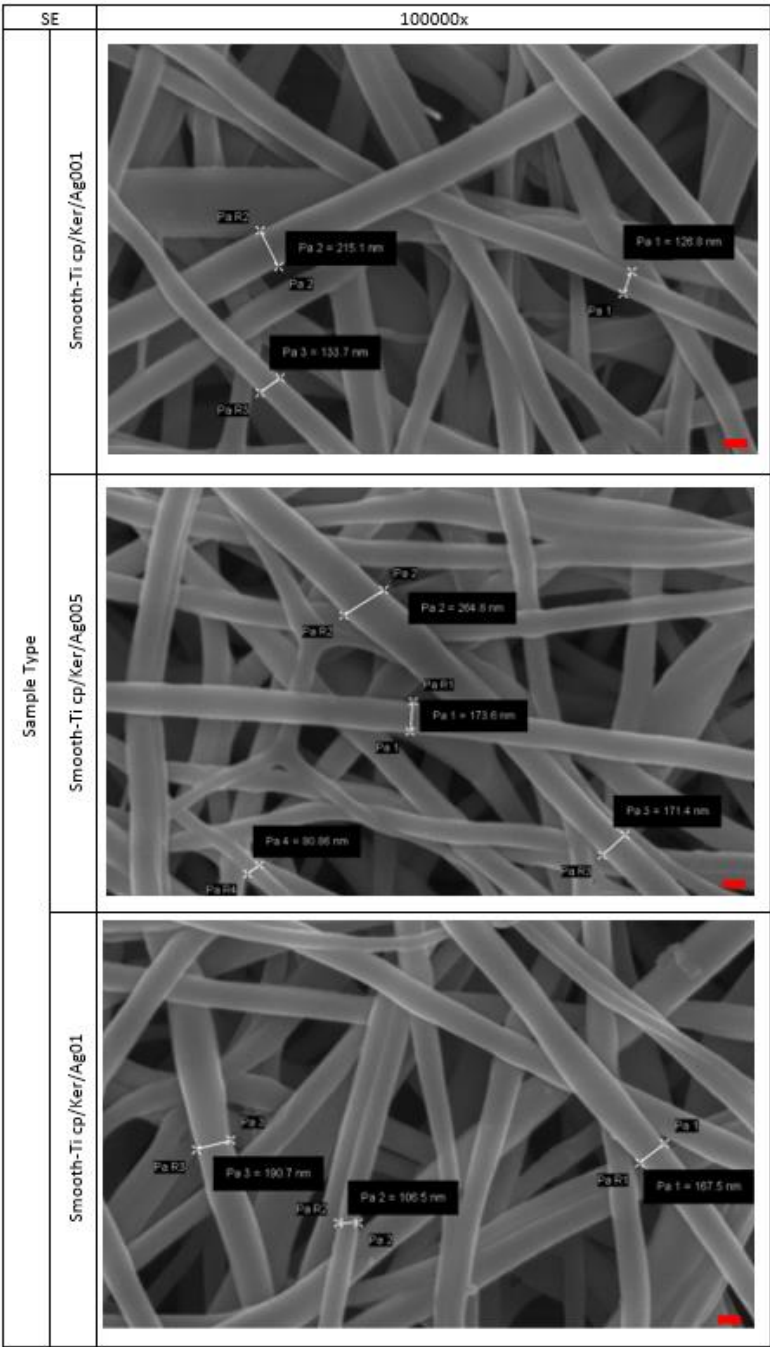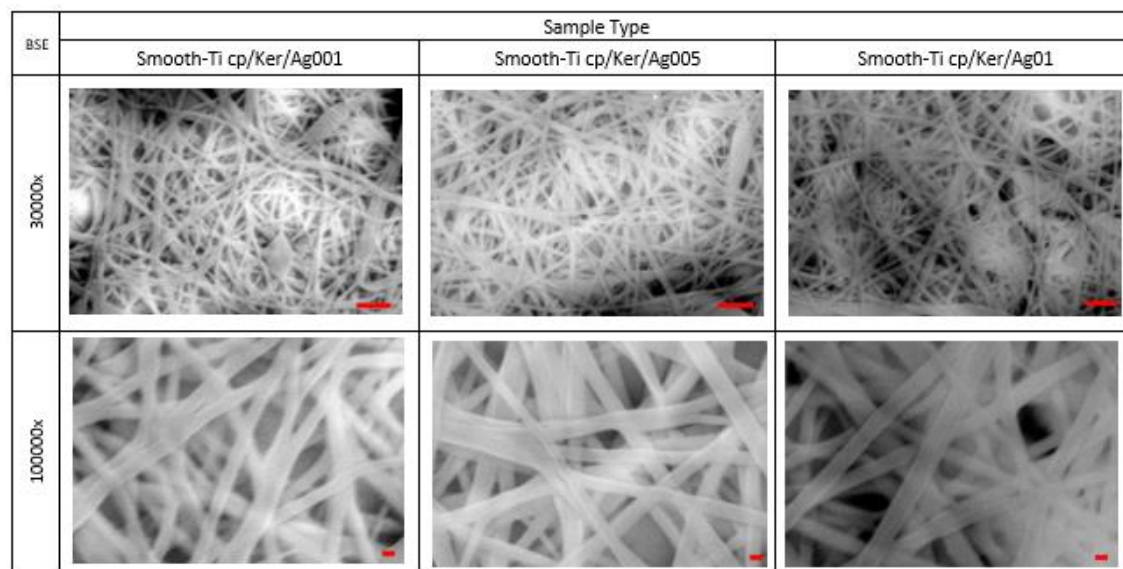

Figure 75a. FESEM images (SE) of the three samples treated with AgNO3, with fiber diameters. Bar scale= 100nm at magnification 10000x
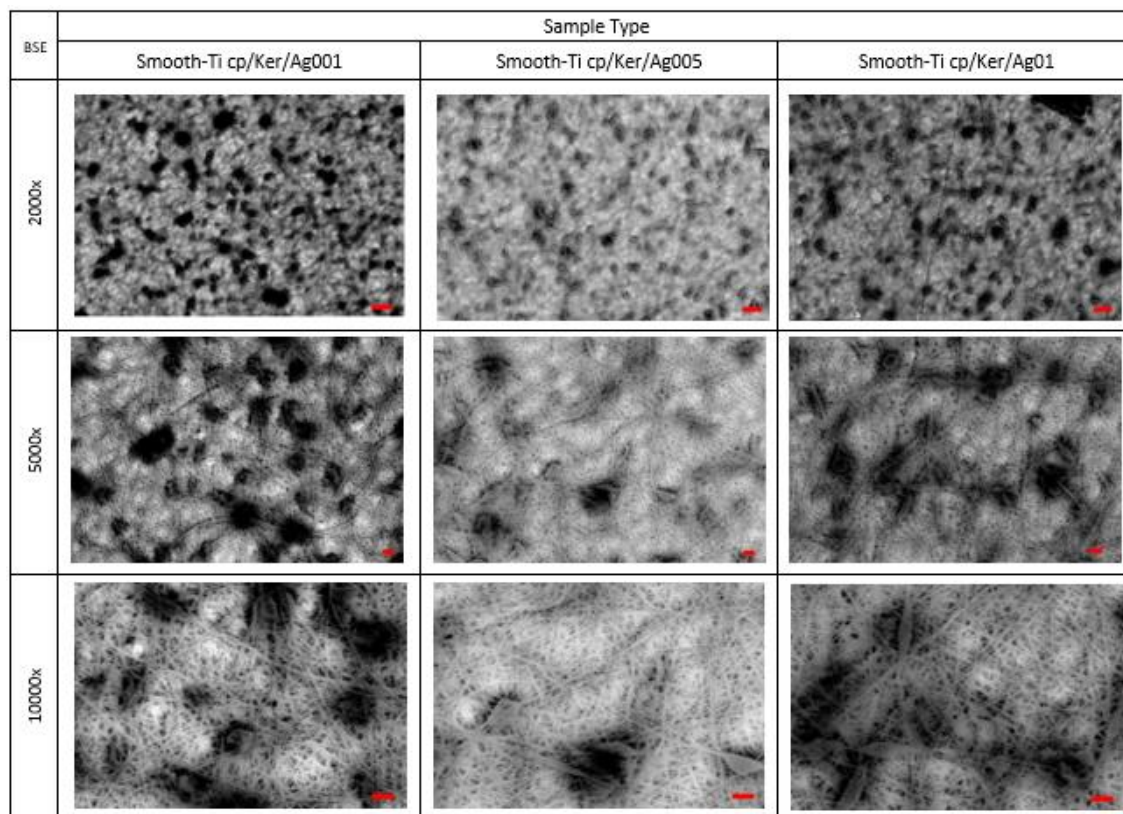
Figure 76. FESEM images (BSE) of the three samples treated with AgNO3. Bar scale= 10μm at magnification 2000x, bar scale= 2μm at magnification 5000x and bar scale= 2μm at magnification 10000x

Figure 77. FESEM images (BSE) of the three samples treated with AgNO3. Bar scale= 1μm at magnification 30000x and bar scale= 100nm at magnification 100000x

153

Figures 76 and 77 are images, which show the acquisitions, for these three samples, in back scattering, at 2kx, 5kx, 10kx and 30kx, 100kx magnification, respectively. In this mode heavier elements are visualized in lighter color compared to lighter ones, such as silver, which appears bright and clear. Silver, unlike previous work (56), is not observed in the form of precipitates (scattered white dots), but in the form of light halos; while lighter elements, such as carbon, appear dark. To determine whether the white halos are attributable to the presence of silver, the EDS analysis was performed, while to say whether it is ionic or metallic silver, the XPS analysis was carried out, discussed in the next paragraphs.

2.2. **EDS**

Parallel to the FESEM analysis, the EDS analysis was performed to observe the superficial elemental composition. The EDS analysis was carried out to obtain additional information to those deriving from the sole FESEM analysis regarding the surface chemical composition of the samples. It was carried out on: area and nanofiber. The penetration depth of this technique is quite high (around the micron) and therefore the Ti peaks are always present, even in the globule and fiber spectrum. For the same reason, silver, which is present in small quantities, is not always detected. Sulfur, the presence of which is indicative of cysteine residues present in keratin nanofibres.

Smooth-Ti cp/Ker/Ag001 sample
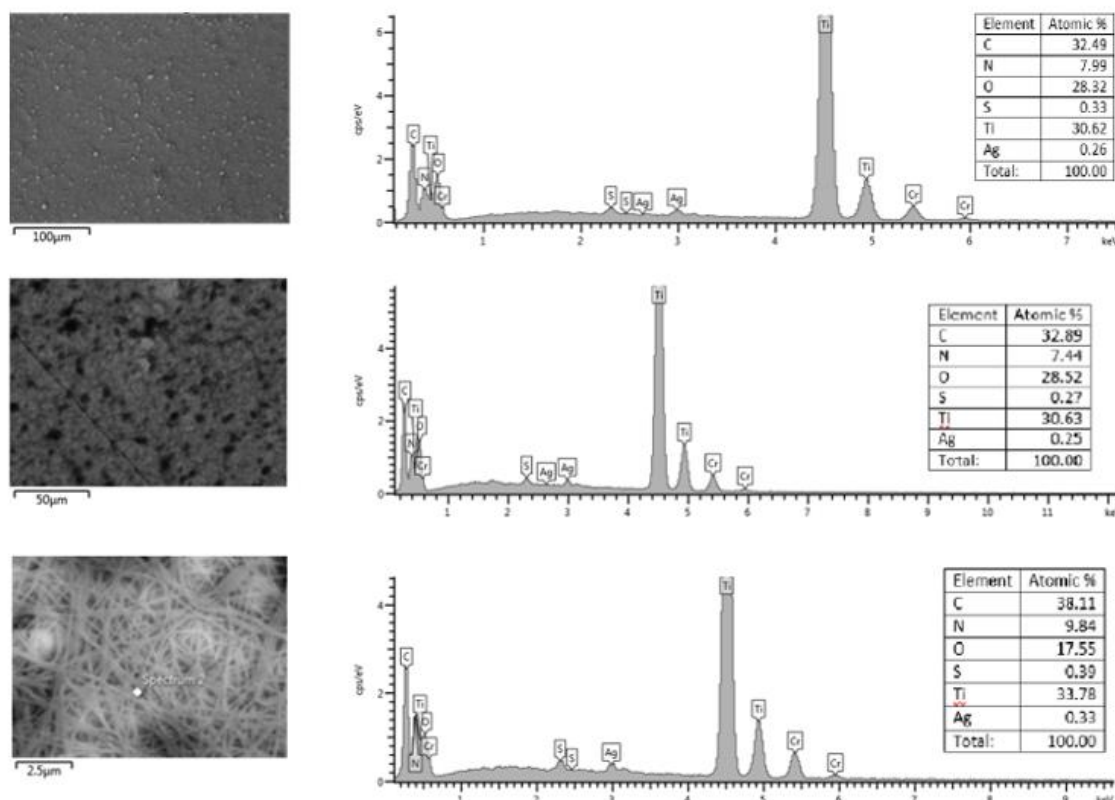
Figure 78. EDS analysis of the areas and the keratin nanofiber of the sample "Smooth-Ti cp/Ker/Ag 001"

In the spectrum 2 of Figure 78, related to the nanofiber, appear the C and S indicative keratin peaks and a peak of Ag, which reveals the occurrence of silver absorption within the keratin coating. However, the atomic percentage is higher than those of the first and second spectrum of Figure 78, since the nanofiber is very thin, and the EDS has a high penetration depth in relation to it; therefore, in the totality of the atomic percentages, S and Ag represent a very small part.

Smooth-Ti cp/Ker/Ag005 sample
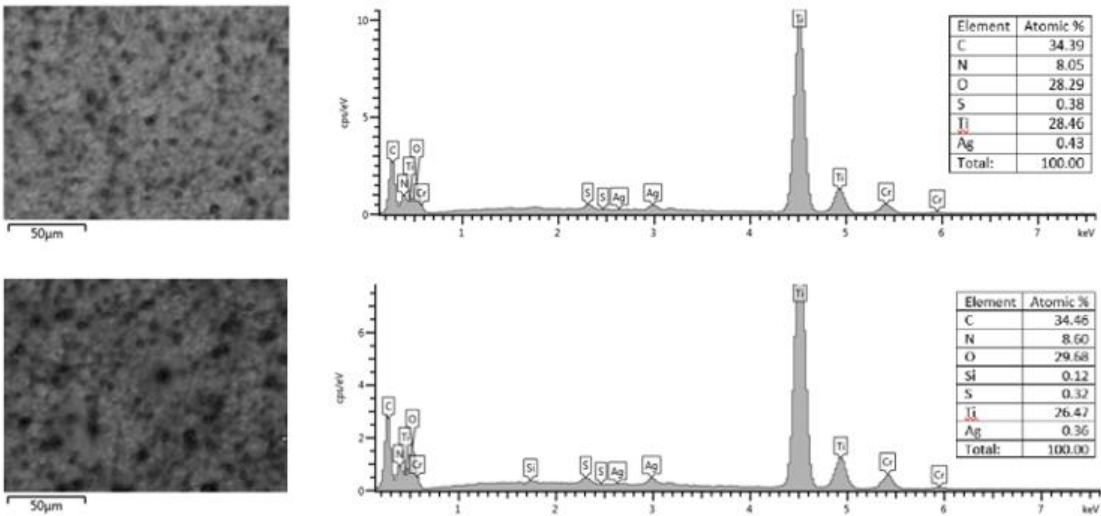
Figure 79. EDS analysis of the areas of the sample "Smooth-Ti cp/Ker/Ag 005"

As can be seen in Figure 79, the sample shows a peak of Ag on both the areas observed. In this sample, the second spectrum of Figure 79 shows a Si peak, probably due to contamination during the mechanical polishing phase of the samples, in which colloidal silica was used.

Smooth-Ti cp/Ker/Ag01 sample
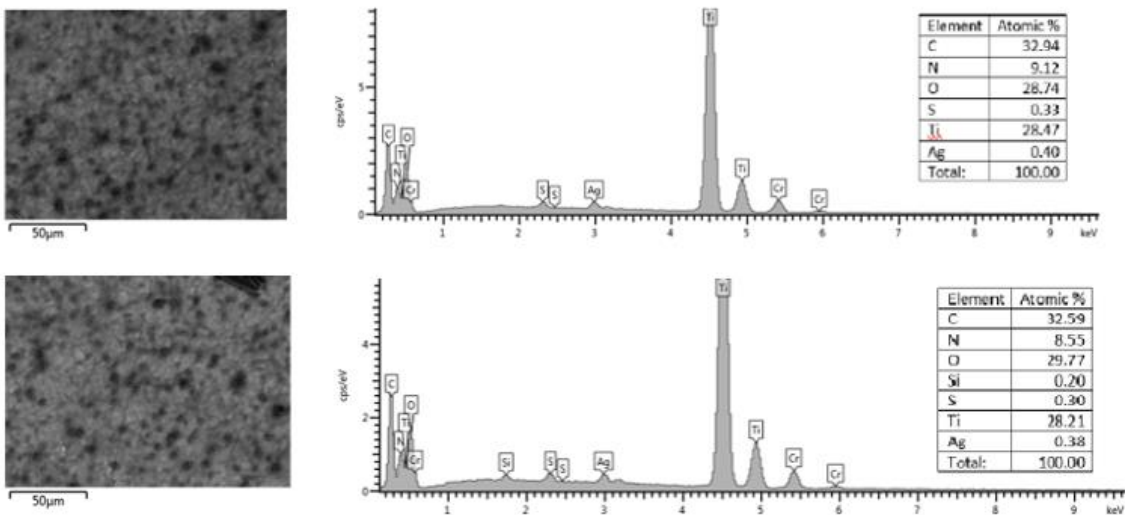
Figure 80. EDS analysis of the areas of the sample "Smooth-Ti cp/Ker/Ag 01"

Here, as in the previous sample, the Ag peak is found in both areas, and the major value is observed in the first spectrum of Figure 80. Furthermore, even in this sample, the second spectrum shows a Si peak, probably due to contamination.

Area EDS		Smooth-Ti cp/Ker/Ag001		Smooth-Ti cp/Ker/Ag005		Smooth-Ti cp/Ker/Ag01	
		Average	Standard Deviation	Average	Standard Deviation	Average	Standard Deviation
	C	32.69	0.282	34.425	0.049	32.765	0.247
	N	7.715	0.388	8.325	0.388	8.835	0.403
	O	28.42	0.141	28.985	0.982	29.255	0.728
Element [%]	S	0.3	0.042	0.35	0.042	0.315	0.021
	Ti	30.625	0.007	27.465	1.407	28.34	0.183
	Ag	0.255	0.007	0.39	0.049	0.395	0.014
	Si	/	/	0.06	0.084	0.1	0.141

Table 26. Summary of averages and standard deviations of elements from area EDS for all samples with Ag treatment

From Table 26 it is possible to observe how the high average percentage of Ti has been detected on all samples and in almost equal percentages, followed by the high average percentages of carbon and oxygen. The detection of titanium shows the range of depth that this type of analysis is able to achieve, in fact, thanks to this analysis we have information about the interface area between keratin coating enriched with Ag and titanium substrate. the amount of silver increases moving from samples treated with Ag 0.001 to Ag 0.005 but remains stable further increasing the silver content in the treatment solution.

2.3. **FT-IR**

The FT-IR analysis was carried out to observe on the surface of the samples the presence and the type of atomic bonds. In this case, the atomic bonds characteristic of the keratin nanofibers treated with silver, in order to observe the eventual presence of atomic bonds or functional groups with antibacterial action. This analysis was conducted on the following samples:

- Smooth-Ti cp/Ker
- Smooth-Ti cp/Ker/Ag001
- Smooth-Ti cp/Ker/Ag005
- Smooth-Ti cp/Ker/Ag01

Below are the FT-IR spectra of each sample in a single chart:
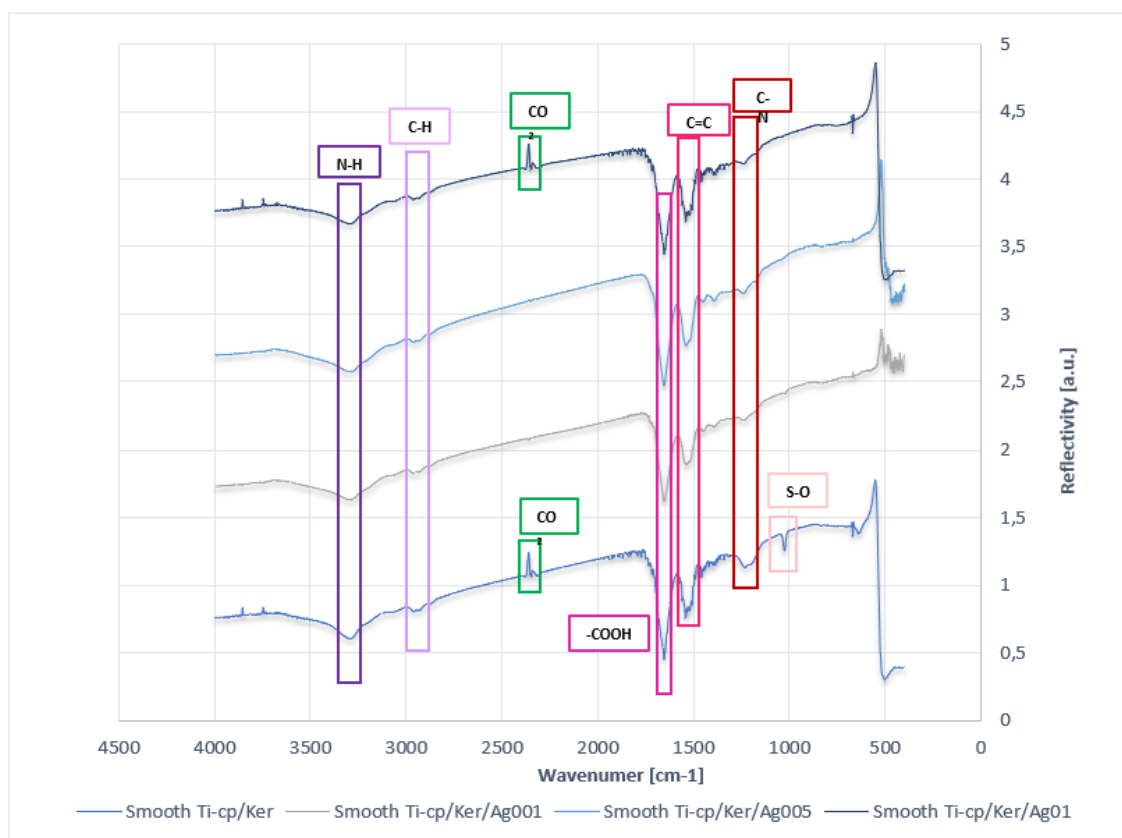
Figure 81. FT-IR characterization of the samples with the Ag treatment

The peaks highlighted in figure 81 are related to the following chemical bonds (132):

- **N-H** at 3278 cm^{-1};

- **C-H** at 2921 cm^{-1};

- **CO$_2$** not well compensated at 2355 cm^{-1};

- **-COOH** at 1650 cm^{-1};

- **C=C** at 1523-1542 cm^{-1};

- **C-N** at 1221 cm^{-1};

- **S-O** at 1020 cm^{-1};

In Figure 81 it is observed that most of the peaks present in the spectra of the samples analyzed are identifying the same types of bonds, although the intensity is sometimes weaker. This may be due not only to a homogeneous distribution of the keratin coating but also to its thickness, which could prevent the detection of various chemical bonds as well as take into account the fact that the measurement was performed even on a limited area of the surface of the samples.

It is possible to observe from the FT-IR image of figure 81, that the spectrum of the sample used as a control and therefore without treatment with Ag, has peaks which are as those reported in the literature for keratin fibers, the same peaks reported in figure 68 for samples with surface treatments to improve the adhesion of the keratin coating to the titanium substrate. (142)

In Figure 81, it is observed that after the enrichment with Ag the S-O signal disappears at 1020 cm^{-1} and comparing this result with the subsequent XPS analysis we can suppose the formation of S-Ag bonds. Unlike what was reported in the literature for copper, no changes in the C=O signals are observed. (143)

2.4.**XPS**

Table 27 shows the atomic percentages obtained from the Survey spectra of the various samples:

Element	Smooth-Ti cp/Ker	Smooth-Ti cp /Ker/Ag001	Smooth-Ti cp /Ker/Ag005	Smooth-Ti cp /Ker/Ag01
C	60.70	61.80	63.80	60.40
O	21.10	20.30	19.00	18.90
N	14.00	14.30	14.20	15.00
Na	2.30	0.20	/	/
S	1.90	1.70	1.10	1.40
Ag	/	1.70	1.90	1.90
F	/	/	/	2.30

Table 27. Atomic percentages from the four-sample Survey spectra

From the Table 27 it can be seen that compared to the EDS analysis, titanium was not detected here, due to the lower penetration depth of the XPS (4-5 nanometers), while the atomic percentages of carbon are higher. Carbon is present partly in the keratin coating and partly as surface contamination, typical of reactive surfaces observed by XPS analysis. The significant amount of oxygen usually attributed to titanium oxide TiO_2, which is created spontaneously on the surface of the titanium sample, in this work can be mainly attributed to keratin because the depth range reached by the XPS analysis cannot reach the interface between titanium substrate and keratin coating. As for silver, it was detected on all samples, except for the one used as a control. As can be seen from Table 27, it is possible to observe that the atomic percentage of Ag is almost constant. However, it is possible to notice a slight increase in Ag in the case of intermediate and high concentration of the $AgNO_3$ solution compared to the case of low concentration, according to EDS analyses Nitrogen and sulfur are attributable to the keratin coating, although the former is present with a higher atomic percentage. Finally, the presence of fluorine and sodium is instead due to contamination.

Below, in figures 82a, 82b, 82c and 82d the Survey spectra for the three samples are shown:
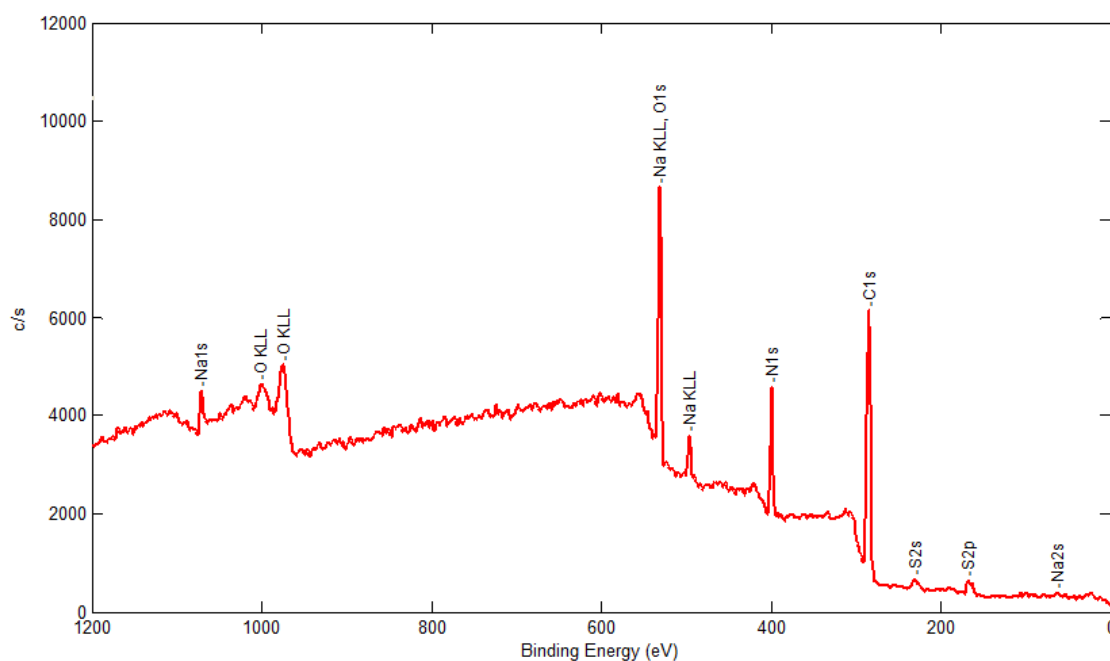
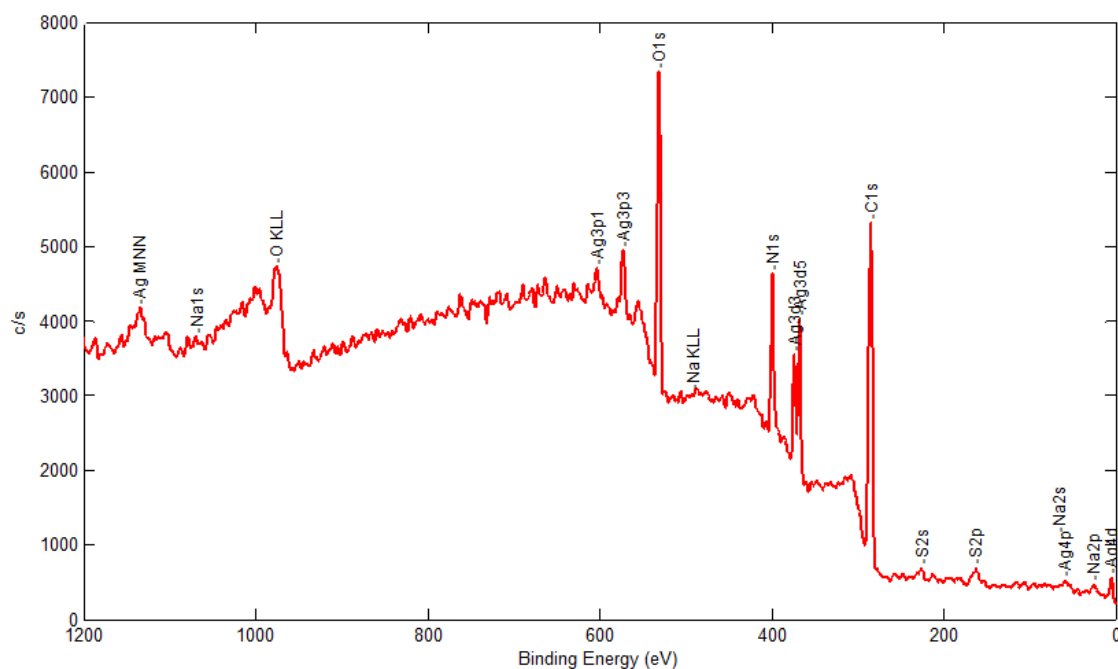*Figure 82a. Survey spectrum of Smooth-Ti cp/Ker sample*

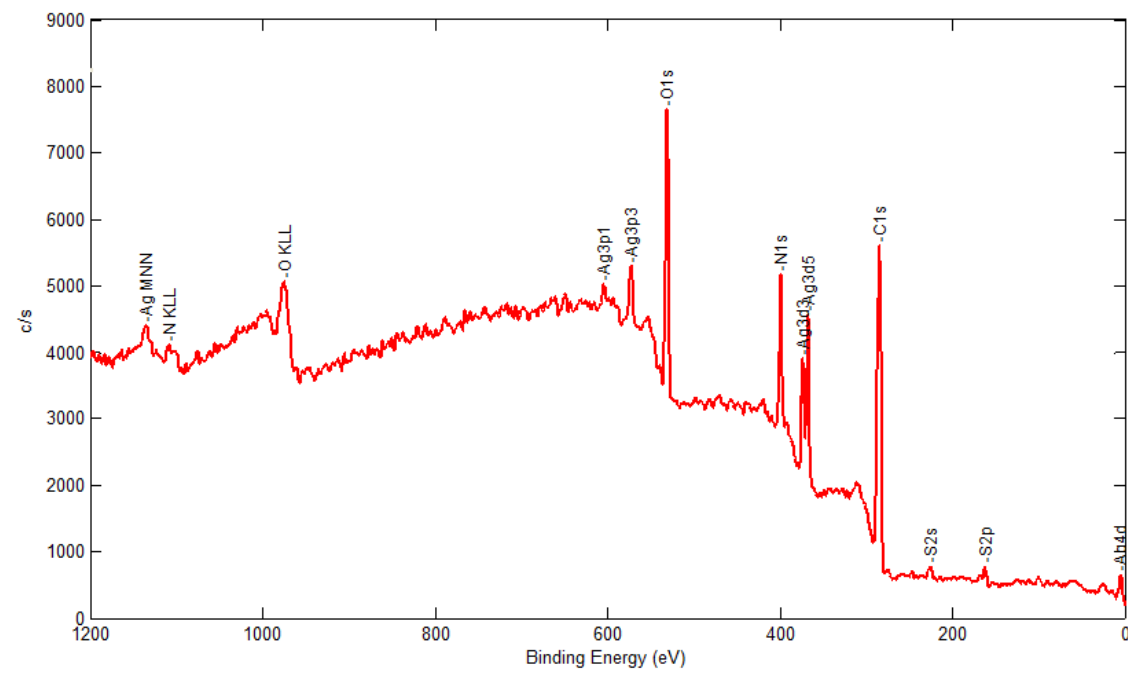*Figure 82b. Survey spectrum of Smooth-Ti cp/Ker/Ag001 sample*

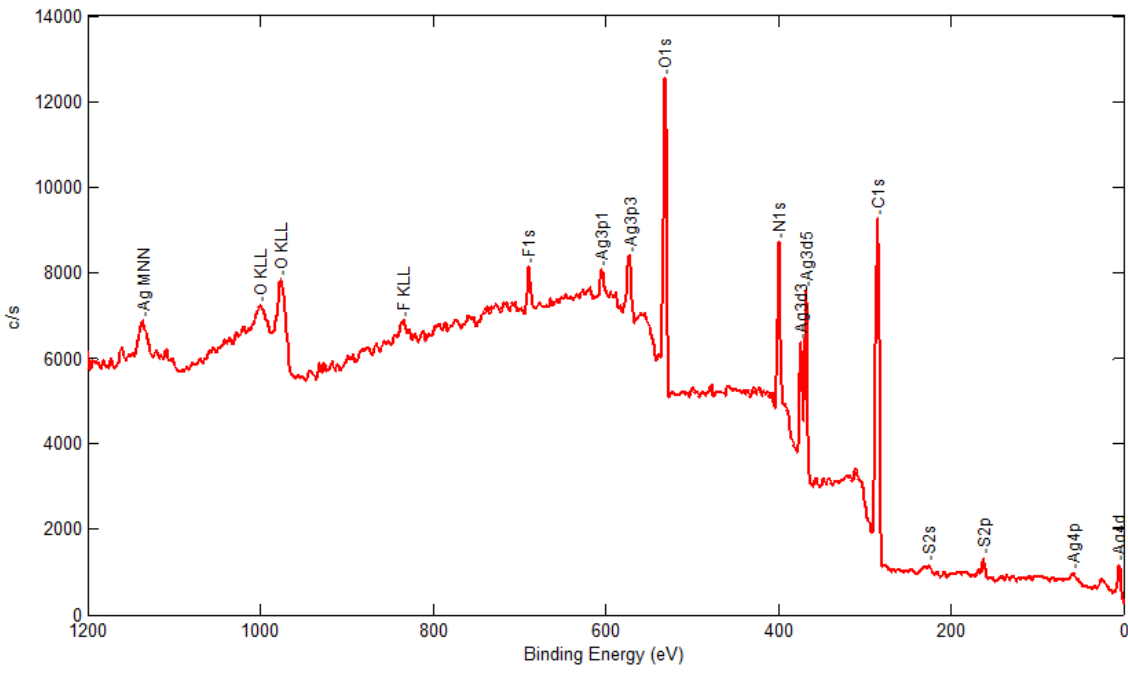*Figure 82c. Survey spectrum of Smooth-Ti cp/Ker/Ag005 sample*

Figure 82d. Survey spectrum of Smooth-Ti cp/Ker/Ag01 sample

For each sample the high-resolution HR spectra of the carbon, oxygen, nitrogen and silver regions were then acquired. The binding energies were corrected by matching the main carbon peak to the bonding energy of 284.6 eV, according to conventional use. (134) The possible attribution of the individual peaks was made on the basis of what reported in the literature. (135) (136) In the following figures, the possible attributions of the binding energies detected during the analysis are listed according to the detained element:
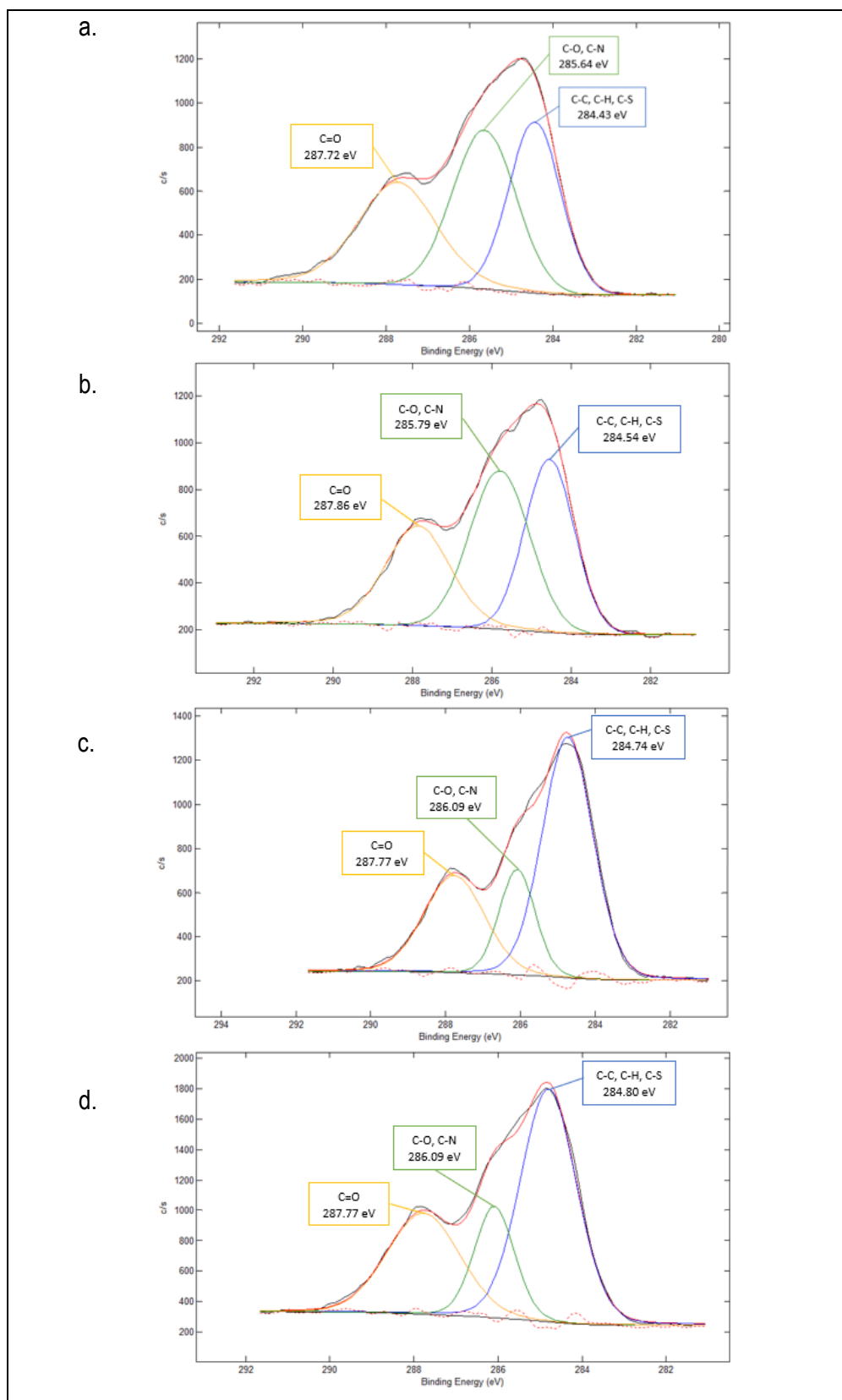
Figure 83. HR carbon spectra for: a. Smooth Ti-cp/Ker, b. Smooth-Ti cp/Ker/Ag001, c. Smooth-Ti cp/Ker/Ag005, d. Smooth-Ti cp/Ker/Ag01.

The C-C, C-H, C-O and C=O bonds that appear in the spectra of both Figure 83 are present probably due to the carbon as contaminant. These bonds, together with the C-S and C-N, present in figure 83 and figure 84, are also contained in the primary structure of keratin, so the contribution to the peaks in question is twofold. (137) (138)

For each sample the ratio between the percentage area of the detected peaks and the peak area at 284 eV taken as reference was calculated (Table 28). It is observed for all samples the presence of a relative reduction in the abundance of the attribution C-O/C-N compared to the reference with the increase of the concentration of Ag. Also, for the attribution C=O a relative reduction of the abundance with respect to the reference to the increase of the concentration of Ag is detected, a small exception is made for the sample with a high concentration of Ag, so there is a slight increase in relative abundance compared to cases of samples with a low and intermediate concentration of silver. No peak displacement was observed as a function of the increase in Ag concentration in the coating.

Smooth Ti-cp/Ker	Area [%]	Ratio
284.43 eV	32.24	1
285.64 eV	36.16	1.12
287.72 eV	31.60	0.98

Smooth-Ti cp/Ker/Ag001	Area [%]	Ratio
284.54 eV	34.21	1
285.79 eV	37.84	1.1
287.86 eV	27.96	0.817

Smooth-Ti cp/Ker/Ag005	Area [%]	Ratio
284.74 eV	55.67	1
286.09 eV	17.32	0.311
287.77 eV	27.01	0.48

Smooth-Ti cp/Ker/Ag01	Area [%]	Ratio
284.80 eV	52.46	1
286.09 eV	18.05	0.34
287.77 eV	29.49	0.56

Table 28. Summary of the percentage areas and ratios for the HR carbon spectra
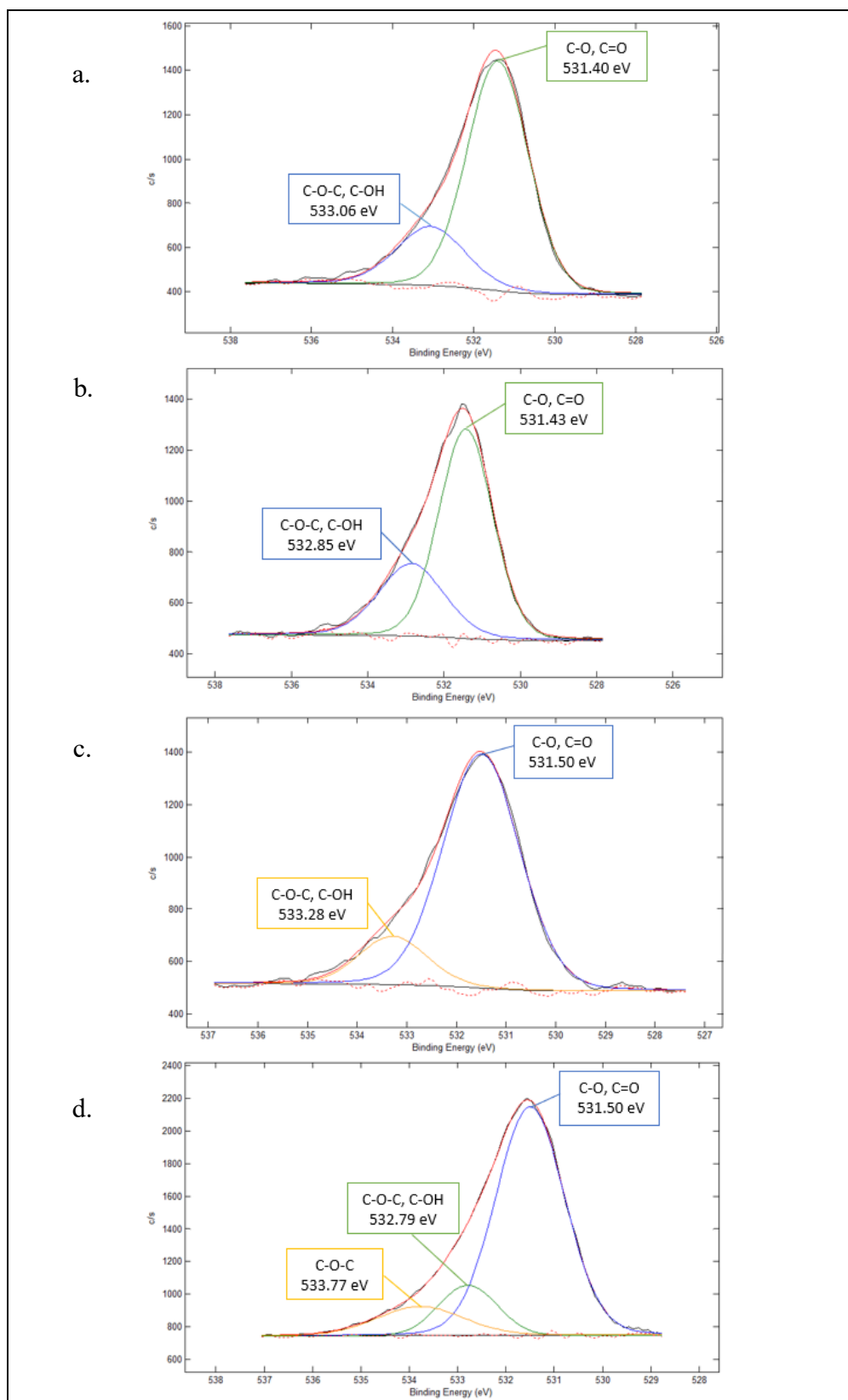
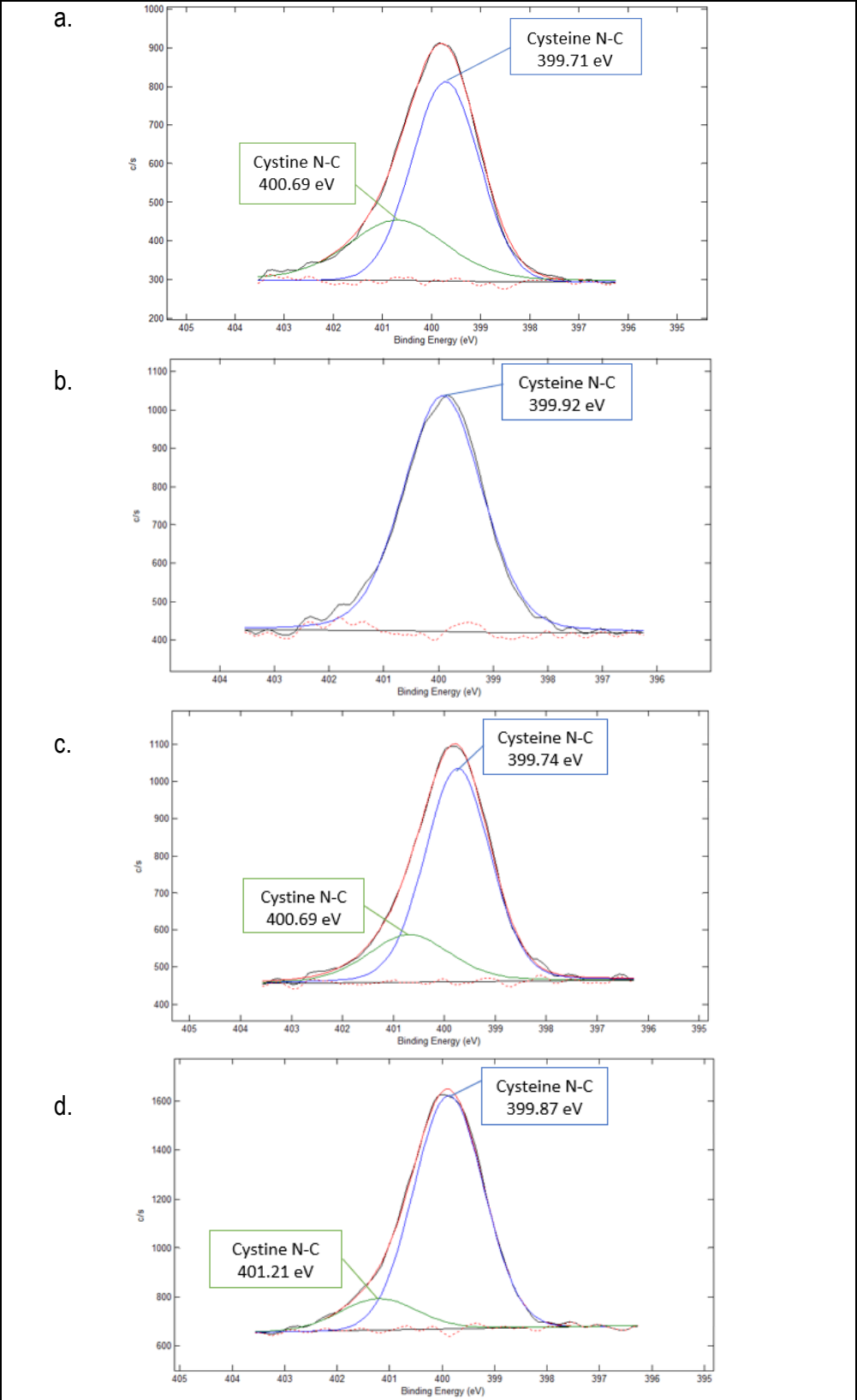*Figure 84. HR oxygen spectra for: a. Smooth Ti-cp/Ker, b. Smooth-Ti cp/Ker/Ag001, c. Smooth-Ti cp/Ker/Ag005, d. Smooth-Ti cp/Ker/Ag01*

In figure 84, for the first three samples, it is possible to identify two peaks, while for the sample with a high concentration of Ag three contributions were identified. In all samples, each peak corresponds to a specific bond with oxygen. The presence of the double carbon C=O oxygen bond and the C-O bond is derived from keratin. (138) (139) While, the peaks attributed to C-O-C, C-OH at higher energies, especially the peak at 533.77 eV in Figure 84d., can be attributed to the water present in the solution of $AgNO_3$, which during the enrichment with silver phase reacted with the keratin itself. For the samples in Figures 84a., 84b., 84c. and 84d., the ratio between the percentage area of the peak with the C-O/C=O attribution and that of the peak attributed to C-O-C/C-OH has been calculated (Table 29): For these samples we observe the presence of a relative abundance of the C-O/C=O attribution increasing with increasing Ag concentration.

Smooth Ti-cp/Ker	Area [%]	Ratio
531.40 eV	76.40	1
533.06 eV	23.60	0.308
Smooth-Ti cp/Ker/Ag001	**Area [%]**	**Ratio**
531.43 eV	69.28	1
532.85 eV	30.72	0.443
Smooth-Ti cp/Ker/Ag005	**Area [%]**	**Ratio**
531.50 eV	84.12	1
533.28 eV	15.88	0.188
Smooth-Ti cp/Ker/Ag01	**Area [%]**	**Ratio**
531.50 eV	74.61	1
532.79 eV	13.30	0.178
533.77 eV	12.09	0.162

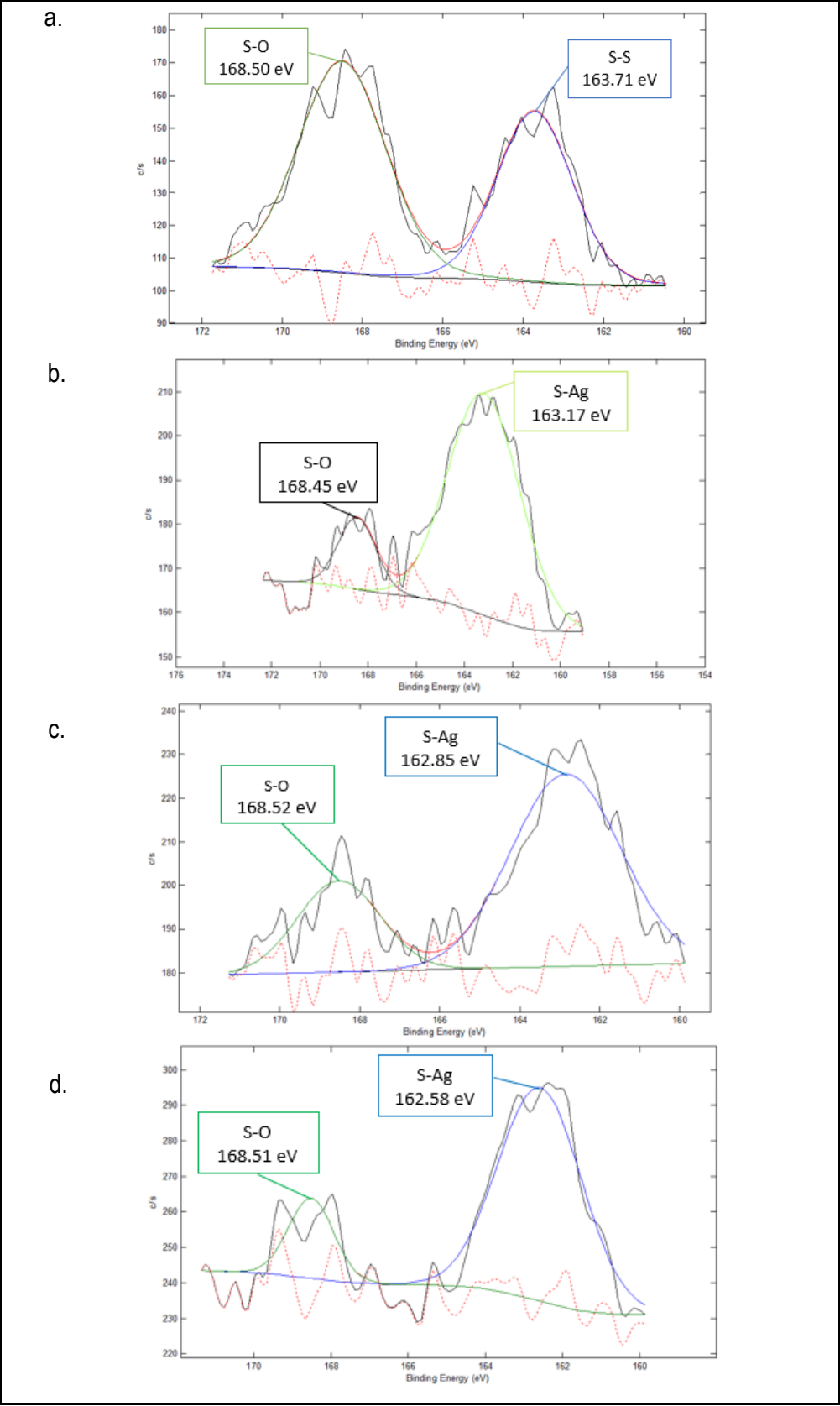*Table 29. Summary of the percentage areas and ratios for the HR oxygen spectra*

Figure 85. HR nitrogen spectra for: a. Smooth Ti-cp/Ker, b. Smooth-Ti cp/Ker/Ag001, c. Smooth-Ti cp/Ker/Ag005, d. Smooth-Ti cp/Ker/Ag01

Regarding the nitrogen HR spectra, in Figure 85, the nitrogen peaks were attributed to cysteine N-C (at 400 eV) and cystine N-C (at 401 eV) due to the confirmed presence of sulfur fractions both in Table 27 and in the HR spectra in Figure 86. However, due to the variety of amino acids present in keratin and the overlapping binding energies of cystine in HR spectrum of nitrogen (N 1s), i.e. glycine, which is also present in the polypeptide chain, these cannot be definitively assigned. (140) For each sample the ratio between the percentage area of the peak attributed to the cysteine N-C bond and the percentage area attributed to the cystine N-C bond was calculated (Table 30). The presence of an increasing relative abundance of the cysteine N-C attribution with respect to cystine N-C is observed for all samples, except for the sample with a low concentration of Ag, figure 85b., for which only the peak attributed to cysteine N-C is present. In particular, the sample with a high concentration of Ag (Figure 85d.) shows a relative abundance of cysteine N-C almost double compared to the sample with intermediate concentration of Ag (Figure 85c.) and almost triple compared to the sample used as a control (Figure 85a.) in addition to shifting both peaks, cysteine N-C to 399.87 eV and cystine N-C 401.21 eV to higher energies.

Smooth Ti-cp/Ker	Area [%]	Ratio
399.71 eV	66.53	1
400.69 eV	33.47	0.503
Smooth-Ti cp/Ker/Ag001	Area [%]	Ratio
399.92 eV	100	1
Smooth-Ti cp/Ker/Ag005	Area [%]	Ratio
399.74 eV	76.81	1
400.69 eV	23.19	0.301
Smooth-Ti cp/Ker/Ag01	Area [%]	Ratio
399.87 eV	86.52	1
401.21 eV	13.48	0.155

Table 30. Summary of the percentage areas and ratios for the HR nitrogen spectra

Figure 86. HR sulfur spectra for: a. Smooth Ti-cp/Ker, b. Smooth-Ti cp/Ker/Ag001, c. Smooth-Ti cp/Ker/Ag005, d. Smooth-Ti cp/Ker/Ag01

Regarding the sulfur HR spectra, in Figure 86, the peaks were attributed to S-O (at 168.2-168.7 eV), i.e. oxidised disulfide bonds of the cysteic acid residues of keratin, and to S-S (at 163.9-164.0 eV), i.e. cystine disulfide bonds. As can be seen from Figure 86, all spectra present noisy signals. (141) For the control sample the ratio between the percentage area of the peak with attribution S-S and that of the peak with attribution S-O was calculated (Table 31). While, for each of the samples with increasing Ag concentration, the peak at lower energy undergoes a translation towards the low energies, at 163.17 eV, 162.85 eV and 162.58 eV respectively; reason why in these cases the ratio between the percentage areas of the peaks was calculated between the S-Ag and S-O assignments. In particular, the sample with a low concentration of Ag (Figure 86a.) shows a relative abundance of S-Ag almost double compared to the sample with intermediate concentration of Ag (Figure 86c.) and slightly higher than the sample with a high concentration of Ag (Figure 86d.). This result, already anticipated by the FT-IR analysis, shows that silver in $AgNO_3$ solution at different concentrations has been linked to sulfur instead of oxygen.

Smooth Ti-cp/Ker	Area [%]	Ratio
163.71 eV	41.18	1
168.5 eV	58.82	1.428
Smooth-Ti cp/Ker/Ag001	**Area [%]**	**Ratio**
163.17 eV	85.52	1
168.45 eV	14.48	0.169
Smooth-Ti cp/Ker/Ag005	**Area [%]**	**Ratio**
162.85 eV	73.80	1
168.52 eV	26.20	0.355
Smooth-Ti cp/Ker/Ag01	**Area [%]**	**Ratio**
162.58 eV	83.14	1
168.51 eV	16.86	0.202

Table 31. Summary of the percentage areas and ratios for the HR sulfur spectra
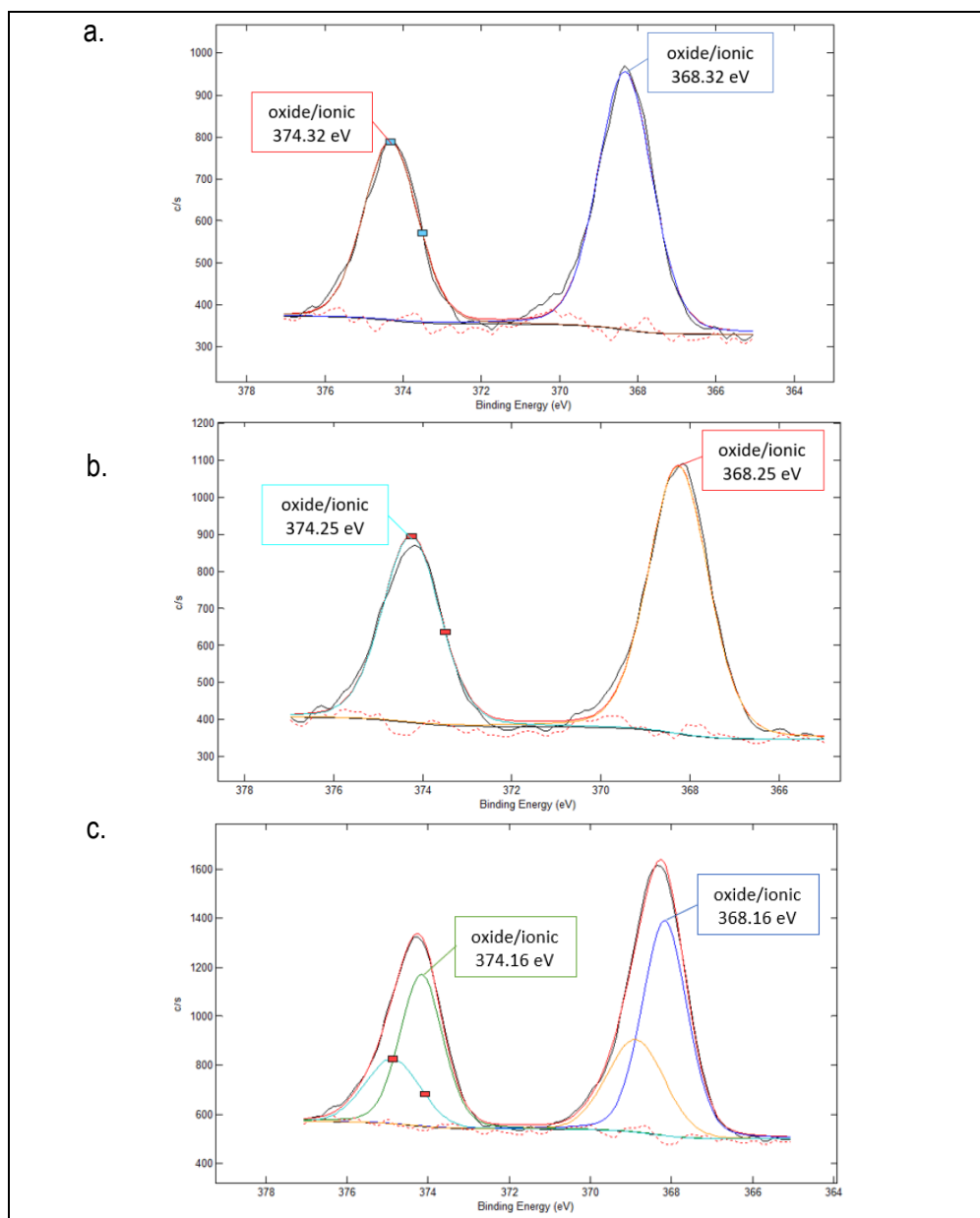
Figure 87. HR silver spectra for: a. Smooth-Ti cp/Ker/Ag001, b. Smooth-Ti cp/Ker/Ag005, c. Smooth-Ti cp/Ker/Ag01

The silver HR spectra, in Figure 87, allow the identification of two contributions for samples at low and intermediate concentration of Ag (Figures 87a. and 87b). For the sample with a high concentration of silver (figure 87c.) four peaks are identifiable: the two at lower energy, 368.16 eV and 374.16 eV, are attributable to Ag metallic or S-Ag, and in this case S-Ag was assumed as it would confirm what was seen in the FT-IR analysis, while the two contributions to higher energies are satellite peaks attributable to "charge transfer effects". (141) (144)

2.5.**Biological Tests**

2.5.1. Bacterial tests

This test is used because of its greater specificity compared to the FESEM analysis. The test involves the marking of bacteria, *S. Aureus*, with fluorophores thus being able to distinguish between live and dead bacteria. Figures 88, 89 and 90 compares the viability of the biofilm between the control samples and the samples with increasing concentration of Ag, divided into the various classes:

- Polystyrene (as control);
- Smooth Ti-cp/Ker (as control);
- Smooth Ti-cp/Ker/Ag001;
- Smooth Ti-cp/Ker/Ag005;
- Smooth Ti-cp/Ker/Ag01.

The viability of bacteria on these samples was assessed at 24, 48 and 72 hours, respectively. In particular, optical density (O.D.) has been considered by means of a spectrophotometer with a wavelength of 590 nm.
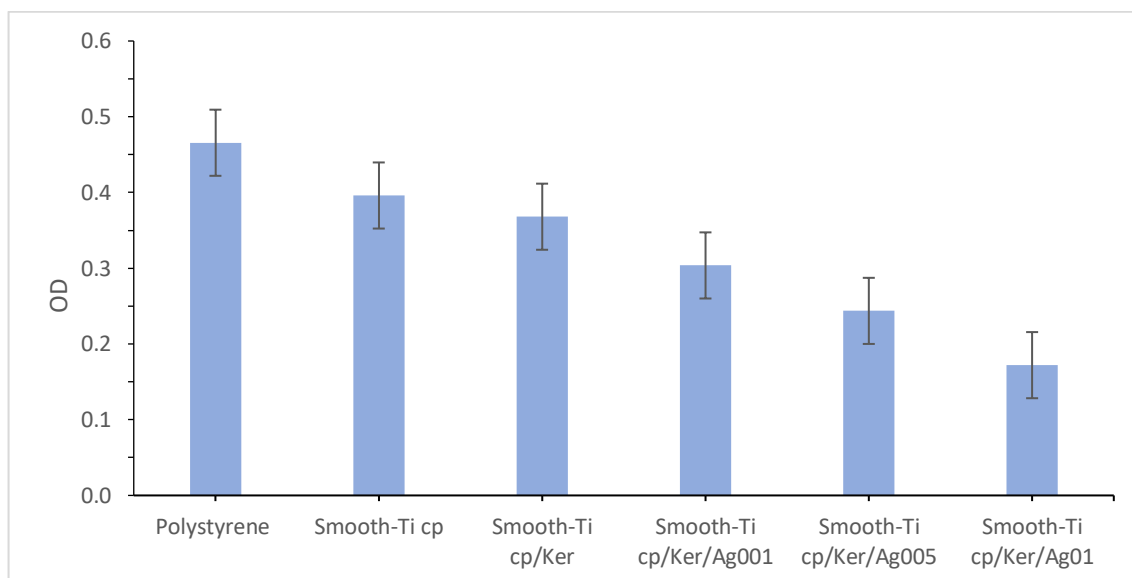
Figure 88. S. Aureus after 24h biofilm, XTT comparison between control samples and samples with increasing concentration of Ag
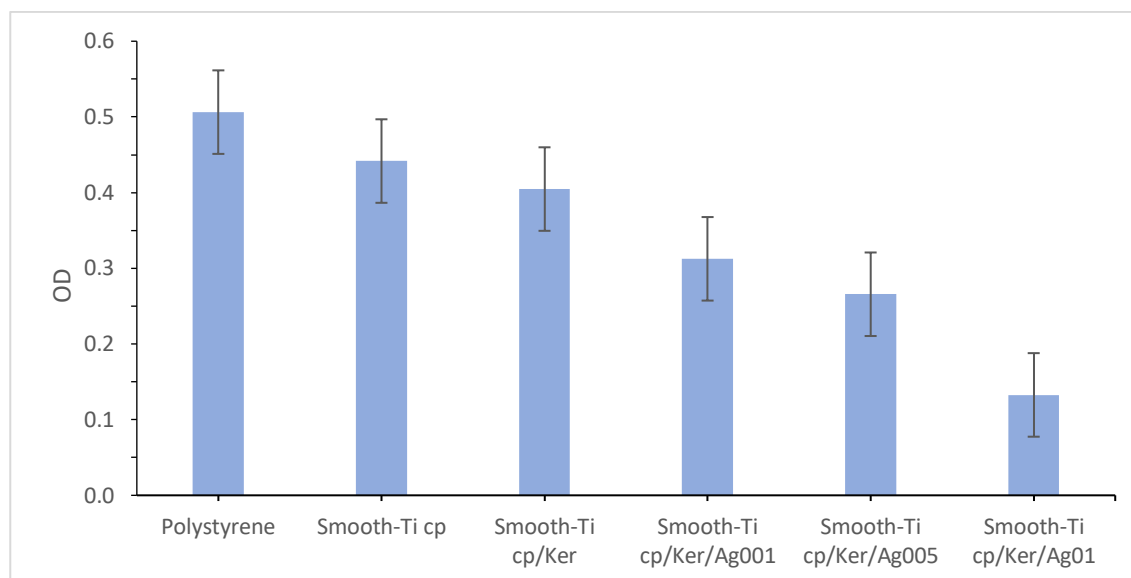
Figure 89. S. Aureus after 48h biofilm, XTT comparison between control samples and samples with increasing concentration of Ag
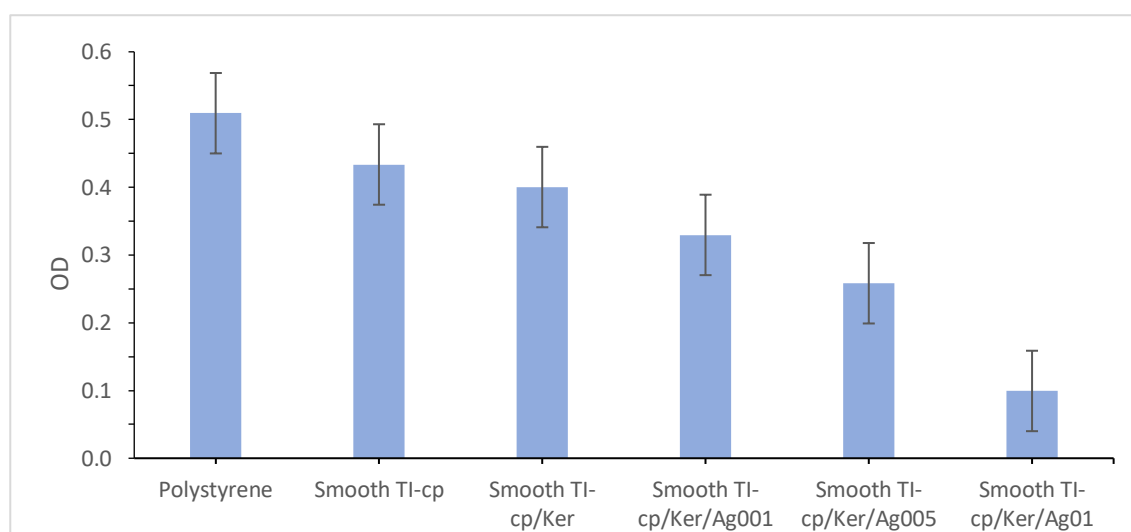
Figure 90. S. Aureus after 72h biofilm, XTT comparison between control samples and samples with increasing concentration of Ag

It is possible to observe, in all the figures 88, 89 and 90, that the number of live bacteria decreases with increasing silver concentration, however only the sample with the highest concentration shows a significant difference compared to the control. There are significant differences of the sample with the highest concentration of Ag, both with respect to the controls and to samples with a low and intermediate concentration of Ag.
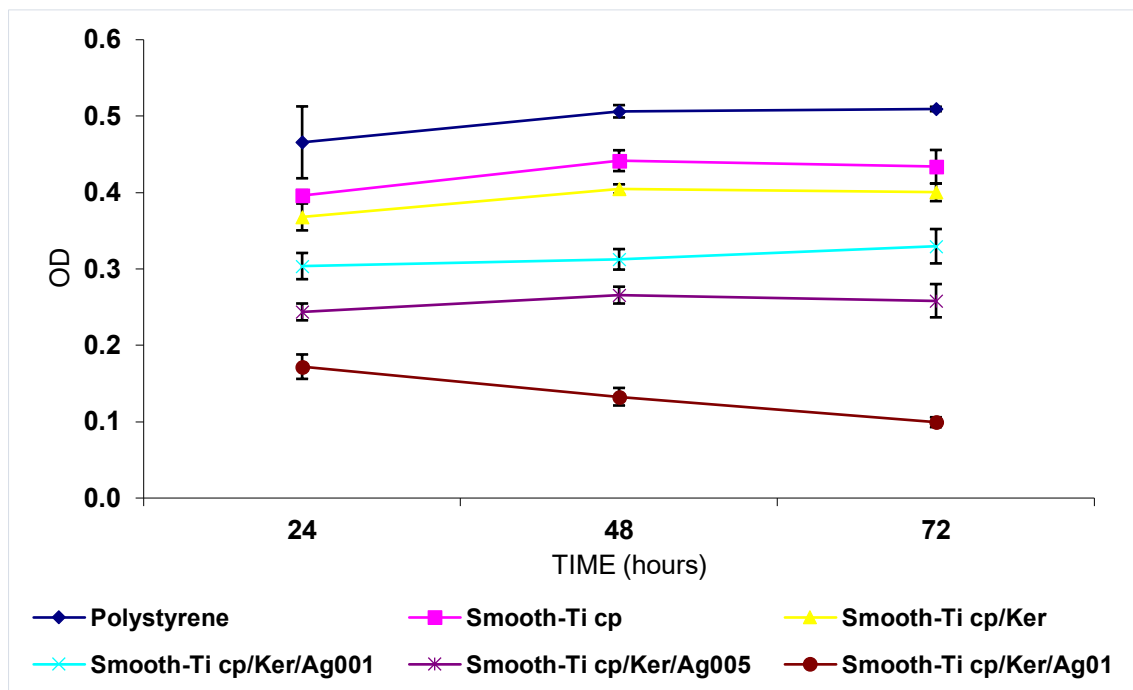
Figure 10. Summary of XTT comparison between control samples and samples with increasing concentration of Ag at different hours

This biological test has therefore confirmed what was observed in the FESEM images: the samples with the keratin coating enriched with high concentration silver show the best antibacterial behavior.

2.5.1.1 FESEM after bacterial test
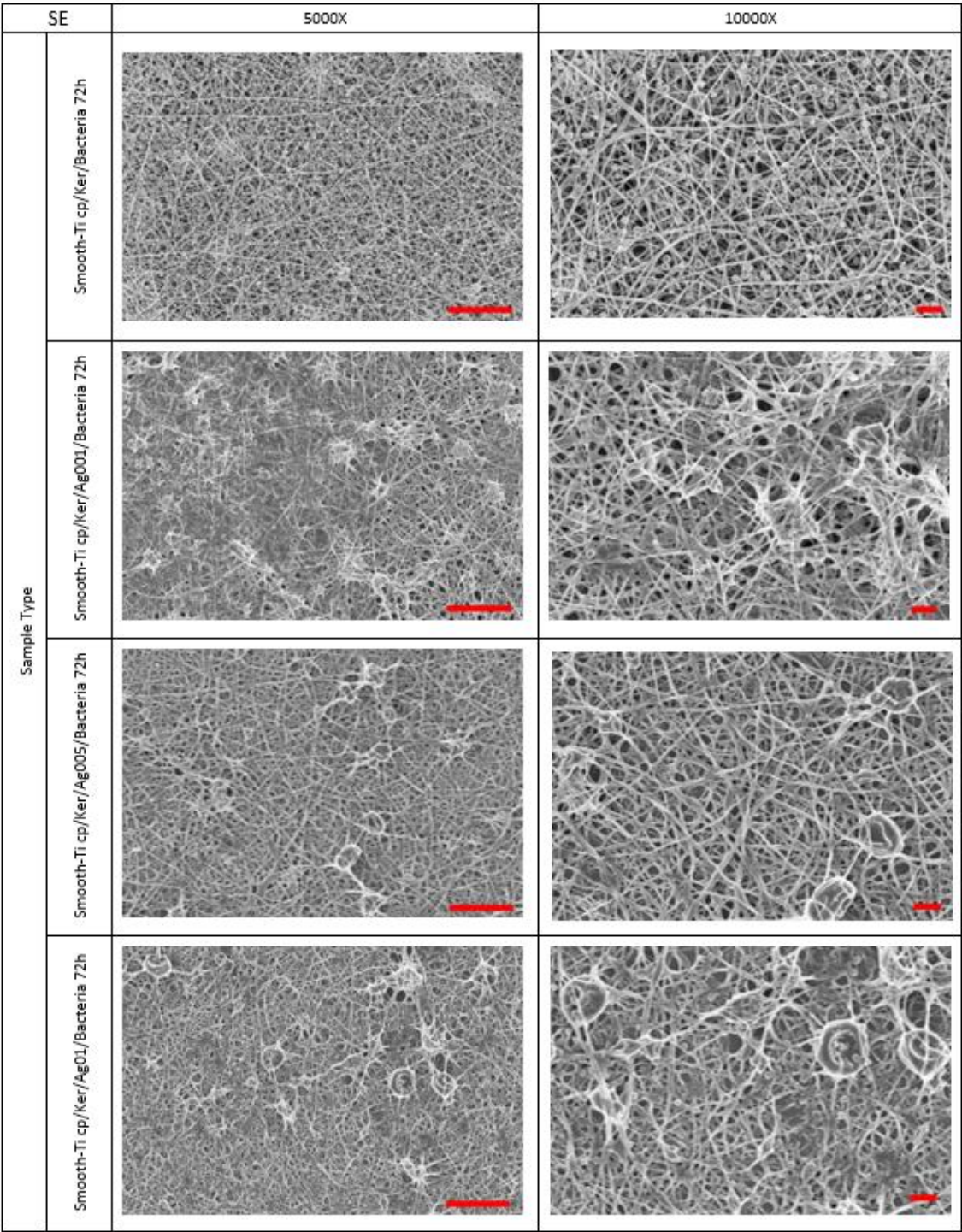
Figure 11. FESEM images after bacterial test of the four samples. Bar scale = 10μm at magnifications of 5000x and bar scale= 2μm at magnification 10000x

Observing the FESEM images of figure 92, it can be stated that the quantity of bacteria on the control sample, i.e. the one without silver, is considerably higher than the amount present on the samples treated with Ag, for both magnification. It is possible to observe

a trend of the quantity and distribution of bacteria as a function of the concentration of Ag, with the increase of the latter the quantity of bacteria decreases.

2.5.2. Cell test

This test is used because of its greater specificity compared to the FESEM analysis. The graphs below (figures 93, 94 and 95) show the data obtained from the evaluation of the vitality of HGFs cells (Human gingival fibroblasts) after 24, 48 and 72 hours of seeding. Figures 93, 94 and 95 compares the control samples and the samples with increasing concentration of Ag, divided into the various classes:

- Polystyrene (as control);
- Smooth Ti-cp/Ker (as control);
- Smooth Ti-cp/Ker/Ag001;
- Smooth Ti-cp/Ker/Ag005;
- Smooth Ti-cp/Ker/Ag01.

Cell viability was studied using the Alamar Blue method, detecting the RFU or the "Relative Fluorescence Unit", that is a unit of measurement used in the electrophoresis analysis method which employs fluorescence detection.
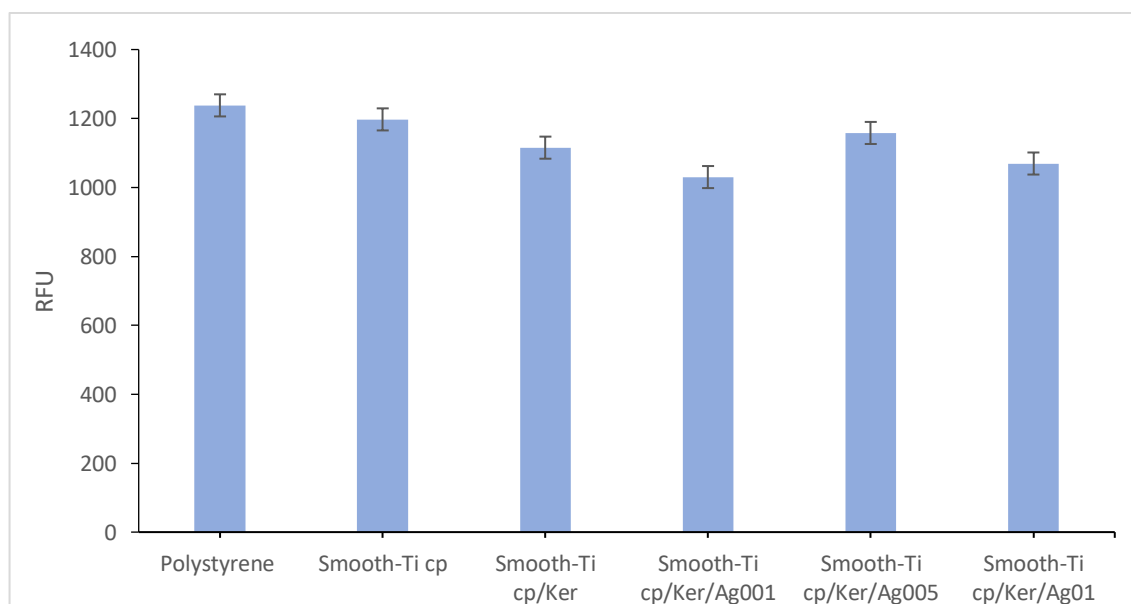
Figure 12. HGFs after 24h, comparison between control samples and samples with increasing concentration of Ag
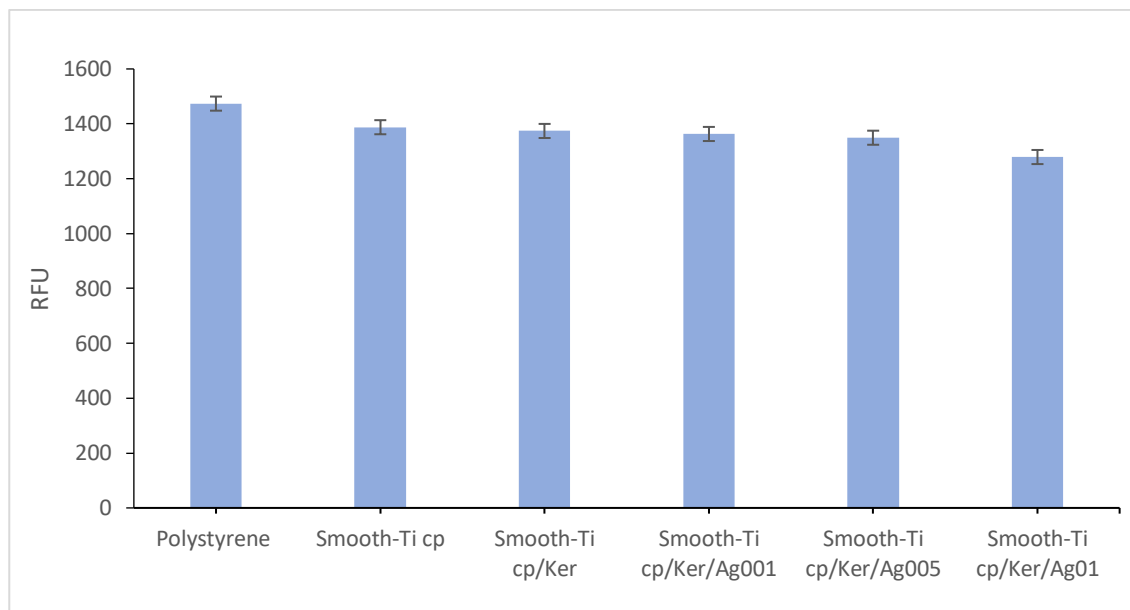
Figure 13. HGFs after 48h, comparison between control samples and samples with increasing concentration of Ag
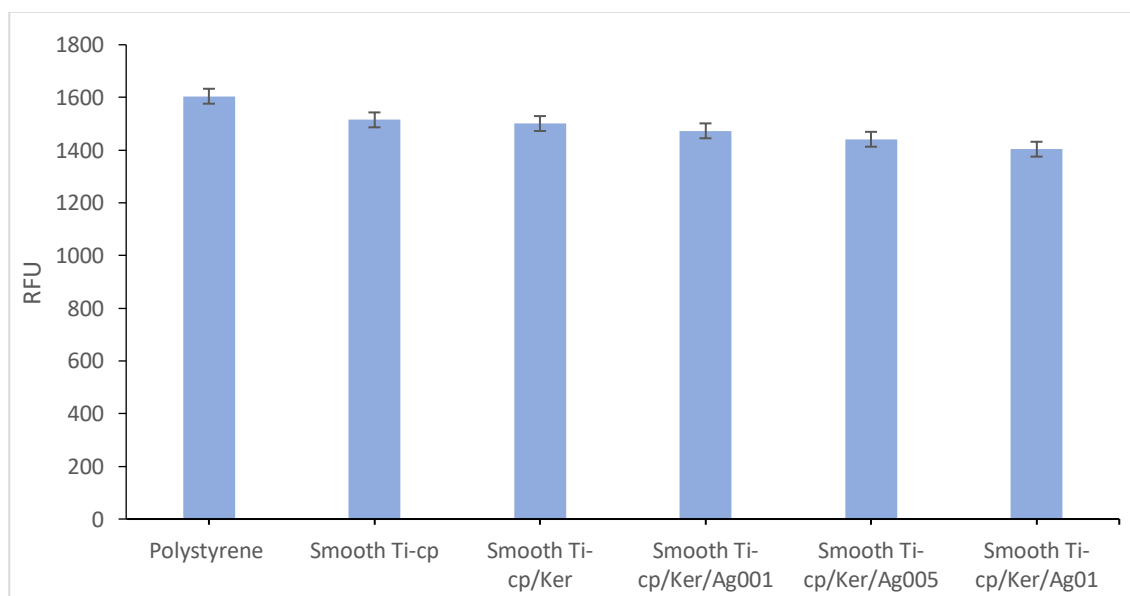

Figure 14. HGFs after 72h, comparison between control samples and samples with increasing concentration of Ag

As it is possible to see in Figures 93, 94 and 95, substantial differences between the various samples for cell viability are not observable, this means that all the samples, including the controls, are considered by the cells used, as favorable substrates for cell adhesion. Unlike the case of the bacterial test (Figures 88, 89 and 90), the Ag high concentration sample does not present, in a tangible way, a better behavior than both the

low and intermediate Ag concentration samples, but also with respect to the two control samples.
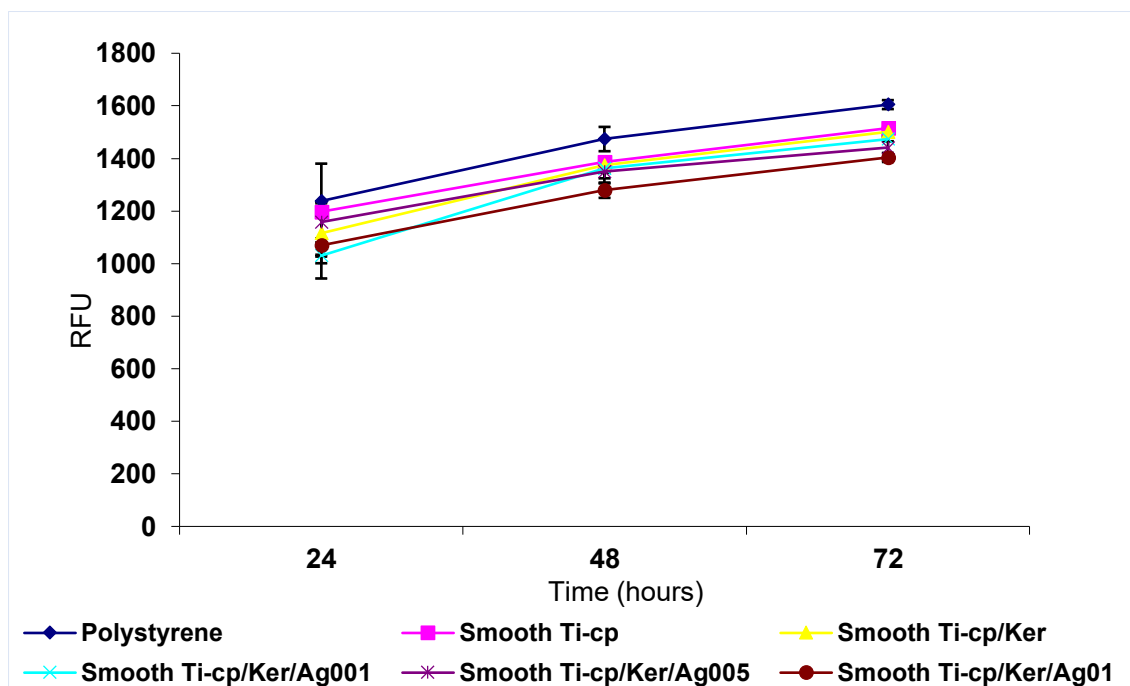
Figure 15. Summary of comparisons between control samples and samples with increasing concentration of Ag at different hours

The extracellular matrix (ECM) deposition was investigated by means of collagen deposition; results are reported in Figure 97. This observation looks particular evident by checking the staining of actin filaments, stained in red with phalloidin, and vimentin, stained in green. In general, no conspicuous differences were noticed between samples with different Ag concentration. In fact, cells were able to correctly deposit collagen independently from the antibacterial treatment intensity.
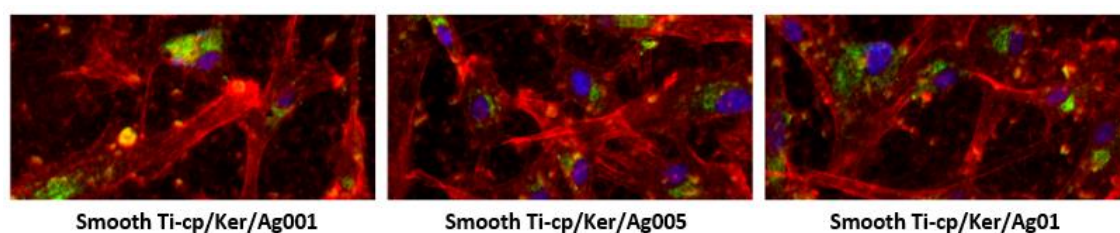
Figure 16. Cell matrix deposition onto samples with antibacterial treatment
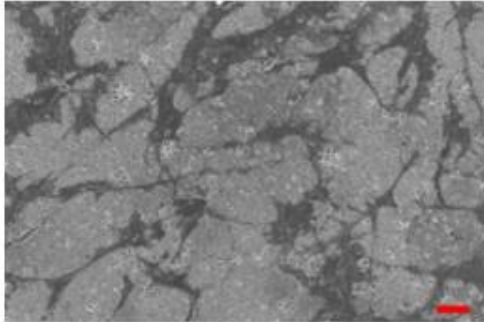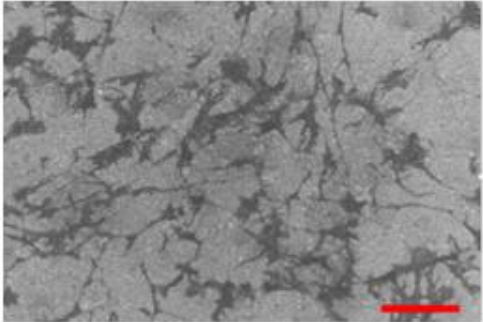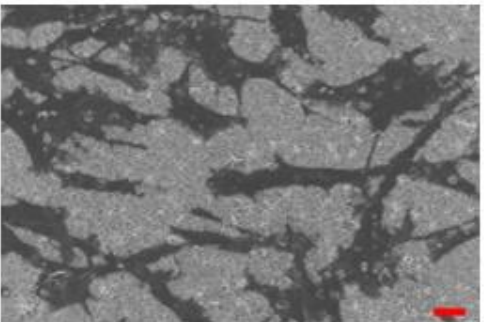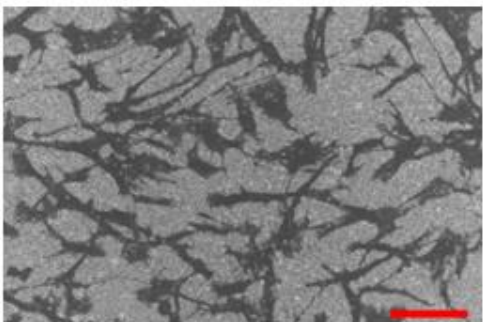
2.5.2.1. FESEM after cell test

Figure 17. FESEM images after cellalur test of the samples treated with Ag. Bar scale = 100μm at magnification 500x and bar scale = 20 μm at magnification 1000x

Figure 18. FESEM images after cellalur test of the samples treated with Ag. Bar scale = 20µm at magnification 2000x and bar scale = 10µm at magnification 5000x
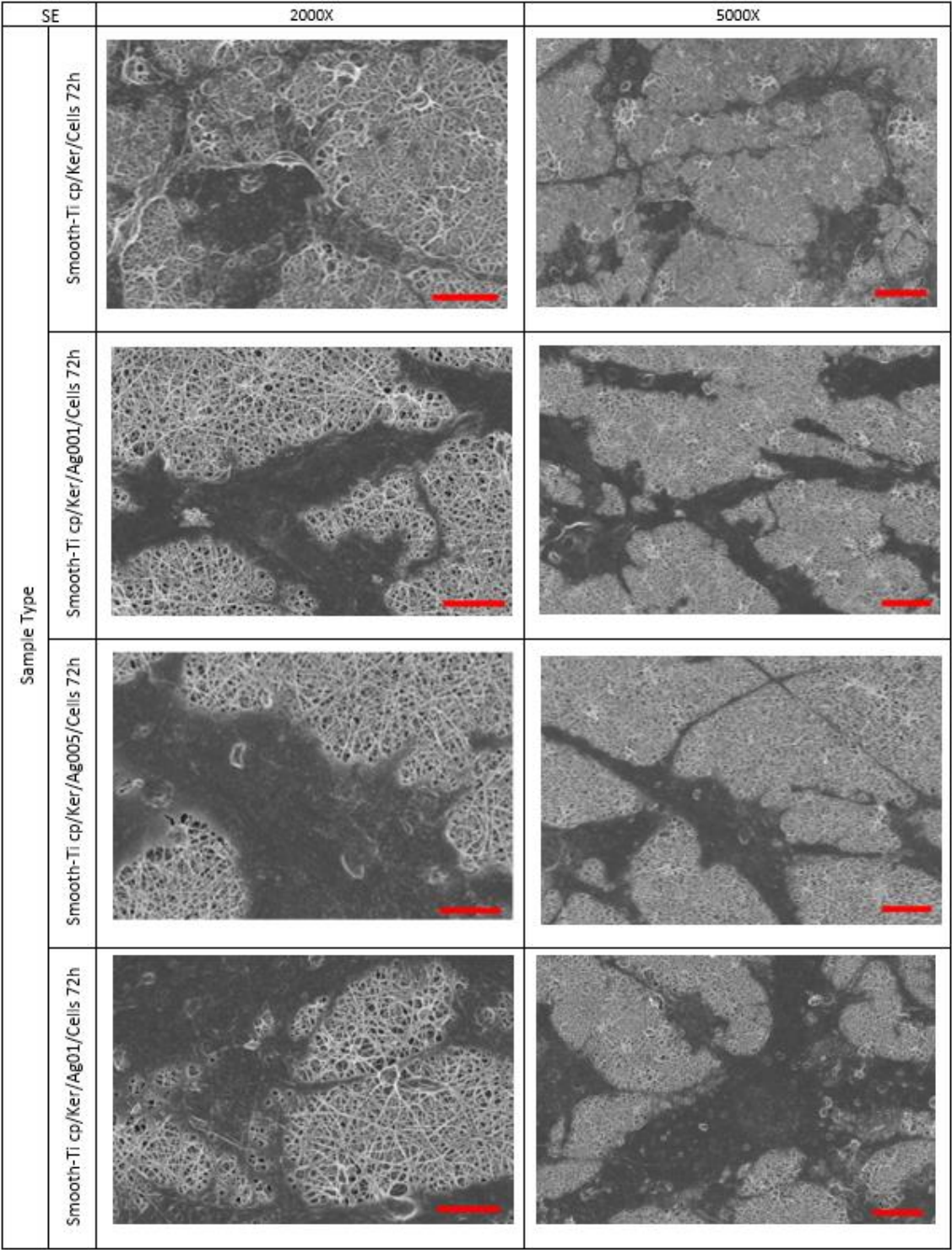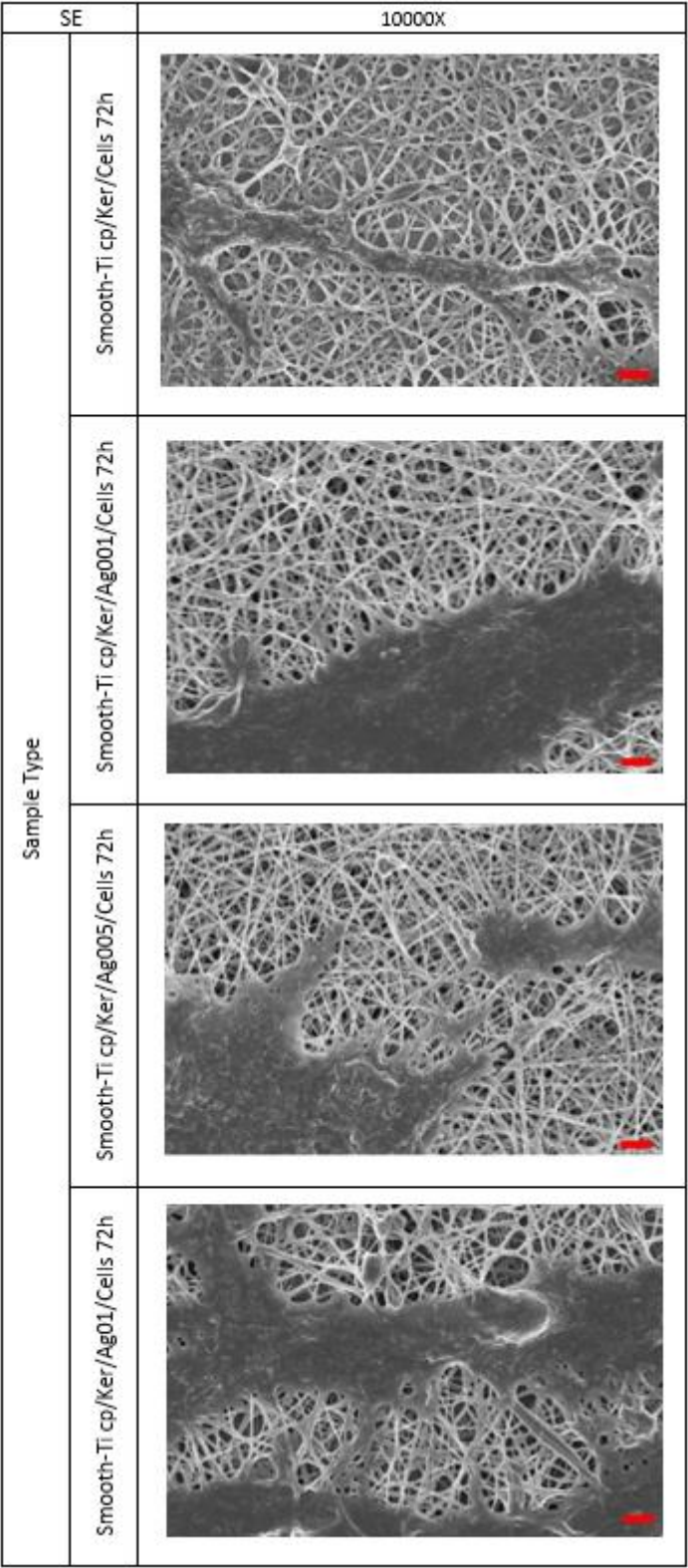
Figure 100. FESEM images after cellalur test of the samples treated with Ag. Bar scale = 2μm, magnification 10000x

Observing the FESEM images of Figures 98, 99 and 100, it can be stated, though in a qualitative way, that the amount of HGF on the control sample after 72 hours of seeding, i.e. the one without silver (Smooth-Ti cp/Ker/Cells 72h), is equal to the amount present on the samples treated with Ag, for all the magnifications. This data demonstrates the non-cytotoxicity of the substrate also in the presence of silver, which in addition to having an antibacterial effect, reveals, at high concentrations of Ag, a cytotoxic effect. It is possible to observe, in addition to a homogeneous distribution of the cells on the surface of the samples, that the cells have a "flattened" conformation, i.e. the occurrence of cellular spreading can be noted; this means that the substrate with keratin nanofiber coating and antibacterial solutions, is a cytocompatible substrate that promotes cell adhesion.

3. EBW SAMPLES STUDY

3.1. Wettability

Two wettability tests were performed, both under ambient conditions. The first test was performed on samples stored in Petri dishes, the second test, however, was performed on samples with bacterial broth, in order to detect any change in the hydrophilic/hydrophobic characteristics of the sample surface. Tables 32 and 33 show the wettability values for the samples analyzed. The mean and standard deviation of the values obtained for both tests were calculated. In order to facilitate the comparison between the sample types and between the two tests, the data were reported on a bar graph (Fig. 101 and Fig. 102), enriched with the images of the morphology assumed by the drop of water milli-Q on the surface of the sample.

	Smooth-Ti cp	Mechanically roughed-Ti cp	EBW 5	EBW 10	EBW 30
	72.4	78.2	80.3	103.8	88.8
Values	79.9	79.8	90.7	81.8	88.04
	76.8	89.5	84.1	91.4	79.4
	71.8	85.5	77.6	89.2	87.0
Average	75.225	83.25	83.175	91.55	85.81
Standard Deviation	3.831	5.213	5.681	9.140	4.336

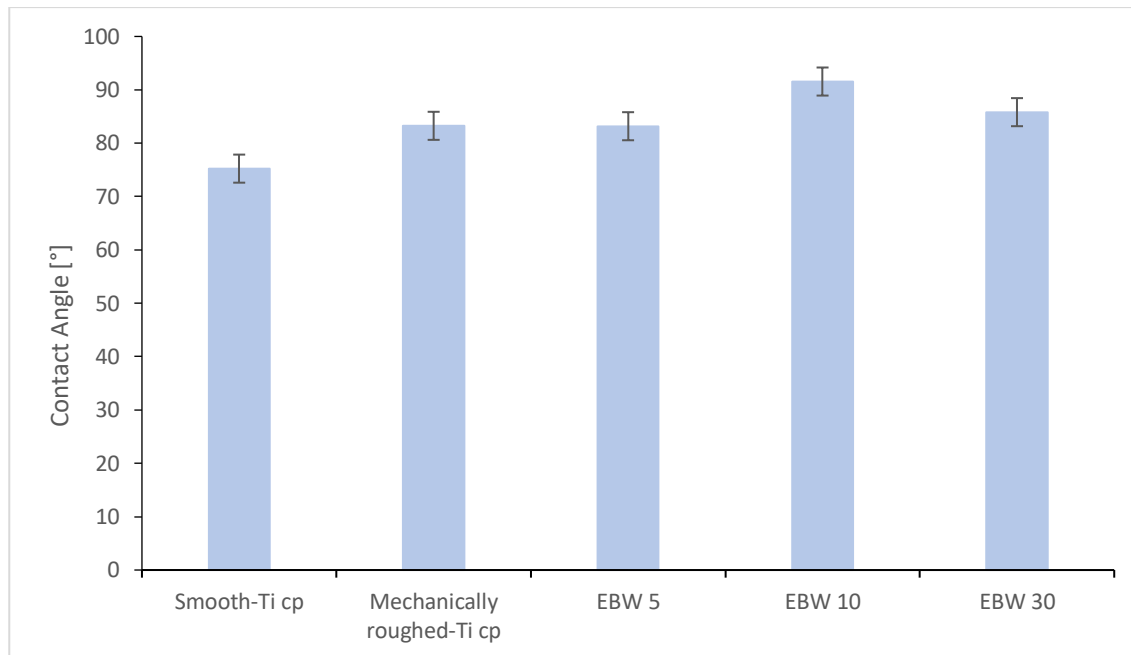*Table 32. Table of wettability in case of dry conserved samples*

Figure 19. Change in wettability with superficial topography of titanium expressed as an average of the values measured during the first wettability test.

As can be seen in Figure 101, the contact angle tends to slightly increase in the presence of grooves with respect to both the smooth sample and the mechanically roughened sample. In particular, the sample with grooves of 10 µm makes the titanium substrate more hydrophobic, to follow the sample with grooves of 30 µm and then 5 µm. This means that superficial topography plays a key role in this scope. Compared to previous works the values obtained are different, in this case the samples have a more marked hydrophobicity, that is a greater contact angle.

The explanation could lie in a possible contamination of the samples, which tends to make the surface more hydrophobic. In this work, this result will be compared with the results of cell and bacterial tests, since it is known in the literature that the superficial topography is able to influence the capacity of cell adhesion and consequently also the proliferation, as well as the hydrophobicity/hydrophilicity of the surface.

	Smooth-Ti cp	EBW 5	EBW 10	EBW 30
Values	72.5	76.4	67.9	78.0
	69.0	69.5	69.0	79.6
	65.7	79	/	74.2
	74.1	/	/	70.0
Average	70.325	74.966	68.450	75.450
Standard Deviation	3.747	4.909	0.777	4.281

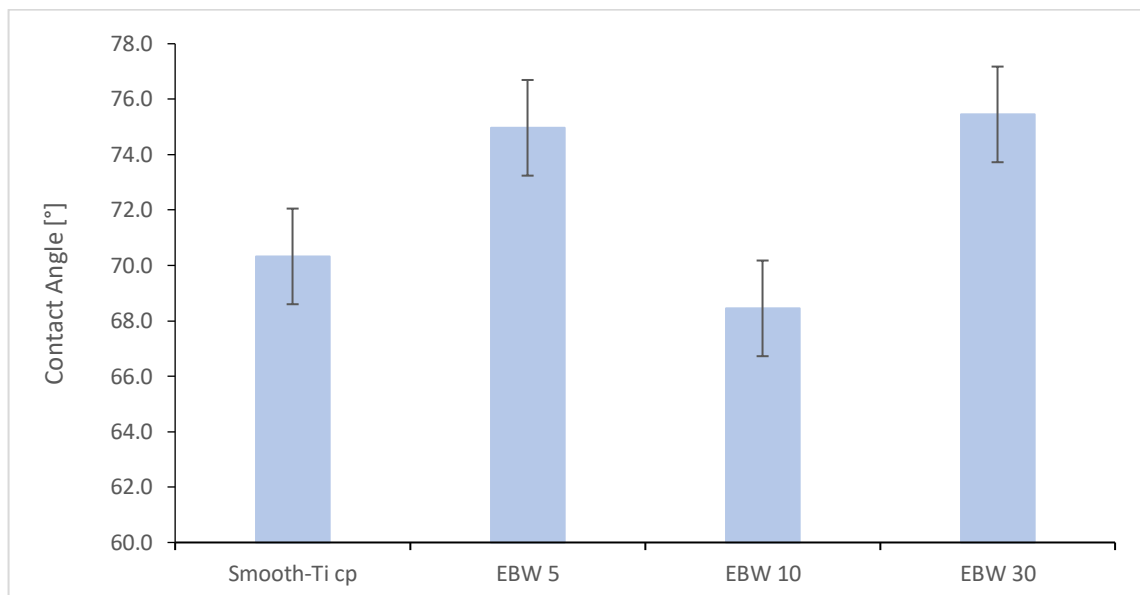*Table 33. Table of wettability in the case of samples previously stored in bacterial broth*

Figure 20. Change in wettability with superficial topography of titanium expressed as an average of the values measured during the second wettability test

As can be seen in Figure 102, in presence of bacterial broth, the contact angle tends increases in EBW samples with 30 µm and 5 µm grooves dimensions respect to the smooth sample. Compared to previous wettability test, in which the samples were maintained in Petri dishes before the test, the values obtained are very different, in fact the samples present a less hydrophobicity. The explanation could lie in the bacterial adhesion on the substrates, which tends to make the surfaces less hydrophobic. These results will be compared with the results of cell and bacterial tests.

185

3.2. **Zeta potential**

The measurement of the zeta potential was performed on the following samples, in order to investigate the surface charge:

- EBW5 samples;
- EBW10 samples;
- EBW30 samples;
- Smooth-Ti cp samples (as controls);
- Metallic Ag foils.

Here are curves that represent the potential zeta of the samples listed above. The commercially pure smooth titanium sample used as a control, was obtained from a previous work and shows an acid behavior: its isoelectric point is at $pH = 4$ and at physiological pH ($pH = 7.4$) its surface is negatively charged.
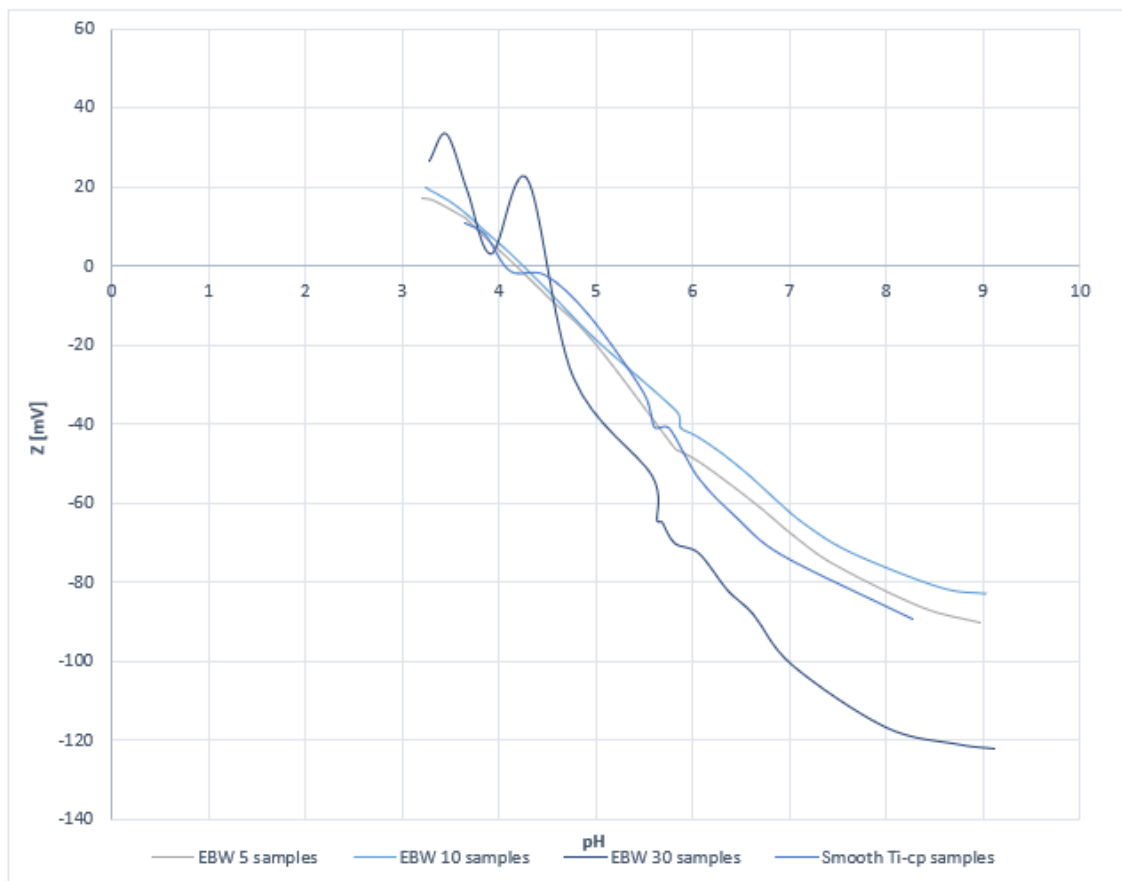

Figure 21. Zeta potential of the analyzed samples

From the observation of Figure 103 it would seem that all the curves have a decreasing trend as the pH increases and therefore at physiological pH the surface charge of the samples is negative. Moreover, as the size of the grooves augments, the isoelectric point slightly increases, i.e. higher pH values are observed with respect to the pH value of the isoelectric point of the sample used as control. The surface charge at physiological pH is maintained, for all samples, on negative values, although it is not possible to find a trend according to the increasing dimensions of the grooves. Table 34 provides a summary of the considerations made previously:

Type of Sample	IEP	z (pH=7.4) [mV]
EBW 5	4.2	-75.85
EBW 10	4.25	-72
EBW 30	4.51	-116.68
Smooth-Ti cp	4	-80

Table 34. IEP and surface charge at pH=7.4 of analyzed samples
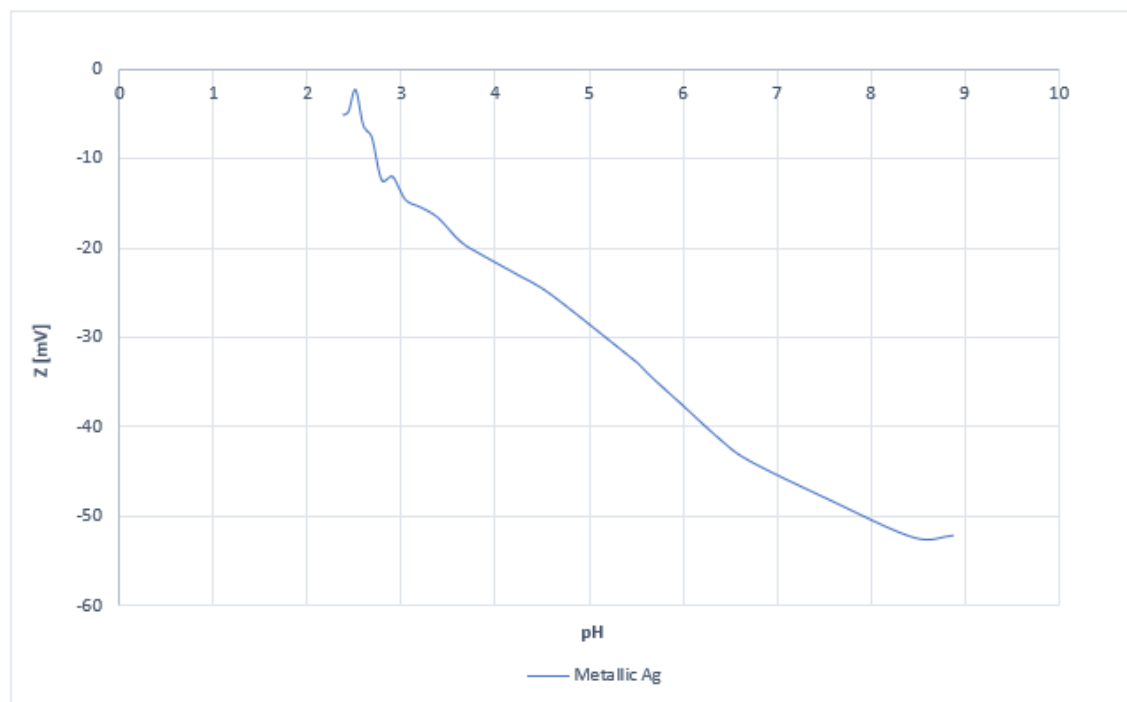
Figure 104. Zeta potential of the Metallic Ag foils

Figure 104 represents the zeta potential for the silver-only sample. It is possible to see, there it was not possible to determine the isoelectric point (it falls at too acidic values, probably close to 2.5), although the literature reports an IEP of 10.4 for silver films. (145) A possible explanation of the detected IP value for metallic Ag could be its oxidation before performing the zeta potential measurement.

3.3. **Biological tests**

3.3.1. *Bacterial test*

The test involves the marking of bacteria, *S. Aureus*, with fluorophores thus being able to distinguish between live and dead bacteria. Results obtained by infecting bare titanium control and EBW treated samples with S. aureus biofilm are reported in Figure 105.
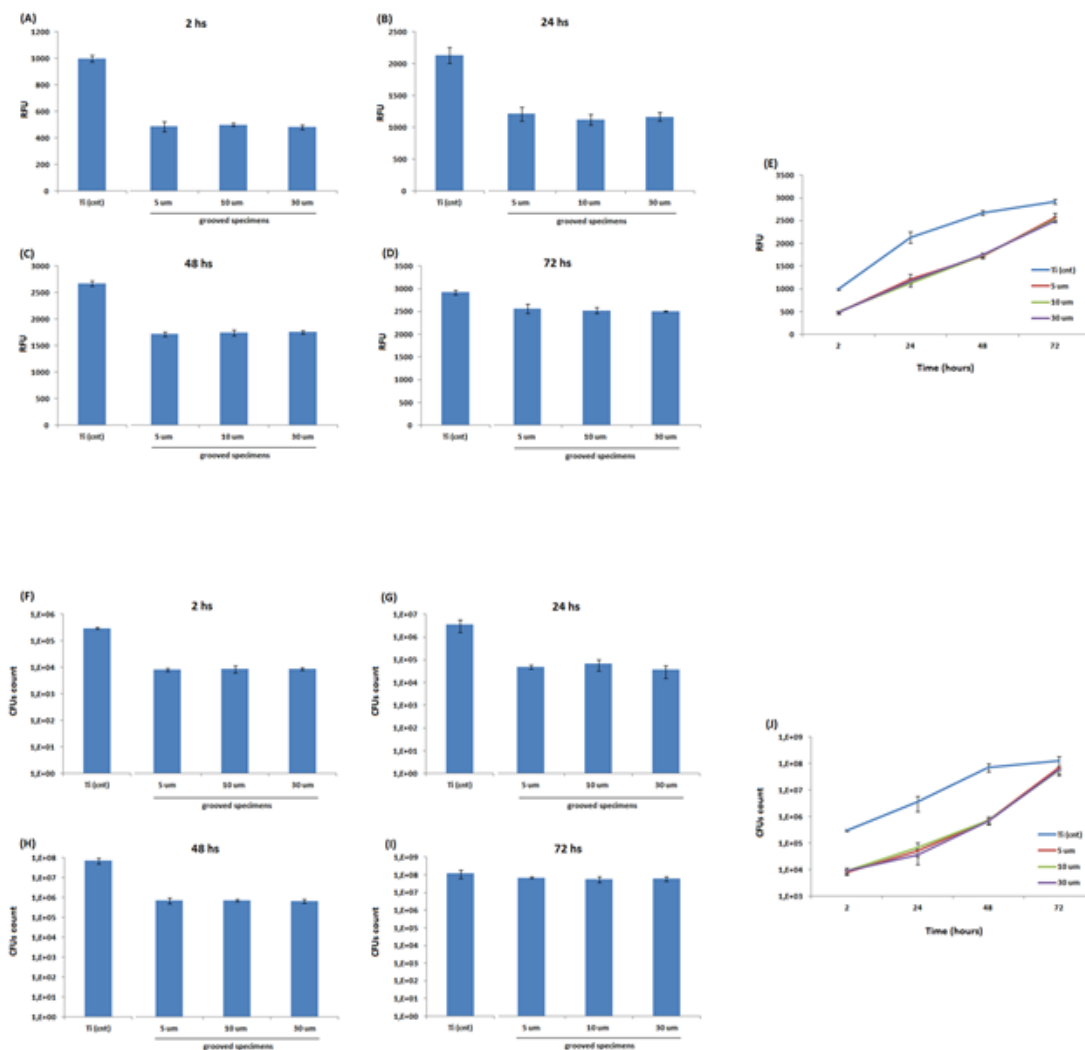
Figure 22. Antibacterial activity. Results are summarized in function of time in (E) and (J). Bars represent averages and standard deviations

The EBW treatment introduced anti-adhesive properties for bacteria to the samples surfaces up to 48h. In general, the EBW treatment introduced anti-adhesive properties to the treated samples surfaces that made difficult bacteria adhesion. In fact, after 2 hours infection the viable biomass was lower in grooved samples in comparison with untreated controls (A). Similar results were noticed at 24h (B), 48h (C) and 72h (D), where the

grooved samples result less contaminated, as summarized in (E). However, for all the samples bacteria growth was quite linear (E) thus leading to the supposition that the EBW were not effective in cause bacteria death but in decreasing the number of adherent bacteria. Consequently, the CFUs count was assayed at the same time-points achieved for the Alamar blue test. A possible explanation comes from attached colonies count: after 2h the number of adhered bacteria was about 2 logs reduced onto EBW grooved samples in comparison to the controls (F). Accordingly, similar results were achieved at 24h (G), 48h (H) and 72h (I), confirming bacteria difficulty to colonize treated surfaces. However, also CFUs count assay confirmed that the number of viable bacteria increased in function of time (J) thus confirming that the antibacterial properties introduced by the EBW treatment are actually related to the enhanced bacteria difficulty to adhere to the surface.

3.3.2. Cell test

Cells viability evaluation results are reported in Figure 106. Both direct (A) and indirect assay (B) did not reported any significant differences between the grooved samples and the control sample ($p > 0.05$) after 48 hours cultivation. Moreover, no statistically significant differences were noticed between data representative for different groove sizes ($p > 0.05$). Subsequently, it can be supposed that the surface modification made by EBW technique did not introduce any toxic compound.
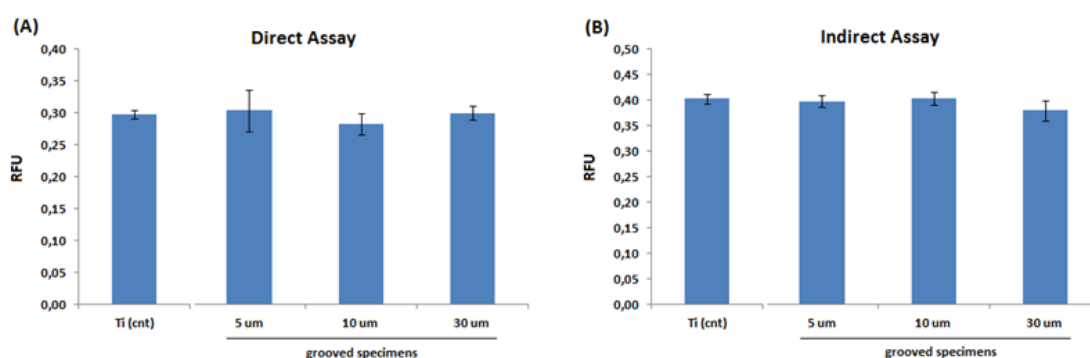

Figure 23. Cytocompatibility evaluation. Bars represent averages and standard deviations

It is observed how the different surface grooves size influence cells spread and cytoskeleton orientation during the 48 hours cultivation. In fact, as shown in Figure 107, cells seem to follow grooves orientation when groove size is of 10 μm (B): this observation looks particular evident by checking the staining of actin filaments (stained in red with phalloidin) and of vimentin (stained in green). On the opposite, only a moderate surface influence was noticed for 5 μm sized grooves where cells differed in terms of cytoskeleton orientation when random regions of samples were microscope investigated (A). Similarly, no surface influence was detected when cells were cultivated onto 30 μm sized grooves: cells cytoskeleton orientation was found to be randomly different onto different samples areas (C).
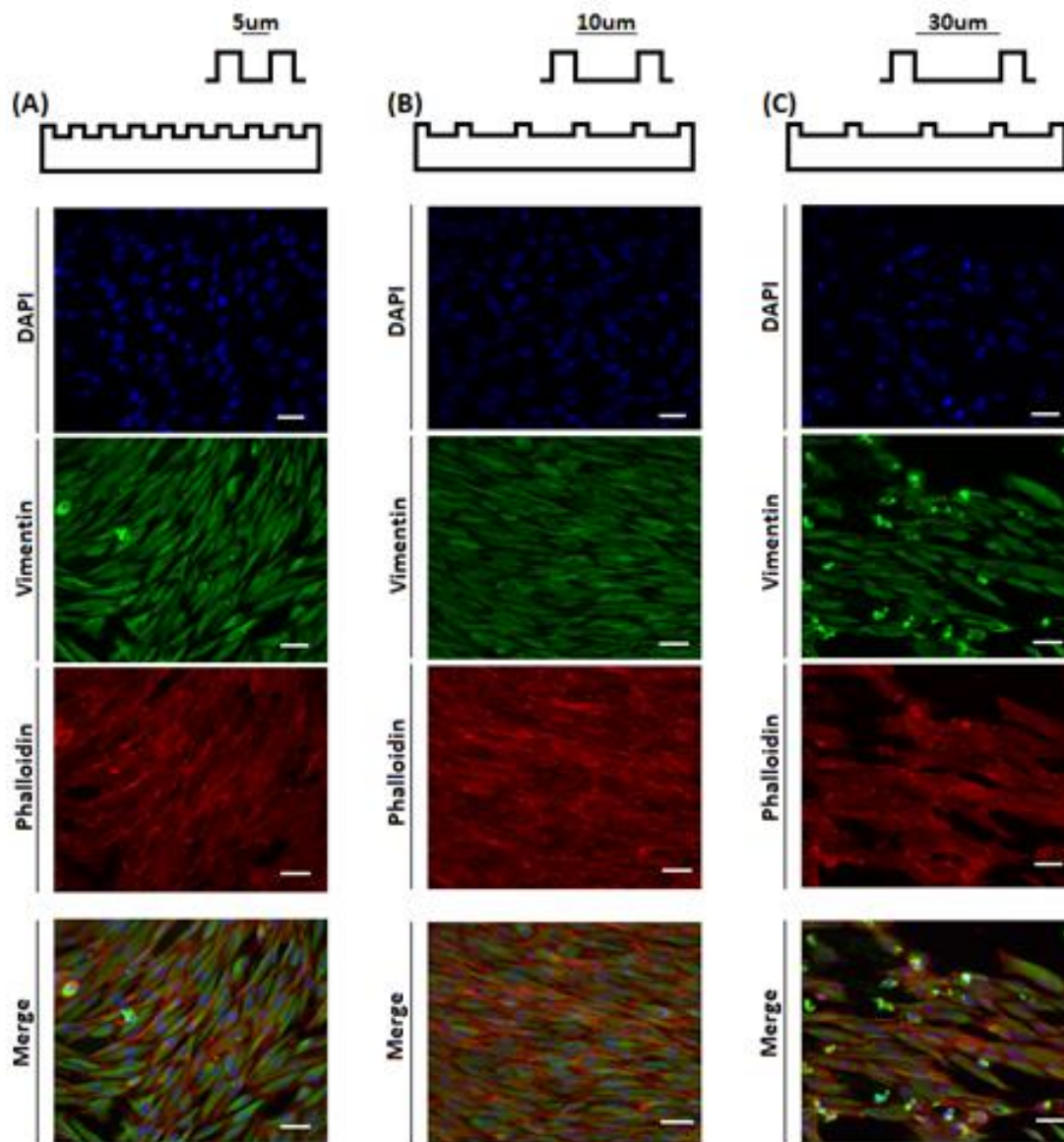

Figure 24. Surface grooves influence on cells cytoskeleton orientation. Bar scale= 50μm at magnification 20x

The extracellular matrix (ECM) deposition was investigated by means of collagen deposition. Results are reported in Figure 108 and revealed no conspicuous differences between different sized grooves samples. In fact, cells were able to correctly deposit collagen independently from the surface grooves size. Therefore, cells extracellular matrix (ECM) statement was not found to be related or influenced by the different size of samples' surface grooves. However, as prior showed by vimentin staining, also collagen confirmed that cells were influenced by the presence of 10 µm grooves as also the ECM was deposited following the substrate surface topography.
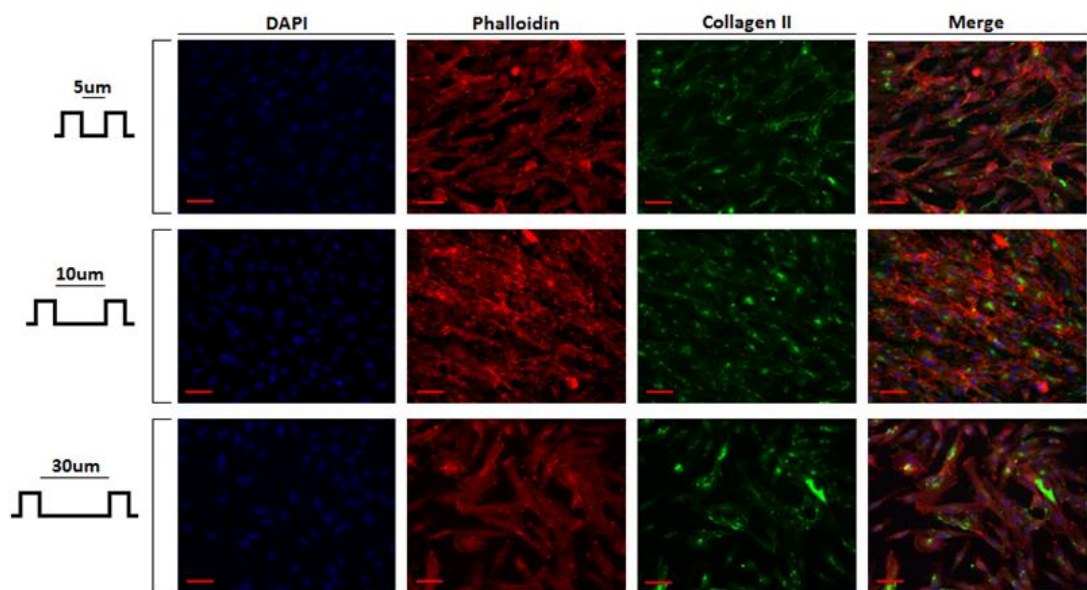

Figure 25. Cell matrix deposition onto grooved samples. Bar scale= 50µm at magnification of 20x

In general, HGFs were able to correct adhere and subsequently deposit collagen (stained in green) onto all different grooved samples.

The aim of this thesis work has been to carry out a superficial modification on the collars of titanium dental implants, which is optimal both in promoting cell adhesion and in preventing bacterial adhesion. To do this, we focused on four main aspects: the topography, the surface coating in keratin, the treatment of the titanium surface to stimulate the adhesion of the keratin coating and the enrichment with silver ions of this coating. Regarding topography, commercially pure titanium (grade 2) samples have been submitted to two types of treatment. The first consisted of making parallel grooves using Electron Beam Welding (a process in which a high-speed electron beam is bombarded on the material), at the Technical University of Graz. These samples were superficially characterized by analysis of ζ potential, and the cytocompatibility against human gingival fibroblasts (HGFs) and the antibacteriality against Staphylococcus Aureus bacteria were evaluated. The superficial topography, with the grooves, turns out to be able to influence the orientation of the cells. On the other hand, the second type of samples was subjected to a superficial mechanical modification at the Polytechnic of Turin: the samples were polished to a mirror (smooth) and on a part of them surface treatments were performed such as plasma activation with oxygen, in order to make the surface more reactive to the subsequently deposited nanofiber coating, while a second part has not been treated. Both types of surfaces were coated with keratin nanofibers, deposited by the electrospinnig technique. Some samples, only coated with nanofibers, underwent a post treatment with UV irradiation in order to "activate" the surface and make the keratin coating more adherent to the titanium substrate. The evaluation of the quality of the adhesion was made

by Tape Test, while the FT-IR and XPS analyzes of the samples used for the adhesion study did not show distinctive and significant results depending on the type of surface treatment applied to the surface in titanium. It can be concluded that this is due exclusively to the high thickness of the keratin coating obtained during the deposition phase. Instead, for the part of samples intended for antibacterial treatment, these were immersed in a solution of silver nitrate at various concentrations (low, intermediate and high) exploiting the ability of keratin to retain metal ions. The analyzes at FESEM have shown that keratin is deposited on titanium in the form of nanofibers with an arrengment in such a way as to form skeins. Unlike previous works, no sub-micrometric precipitates of silver were observed on all samples. In addition, silver percentages were found on the nanofibers, indicative of the fact that the antibacterial agent was retained by keratin, as was expected. The high resolution XPS analysis confirmed the presence on all samples of ionic silver, which in the case of higher concentration of silver directly binds to the sulfur of keratin. The results of the bacterial adhesion test on these samples showed that both the adhesion and the metabolism of the bacteria decrease with increasing silver concentration. The images at FESEM and the spectrophotometric ones show that the samples coated with keratin and enriched with silver at higher concentration have the best antibacterial behavior. In addition, the results of cellular tests show good cell adhesion, followed by spreading, on all samples, a sign that the silver has no cytotoxic effects. For the group of samples treated with Eectron Beam Welding technique, with grooves of three different sizes, 5µm, 10µm and 30 µm respectively, the wettability studies show a reduced hydrophilicity compared to the smooth titanium surface, regardless of the groove size. Biological tests on these samples revealed the anti-adhesive ability against bacteria, rather than a bactericidal ability. This capacity increases with increasing grooves size. As for cellular tests on these samples, the grooves encourage both cell adhesion and spreading, favoring the orientation of the adherent cells to the substratum and favoring the deposition of collagen by fibroblasts. In conclusion, it can be said that the grooves of 10µm and above 30µm could be a valid alternative to mechanical surface treatment. Additional future prospects could be those able to steer the keratin nanofibers parallel to the grooves, in an attempt to increase the cellular response.

BIBLIOGRAPHY

1. *Feughelman M 1997 Mechanical Properties and Structure of Alpha-Keratin Fibres: Wool Human Hair and Related Fibres.* University of New South Wales Press, Sydney;

2. Sun TT, Green H. *Keratin filaments of cultured human epidermal cells. Formation of intermolecular disulfide bonds during terminal differentiation*, J Biol Chem. 1978; 253:2053–2060;

3. Fraser R D B, MacRae T P, Rogers G E 1972 *Keratins, Their Composition Structure and Biosynthesis.* CC Thomas Publishing, Springfield, MA;

4. Bowden PE, Quinlan RA, Breitkreutz D, Fusenig NE. *Proteolytic modification of acidic and basic keratins during terminal differentiation of mouse and human epidermis*, Eur J Biochem. 1984; 142:29–36;

5. Marshall RC. Characterization of the proteins of human hair and nail by electrophoresis. J Invest Dermatol. 1983; 80:519–524;

6. Hanukoglu I, Fuchs E. The cDNA sequence of a Type II cytoskeletal keratin reveals constant and variable structural domains among keratins. Cell. 1983; 33:915–924;

7. H.H. Bragulla, D.G. Homberger, *Structure and functions of keratin proteins in simple, stratified, keratinized and cornified epithelia*, Journal of Anatomy 214 (2009), pp 516-559;

8. Buschow, K.H. Jürgen Cahn, Robert W. Flemings, Merton C. Ilschner, Bernhard Kramer, Edward J. Mahajan, Subhash, *Encyclopedia of Materials Science and Technology*, 2001, Volumes 1-11, pp 4363-4368. Elsevier;

9. *M. Feughelman, Mechanical Properties and Structure of Alpha-Keratin Fibres: Wool Human Hair and Related Fibres*, 1997, University of New South Wales Press, Sydney;

10. N. Eslahi, F. Dadashian, N. Hemmati Nejad, *AN INVESTIGATION ON KERATIN EXTRACTION FROM WOOL AND FEATHER WASTE BY ENZYMATIC HYDROLYSIS*, Volume 43, 2013, issue 7, Preparative Biochemistry and Biotechnology, pp 624-648;

11. P. Kakkar, B. Madhan, G. Shanmugam, *Extraction and characterization of keratin from bovine hoof: A potential material for biomedical applications*, Springerplus, 2014, pp 3:596;

12. http://www.cittastudi.org/flex/files/D.ab24f0d30c930be8056b/tesina_dotti.pdf;

13. N. Bhardwaj, S. C. Kundu, *Electrospinning: A fascinating fiber fabrication technique*, Volume 28, Issue 3, May–June 2010, pp 325–347;

14. Sutter, V. L. (1984). *Anaerobes as normal oral flora. Reviews of infectious diseases*. 6 Suppl 1: S62–S66. PMID 6372039;

15. https://it.wikipedia.org/wiki/Batteri_Gram-positivi;

16. Rogers A H (editor). (2008). *Molecular Oral Microbiology*. Caister Academic Press. ISBN 978-1-904455-24-0;

17. M. Sundaram, R. Legadevi, N. Afrin Banu, V. Gayathri, A. Palanisammy, *A Study on Anti-Bacterial Activity of Keratin Nanoparticles from Chicken Feather Waste Against Staphylococcus aureus (Bovine Mastitis Bacteria) and its Anti-Oxidant Activity.* European Journal of Biotechnology and Bioscience, Volume: 3, Issue: 6, 01-05June 2015;

18. https://www.google.com/patents/US6214576;

19. F.H.M. Mikx, M.H. De Jong, *Keratinolytic activity of cutaneous and oral bacteria*, Infection and Immunity 55 (1987), pp 621-625;

20. A. Riffel, A. Brandelli, Keratinolityc bacteria isolated from feather waste, Braz. J. Microbiol. Vol. 37, No. 3, July/Sept. 2006;

21. U. Samen, B.J. Eikmanns, D.J. Reinscheid, F. Borges, *The Surface Protein Srr-1 of Streptococcus agalactiae Binds Human Keratin 4 and Promotes Adherence to Epithelial HEp-2 Cells*, Infect Immun. 2007 Nov; 75(11): 5405–5414;

22. Batchelor, M., J. Guignot, A. Patel, N. Cummings, J. Cleary, S. Knutton, D. W. Holden, I. Connerton, and G. Frankel. 2004. Involvement of the intermediate filament protein cytokeratin-18 in actin pedestal formation during EPEC infection. EMBO Rep. 5:104–110;

23. *"Fibroblast"*. Genetics Home Reference. U.S. National Library of Medicine. 2014-05-05. Retrieved 2014-05-10;

24. https://www.ncbi.nlm.nih.gov/pubmed/9553764;

25. http://www.acrobiosystems.com/A481-CD71--TFRC--TFR-Molecule.html;

26. https://www.ncbi.nlm.nih.gov/gene/942;

27. https://www.ncbi.nlm.nih.gov/gene/4267;

28. *"The interrelationship between human gingival fibroblast differentiation and cultivating time"*, Tissue Engineering and Regenerative Medicine, April 2013, Volume 10, Issue 2, pp 60-64;

29. S. Wang, F. Taraballi, L. Poh, T.K. Woei, *Human keratin hydrogels support fibroblast attachment and proliferation in* vitro, Cell Tissue Res (2012) 347, pp 795–802;

30. R.V. Zackroff, *Isolation and Characterization of Keratin-like Proteins from Cultured Cells with Fibroblastic Morphology*, J Cell Biol. 1984 Apr;98(4), pp 1231-7;

31. A. Tachibana, Y. Furuta, H. Takeshima, T. Tanabe, K. Yamauchi, *Fabrication of wool keratin sponge scaffolds for long-term cell cultivation*, Journal of Biotechnology 93 (2002), pp 165–170;

32. http://www.chimicamo.org/tutto-chimica/proprieta-antimicrobiche-dellargento.html;

33. I. Sondi, B. S. Sondi, *Silver nanoparticles as antimicrobial agent: a case study on E. coli as a model for Gram-negative bacteria*, Journal of Colloid and Interface Science 275 (2004), pp 177–182;

34. J. S. Kim, E. Kuk, K. N. Yu, J. Kim, *Antimicrobial effects of silver nanoparticles*, Nanomedicine: Nanotechnology, Biology, and Medicine 3 (2007), pp 95– 101;

35. D. Yu, W. Tian, B. Sun, Y. Li, W. Wang, W. Tian, *Preparation of silver-plated wool fabric with antibacterial and anti-mould properties*, Materials Letters 151 (2015), pp 1-4;

36. L. Hadad, N. Perkas, Y. Gofer, A. Ghule, A. Gedanken, *Sonochemical Deposition of Silver Nanoparticles on Wool Fibers*, Wiley InterScience (2006);

37. Gedanken, A. Ultrason Sonochem 2004, 11, 47;

38. X. Lü, S. Cui, *Wool keratin-stabilized silver nanoparticles*, Bioresource Technology 101 (2010), pp 4703–4707;

39. www.medeco.de/it/odontostomatologia;

40. Mupparapu M, Beideman R. Imaging for maxillofacial reconstruction and implantology. In: Fonseca RJ, editor. Oral and maxillofacial surgery: reconstructive and implant surgery. Philadelphia: Saunders; 2000. p. 17e34;

41. PI Branemark, *Osseointegration and its experimental background*. J Prosthet Dent 1983; 50:399e410;

42. PI Branemark, R. Adell, U Breine, BO Hansson, J Lindstrom, A. Ohlsson, *Intraosseous anchorage of dental prostheses*. I. Experimental studies. Scand J PlastReconstr Surg 1969; 3:81e100;

43. A.D. Pye, D.E.A. Lockhart, M.P. Dawson, C.A. Murray, A.J. Smith, *A review of dental implants and infection*, Journal of Hospital Infection (2009) 72, 104e110;

44. F. Signoriello, Università di Padova, Fallschussel G.K.H., *Implantologia odontoiatrica: teoria e pratica*, Edinava, 1989;

45. http://www.treccani.it/enciclopedia/implantologia_(Dizionario-di-Medicina);

46. http://www.ing.unitn.it/~colombo/Materiali%20per%20l'implantologia%20dentale/9.%20L'implantologia%20dentale.htm;

47. F. Truffa Giachet, Politecnico di Torino, MODIFICHE MICROTOPOGRAFICHE E DEPOSIZIONE DI NANOFIBRE DI CHERATINA PER OTTIMIZZARE LE INTERAZIONI DEL TITANIO CON I TESSUTI MOLLI, 2014;

48. http://traveltodentist.com/it/servizi/implantologia-dentale/impianti-a-carico-immediato-o-impianti-a-carico-differito/;

49. http://www.osstell.com/$-1/file/25045-00-it-isq-whitebook-lr.pdf;

50. Demetrescu I., Pirvu C., Mitran V., *Effect of nano-topographical features of Ti/Tio2electrode surface on cell response and electrochemical stability in artificial saliva.* Bioelectrochemistry 79 (2010): 122 – 129;

51. M. Yoshinari, K. Matsuzaka, T. Inoue, Y. Oda, M. Shimono, *Effects of multigrooved surfaces on fibroblast behaviour.* Biomed Mater Res 65A, 359-368, 2003;

52. Franco Bengazi, Jan L. Wennströme Ulf Lekhom, *Recession of the soft tissue margin at oral implants.* Clin Oral Imple Res 1996: 7: 303-310;

53. http://www.treccani.it/enciclopedia/periodonto/;

54. *Redesigning Macrostructure of Dental Implant for Better Initial Stability & Reduction of Tissue Recession*, 6/22/2011;

55. C. Bruckmann, X. F. Walboomers, K. Matsuzaka, J. A. Jansen, *Periodontal ligament and gingival fibroblast adhesion to dentin-like textured surfaces*, Biomaterials 26 (2005), 339-346;

56. Tesi cerone;

57. Buser D, Merickse-Stern R. Long term evaluation of nonsubmerged ITI implants. Part 1: 8-year life table analysis of a prospective multicenter study with 2359 implants. Clin Oral Implant Res. 1997; 8:161–72;

58. Kolenbrander PE, Anderson RN, Blehart DS. Communications among oral bacteria. Microbiol Mol Bio Rev. 2002; 66:486–05;

59. Hojo K, Nagaoka S, Oshima T. Bacterial interactions in dental biofilm development. J Dent Res. 2009; 88: 982–90;

60. Bassler BL, Wright M, Silverman MR. Multiple signaling systems controlling expressions of luminescence in Vibrio harveyii: Sequence and function of genes encoding a secondary sensory pathway. Mol Microbio. 1994; 13:273–86;

61. Mombelli A. *Prevention and therapy of peri-implant infections*. In: Lang NP, Karring T, Lindhe J, editors. *Proceedings of the 3rd European Workshop on Periodontology: implant dentistry*. Berlin: Quintessence; 1999. p. 281e303;

62. A.G. Gristina*, Biomaterial-centered infection: microbial adhesion versus tissue integration*. Science 1987;237: 1588;

63. S. Manoj, D. K. Prasad, U.N. Sangeetha, C. Hedge, *Platform Switching: A New Era in Implant Dentistry*, Int J of Oral Implantology and Clinical Reasearch, May-August 2010; 1(2): 61-65;

64. https://en.wikipedia.org/wiki/Platform_switching;

65. R. Vijayalakshmi, T. Ramakrishnan, *Platform switch dental implants – Search for evidence: An overview*. SRM J Res Dent Sci 2016; 7:101-5;

66. R.J. Lazzara, S.S. Porter, *Platform switching: A new concept in implant dentistry for controlling postrestorative crestal bone levels*, Int J Periodontics Restorative Dent 2006; 26:9-17;

67. B. Wagenberg, S.J. Froum, *Propspective study of 94 platform-switched implants observed from 1992 to 2006*, Int J Priodontics Restorative Dent 2010; 30: 9-17;

68. X. Rodriguez-Ciurana, X. Vela-Nebot, M. Segala-Torres, *The effect of interimplant distance on the heigh of the interimplant bone crest when using platform-switcheed implants.* Int J Periodontics Restorative Dent 2009; 29:141-151;

69. *Yu, A short term clinical study of marginal bone level change around microthreaded and platform-switched implants*, J Periodontal Implant Sci. 2011 October; 41(5): 211-217;

70. C. Mangano, F. Mangano, J.A. Shibli, L. Tettamanti, M. Figliuzzi, S. d'Avila, R.L. Sammons, A. Piattelli, *Prospective Evaluation of 2,549 Morse Taper Connection Implants: 1- to 6-Year Data*, J Periodontol • January 2011;

71. Tesmer M, Wallet S, Koutouzis T, Lundgren T. *Bacterial colonizationof the dental implant fixture–abutment interface: An in vitro study.* J Periodontol 2009; 80:1991–1997;

72. Merz BR, Hunenbart S, Belser UC. Mechanics of the implant–abutment connection: An 8-degree taper compared to a butt joint connection. Int J Oral Maxillofac Implants 2000; 15:519–526;

73. C.M. Schmitt, G. Nogueira-Filho, H.C. Tenenbaum, J.Y. Lai, C. Brito, H. Doring, J. Nonhoff, *Performance of conical abutment (Morse Taper) connection implants: A systematic review*, 2013;

74. D. LAURITANO, C.A. BIGNOZZI, D. PAZZI, F. CURA, F. CARINCI, Efficacy of a new coating of implant-abutment connections in reducing bacterial loading: an *in vitro* study;

75. Yeo IS, Min S, Yang JH. An Influence of bioactive material coating of Ti dental implant surfaces on early healing and osseointegration of bone. J Kor Phys Soc. 2010;57: 1717–20;

76. H.I. Nassar, M.F. Abdalla, Bacterial leakage of different internal implant/abutment connection, future dental Journal I (2015) I-5;

77. Harder S, Dimaczek B, Acil Y, Terheyden H, Freitag-Wolf S, Kern M. Molecular leakage at implant-abutment connectionein vitro investigation of tightness of internal conical implant-abutment connections against endotoxin penetration. Clin Oral Investig 2010;14(4):427e32;

78. Cosyn J, Van Aelst L, Collaert B, Persson GR, De Bruyn H. The peri-implant sulcus compared with internal implant and suprastructure components: a microbiological analysis. Clin Implant Dent Relat Res 2011;13(4):286-95;

79. Steinebrunner L, Wolfart S, Bossmann K, Kern M. In vitro evaluation of bacterial leakage along the implant-abutment interface of different implant systems. Int J Oral Maxillofac Implants 2005;20(6):875-81;

80. Hazel Assender, Valery Bliznyuk, Kyriakos Porfyrakis, How Surface Topography Relates to Materials' Properties, Science 297, 973 (2002);

81. A. Curtis, C. Wilkinson, Biomaterials 18, 1573 (1997);

82. Hazel Assender, Valery Bliznyuk, Kyriakos Porfyrakis, How Surface Topography Relates to Materials' Properties, Science 297, 973 (2002);

83. Albrektsson et al. 1981) (Albrektsson, T., Branemark, P.I., Hansson, H.A. & Lindstom, J. (1981) Osseointegrated titanium implants. Acta Orthopaedica Scandinavica 52:155–170;

84. Stout, K.J., Davis, E.J.& Sullivan, P.J. (1990) Atlas of Machined Surfaces. Chapman and Hall: London;

85. Albrektsson, T. & Wennerberg, A. (2004) Oral implant surfaces: part 1 – review focusing on topographic and chemical properties of different surfaces and in vivo responses to them. International Journal of Prosthodontics 17: 536–543;

86. Albrektsson T, Wennerberg A. (2004) Oral implant surfaces: part 2 – review focusing on clinical knowledge of different surfaces. Int J Prosthodont 2004; 17:544–64;

87. Cochran DL. A comparison of endosseous dental implant surfaces. J Periodontol 1999; 70:1523–39;

88. Gustavo Mendonça, Daniela B.S. Mendonça, Francisco J.L. Aragaˇo, Lyndon F. Cooper, Advancing dental implant surface technology – From micron to nano topography, Biomaterials 29 (2008) 3822–3835;

89. J. Chen, R.A. Bly, M.M. Saad, M.A. AlKhodary, R.M. El-Backly, D.J. Cohen, N. Kattamis, M.M. Fatta, W.A. Moore, C.B. Arnold, M.K. Marei, W.O. Soboyejo, In-vivo study of adhesion and bone growth around implanted laser groove/RGD-functionalized Ti-6Al-4V pins in rabbit femurs Materials Science and Engineering C 31 (2011) 826–832;

90. Rickard Brånemark, MSc, PhD, MDa, Lena Emanuelsson, BSb, Anders Palmquist, MSc, PhDb, ∗, Peter Thomsen, PhD, MDb, Bone response to laser-induced micro- and nano-size titanium surface features, Nanomedicine: Nanotechnology, Biology, and Medicine 7 (2011) 220–227;

91. Milan Trtica, Biljana Gakovic b, Dimitri Batani c, Tara Desai c, Peter Panjan d, Bojan Radak, Surface modifications of a titanium implant by a picosecond Nd: YAG laser operating at 1064 and 532 nm, Applied Surface Science 253 (2006) 2551–2556;

92. P. Kwasniak, et al., Laser and chemical surface modifications of titanium grade 2 for medical application, Appl. Surf. Sci. (2014);

93. C. Bertrand, Y. le Petitcorps, L. Albingre, V. Dupuis, Optimization of operator and physical parameters for laser welding of dental materials, BRITISH DENTAL JOURNAL VOLUME 196 NO. 7 APRIL 10, 2004;

94. P. Kwasniak, et al., Laser and chemical surface modifications of titanium grade 2 for medical application, Appl. Surf. Sci. (2014);

95. Mohamed Ahmed Alkhodary, Laser micro-grooved, Arginine-Glycine-Apspartic acid (RGD) coated dental implants, a 5 years radiographic follow-up, International Journal of Health Sciences, Qassim University, Vol. 8, No. 4 (Oct-Dec 2014);

96. S. Kalpakjian, S. R. Schmid, Manufacturing Engineering and Technology, 6ªed., Pearson Prentice Hall, 2010, p.777;

97. https://en.wikipedia.org/wiki/Electron-beam_technology;

98. C. Ramskogler, S. Mostofi, F. Warchomicka, A. Weinberg, C. Sommitsch, Surface structuring by electron beam technique in titanium grade 2 and Ti6Al4V for biomedical application, TMS-The Minerals, Metals & Materials Society, 2016;

99. http://www.techbriefs.com/component/content/article/9998?start=2&Itemid=690;

100. Anselme K., Davidson P., Popa A. M., Giazzon M., Liley M., Ploux L., The interaction of cells and bacteria with surfaces structured at the nanometre scale. Acta Biomaterialia 6 (2010): 3824 – 3846;

101. Katrina J. Edwards a, Andrew D. Rutenberg Microbial response to surface microtopography: the role of metabolism in localized mineral dissolution, Chemical Geology 180 2001 19–32;

102. Vi Khanh Truong, Vy T. H. Pham, Alexander Medvedev, Rimma Lapovok, Yuri Estrin, Terry C. Lowe, Vladimir Baulin, Veselin Boshkovikj, Christopher J. Fluke, Russell J. Crawford, Elena P. Ivanova, Self-organised nanoarchitecture of titanium surfaces influences the attachment of Staphylococcus aureus and Pseudomonas aeruginosa bacteria Appl Microbiol Biotechnol DOI 10.1007/s00253-015-6572-7;

103. S.D. Puckett, E. Taylor, T. Raimondo, T.J. Webster, The relationship between the nanostructure of titanium surfaces and bacterial attachment, Biomaterials 31 (2010): 706-713;

104. Fu G, Vary PS, Lin CT, Anatase TiO2 nanocomposites for antimicrobial coatings, Phys Chem 2005 May 12;109(18):8889-98;

105. Vi K. Truong, Rimma Lapovok, Yuri S. Estrin, Stuart Rundell b, James Y. Wang e, Christopher J. Fluke f, Russell J. Crawford, Elena P. Ivanova, The influence of nano-scale surface roughness on bacterial adhesion to ultrafine-grained titanium, Biomaterials 31 (2010) 3674–3683;

106. Scheuerman TR, Camper AK, Hamilton MA. Effects of substratum topography on bacterial adhesion. J Colloid Interface Sci 1998; 208:23–33;

107. Harris LG, Richards RG, Staphylococcus aureus adhesion to different treated titanium surfaces. J Mater Sci Mater Med 2004; 15:311–4;

108. Zamir E, Katz M, Posen Y, Erez N, Yamada KM, Katz BZ, Lin S, Lin DC, Bershdsky A, Kam Z, Dynamics and segregation of cell-matrix adhesons in cultured fibroblasts. Nat Cell Biol. 2:191-196;

109. John C. Grew, John L. Ricci, Harold Alexander, Connective-tissue responses to defined biomaterial surfaces. II. Behavior of rat and mouse fibroblasts cultured on microgrooved substrates. Journal of Biomedical Materials Research Part A;

110. A.M. Andersson, P. Olsson, U. Lidberg, D. Sutherland, The effects of continuous and discontinuous groove edges on cell shape and alignment, Exp. Cell Res. 288 (2003) 177–188;

111. Teixeira A. I., Nealey P. F., Murphy C. J., Responses of human keratocytes to micro- and nanostructured substrates. J Biomed Mater Res 2004; 71;

112. Hamilton D. W., Brunette D. M., "Gap guidance" of fibroblast and epithelial cells by discontinuous edged surfaces. Experimentale Cell Research 309 (2005): 429-437;

113. Su-Yeon Kim, Namsik Oh, Myung-Hyun Lee, Sung-Eun Kim, Richard Leesungbok, Suk- Won Lee, Surface microgrooves and acid etching on titanium substrata alter various cell behaviors of cultured human gingival fibroblasts. Clin. Oral Impl. Res. 20, 2009; 262-272;

114. M. Nevins, M. Camelo, Connective Tissue Attachment to Laser-Microgrooved Abutments: A Human Histologic Case Report, Volume 32, Issue 4 2012, 385-392;

115. Marco Wieland,1,2 Babak Chehroudi, Marcus Textor, Donald M. Brunette, Use of Ti-coated replicas to investigate the effects on fibroblast shape of surfaces with varying roughness and constant chemical composition, 2002 Wiley Periodicals, Inc.;

116. G. E. Pecora, DDS, MD, R. Ceccarelli, DDS, M. Bonelli, H. Alexander, J. L. Ricci, Clinical Evaluation of Laser Microtexturing for Soft Tissue and Bone Attachment to Dental Implants, IMPLANT DENTISTRY / VOLUME 18, NUMBER 1 2009;

117. John C. Grew, John L. Ricci, Harold Alexander, Connective-tissue responses to defined biomaterial surfaces. II. Behavior of rat and mouse fibroblasts cultured on microgrooved substrates, 2007 Wiley Periodicals, Inc.;

118. https://en.wikipedia.org/wiki/Plasma_activation;

119. https://it.scribd.com/doc/312685009/titanio-ti-6al-4v;

120. http://www.tecnotex.it/documenti/Pure-Health_brochure.pdf;

121. Jiang Chen, Ping Yang, Yuzhen Liao, Jinbiao Wang, Huiqing, *Effect of the Duration of UV Irradiation on the Anticoagulant Properties of Titanium Dioxide Films*, ACS Appl. Mater. Interfaces 2015, 7, 4423−4432;

122. Fuminori Iwasa, Norio Hori, Takeshi Ueno, Hajime Minamikawa, Masahiro Yamada, Takahiro Ogawa, *Enhancement of osteoblast adhesion to UV-photofunctionalized titanium via an electrostatic mechanism*, Biomaterials 31 (2010) 2717–2727;

123. N. Bhardwaj, S. C. Kundu, *Electrospinning: A fascinating fiber fabrication technique*, Volume 28, Issue 3, May–June 2010, pp 325–347;

124. Biella;

125. http://www.charfac.umn.edu/instruments/eds_on_sem_primer.pdf;

126. https://en.wikipedia.org/wiki/X-ray_photoelectron_spectroscopy;

127. http://www.casaxps.com/help_manual/manual_updates/xps_spectra.pdf;

128. http://biomateriali.files.wordpress.com/2012/12/ftir.pdf;

129. https://en.wikipedia.org/wiki/Wetting;

130. Nygard et al., 2002; Bohme et al., 2001;

131. Jendrik Hardesa, Helmut Ahrensa, *Carsten Geberta Lack of toxicological side effects in silver-coated megaprostheses in humans Biomaterials 28 (2007)* 2869–2875;

132. https://webspectra.chem.ucla.edu/irtable.html;

133. A. Aluigi, A. corbellini, F. Rombaldoni, M. Zoccola, M. Canetti, Morphological and structural investigation of wool derived keratin nanofibres crosslinked by thermal treatment, International Journal of Biological Macromolecules 57 (2013) 30-37;

134. Zhang X., Ferraris S., Prenesti E., Vernè E., *Surface functionalization of bioactive glasses with natural molecules of biological significance, Part I: Gallic acid as model molecule.* Applied Surface Science 287 (2013) 329 – 340;

135. Patil K., Smith S. V., Rajkhowa R., Tsuzuki T., Wang X., Lin T*., Milled cashmere guard hair powders: Absorption properties to heavy metal ions*. Powder Technology 218 (2012) 162 – 168;

136. http://www.xpsfitting.com;

137. Michael J. Richardson, James H. Johnston Sorption and binding of nanocrystalline gold by Merino wool fibres—An XPS study, Journal of Colloid and Interface Science 310 (2007) 425–430;

138. R. Molina, J.P. Espino′s, F. Yubero, P. Erra, A.R. Gonza′lez-Elipe, XPS analysis of down-stream plasma treated wool: Influence of the nature of the gas on the surface modification of wool, Applied Surface Science 252 (2005) 1417–1429;

139. Aggingere xps O;

140. Kiran Patil, Suzanne V. Smith, Rangam Rajkhowa, Takuya Tsuzuki, Xungai Wang, Tong Lin, Milled cashmere guard hair powders: Absorption properties to heavy metal ions, Powder Technology 218 (2012) 162–168;

141. Xiangqin Zou, Haifeng Bao, Hongwei Guo, Lei Zhang, Li Qi, Junguang Jiang, Li Niu, Shaojun Dong, Mercaptoethane sulfonate protected, water-soluble gold and silver nanoparticles: Syntheses, characterization and their building multilayer films with polyaniline via ion–dipole interactions, Journal of Colloid and Interface Science 295 (2006) 401–408;

142. A. Aluigi, A. corbellini, F. Rombaldoni, M. Zoccola, M. Canetti, Morphological and structural investigation of wool derived keratin nanofibres crosslinked by thermal treatment, International Journal of Biological Macromolecules 57 (2013) 30-37;

143. A. Aluigi, C. Tonetti, C. Vineis, C. Tonin, G. Mazzuchetti, Adsorption of copper (II) ions by keratin/PA6 blend nanofibers, Eur. Polym. J., 2011, 47, 1756–1764;

144. AM Ferraria, AP Carapeto, AM Botelho do Rego, X-ray photoelecton spectroscopy: silver salts revisited, Vacuum 86(2012) 1988-1991;

145. L-K. Chau, M.D. Porter, *Surface isoelectric point of evaporated silver films: Determination by contact angle titration*, Journal of Colloid and Interface Science 145, 1 (1991): 283 – 286;

IMAGES

F1 *Muhammad A Khosa and Aman, A Sustainable Role of Keratin Biopolymer in Green Chemistry: A Review, Journal of Food Processing & Beverages, ISSN: 2332-4104;*

F2 *http://jpkc.qdu.edu.cn/fzclx/english%20course/pic/36.JPG;*

F3 S. Wang, F. Taraballi, L. Poh, T.K. Woei, *Human keratin hydrogels support fibroblast attachment and proliferation in* vitro, Cell Tissue Res (2012) 347, pp 795–802;

F4 S. Wang, F. Taraballi, L. Poh, T.K. Woei, *Human keratin hydrogels support fibroblast attachment and proliferation in* vitro, Cell Tissue Res (2012) 347, pp 795–802;

F5 Tachibana, Y. Furuta, H. Takeshima, T. Tanabe, K. Yamauchi*, Fabrication of wool keratin sponge scaffolds for long-term cell cultivation*, Journal of Biotechnology 93 (2002), pp 165–170;

F6 Tachibana, Y. Furuta, H. Takeshima, T. Tanabe, K. Yamauchi*, Fabrication of wool keratin sponge scaffolds for long-term cell cultivation*, Journal of Biotechnology 93 (2002), pp 165–170;

F7 Sondi, B. S. Sondi, *Silver nanoparticles as antimicrobial agent: a case study on E. coli as a model for Gram-negative bacteria*, Journal of Colloid and Interface Science 275 (2004), pp 177–182;

F8 L. Hadad, N. Perkas, Y. Gofer, A. Ghule, A. Gedanken*, Sonochemical Deposition of Silver Nanoparticles on Wool Fibers*, Wiley InterScience (2006);

F9 http://www.easynotecards.com/uploads/365/29/593ab409_13673075871__8000_00000014.jpg;

F10 http://philschatz.com/anatomy-book/resources/2409_Tooth.jpg;

F11 https://pocketdentistry.com/wp-content/uploads/285/QE01_chapple_fig002a.jpg;

F12 http://ars.els-cdn.com/content/image/1-s2.0-S0002817714639635-gr1.jpg;

F13 http://www.dentalimplantskerala.com/wp-content/uploads/2011/08/implants-types.jpg;

F14 http://www.consumersdigest.com/images/made/images/uploads/article/Dental_Implants_chart_3 20_230_s_c1_c_t_0_0.jpg;

F15 http://1.bp.blogspot.com/CSfvIrcHH9g/TiRgG66T3pI/AAAAAAAAAnc/e343_Yz5l6U/s1600/i mplant+parts.jpg;

F16 https://titaniumprocessingcenter.com/wp-content/uploads/2015/08/grades_ti_datasheet.png;

F17 http://www.trendsperioimplantresourcecenter.com/sites/default/files/3d7e70517504420e83534a5 70d616991-71.jpg;

F18 http://blog.medicalcanada.es/wp-content/uploads/2015/06/blog4.jpg;

F19 C. Mangano, F. Mangano, J.A. Shibli, L. Tettamanti, M. Figliuzzi, S. d'Avila, R.L. Sammons, A. Piattelli, *Prospective Evaluation of 2,549 Morse Taper Connection Implants: 1- to 6-Year Data*, J Periodontol, January 2011;

F20 D. LAURITANO, C.A. BIGNOZZI, D. PAZZI, F. CURA, F. CARINCI, Efficacy of a new coating of implant-abutment connections in reducing bacterial loading: an *in vitro* study;

F21 H.I. Nassar, M.F. Abdalla, Bacterial leakage of different internal implant/abutment connection, future dental Journal I (2015) I-5;

F22 Gustavo Mendonça, Daniela B.S. Mendonça, Francisco J.L. Aragão, Lyndon F. Cooper, Advancing dental implant surface technology – From micron to nano topography, Biomaterials 29 (2008) 3822–3835;

F23 C. Bertrand, Y. le Petitcorps, L. Albingre, V. Dupuis, Optimization of operator and physical parameters for laser welding of dental materials, BRITISH DENTAL JOURNAL VOLUME 196 NO. 7 APRIL 10, 2004;

F24 P. Kwasniak, et al., Laser and chemical surface modifications of titanium grade 2 for medical application, Appl. Surf. Sci. (2014);

F25 P. Kwasniak, et al., Laser and chemical surface modifications of titanium grade 2 for medical application, Appl. Surf. Sci. (2014);

F26 Mohamed Ahmed Alkhodary, Laser micro-grooved, Arginine-Glycine-Apspartic acid (RGD) coated dental implants, a 5 years radiographic follow-up, International Journal of Health Sciences, Qassim University, Vol. 8, No. 4 (Oct-Dec 2014);

F27 Mohamed Ahmed Alkhodary, Laser micro-grooved, Arginine-Glycine-Apspartic acid (RGD) coated dental implants, a 5 years radiographic follow-up, International Journal of Health Sciences, Qassim University, Vol. 8, No. 4 (Oct-Dec 2014);

F28 J. Chen, R.A. Bly, M.M. Saad, M.A. AlKhodary, R.M. El-Backly, D.J. Cohen, N. Kattamis, M.M. Fatta, W.A. Moore, C.B. Arnold, M.K. Marei, W.O. Soboyejo, In-vivo study of adhesion and bone growth around implanted laser groove/RGD-functionalized Ti-6Al-4V pins in rabbit femurs Materials Science and Engineering C 31 (2011) 826–832;

F29 https://ebteccorp.com/app/uploads/2016/05/how_ebweld-1.jpg;

F30 C. Ramskogler, S. Mostofi, F. Warchomicka, A. Weinberg, C. Sommitsch, Surface structuring by electron beam technique in titanium grade 2 and Ti6Al4V for biomedical application, TMS-The Minerals, Metals & Materials Society, 2016;

F31 C. Ramskogler, S. Mostofi, F. Warchomicka, A. Weinberg, C. Sommitsch, Surface structuring by electron beam technique in titanium grade 2 and Ti6Al4V for biomedical application, TMS-The Minerals, Metals & Materials Society, 2016;

F32 C. Ramskogler, S. Mostofi, F. Warchomicka, A. Weinberg, C. Sommitsch, Surface structuring by electron beam technique in titanium grade 2 and Ti6Al4V for biomedical application, TMS-The Minerals, Metals & Materials Society, 2016;

F33 Vi Khanh Truong, Vy T. H. Pham, Alexander Medvedev, Rimma Lapovok, Yuri Estrin, Terry C. Lowe, Vladimir Baulin, Veselin Boshkovikj, Christopher J. Fluke, Russell J. Crawford, Elena P. Ivanova, Self-organised nanoarchitecture of titanium surfaces influences the attachment of Staphylococcus aureus and Pseudomonas aeruginosa bacteria Appl Microbiol Biotechnol DOI 10.1007/s00253-015-6572-7;

F34 S.D. Puckett, E. Taylor, T. Raimondo, T.J. Webster, The relationship between the nanostructure of titanium surfaces and bacterial attachment, Biomaterials 31 (2010): 706-713;

F35 Vi K. Truong, Rimma Lapovok, Yuri S. Estrin, Stuart Rundell b, James Y. Wang e, Christopher J. Fluke f, Russell J. Crawford, Elena P. Ivanova, The influence of nano-scale surface roughness on bacterial adhesion to ultrafine-grained titanium, Biomaterials 31 (2010) 3674–3683;

F36 Vi K. Truong, Rimma Lapovok, Yuri S. Estrin, Stuart Rundell b, James Y. Wang e, Christopher J. Fluke f, Russell J. Crawford, Elena P. Ivanova, The influence of nano-scale surface roughness on bacterial adhesion to ultrafine-grained titanium, Biomaterials 31 (2010) 3674–3683;

F37 Harris LG, Richards RG, Staphylococcus aureus adhesion to different treated titanium surfaces. J Mater Sci Mater Med 2004; 15:311–4;

F38 Fujita S, Ohshima M, Iwata H. Time-lapse observation of cell alignment on nanogrooved patterns. J R Soc Interface 2009; 6: S269–77;

F39 Teixeira A. I., Nealey P. F., Murphy C. J., Responses of human keratocytes to micro- and nanostructured substrates. J Biomed Mater Res 2004; 71;

F40 Marco Wieland,1,2 Babak Chehroudi,1 Marcus Textor,2 Donald M. Brunette1 Use of Ti-coated replicas to investigate the effects on fibroblast shape of surfaces with varying roughness and constant chemical composition, 2002 Wiley Periodicals, Inc.;

F41 G. E. Pecora, DDS, MD, R. Ceccarelli, DDS, M. Bonelli, H. Alexander, PhD, and J. L. Ricci, PhD, Clinical Evaluation of Laser Microtexturing for Soft Tissue and Bone Attachment to Dental Implants, IMPLANT DENTISTRY / VOLUME 18, NUMBER 1 2009;

F42 John C. Grew, John L. Ricci, Harold Alexander, Connective-tissue responses to defined biomaterial surfaces. II. Behavior of rat and mouse fibroblasts cultured on microgrooved substrates, 2007 Wiley Periodicals, Inc.;

F43 John C. Grew, John L. Ricci, Harold Alexander, Connective-tissue responses to defined biomaterial surfaces. II. Behavior of rat and mouse fibroblasts cultured on microgrooved substrates, 2007 Wiley Periodicals, Inc.;

F44 https://commons.wikimedia.org/w/index.php?curid=19474487;

F45 https://commons.wikimedia.org/w/index.php?curid=5521755;

F46 https://encrypted-tbn0.gstatic.com/images?q=tbn:ANd9GcQPTFRB7LHrv4Q_-artb9j8foZo_VWtimldSAfVEXjAknkD-K0j;

F47 http://www.charfac.umn.edu/instruments/eds_on_sem_primer.pdf;

F48 https://commons.wikimedia.org/wiki/File:XPS_PHYSICS.png#/media/File:XPS_PHYSICS.png;

F49 http://www.machinerylubrication.com/Read/30205/ftir-oil-analysis;

F50 http://lotusrock.com/wp-content/uploads/2015/05/Classification-of-Cross-Cut-Adhesion-Test-Results.jpg;

F51 https://ndtesting.ru/wa-data/public/shop/products/23/44/4423/images/2047/2047.970.jpg;

F52 http://www.ramehart.com/contactangle.htm;

F53 http://wiki.anton-paar.com/wp-content/uploads/electric-double-layer.jpg;

F54 Nygard et al., 2002; Bohme et al., 2001;

Tables

T1 *Microbiologia Orale*, Dispense di Microbiologia, Università di Genova;

T2 M. Sundaram, R. Legadevi, N. Afrin Banu, V. Gayathri, A. Palanisammy, *A Study on Anti-Bacterial Activity of Keratin Nanoparticles from Chicken Feather Waste Against Staphylococcus aureus (Bovine Mastitis Bacteria) and its Anti-Oxidant Activity.* European Journal of Biotechnology and Bioscience, Volume: 3, Issue: 6, 01-05June 2015;

T3 F.H.M. Mikx, M.H. De Jong, *Keratinolytic activity of cutaneous and oral bacteria*, Infection and Immunity 55 (1987), pp 621-625;

T4 F. Truffa Giachet, Politecnico di Torino, MODIFICHE MICROTOPOGRAFICHE E DEPOSIZIONE DI NANOFIBRE DI CHERATINA PER OTTIMIZZARE LE INTERAZIONI DEL TITANIO CON I TESSUTI MOLLI, 2014;

T5 A.G. Gristina*, Biomaterial-centered infection: microbial adhesion versus tissue integration.* Science 1987;237: 1588;

T6 http://www.camvaceng.com/assets/uploads/documents/EBW_versus_laser.pdf;

T7 Vi Khanh Truong, Vy T. H. Pham, Alexander Medvedev, Rimma Lapovok, Yuri Estrin, Terry C. Lowe, Vladimir Baulin, Veselin Boshkovikj, Christopher J. Fluke, Russell J. Crawford, Elena P. Ivanova, Self-organised nanoarchitecture of titanium surfaces influences the attachment of Staphylococcus aureus and Pseudomonas aeruginosa bacteria Appl Microbiol Biotechnol DOI 10.1007/s00253-015-6572-7;

T8 Vi K. Truong a, Rimma Lapovok b, c, Yuri S. Estrin b, c, d, Stuart Rundell b, James Y. Wang e, Christopher J. Fluke f, Russell J. Crawford a, Elena P. Ivanova a, The influence of nano-scale surface roughness on bacterial adhesion to ultrafine-grained titanium, Biomaterials 31 (2010) 3674–3683;

T9 Harris LG, Richards RG, Staphylococcus aureus adhesion to different treated titanium surfaces. J Mater Sci Mater Med 2004; 15:311–4;

T10 Harris LG, Richards RG, Staphylococcus aureus adhesion to different treated titanium surfaces. J Mater Sci Mater Med 2004; 15:311–4;

T11 https://en.wikipedia.org/wiki/Wetting;

RINGRAZIAMENTI